

**THREE-DIMENSIONAL IMAGING
OF
MULTI-COMPONENT
GROUND PENETRATING RADAR DATA**

**THREE-DIMENSIONAL IMAGING
OF
MULTI-COMPONENT
GROUND PENETRATING RADAR DATA**

PROEFSCHRIFT

ter verkrijging van de graad van doctor
aan de Technische Universiteit Delft,
op gezag van de Rector Magnificus Prof. ir. K.F. Wakker,
voorzitter van het College voor Promoties,
in het openbaar te verdedigen op 7 juni 2001 om 13.30 uur

door

Jan van der Kruk

elektrotechnisch ingenieur
geboren te Monster

Dit proefschrift is goedgekeurd door de promotoren:
Prof.dr.ir. J.T. Fokkema
Prof.dr.ir. P.M. van den Berg

Samenstelling promotiecommissie:

Rector Magnificus	Voorzitter,
Prof.dr.ir. J.T. Fokkema,	Technische Universiteit Delft, promotor
Prof.dr.ir. P.M. van den Berg,	Technische Universiteit Delft, promotor
Prof.dr.ir. C.P.A. Wapenaar,	Technische Universiteit Delft
Prof.ir. P. Hoogeboom,	Technische Universiteit Delft
Prof.dr. A.G. Green,	Eidgenössische Technische Hochschule (ETH) Zürich,
Dr. J.A.C. Meekes,	Netherlands Institute of Applied Geoscience TNO
A.P. Annan, Ph.D., P.Eng.	Sensors & Software Inc.

ISBN 90-9014706-3

Copyright ©2001 by J. van der Kruk, Section of Applied Geophysics, Department of Applied Earth Sciences, Faculty of Civil Engineering and Geosciences, Delft University of Technology.

All rights reserved. No parts of this publication may be reproduced, stored in a retrieval system or transmitted, in any form or by any means, electronic, mechanical, photocopying, recording, or otherwise, without the prior written permission of the author.

corrections: The 'introduction', 'conclusions and recommendations' and 'abstract' have been edited by Erody Consultants Ltd., G. Taylor.

aan mijn ouders

Support

The research reported in this thesis has been financially supported by the Dutch Technology Foundation (STW) and the Netherlands Institute of Applied Geoscience TNO.

Contents

1	Introduction	5
1.1	Principles of a ground penetrating radar survey	5
1.2	Reason for the research	9
1.3	Scientific strategy	11
1.4	Outline of the thesis	14
2	Basic electromagnetic equations	17
2.1	Maxwell's equations	18
2.2	The boundary conditions	19
2.3	The Laplace transformation	20
2.4	The temporal Fourier transformation	21
2.5	The spatial Fourier transformation	22
2.6	Transition to polar coordinates	23
2.7	Reciprocity theorem of Lorentz	24
2.7.1	The ω -domain wavefield reciprocity theorem	24
2.7.2	The limiting case of an unbounded domain	25
3	Solution procedure for the Maxwell equations in a horizontally layered medium	29
3.1	Basic relations for the electromagnetic waves in Fourier domain	30
3.2	Wavefield decomposition	31
3.3	Bi-orthogonal relations for eigenfunctions	36
3.4	Scattering theory	39

3.4.1	The scattering operator of a homogeneous interval . . .	41
3.4.2	The scattering operator of an interface	42
3.5	The presence of sources on an interface	43
3.5.1	Sources at an artificial interface	44
3.5.2	Sources at an interface between two different media . .	45
4	The electromagnetic field in a two-media configuration	49
4.1	Different regimes of the Maxwell's equations	50
4.2	Electromagnetic field expressions in the horizontal wavenumber domain	51
4.2.1	Electromagnetic field in two homogeneous half-spaces	52
4.2.2	Electromagnetic field in homogeneous space	54
4.3	Analytical derivation of closed-form expressions in the space-frequency domain	55
4.3.1	Electromagnetic field in homogeneous space	56
4.3.2	Electromagnetic field in two homogeneous half-spaces at the interface	60
4.4	Asymptotics for electric field generated by a horizontal electric dipole on an interface	63
4.5	Numerical evaluation of the integral expressions	66
4.6	Validation of the asymptotic expressions for the electric field	68
5	Theory of a ground penetrating radar survey	81
5.1	Forward source problem	82
5.2	Forward scattering problem	85
5.3	Scattering by a point scatterer	87
5.4	Scattering from an ensemble of point scatterers	89
5.5	Scattering formalism using the modified Born approximation	90
5.6	Acquisition set-up of a GPR survey	93
5.6.1	Orientations of the source and receiver antennas . . .	93
5.6.2	Common-offset measurement (profiling)	95
5.6.3	Common-midpoint measurement	96
5.6.4	3D survey measurements	97
5.7	Temporal and spatial sampling	98
5.7.1	Temporal sampling	99
5.7.2	Spatial sampling	99
5.7.3	Spatial sampling criterion for a point diffractor	100
5.7.4	Temporal and spatial bandwidth	103
5.8	Modelling results	108

5.8.1	The source wavelet	108
5.8.2	Measurement of different component of the scatter source	109
5.8.3	Measurements along an acquisition line	115
5.8.4	Measurements on an acquisition surface	119
5.9	Reduction of unwanted reflections from above surface objects	125
5.9.1	Field survey in Delft	126
5.9.2	Sensitivity for unwanted reflections from above surface objects	127
5.9.3	Numerical modelling of reflections from above surface objects.	129
5.9.4	Identification and reduction of unwanted reflections from above surface objects	134
6	Three-Dimensional Multi-Component Imaging	137
6.1	Introduction	138
6.2	Two-way wavefield extrapolator	140
6.3	Wavefield extrapolator in horizontal spatial Fourier domain .	142
6.4	Scalar inverse wavefield extrapolators	143
6.4.1	Gazdag Phase shift extrapolator	147
6.4.2	Synthetic Aperture Radar imaging	147
6.4.3	Comparison of scalar inverse wavefield extrapolators .	149
6.4.4	Inverse of scalar 3-D two-way wavefield extrapolator in a homogeneous space	150
6.5	Multi-component imaging algorithm	152
6.5.1	Multi-component 3D two-way wavefield extrapolator in a homogeneous space	152
6.5.2	Inverse of multi-component 3-D two-way wavefield extrapolator in a homogeneous space	153
6.5.3	Inverse of multi-component wavefield extrapolator in two homogeneous half-spaces	154
6.6	Imaging principle	155
6.7	Spatial resolution functions	158
6.7.1	Spatial resolution for Gazdag phase shift operator . .	162
6.7.2	Spatial resolution for SAR operator	163
6.7.3	Spatial resolution for 3-D downward extrapolation using the multi-component operator	164
6.7.4	Modified scalar inverse wavefield extrapolators	164
6.7.5	Spatial resolution function for a point scatterer in two homogeneous half-spaces	169

7	Experimental results at the testing site	179
7.1	Testing site	179
7.2	Buried objects	180
7.3	Description of the measurement set-up	181
7.4	Acquisition parameters	183
7.5	Pre-processing	184
7.6	Medium properties	185
7.7	Three-dimensional imaging results	187
7.7.1	Equi-amplitude surfaces for the multi-component imaging results in a three-dimensional volume	189
7.7.2	Comparison between the imaging algorithms in different planes	189
7.7.3	Comparison between the imaging algorithms along lines	199
8	Conclusions and Recommendations	211
A	Use of Stationary phase approximation for horizontal Fourier transformation	219
	Bibliography	223
	Summary	231
	Samenvatting	235
	Curriculum Vitae	239
	Dankwoord /Acknowledgements	241

Introduction

1.1 Principles of a ground penetrating radar survey

The shallow subsurface is becoming more important for engineering activities, environmental issues and archaeological investigations. It is important to obtain an image of the subsurface to find out the position of buried objects and the composition of the subsurface. This information is preferably obtained without disrupting the subsurface, and the technique dedicated to this task is called a non-destructive technique.

There are two important non-destructive techniques used to investigate the subsurface. The first uses sound waves which carry information about the different mechanical properties of the subsurface and any buried objects. Since buried objects and, for example, layers of sand and clay have different mechanical properties, their presence and delineation can be determined and visualised. Two examples of this mechanical technique are the high-resolution seismic reflection method and the seismic refraction method. The second technique uses electromagnetic waves and makes use of the electromagnetic properties of the subsurface. Here too, the differences in electromagnetic properties of objects and subsurface are used to produce an image of the subsurface. This technique is used by Ground Penetrating Radar systems (GPR) and is the main subject of this thesis.

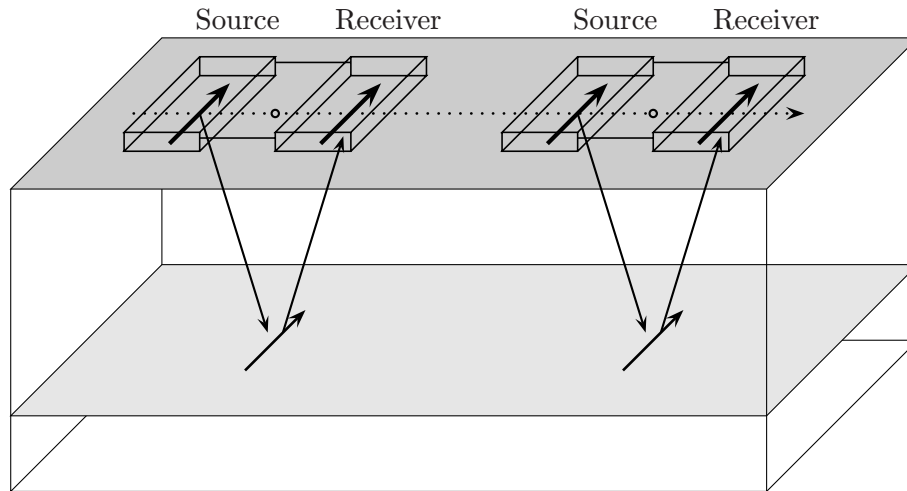


Figure 1.1: Common-offset measurement: Repeated measurements are made along a survey line.

A ground penetrating radar system consists of two antennas: a transmitting antenna, which emits an electromagnetic wave into the subsurface, and a receiving antenna, which detects the reflected waves coming from the subsurface. The reflected waves occur when the emitted electromagnetic waves encounter a different type of soil or an object. If the positions of the source and the receiver, or just the receiver, are varied, the data will contain information on the spatial variations of the subsurface and any buried objects. These data are used to obtain an image of the subsurface, for which various so-called *imaging techniques* are available. Sometimes an imaging technique that does not consider the polarisation of the waves or the radiation characteristics of the antennas is sufficient. Such a technique is attractive because it is quick and simple. However, the radiation characteristics and polarisation determine the strength of the reflected waves, and become more important as the subsurface becomes more complex. In this thesis we will develop an imaging algorithm which will incorporate these parameters and so obtain a representative image of a complicated subsurface. We will now discuss some examples in order to give an overview of the possible complexity of the subsurface and the required processing techniques.

If the subsurface consists of horizontal layers that vary gradually with depth,

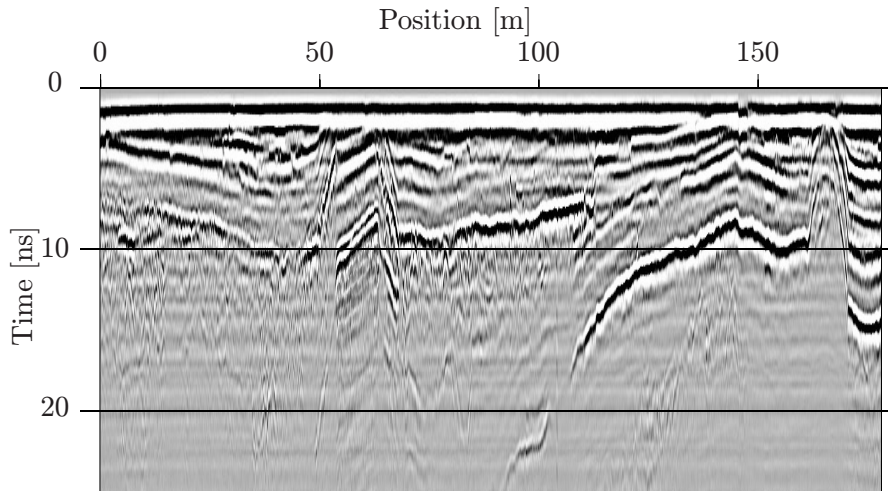


Figure 1.2: Measured reflections from a GPR survey along a survey line on a highway to determine the thickness of the asphalt layers.

the data require a minimum processing effort to obtain an image of these layers. The reason is that the visualisation of the data as a time-space representation already gives the desired image, as it may be assumed that the waves follow a path that lies right below the source and receiver positions as is indicated in Figure 1.1. Then the time information is simply converted to depth by using the measured wave speed. Figure 1.2 shows the data of a GPR measurement survey. This survey was carried out on a 200 m stretch of highway to determine the thickness of the asphalt layers. This investigation was commissioned by Rijkswaterstaat¹, who usually carry out such surveys by taking cores from the asphalt every 50 m. This damages the road and provides only local information. The GPR clearly indicated the lateral changes of the layers by plotting the data. In order to interpret the obtained results, we needed the wave speeds of the different asphalt layers. These wave speeds can be determined by correlating the arrival times of the reflected waves in the data with the thickness of the asphalt cores.

The next example is an investigation commissioned by Gasunie². We exam-

¹Rijkswaterstaat is the Road and Hydraulic Engineering Division of the Directorate General of Public Works and Water Management in the Netherlands

²Gasunie supplies gas to the Netherlands and Western Europe.

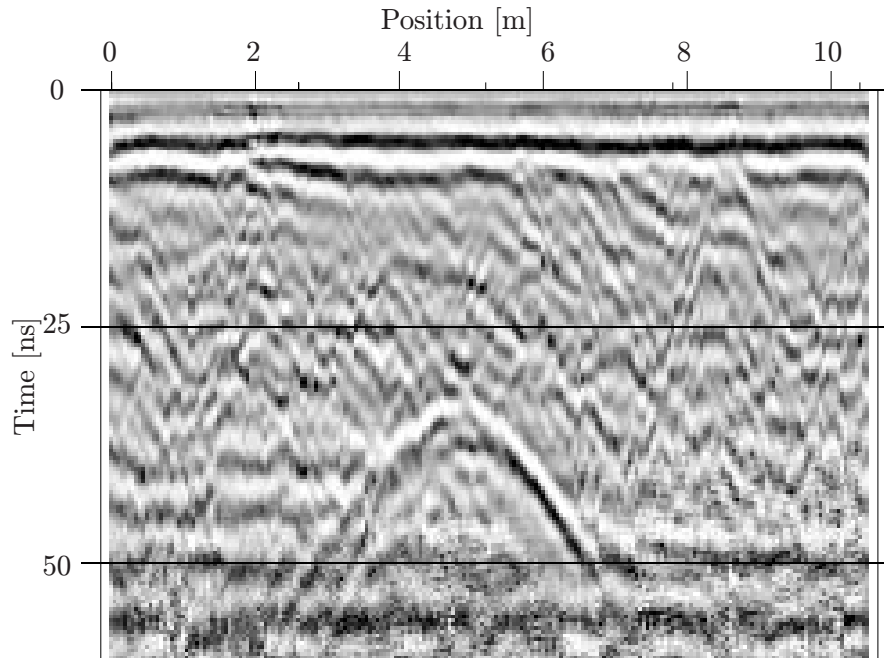


Figure 1.3: Measured reflections of a GPR survey along a survey line perpendicular to a buried gas pipe, which is visible as a clear hyperbola.

ined a long pipe lying horizontally, but running perpendicular to the survey line. Here we took the precaution of ensuring that the polarisation of the electric field was oriented parallel to the pipe to maximise the magnitude of the reflections. The object causes a hyperbolic event to appear in the data where it is plotted as a function of position and time. In Figure 1.3 the hyperbola from the gas pipe is clearly visible and has its apex at 5 m. Besides this event, many other smaller events can be observed. These are commonly called clutter, and are most likely due to inhomogeneities and other small objects in the soil. Due to the orientation of the gas pipe with respect to the survey line, the visualised data does not directly represent the position of the buried pipe, which is actually located at the apex. The algorithm needed to process the data so that the image will represent the pipe is called *imaging or migration*. For this, a two-dimensional (2D) algorithm is required which will map all the reflections to the apex. Heuristic imaging algorithms are based

on simple geometrical considerations. They stack the data of each separate trace at the point where it intersects a semi-hyperbola. The resulting amplitude is placed at the apex of the semi-hyperbola to obtain a 2D image. The wave speed needs to be known in order to perform this imaging procedure. If the pipe does not run horizontal and perpendicular to the survey line, as in Figure 1.3, a 2D imaging algorithm will give incorrect results. The reason is that the waves may reflect quite strongly from parts of the pipe that do not lie below the survey line. This is a complication that can be overcome by employing a three-dimensional (3D) imaging algorithm that accounts for wave propagation away from the survey line.

Other cases that motivate the use of 3D imaging are, for example, objects with finite extensions in all three dimensions or several pipes close to each other. In these cases, 3D imaging will improve spatial resolution and localisation of buried objects. 3D imaging will also require more measurements, which may be used to improve the signal-to-noise ratio, meaning the GPR can be used at greater depths. This possibility of obtaining high-resolution 3D images of the subsurface using ground penetrating radar, together with improved hardware and increased computing power, will lead to more 3D surveys using the GPR system. This has already been indicated by the increasing variety of applications presented at the bi-annual conferences on ground penetrating radar.

1.2 Reason for the research

Seismic imaging techniques were initially used for the imaging of GPR data because of similarities between acoustic and electromagnetic prospecting methods. Seismic techniques are used in oil and gas exploration to obtain an image of the subsurface (10 – 5000 m) by employing sound waves. The processing techniques necessary for such an image are far better developed than those for imaging the subsurface with Ground Penetrating Radar (GPR). The important differences are the vectorial character of electromagnetic waves compared to scalar acoustic waves, and the electromagnetic lossy properties of the earth compared to the acoustic properties, which are mostly lossless in the commonly used frequency band. Another difference is the acquisition setup. A GPR survey is usually carried out with one source and one receiver at a fixed distance, also called a common-offset measurement (see Figure 1.1). Whereas, a seismic survey needs for every source a number of receivers, also called a multi-offset measurement. These differences can make seismic

processing techniques inadequate for GPR data.

Three important parameters, which must be taken into account to obtain a representative image of the subsurface are, in order of importance, the wave speed, the polarisation and the amplitude of the electromagnetic waves. The most important parameter needed to obtain a good image of the subsurface is the (frequency dependent) wave speed. In a subsurface where losses have a great influence on the wave propagation, a frequency dependent wave speed or attenuation is present. This is also called dispersion [Sheriff, 1984]. Dispersion manifests itself as a pulse-shaped distortion as the travel path increases, caused by the fact that low-frequency energy suffers less attenuation and travels slower than high-frequency energy [Annan, 1996].

The second important parameter is the polarisation of the electromagnetic waves. Several papers have investigated the influence of polarisation on measured reflections as done by Radzevicius and Daniels [2000b], who showed that the backscattering properties become more polarisation dependent as the radius-to-wavelength ratio decreases. They also showed that low impedance dielectric pipes and metallic pipes are best imaged with the long axis of the dipole antennas oriented parallel to the long axis of the pipes. In this way the magnitude of the reflections is maximised as was done in order to obtain the results in Figure 1.3. The polarisation of the electromagnetic field manifests itself in the dipole nature of the source and the receiver antennas. This dipole nature results in the highly directional character of the radiation patterns of the source and the receiver antennas. These radiation characteristics determine to a large extent the amplitudes of the measured electromagnetic field, which is the third important parameter. Investigation of the amplitude characteristics by Zeng et al. [2000] shows that at the critical angle in the antenna radiation pattern a locally high amplitude in amplitude-versus-offset variations was present. Theoretical radiation characteristics have been validated in experiments carried out by Jiao et al. [2000], which show that these radiation characteristics play an important role in the amplitude of the measured reflections. On the whole, previously published results show that the polarisation, which manifests itself in the dipole nature of the source and the receiver antennas, and the pertaining radiation characteristics, play an important role in the measured reflections. However, the polarisation and radiation characteristics are rarely incorporated in the 3D imaging algorithms of GPR data.

Numerous papers describe the use of scalar seismic or remote sensing 2D imaging algorithms for the processing of GPR data [e.g. Fisher et al., 1992a;

Fisher et al., 1992b; Leuschen and Plumb, 2000]. These 2D imaging algorithms can also be adapted for the 3D case [e.g. Mast and Johansson, 1994; Johansson and Mast, 1994; Grasmueck, 1996; Binningsbø et al., 2000]. Seismic imaging algorithms are based on the fact that the source and receiver emit and receive acoustic waves with a circularly symmetrical radiation characteristic. GPR antennas radiate and receive electromagnetic waves with a strong directional dependence, which results in amplitude and phase variations of the reflections along the surfaces of equal travel time. These variations are not correctly employed when scalar imaging algorithms are used, which suggests that 3D imaging of GPR data can be enhanced by taking the radiation characteristics into account.

Recently, the radiation characteristics of elementary GPR antennas for GPR data imaging have been taken into account. Moran et al. [2000] used a modified Kirchhoff integral by inclusion of a half-space interfacial radiation pattern. Lehmann et al. [2000] combined coincidental georadar data sets with two pairs of parallel source-receiver antennas, one oriented perpendicular to the other to obtain a "pseudo scalar" wave field. Next, this pseudo scalar wave field was imaged using a standard 3D Kirchhoff time-migration scheme. Van Gestel and Stoffa [2000] modified a regular Kirchhoff migration by limiting the migration to those paths that are within the predicted angle of orientation. However, all these algorithms were still adapted from scalar imaging algorithms and use the knowledge of the radiation characteristics of elementary GPR antennas heuristically to obtain a better image. Scalar or heuristically based imaging algorithms, which do not incorporate the three important parameters adequately, will probably result in a distorted image. In more complicated investigations which demand an accurate representation of the subsurface, an improved and more representative image of the subsurface will be obtained by taking into account the vectorial character and the radiation characteristics.

1.3 Scientific strategy

The aim is to derive a three-dimensional imaging algorithm, which maps the measured reflections at the location where they originally came from and returns an image which represents the properties of the scatterer. As indicated previously, three important parameters are responsible for the performance of the imaging algorithm; the wave speed, and polarisation and amplitudes of the measured electromagnetic wavefield. The imaging algorithm must ju-

iciously incorporate these parameters. The forward model is used by the imaging algorithm and describes the influence of the three important parameters on the electromagnetic wavefield emitted by a GPR system, reflected by a scatterer and finally measured by a receiver.

Modelling and imaging are techniques which are closely related: modelling involves *forward extrapolation* and simulates the effects of wavefield propagation; imaging or migration involves *inverse extrapolation* and removes the effects of wavefield propagation. The relationship between forward extrapolation and inverse extrapolation of acoustic waves for the scalar wave equation, is described by Berkhout [1981] who shows that knowledge of the forward extrapolator is indispensable to obtaining an appropriate inverse extrapolator. GPR measurements are usually carried out on the surface of the earth, which requires a thorough analysis of the electromagnetic wave propagation (forward extrapolation) due to elementary antennas in the presence of a lossy layered half-space. A decomposition of the electromagnetic wavefield into up and downgoing decoupled propagating modes of different polarisations is carried out, which facilitates a thorough analysis and results in a better understanding of electromagnetic wave propagation in a lossy layered half-space.

To limit the calculation time of the imaging process, closed-form expressions for the radiation characteristics are required, which describe the amplitude and polarisation of the electric field being emitted. The steady-state far-field solutions for an interfacial infinitesimal dipole on a *lossless* dielectric half-space are well known and have been discussed by Annan [1973], Annan et al. [1975], Engheta et al. [1982] and Smith [1984]. This two-media configuration is a special case of a layered half-space. Asymptotic expressions for the electric field in a *high-loss* two-media configuration are given by Baños [1966] and King and Smith [1981] after neglecting the displacement currents. The relationship between the asymptotic expressions in a *lossless* and *high-loss* medium will be analysed. The obtained closed-form expressions are compared to the exact expressions for the electric wavefield, which are evaluated by numerical calculation of the integral expressions.

The forward model is a starting point for the imaging algorithm and will be incorporated into the imaging algorithm. The forward model used is the 3D vectorial scattering formalism of an elementary point scatterer using elementary dipole antennas on the interface of two homogeneous half-spaces. Several independent point scatterers are considered to represent a bounded contrasting domain. Both source and receiver influence the measured elec-

tric field. Similar radiation characteristics for the source antenna can be used to describe the performance of the receiver antenna. The appropriate acquisition set-up for a three-dimensional survey is analysed by discussing the temporal and spatial sampling criteria and the possible orientation of the source and receiver antennas. Synthetic data is presented, which clearly reflect the influence of the polarisation and the amplitude characteristics of the source and receiver antennas. In this way a sensitivity analysis can be carried out for possible scatterers. A qualitative indication of the sensitivity of the reflections is obtained by analysing the orientation of the scatterer, the radiation characteristics and the vectorial scattering formalism. These results show how to increase the sensitivity of subsurface reflections. On the other hand, these results also demonstrate how to reduce the measurement of unwanted reflections from objects on or above the soil.

For an optimal reconstruction it is necessary to measure the data that completely surround the contrasting domain. However, this was not possible in our case; we were restricted to measurements carried out on the surface of the earth. These measurements were carried out with specific time and spatial sampling. For an accurate sampling of the measured reflections the temporal and spatial sampling criteria must be satisfied. The influence of the limited acquisition plane and the radiation characteristics of the source and receiver antennas on the spatial sampling criterion were investigated. The results obtained also show the spatial and temporal bandwidths of the measurements, which were available for the imaging procedure.

An inverse extrapolation was carried out using the available information dictated by the temporal and spatial bandwidths, which took into account the source and receiver antenna radiation characteristics, subsequently followed by the imaging principle, which changes the temporal dependency into depth dependency. This resulted in a representative image of the contrasting domain. A consequence of the vectorial character of the scattered electric wavefield is that for a stable inverse extrapolation more components must be combined, resulting in a multi-component 3D imaging algorithm for GPR data. The performance of the multi-component, 3D imaging algorithm is validated by the imaging of a point scatterer in a dielectric medium.

A full-size testing site was constructed in the city of Scheveningen at the site of FEL-TNO³ on the initiative of the Department of Applied Earth Sciences, which made it possible to obtain measurements under controlled conditions. Experiments were carried out at the testing site to investigate

³TNO Physics and Electronics Laboratory

the performance of the multi-component imaging algorithm.

The obtained image is the final result of a field survey, which comprised the design of the antennas, the acquisition of field data and the imaging procedure, in which the appropriate accurate forward model was used. In this thesis, we will assume that the source and receiver can be considered as point sources and discuss the appropriate elements needed to obtain a three dimensional image of the subsurface.

1.4 Outline of the thesis

After a short introductory chapter we will discuss the fundamental Maxwell equations, the boundary conditions for the electromagnetic wavefield and some mathematical tools. In Chapter 3, the Maxwell equations are analysed in a horizontally layered medium, of which the two-media configuration is a special case. The horizontal components of the electromagnetic wavefield are used to derive a diagonalisation procedure in the horizontal spatial Fourier domain, which facilitates a decomposition into up and down-going elementary waves. The reflection and transmission at the interface and the propagation in the absence of such an interface enables the derivation of expressions for the electromagnetic wavefield in a horizontally layered medium. The two-media configuration in which the source and receiver are present on the interface will be used as a starting point to obtain closed-form asymptotic expressions for the electromagnetic wavefield present in the upper and lower half-space of the two-media configuration. This topic is discussed in the next chapter. In Chapter 4, we will discuss a number of asymptotic expressions. Baños [1966] derived asymptotic expressions for the basic functions in terms of a complex propagation constant used to describe the diffusive field present in two homogeneous half-spaces. It has been observed that the expressions derived by Baños [1966] are equivalent to the far-field expressions given by Engheta et al. [1982]. The latter, however, were derived from a lossless dielectric half-space. The asymptotic expressions obtained are compared with the results for the exact electric wavefield and its validity with respect to GPR applications is discussed.

In Chapter 5 the theoretical framework of a ground penetrating radar survey is discussed. Expressions for the electromagnetic scattering formalism are presented using the results in Chapter 4 and synthetic data results are discussed for different acquisition set-ups. In particular we consider non-interacting point scatterers. This constitutes the basis for the multi-

component imaging algorithm, which is discussed in the next chapter.

In Chapter 6, the scattering formalism is analysed. It is convenient to combine the propagation of the vector electric wavefield from the source towards the scatterer and from the scatterer back to the receiver by introducing a two-way forward wavefield extrapolator. For a zero-offset configuration we can derive analytical expressions for the wavefield extrapolator in a homogeneous space. This forward wavefield extrapolator takes into account the orientation of the source, the scattering discontinuity represented by an equivalent scatter-source and the receiver. The relationship between the forward wavefield extrapolator, and two scalar inverse wavefield extrapolators used by the Synthetic Aperture Radar (SAR) algorithm [Curlander and McDonough, 1991]) and the Gazdag algorithm [Gazdag, 1978], are discussed. These scalar inverse wavefield extrapolators are not based on the forward wavefield extrapolator. We show that the scalar inverse wavefield operators do not reconstruct a point scatterer adequately, which is the reason to introduce modified scalar inverse wavefield extrapolators. Still, these modified SAR and Gazdag extrapolators do not result in the desired circularly symmetric resolution function. This indicates that the vector character and the radiation characteristics of the source and receiver antennas have to be taken into account. To this end, a tensorial two-way wavefield extrapolator is introduced, which needs two source and two receiver orientations. Indeed, the multi-component imaging algorithm results in a circularly symmetric resolution function of the point scatterer. It is not feasible to perform a similar analytical approach for two homogeneous half-spaces. However, the same procedure can be carried out in a numerical way, which has the important benefit that the offset between the source and receiver can also be taken into account. Numerical results are presented for two homogeneous half-spaces and imaging results of the experiments are presented incorporating the vectorial character of the measured electric wavefield and the offset between the source and receiver, which are present on a dielectric homogeneous half-space.

In Chapter 7, the results of the experiments show the imaging results using the multi-component imaging algorithm. These are compared with the results using scalar imaging algorithms and indicate that more representative images are obtained by using the multi-component algorithm.

Chapter 8 summarises the most important conclusions and observations contained in this thesis.

Basic electromagnetic equations

In this chapter the basic electromagnetic equations are discussed, which are described in the space-time domain. To specify position in the used configuration we employ the coordinates (x_1, x_2, x_3) with respect to a fixed, right-handed, orthogonal, Cartesian reference frame with origin \mathcal{O} and with three orthogonal base vectors $(\mathbf{i}_1, \mathbf{i}_2, \mathbf{i}_3)$, where \mathbf{i}_3 is pointing downwards. The subscript notation is chosen to describe the relations between the wavefield vectors and medium properties. Any repeated subscript implies the application of the summation convention. In this way the position in our configuration may be written as $\mathbf{x} = x_1 \mathbf{i}_1 + x_2 \mathbf{i}_2 + x_3 \mathbf{i}_3$ or $\mathbf{x} = x_p \mathbf{i}_p$ with $p \in \{1, 2, 3\}$ and $\mathbf{x} \in \mathbb{R}^3$.

Temporal and spatial transformations are carried out, which enable an analysis for each temporal frequency and spatial frequency component separately. These separate components are more easily analysed than their complete spatial- and time-domain counterparts. The temporal Fourier transformation is used for causal functions in time, and for a bounded or unbounded domain in space we use the two-dimensional spatial Fourier transformation. The reason for this choice stems from the fact that a simplified GPR configuration can be described by a horizontally layered earth, which enables a transformation of the wavefield into its horizontal plane-wave components.

2.1 Maxwell's equations

The electromagnetic field equations, also known as Maxwell's equations, are given by

$$-\epsilon_{k,m,p}\partial_m H_p + \partial_t D_k + J_k = -J_k^e, \quad (2.1a)$$

$$\epsilon_{j,m,r}\partial_m E_r + \partial_t B_j = -K_j^e, \quad (2.1b)$$

where ϵ_{kmp} is a unit tensor of rank three (Levi-Civita tensor) which is defined as

$$\epsilon_{kmp} = \begin{cases} +1 & \text{when } \{k, m, p\} \text{ is an even permutation of } \{1, 2, 3\}, \\ 0 & \text{when two or more subscripts are equal,} \\ -1 & \text{when } \{k, m, p\} \text{ is an odd permutation of } \{1, 2, 3\}. \end{cases} \quad (2.2)$$

Compatibility equations are obtained by applying the operator ∂_k and ∂_j to Eqs. (2.1a) and (2.1b), respectively. This results in

$$\partial_k [J_k + \partial_t D_k] = -\partial_k J_k^e, \quad (2.3a)$$

$$\partial_j \partial_t B_j = -\partial_j K_j^e. \quad (2.3b)$$

The quantities occurring in Eqs. (2.1a) – (2.3b) are given by

- $E_k(\mathbf{x}, t)$ = electric field strength (Vm^{-1}) ,
- $H_j(\mathbf{x}, t)$ = magnetic field strength (Am^{-1}) ,
- $J_k(\mathbf{x}, t)$ = volume density of electric current (Am^{-2}) ,
- $D_k(\mathbf{x}, t)$ = electric displacement flux density (Cm^{-2}) ,
- $B_j(\mathbf{x}, t)$ = magnetic flux density (T) ,
- $J_k^e(\mathbf{x}, t)$ = volume source density of electric current (Am^{-2}) ,
- $K_j^e(\mathbf{x}, t)$ = volume source density of magnetic current (Vm^{-2}) ,
- ∂_m = partial differentiation with respect to x_m (m^{-1}) ,
- ∂_t = partial differentiation with respect to time (s^{-1}) .

Equations (2.1a) and (2.1b) are now supplemented by three vector relations between the five wavefield quantities, which occur in both equations. These supplementary relations are known as the constitutive relations and give a relation between the quantities $\{J_k, D_k, B_k\}$ and $\{E_k, H_k\}$, which are representative for the macroscopic electromagnetic properties of the media in our configuration. These electromagnetic properties are described by the positive parameters ; permittivity ϵ (Fm^{-1}), permeability μ (Hm^{-1}) and conductivity

σ (Sm^{-1}). We consider media, which are linear, locally and instantaneously reacting, time invariant, isotropic, and inhomogeneous. The constitutive relations are given by

$$J_k(\mathbf{x}, t) = \sigma(\mathbf{x})E_k(\mathbf{x}, t), \quad (2.4a)$$

$$D_k(\mathbf{x}, t) = \varepsilon(\mathbf{x})E_k(\mathbf{x}, t), \quad (2.4b)$$

$$B_k(\mathbf{x}, t) = \mu(\mathbf{x})H_k(\mathbf{x}, t). \quad (2.4c)$$

Substitution of the former three equations in Maxwell's equations, Eqs. (2.1a) and (2.1b), results in

$$-\epsilon_{kmp}\partial_m H_p(\mathbf{x}, t) + [\sigma(\mathbf{x}) + \varepsilon(\mathbf{x})\partial_t]E_k(\mathbf{x}, t) = -J_k^e(\mathbf{x}, t), \quad (2.5a)$$

$$\epsilon_{jmr}\partial_m E_r(\mathbf{x}, t) + \mu(\mathbf{x})\partial_t H_j(\mathbf{x}, t) = -K_j^e(\mathbf{x}, t). \quad (2.5b)$$

For a medium that is also homogeneous, the scalar conductivity σ , the scalar permittivity ε and the scalar permeability μ are constants and the constitutive relations are then

$$J_k(\mathbf{x}, t) = \sigma E_k(\mathbf{x}, t), \quad (2.6a)$$

$$D_k(\mathbf{x}, t) = \varepsilon E_k(\mathbf{x}, t), \quad (2.6b)$$

$$B_k(\mathbf{x}, t) = \mu H_k(\mathbf{x}, t). \quad (2.6c)$$

2.2 The boundary conditions

When the wavefield is present in a piecewise continuous medium, the wavefield solutions are constrained by the boundary conditions valid on the interface between the continuous media. At the interface \mathcal{S} between \mathbb{D}_s and \mathbb{D}_{s+1} as depicted in Figure 2.1, the constitutive parameters may jump by finite amounts. As a consequence of this, some components of the electromagnetic field quantities may show a discrete discontinuity. In case the partial derivatives perpendicular to \mathcal{S} would meet functions that show a discontinuity, this would lead to interface Dirac distributions located at the interface \mathcal{S} , and represent impulsive interface sources. In the absence of such sources, the absence of such interface impulses in the partial derivatives across the interface must be enforced, so the following boundary conditions are valid at a source free interface:

$$\epsilon_{kmp}\nu_m H_p \text{ is continuous across } \mathcal{S}, \quad (2.7a)$$

$$\epsilon_{jmr}\nu_m E_r \text{ is continuous across } \mathcal{S}, \quad (2.7b)$$

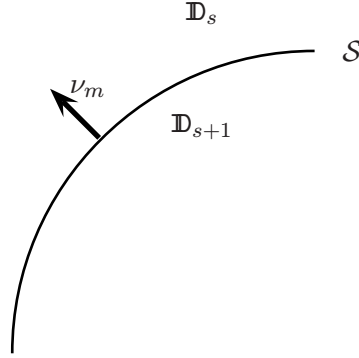


Figure 2.1: Interface between two media with different electromagnetic properties.

and

$$\nu_k(\sigma + \varepsilon\partial_t)E_k \text{ is continuous across } \mathcal{S}, \quad (2.8a)$$

$$\nu_j\mu\partial_t H_j \text{ is continuous across } \mathcal{S}. \quad (2.8b)$$

Notice that Eqs. (2.8a) and (2.8b) are not independent conditions; they are conditions corresponding to the compatibility equations (2.3a) and (2.3b).

2.3 The Laplace transformation

Let us assume that the source that generates the electromagnetic wave is switched on at the instant $t = 0$. In view of the causality condition the source affects the wavefield in the interval T defined as

$$T = \{t \in \mathbb{R}; t > 0\}. \quad (2.9)$$

The complement T' of the interval T and the boundary ∂T between the two intervals are defined according to

$$T' = \{t \in \mathbb{R}; t < 0\}, \quad (2.10a)$$

$$\partial T = \{t \in \mathbb{R}; t = 0\}. \quad (2.10b)$$

The characteristic function $\chi_T(t)$ of the set T is introduced as

$$\chi_T(t) = \{1, \frac{1}{2}, 0\}, \text{ when } t \in \{T, \partial T, T'\}. \quad (2.11)$$

Now, we define the one-sided Laplace transformation of some causal space time quantity $f(\mathbf{x}, t)$ as

$$\hat{f}(\mathbf{x}, s) = \int_{t \in \mathbf{R}} \exp(-st) \chi_T(t) f(\mathbf{x}, t) dt, \quad \text{for } \text{Re}(s) > 0. \quad (2.12)$$

A function in the time domain can be reconstructed from its Laplace transform by explicitly evaluating the Bromwich integral, which acts as the inverse Laplace transformation. The Bromwich integral is expressed as

$$\chi_T(t) f(\mathbf{x}, t) = \frac{1}{2\pi j} \int_{s_0 - j\infty}^{s_0 + j\infty} \exp(st) \hat{f}(\mathbf{x}, s) ds, \quad (2.13)$$

where the path of integration of the Bromwich integral is parallel to the imaginary axis of the complex s -plane ($s = s_0, s_0 \in \mathbf{R}$) situated in the right half of the complex s -plane where the Laplace transform itself is analytic ($s_0 > 0$). Simple rules of the one-sided Laplace transformation hold, such as the replacement of ∂_t by s and the replacement of a convolution of two time domain quantities by the product of two complex s -domain quantities.

2.4 The temporal Fourier transformation

We define the temporal Fourier transformation acting on some causal space-time quantity $f(\mathbf{x}, t)$ as the limiting behaviour of the Laplace transformation for imaginary transform parameter, $s \rightarrow j\omega$, leading to

$$\hat{f}(\mathbf{x}, \omega) = \int_{t \in \mathbf{R}} \exp(-j\omega t) \chi_T(t) f(\mathbf{x}, t) dt. \quad (2.14)$$

The inverse Fourier transformation is found by taking the inverse Laplace transformation in the limit of imaginary transform parameter resulting in

$$\chi_T(t) f(\mathbf{x}, t) = \frac{1}{2\pi} \int_{\omega \in \mathbf{R}} \exp(j\omega t) \hat{f}(\mathbf{x}, \omega) d\omega. \quad (2.15)$$

Applying the rule in Eq. (2.5) that ∂_t transforms to $j\omega$ leads to the following electromagnetic equations in the ω -domain valid for homogeneous media

$$-\epsilon_{kmp} \partial_m \hat{H}_p(\mathbf{x}, \omega) + \hat{\eta} \hat{E}_k(\mathbf{x}, \omega) = -\hat{J}_k^e(\mathbf{x}, \omega), \quad (2.16a)$$

$$\epsilon_{jmr} \partial_m \hat{E}_r(\mathbf{x}, \omega) + \hat{\zeta} \hat{H}_j(\mathbf{x}, \omega) = -\hat{K}_j^e(\mathbf{x}, \omega), \quad (2.16b)$$

in which the quantities $\hat{\eta}$ and $\hat{\zeta}$ are defined as

$$\hat{\eta} = \sigma + j\omega\varepsilon, \quad (2.17a)$$

$$\hat{\zeta} = j\omega\mu. \quad (2.17b)$$

2.5 The spatial Fourier transformation

In this thesis we will focus mainly on horizontally layered homogeneous media. To take advantage of the shift invariance of this configuration in the horizontal directions, we introduce the Fourier transformations with respect to the horizontal coordinates x_1 and x_2 . Let a scalar function $\hat{f}(\mathbf{x}, \omega)$ be defined in some bounded or unbounded domain \mathbf{D} in two-dimensional (horizontal) space. The characteristic function $\chi_{\mathbf{D}}$ of its domain, can be defined in terms of \mathbf{D} , the boundary surface $\partial\mathbf{D}$ and domain \mathbf{D}' , the complement $\mathbf{D} \cup \partial\mathbf{D}$ in \mathbb{R}^2 , as

$$\chi_{\mathbf{D}}(\mathbf{x}) = \left\{1, \frac{1}{2}, 0\right\}, \text{ when } \{x_1, x_2\} \in \{\mathbf{D}, \partial\mathbf{D}, \mathbf{D}'\}. \quad (2.18)$$

Now we can define the horizontal Fourier transformation acting on a quantity $\hat{f}(\mathbf{x}, \omega)$, defined in the unbounded or bounded domain \mathbf{D} in terms of the real horizontal angular wavenumbers k_1 and k_2 , as

$$\tilde{f}(k_1, k_2, x_3, \omega) = \int_{(x_1, x_2) \in \mathbb{R}^2} \exp(jk_\alpha x_\alpha) \chi_{\mathbf{D}}(\mathbf{x}) \hat{f}(\mathbf{x}, \omega) dA, \quad (2.19)$$

where Greek lower-case subscripts are used to indicate the horizontal angular wavenumbers; they run through the values 1 and 2 only. The transformation parameters are k_1 and k_2 with $\{k_1, k_2\} \in \mathbb{R}^2$, which are associated with x_1 and x_2 , respectively. The transformation from the horizontal wavenumber domain back to the spatial domain is carried out by employing the Fourier inversion integral

$$\chi_{\mathbf{D}}(\mathbf{x}) \hat{f}(\mathbf{x}, \omega) = \left(\frac{1}{2\pi}\right)^2 \int_{(k_1, k_2) \in \mathbb{R}^2} \exp(-jk_\alpha x_\alpha) \tilde{f}(k_1, k_2, x_3, \omega) dA. \quad (2.20)$$

Applying the rule that $\partial_\alpha \rightarrow -jk_\alpha$, the application of the transformation indicated in Eq. (2.19) to Eqs. (2.16a) and (2.16b), leads to the following Maxwell's equations in the transform domain

$$\begin{aligned} -\epsilon_{k3p} \partial_3 \tilde{H}_p(k_1, k_2, x_3, \omega) + jk_\alpha \epsilon_{k\alpha p} \tilde{H}_p(k_1, k_2, x_3, \omega) + \hat{\eta} \tilde{E}_k(k_1, k_2, x_3, \omega) \\ = -\tilde{J}_k^e(k_1, k_2, x_3, \omega), \end{aligned} \quad (2.21a)$$

$$\begin{aligned} \epsilon_{j3r} \partial_3 \tilde{E}_r(k_1, k_2, x_3, \omega) - j k_\beta \epsilon_{j\beta r} \tilde{E}_r(k_1, k_2, x_3, \omega) + \hat{\zeta} \tilde{H}_j(k_1, k_2, x_3, \omega) \\ = -\tilde{K}_j^e(k_1, k_2, x_3, \omega). \end{aligned} \quad (2.21b)$$

2.6 Transition to polar coordinates

When the configuration is shift invariant in the horizontal direction, it is efficient to change to polar coordinates, because this can reduce the number of integrals. Polar coordinates (r, ϕ) are introduced, according to

$$x_1 = r \cos(\phi), \quad (2.22a)$$

$$x_2 = r \sin(\phi). \quad (2.22b)$$

In a similar way, we introduce the polar coordinates (κ, ψ) as

$$k_1 = \kappa \cos(\phi - \psi), \quad (2.23a)$$

$$k_2 = \kappa \sin(\phi - \psi), \quad (2.23b)$$

so that

$$dk_1 dk_2 = \kappa d\kappa d\psi, \text{ where } 0 < \kappa < \infty, \quad 0 < \psi < 2\pi. \quad (2.24)$$

In the following analysis we assume that $\tilde{f}(\kappa, \psi, x_3, \omega)$ is independent of ψ . We denote this function as $\tilde{f}(\kappa, x_3, \omega)$. Using the goniometric identity

$$\cos(\phi) \cos(\phi - \psi) + \sin(\phi) \sin(\phi - \psi) = \cos(\psi), \quad (2.25)$$

the inverse spatial Fourier transformation as in Eq. (2.20) can then be rewritten for an unbounded domain \mathbb{D} as

$$\hat{f}(r, \phi, x_3, \omega) = \left(\frac{1}{2\pi}\right)^2 \int_{\kappa=0}^{\infty} \kappa d\kappa \int_{\psi=0}^{2\pi} \exp[-j\kappa r \cos(\psi)] \tilde{f}(\kappa, x_3, \omega) d\psi. \quad (2.26)$$

Using the fact that, [Abramowitz and Stegun, 1964]

$$\int_{\psi=0}^{2\pi} \exp[j\kappa r \cos(\psi)] \cos(n\psi) d\psi = 2\pi j^n J_n(\kappa r), \quad (2.27)$$

Equation (2.26) can now be written as

$$\hat{f}(r, \phi, x_3, \omega) = \frac{1}{2\pi} \int_{\kappa=0}^{\infty} \tilde{f}(\kappa, x_3, \omega) J_0(\kappa r) \kappa d\kappa, \quad (2.28a)$$

$$= \frac{1}{4\pi} \int_{\kappa=-\infty}^{\infty} \tilde{f}(\kappa, x_3, \omega) H_0^{(2)}(\kappa r) \kappa d\kappa. \quad (2.28b)$$

2.7 Reciprocity theorem of Lorentz

A reciprocity theorem interrelates, in a specific way, the field quantities associated with two non-identical physical states that could occur in one and the same, time-invariant, domain \mathbf{D} in space. The media in this domain are assumed to be time-invariant as well as linear in their electromagnetic behaviour. The boundary surface of \mathbf{D} is denoted by $\partial\mathbf{D}$; the normal vector ν_k on $\partial\mathbf{D}$ is directed away from \mathbf{D} . The complement of $\mathbf{D} \cup \partial\mathbf{D}$ in \mathbb{R}^3 is denoted by \mathbf{D}' .

2.7.1 The ω -domain wavefield reciprocity theorem

We start with the basic ω -domain electromagnetic field equations. State A is characterized by the wavefield $\{\hat{E}_k^A, \hat{H}_j^A\}$, the constitutive parameters $\{\varepsilon^A, \sigma^A, \mu^A\}$ and the source distributions $\{\hat{J}_k^{e;A}, \hat{K}_j^{e;A}\}$. Similarly, State B is characterized by the wavefield $\{\hat{E}_k^B, \hat{H}_j^B\}$, the constitutive parameters $\{\varepsilon^B, \sigma^B, \mu^B\}$ and the source distributions $\{\hat{J}_k^{e;B}, \hat{K}_j^{e;B}\}$. The electromagnetic field equations pertaining to State A are then

$$-\epsilon_{kmp}\partial_m\hat{H}_p^A + \hat{\eta}^A\hat{E}_k^A = -\hat{J}_k^{e;A}, \quad (2.29a)$$

$$\epsilon_{jmr}\partial_m\hat{E}_r^A + \hat{\zeta}^A\hat{H}_j^A = -\hat{K}_j^{e;A}. \quad (2.29b)$$

Similarly, the electromagnetic field equations pertaining to State B are

$$-\epsilon_{kmp}\partial_m\hat{H}_p^B + \hat{\eta}^B\hat{E}_k^B = -\hat{J}_k^{e;B}, \quad (2.30a)$$

$$\epsilon_{jmr}\partial_m\hat{E}_r^B + \hat{\zeta}^B\hat{H}_j^B = -\hat{K}_j^{e;B}. \quad (2.30b)$$

If, in \mathbf{D} , surfaces of discontinuity in electromagnetic properties are present, Eqs. (2.29a) - (2.30b) are supplemented by boundary conditions. In the time convolution type reciprocity relation, that is named after H.A. Lorentz, the fundamental interaction quantity between the two states is

$$\begin{aligned} & \epsilon_{mkj}\partial_m(\hat{E}_k^A\hat{H}_j^B - \hat{E}_k^B\hat{H}_j^A) \\ & = \epsilon_{mkj}(\hat{H}_j^B\partial_m\hat{E}_k^A + \hat{E}_k^A\partial_m\hat{H}_j^B - \hat{H}_j^A\partial_m\hat{E}_k^B + \hat{E}_k^B\partial_m\hat{H}_j^A). \end{aligned} \quad (2.31)$$

Upon multiplying Eq. (2.29a) by \hat{E}_k^B , Eq. (2.29b) by \hat{H}_j^B , Eq. (2.30a) by \hat{E}_k^A and Eq. (2.30b) by \hat{H}_j^A , and using the result in Eq. (2.31), we arrive at

$$\begin{aligned} & \epsilon_{mkj} \partial_m (\hat{E}_k^A \hat{H}_j^B - \hat{E}_k^B \hat{H}_j^A) \\ &= (\hat{\zeta}^B - \hat{\zeta}^A) \hat{H}_j^A \hat{H}_j^B - (\hat{\eta}^B - \hat{\eta}^A) \hat{E}_k^A \hat{E}_k^B \\ & \quad - \hat{K}_j^{e;A} \hat{H}_j^B - \hat{J}_k^{e;B} \hat{E}_k^A + \hat{K}_j^{e;B} \hat{H}_j^A + \hat{J}_k^{e;A} \hat{E}_k^B. \end{aligned} \quad (2.32)$$

Equation (2.32) is the local form of the Lorentz reciprocity theorem. Integration of Eq. (2.32) over the domain \mathbf{D} and the use of Gauss' theorem in the resulting left-hand side leads to

$$\begin{aligned} & \int_{\mathbf{x} \in \partial \mathbf{D}} \epsilon_{mkj} (\hat{E}_k^A \hat{H}_j^B - \hat{E}_k^B \hat{H}_j^A) \nu_m dA \\ &= \int_{\mathbf{x} \in \mathbf{D}} [(\hat{\zeta}^B - \hat{\zeta}^A) \hat{H}_j^A \hat{H}_j^B - (\hat{\eta}^B - \hat{\eta}^A) \hat{E}_k^A \hat{E}_k^B] dV \\ & \quad + \int_{\mathbf{x} \in \mathbf{D}} (\hat{J}_r^{e;A} \hat{E}_r^B - \hat{K}_p^{e;A} \hat{H}_p^B - \hat{J}_k^{e;B} \hat{E}_k^A + \hat{K}_j^{e;B} \hat{H}_j^A) dV. \end{aligned} \quad (2.33)$$

Equation (2.33) is Lorentz's reciprocity theorem in its global form for the domain \mathbf{D} . First of all, it is remarked that the first and the second term on the right-hand side of Eq. (2.32), as well as the first integral on the right-hand side of Eq. (2.33), vanish in case the media in the two states are chosen such that $\hat{\eta}^A = \hat{\eta}^B$ and $\hat{\zeta}^A = \hat{\zeta}^B$. Under these conditions, the interaction between the two states is only related to the source distributions in the two states. If, in addition, these source distributions vanish in some domain, the relevant interactions (local or global) are zero in that domain.

2.7.2 The limiting case of an unbounded domain

In quite a number of cases it is desirable to apply the reciprocity theorem of Eq. (2.33) to an unbounded domain. These cases will always be handled as the limiting one that occurs if \mathbf{D} is taken to be the bounded domain \mathbf{D}_Δ , being the sphere interior to the spherical surface $\partial \mathbf{D}_\Delta$ with radius Δ and center at the origin \mathcal{O} of the chosen coordinate system. In the relevant result the limit $\Delta \rightarrow \infty$ is considered (see Fig. (2.2)).

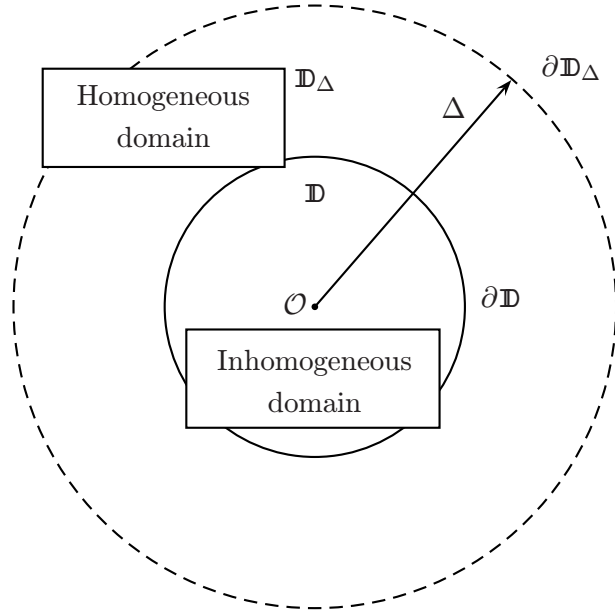


Figure 2.2: Unbounded configuration for the application of the reciprocity theorem.

Obviously, then we must evaluate the left-hand side of Eq. (2.33) on $\partial\mathbb{D}_\Delta$. To this end, we shall always assume that outside some sphere of bounded radius, and center at the origin of the chosen coordinate system, the medium is homogeneous with position independent parameters $\hat{\eta}$ and $\hat{\zeta}$. In the relevant results we let $\Delta \rightarrow \infty$. Taking the electromagnetic wavefield in both states to be causally related to the action of their sources, the latter being non-vanishing in some bounded subdomain of space only, it follows that the contribution from the boundary integral vanishes in the limit $\Delta \rightarrow \infty$. This is confirmed by using the expansion for the wavefield as given in Eqs. (4.16a)-(4.16d) where it follows that, as $\Delta \rightarrow \infty$, the terms in the expansion of $\hat{E}_k \hat{H}_j$ of Order (Δ^{-2}) in the integral over $\partial\mathbb{D}_\Delta$ cancel. The next term in the expansion of $\hat{E}_k \hat{H}_j$ as $\Delta \rightarrow \infty$ is of Order (Δ^{-3}) (the intermediate-region fields). Therefore,

$$\epsilon_{mkj}(\hat{E}_k^A \hat{H}_j^B - \hat{E}_k^B \hat{H}_j^A) = \text{Order } (\Delta^{-3}) \text{ as } \Delta \rightarrow \infty. \quad (2.34)$$

Consequently (note that the area of $\partial\mathbb{D}_\Delta$ is $4\pi\Delta^2$), we obtain the causality

condition

$$\int_{\mathbf{x} \in \partial \mathbf{D}_\Delta} \epsilon_{mkj} (\hat{E}_k^A \hat{H}_j^B - \hat{E}_k^B \hat{H}_j^A) \nu_m dA = \text{Order}(\Delta^{-1}) \text{ as } \Delta \rightarrow \infty, \quad (2.35)$$

and the left-hand side of Eq. (2.33) vanishes in the limit $\Delta \rightarrow \infty$. Further, the integration domain \mathbf{D} of the integrals in the right-hand side of Eq. (2.33) becomes the domain \mathbb{R}^3 . More about the application of the reciprocity theorem may be found, for example, in Fokkema and van den Berg [1993]; de Hoop [1995].

■

The Maxwell equations in temporal frequency and horizontal spatial Fourier domain, given in Section 2.5, form the starting point to describe wave propagation in a horizontally layered medium. The reciprocity theorem is used to motivate our choice of the specific decomposition of the wavefield into a set of independent eigenfunctions, which describe the standard TE and TM polarisation modes. Moreover, the reciprocity theorem forms the basis to derive the vectorial scatter mechanism in Chapter 5.

Solution procedure for the Maxwell equations in a horizontally layered medium

GPR measurements are usually carried out on the surface of the earth. This requires expressions for the electromagnetic field that describe the performance of elementary antennas in the presence of a lossy layered half-space. In particular, the behaviour of sources on the interface is important to describe the performance of GPR antennas correctly. This two-media configuration is a special case of the layered half-space.

A horizontally layered earth enables a transformation of the wavefield into its horizontal plane-wave components. We will show that four independent eigenfunctions of the wave equations in the time and horizontal space transformed domain can be constructed, which can be interpreted as up- or downgoing decoupled polarised modes. These eigenfunctions are used to compose the wavefield solution out of the set of up- and downgoing waves. Inversely, the decomposition matrix is obtained which decomposes a given wavefield into up- and downgoing decoupled polarised modes. The propagation, reflection and transmission of the electromagnetic waves can be expressed in terms of the propagation, reflection and transmission of the two up- and downgoing

decoupled polarised modes. The propagation in a horizontally layered space is much easier analysed for the decoupled modes of polarisation. The field solutions for the decoupled polarised modes valid in homogeneous domains and the interrelation of the modes from different homogeneous domains, dictated by the boundary conditions at the interface, are described using the scattering formalism. Special attention is paid to the location of sources near or on the interface and whether they approach the interface from above or below the interface.

3.1 Basic relations for the electromagnetic waves in Fourier domain

In a horizontally layered medium, the interfaces are horizontal and parallel to the x_1, x_2 -plane, which implies that the structure is shift invariant in the directions of \hat{i}_1 and \hat{i}_2 . These invariance properties of the configuration are most easily taken into account by using the Fourier transformation with respect to the horizontal coordinates x_1 and x_2 as in Eq. (2.19). The Maxwell equations in the transform domain are given in Eq. (2.21a) and (2.21b). These expressions are valid for the electromagnetic fields in horizontally layered, locally reacting, time invariant and isotropic media.

From Eqs. (2.21a) and (2.21b) it is clear that only the differentiation with respect to x_3 is left. The field quantities \tilde{E}_3 and \tilde{H}_3 which are discontinuous across an interface (see Eqs. (2.8a)-(2.8b)) can be expressed using Eqs. (2.21a) and (2.21b) in terms of the source quantities and the field components which are continuous across an interface as

$$\tilde{E}_3 = \frac{1}{\hat{\eta}} \left(-\tilde{J}_3 - jk_1 \tilde{H}_2 + jk_2 \tilde{H}_1 \right), \quad (3.1a)$$

$$\tilde{H}_3 = \frac{1}{\hat{\zeta}} \left(-\tilde{K}_3 + jk_1 \tilde{E}_2 - jk_2 \tilde{E}_1 \right). \quad (3.1b)$$

Through elimination of \tilde{E}_3 and \tilde{H}_3 , Eqs. (2.21a) and (2.21b) can be written in a four by four matrix formalism in which the electromagnetic field vector occurs as the quantity that characterizes the transform-domain electromagnetic wavefield. Therefore, we rewrite Eqs. (2.21a) and (2.21b) in each homogeneous layer, by taking into account the isotropic medium parameters, as a system of first-order homogeneous differential equations of the form [Kooij, 1994],

$$\partial_3 \mathbf{F} + \mathbf{A} \mathbf{F} = \mathbf{Q}, \quad (3.2)$$

in which \mathbf{A} is the four by four electromagnetic system matrix and the vector \mathbf{Q} is the source vector. The four by one electromagnetic field vector consists of those field quantities that are required to be continuous across interfaces and is given by

$$\mathbf{F} = \begin{bmatrix} \tilde{E}_1 \\ \tilde{E}_2 \\ -\tilde{H}_2 \\ \tilde{H}_1 \end{bmatrix}, \quad (3.3)$$

such that the accompanying system matrix consists of two symmetric off-diagonal two by two submatrices. The electromagnetic system matrix is obtained as

$$\mathbf{A} = \begin{bmatrix} \mathbf{0} & \mathbf{A}^{\text{EH}} \\ \mathbf{A}^{\text{HE}} & \mathbf{0} \end{bmatrix}, \quad (3.4)$$

where the submatrices \mathbf{A}^{EH} and \mathbf{A}^{HE} are given by

$$\mathbf{A}^{\text{EH}} = \begin{bmatrix} -k_1^2/\hat{\eta} - \hat{\zeta} & -k_1 k_2/\hat{\eta} \\ -k_1 k_2/\hat{\eta} & -k_2^2/\hat{\eta} - \hat{\zeta} \end{bmatrix}, \quad (3.5a)$$

$$\mathbf{A}^{\text{HE}} = \begin{bmatrix} -k_2^2/\hat{\zeta} - \hat{\eta} & k_1 k_2/\hat{\zeta} \\ k_1 k_2/\hat{\zeta} & -k_1^2/\hat{\zeta} - \hat{\eta} \end{bmatrix}. \quad (3.5b)$$

The expression for the source column matrix is obtained as

$$\mathbf{Q} = \begin{bmatrix} -\tilde{K}_2 + jk_1 \tilde{J}_3/\hat{\eta} \\ \tilde{K}_1 + jk_2 \tilde{J}_3/\hat{\eta} \\ \tilde{J}_1 - jk_2 \tilde{K}_3/\hat{\zeta} \\ \tilde{J}_2 + jk_1 \tilde{K}_3/\hat{\zeta} \end{bmatrix}. \quad (3.6)$$

3.2 Wavefield decomposition

We will construct the solution of the wavefield in layered media using the concept of eigenfunctions of the system equation, formulated in Eq. (3.2) corresponding to the wavefield decomposition as carried out by van der Hijden [1987] and Groenenboom [1998]. An eigenfunction of the system equation is defined to satisfy the following two conditions:

- The n -th eigenfunction $\mathbf{F}^n(k_\alpha, x_3, \omega)$ must be a solution to the system equation.
- The result of the differential operation of the system equation, namely vertical differentiation, ∂_3 , on the eigenfunction corresponds to the same vector multiplied with a scalar function, the so-called eigenvalue.

From the homogeneous form of Eq. (3.2) we observe that the above conditions can be expressed as

$$\begin{aligned}\partial_3 \mathbf{F}^n(k_\alpha, x_3, \omega) &= -\mathbf{A}(k_\alpha, \omega) \mathbf{F}^n(k_\alpha, x_3, \omega), \\ &= -\lambda_3^n(k_\alpha, \omega) \mathbf{F}^n(k_\alpha, x_3, \omega).\end{aligned}\quad (3.7)$$

Hence, an eigenfunction is an independent solution to the system equation. The proportionality factor is given by $\lambda_3^n(k_\alpha, \omega)$, which we denote as the generalized vertical wavenumber. The superscript n has been added to the eigenfunction, denoting the n -th eigenfunction, since we will show that more than one eigenfunction exists for the system equation in Eq. (3.7). Equation (3.7) suggests that we seek eigenfunctions of the form

$$\mathbf{F}^n(k_\alpha, x_3, \omega) = \mathbf{F}^n(k_\alpha, x_3^r, \omega) \exp[-\lambda_3^n(k_\alpha, \omega)(x_3 - x_3^r)], \quad (3.8)$$

in which \mathbf{F}^n represents the polarization vector of the field vector at the reference level $x_3 = x_3^r$. From Eq. (3.7) we extract the condition under which the vector $\mathbf{F}^n(k_\alpha, x_3^r, \omega)$ forms an eigenfunction, with eigenvalue λ_3^n as

$$(\mathbf{A} - \lambda_3^n \mathbf{I}) \mathbf{F}^n(k_\alpha, x_3^r, \omega) = 0, \quad (3.9)$$

from which can be concluded that

$$\mathbf{A} \mathbf{F}^n(k_\alpha, x_3^r, \omega) = \mathbf{F}^n(k_\alpha, x_3^r, \omega) \lambda_3^n. \quad (3.10)$$

Note that the vertical wavenumbers $\lambda_3^n(k_\alpha, \omega)$ are the eigenvalues of the system matrix \mathbf{A} , while the polarization vectors $\mathbf{F}^n(k_\alpha, \omega)$ are the eigenvectors of the system matrix \mathbf{A} . We will order the four eigenvectors of Eq. (3.10) into a non-singular matrix \mathbf{L} , which we will denote as the composition matrix, as follows

$$\mathbf{L} = (\mathbf{F}^{\uparrow;1} \mathbf{F}^{\uparrow;2} \mathbf{F}^{\downarrow;3} \mathbf{F}^{\downarrow;4}), \quad (3.11)$$

where the corresponding generalized vertical propagation coefficients of these eigenvectors are given by

$$(\lambda_3^1, \lambda_3^2, \lambda_3^3, \lambda_3^4) = (-\Gamma, -\Gamma, \Gamma, \Gamma), \quad (3.12)$$

respectively, in which the vertical propagation coefficient Γ is defined as

$$\Gamma = \sqrt{\gamma^2 + k_1^2 + k_2^2}, \text{ with } \text{Re}(\Gamma) \geq 0, \quad (3.13)$$

where the propagation coefficient γ is defined using Eqs. (2.17a) and (2.17b) as

$$\gamma = \sqrt{\hat{\eta}\hat{\zeta}}, \text{ with } \text{Re}(\gamma) \geq 0. \quad (3.14)$$

Note that $\mathbf{F}^{\uparrow;1}$ and $\mathbf{F}^{\uparrow;2}$ in Eq. (3.11) describe the two upgoing polarisations at level $x_3 = x_3^r$, which corresponds with the vertical wavenumbers $\lambda_3^1 = \lambda_3^2 = -\Gamma$, whereas $\mathbf{F}^{\downarrow;3}$ and $\mathbf{F}^{\downarrow;4}$ describe the two downgoing polarisations at level $x_3 = x_3^r$, which corresponds with the vertical wavenumbers $\lambda_3^3 = \lambda_3^4 = \Gamma$. In this way exponential decaying electromagnetic field amplitudes are obtained when applying Eq. (3.8) for $\text{Re}(\Gamma) \geq 0$. Having defined the composition matrix \mathbf{L} in Eq. (3.11), which is independent of x_3 , we can summarise the eigenvector equation of Eq. (3.10) for all eigenvectors as

$$\mathbf{A}\mathbf{L} = \mathbf{L}\mathbf{\Lambda}, \quad (3.15)$$

in which the matrix $\mathbf{\Lambda}$ is the diagonal matrix containing all eigenvalues, viz.,

$$\mathbf{\Lambda} = \begin{bmatrix} \mathbf{\Lambda}^{\uparrow} & \mathbf{0} \\ \mathbf{0} & \mathbf{\Lambda}^{\downarrow} \end{bmatrix}. \quad (3.16)$$

The submatrix $\mathbf{\Lambda}^{\uparrow}$ which is related to upgoing waves is defined as

$$\mathbf{\Lambda}^{\uparrow} = \begin{bmatrix} -\Gamma & 0 \\ 0 & -\Gamma \end{bmatrix}, \quad (3.17)$$

and the submatrix $\mathbf{\Lambda}^{\downarrow}$ is related to downgoing waves and is given by

$$\mathbf{\Lambda}^{\downarrow} = \begin{bmatrix} \Gamma & 0 \\ 0 & \Gamma \end{bmatrix} = -\mathbf{\Lambda}^{\uparrow}. \quad (3.18)$$

Left-multiplying Eq. (3.10) with the inverse of the composition matrix, we conclude that the matrix of column vectors acts as the transformation matrix which diagonalises the system matrix \mathbf{A} , expressed as

$$\mathbf{L}^{-1}\mathbf{A}\mathbf{L} = \mathbf{\Lambda}. \quad (3.19)$$

If we now define the wave vector \mathbf{W} , as the four-dimensional vector consisting of the amplitudes of the generalized up- and downgoing waves at a certain reference level, we can compose the field vector out of the up- and downgoing wave amplitudes by using the composition matrix \mathbf{L} as

$$\mathbf{F} = \mathbf{L}\mathbf{W}, \quad (3.20)$$

while we can decompose the field vector into up- and downgoing waves with the decomposition matrix \mathbf{L}^{-1} as

$$\mathbf{W} = \mathbf{L}^{-1}\mathbf{F}. \quad (3.21)$$

Note that the four-dimensional wave vector is composed of two two-dimensional subvectors, containing the amplitudes of the up- and downgoing waves (see Figure 3.1), i.e.

$$\mathbf{W} = \begin{bmatrix} \mathbf{W}^\uparrow \\ \mathbf{W}^\downarrow \end{bmatrix}. \quad (3.22)$$

Next, by substituting Eq. (3.20) into Eq. (3.7) we obtain the wave equation for the wave vector \mathbf{W} as

$$\begin{aligned} \partial_3 \mathbf{W} &= -\mathbf{L}^{-1} \mathbf{A} \mathbf{L} \mathbf{W}, \\ &= -\mathbf{\Lambda} \mathbf{W}, \end{aligned} \quad (3.23)$$

where in the last step we have used the result of Eq. (3.19) that the composition matrix \mathbf{L} acts as the transformation matrix which diagonalises the system matrix \mathbf{A} . Note that because the matrix $\mathbf{\Lambda}$ containing the vertical wavenumbers is diagonal, the wave equation for the wave vector is decoupled for the different polarisation modes in a homogeneous subdomain.

We split the composition matrix into two by two submatrices according to

$$\mathbf{L} = \begin{bmatrix} \mathbf{L}^{\text{E},\uparrow} & \mathbf{L}^{\text{E},\downarrow} \\ \mathbf{L}^{\text{H},\uparrow} & \mathbf{L}^{\text{H},\downarrow} \end{bmatrix}. \quad (3.24)$$

The order of the different eigenvectors in the composition submatrices are chosen such that the first eigenvector \mathbf{F}^1 composes the electromagnetic field-vector using the upgoing electric field mode, which is parallel to the k_β -vector. The k_β -vector corresponds to the plane of incidence approaching a layer in a horizontally layered medium. This electric field mode is denoted

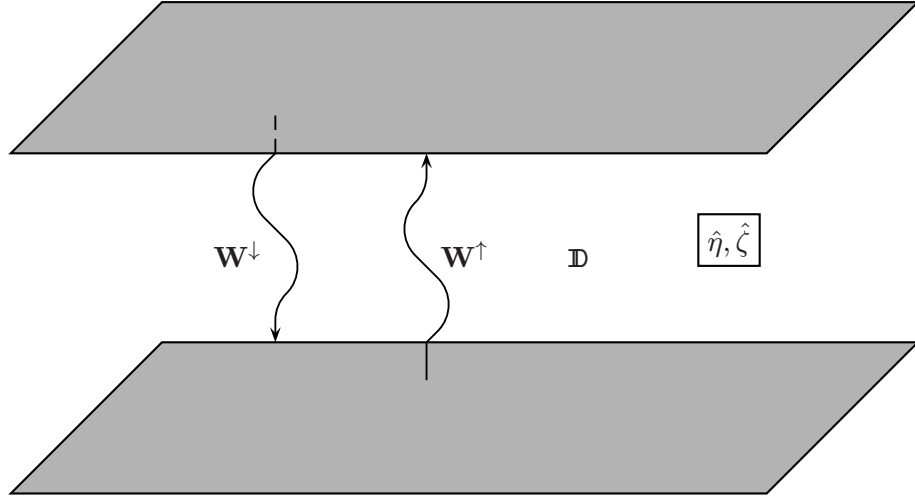


Figure 3.1: The two component up- and downgoing waves \mathbf{W}^\uparrow and \mathbf{W}^\downarrow present in a homogeneous layer.

as the transverse magnetic (TM) polarisation, because the magnetic field is polarised perpendicular to the plane of incidence. Similarly, the second eigenvector \mathbf{F}^2 composes the electromagnetic fieldvector, using the upgoing electric field which is perpendicular to the k_β -vector. This mode is denoted as the transverse electric (TE) polarisation. The third and fourth eigenvectors compose the electromagnetic fieldvector using the downgoing TM and TE polarisation, respectively. The composition submatrices are obtained as

$$\mathbf{L}^{\text{E},\uparrow} = \mathbf{L}^{\text{E},\downarrow} = \begin{bmatrix} k_1 & -k_2 \\ k_2 & k_1 \end{bmatrix} \mathbf{N}^{-1}, \quad (3.25a)$$

$$\mathbf{L}^{\text{H},\uparrow} = -\mathbf{L}^{\text{H},\downarrow} = \begin{bmatrix} Y k_1 & -\bar{Y} k_2 \\ Y k_2 & \bar{Y} k_1 \end{bmatrix} \mathbf{N}^{-1}, \quad (3.25b)$$

where

$$Y = \frac{\hat{\eta}}{\Gamma}, \quad (3.26a)$$

$$\bar{Y} = \frac{\Gamma}{\hat{\zeta}}, \quad (3.26b)$$

and the matrix \mathbf{N} is an arbitrary diagonal matrix containing the normalization constants, which will be determined later.

3.3 Bi-orthogonal relations for eigenfunctions

Inspection of the polarisation submatrices of Eqs. (3.25a) and (3.25b) shows that we have incorporated the choice that the horizontal electric field components of two waves propagating upward and downward are one and the same. As a consequence, the horizontal magnetic field components of two waves propagating upward and downward are each other's opposite. The reciprocity relation for electromagnetic waves as given in Eq. (2.33) will be expressed in terms of the eigenfunctions. As domain of application we consider a homogeneous layer bounded at two depth levels, i.e. $\{x_3^a \leq x_3 \leq x_3^b\}$, defining the volume \mathbf{D} , where the direction x_3 is perpendicular to the layering. In state A and B we will consider different plane wave solutions for the same medium. Then the reciprocity theorem leads to

$$\int_{\mathbf{x} \in \partial \mathbf{D}} \epsilon_{mkj} (\hat{E}_k^A \hat{H}_j^B - \hat{E}_k^B \hat{H}_j^A) \nu_m dA = 0, \quad (3.27)$$

since there are no sources nor discrepancies in the material properties in the domain \mathbf{D} , for the states A and B. We note that $\partial \mathbf{D}$ consists of two infinite planes at the levels x_3^a and x_3^b , respectively. The normal for the level x_3^a points downward similar to \mathbf{i}_3 , whereas the normal for the level x_3^b points in the opposite direction, i.e. $-\mathbf{i}_3$. For state A we have the eigenfunction $\mathbf{F}^A(\mathbf{x}, \omega)$, which describes the plane-wave solution

$$\mathbf{F}^A(\mathbf{x}, \omega) = \mathbf{F}^n(k_\beta^A, x_3, \omega) \exp(-jk_\beta^A x_\beta), \quad (3.28)$$

and similarly for state B

$$\mathbf{F}^B(\mathbf{x}, \omega) = \mathbf{F}^n(k_\beta^B, x_3, \omega) \exp(-jk_\beta^B x_\beta). \quad (3.29)$$

Combined with the arbitrariness of the depth levels x_3^a and x_3^b within the homogeneous layer, and substitution of Eqs. (3.28) and (3.29) into Eq. (3.27) we obtain the algebraic identity

$$\begin{aligned} (\mathbf{F}^n)^T(k_\beta^A, x_3, \omega) \begin{bmatrix} \mathbf{0} & -\mathbf{I} \\ \mathbf{I} & \mathbf{0} \end{bmatrix} \mathbf{F}^n(k_\beta^B, x_3, \omega) \int_{\mathbf{x} \in \mathbb{R}^2} \exp[-j(k_\beta^A + k_\beta^B)x_\beta] dA \\ = C(k_\beta^A, k_\beta^B, \omega), \end{aligned} \quad (3.30)$$

where the superscript T denotes the transpose, and the quantity $C(k_\beta^A, k_\beta^B, \omega)$ signifies that the expression on the left-hand side of Eq. (3.30) does not depend on x_3 , but of course it is still a function of the angular frequency ω and other wave parameters. Using

$$\int_{\mathbf{x} \in \mathbb{R}^2} \exp[-j(k_\beta^A + k_\beta^B)x_\beta] dA = (2\pi)^2 \delta(k_\beta^A + k_\beta^B), \quad (3.31)$$

it follows that $k_\beta^B = -k_\beta^A$, to give a non-zero relation between state A and state B. Using the decomposition in up- and downgoing waves we then obtain

$$(2\pi)^2 \mathbf{W}^T(k_\beta^A, x_3, \omega) \mathbf{L}^T(k_\beta^A, \omega) \begin{bmatrix} \mathbf{0} & -\mathbf{I} \\ \mathbf{I} & \mathbf{0} \end{bmatrix} \mathbf{L}(-k_\beta^A, \omega) \mathbf{W}(-k_\beta^A, x_3, \omega) = C'(k_\beta^A, \omega), \quad (3.32)$$

where we have used $C(k_\beta^A, k_\beta^B, \omega) = C'(k_\beta^A, \omega) \delta(k_\beta^A + k_\beta^B)$. From Eqs. (3.25a) and (3.25b) we obtain the composition submatrices for the sign-reversed horizontal wavenumber as

$$\mathbf{L}^{\text{E},\uparrow}(-k_\beta, \omega) = -\mathbf{L}^{\text{E},\downarrow}(k_\beta, \omega), \quad (3.33a)$$

$$\mathbf{L}^{\text{E},\downarrow}(-k_\beta, \omega) = -\mathbf{L}^{\text{E},\uparrow}(k_\beta, \omega), \quad (3.33b)$$

$$\mathbf{L}^{\text{H},\uparrow}(-k_\beta, \omega) = \mathbf{L}^{\text{H},\downarrow}(k_\beta, \omega), \quad (3.33c)$$

$$\mathbf{L}^{\text{H},\downarrow}(-k_\beta, \omega) = \mathbf{L}^{\text{H},\uparrow}(k_\beta, \omega). \quad (3.33d)$$

Replacing the composition matrix for the sign-reversed horizontal wavenumbers in Eq. (3.32) with the submatrices in Eqs. (3.33a)-(3.33d) we obtain

$$(2\pi)^2 \mathbf{W}^T(k_\beta^A, x_3, \omega) \begin{bmatrix} \mathbf{B}^{\uparrow\uparrow} & \mathbf{B}^{\uparrow\downarrow} \\ \mathbf{B}^{\downarrow\uparrow} & \mathbf{B}^{\downarrow\downarrow} \end{bmatrix} \mathbf{W}(-k_\beta^A, x_3, \omega) = C'(k_\beta^A, \omega), \quad (3.34)$$

where the matrix \mathbf{B} has been defined as

$$\begin{bmatrix} \mathbf{B}^{\uparrow\uparrow} & \mathbf{B}^{\uparrow\downarrow} \\ \mathbf{B}^{\downarrow\uparrow} & \mathbf{B}^{\downarrow\downarrow} \end{bmatrix} = - \begin{bmatrix} \mathbf{L}^{\text{E},\uparrow} & \mathbf{L}^{\text{E},\downarrow} \\ \mathbf{L}^{\text{H},\uparrow} & \mathbf{L}^{\text{H},\downarrow} \end{bmatrix}^T \begin{bmatrix} \mathbf{L}^{\text{H},\downarrow} & \mathbf{L}^{\text{H},\uparrow} \\ \mathbf{L}^{\text{E},\downarrow} & \mathbf{L}^{\text{E},\uparrow} \end{bmatrix}. \quad (3.35)$$

Expanding the matrix multiplication of this equation results in

$$\mathbf{B}^{\uparrow\uparrow} = -(\mathbf{L}^{\text{E},\uparrow})^T \mathbf{L}^{\text{H},\downarrow} - (\mathbf{L}^{\text{H},\uparrow})^T \mathbf{L}^{\text{E},\downarrow}, \quad (3.36a)$$

$$\mathbf{B}^{\uparrow\downarrow} = -(\mathbf{L}^{\text{E},\uparrow})^T \mathbf{L}^{\text{H},\uparrow} - (\mathbf{L}^{\text{H},\uparrow})^T \mathbf{L}^{\text{E},\uparrow}, \quad (3.36b)$$

$$\mathbf{B}^{\downarrow\uparrow} = -(\mathbf{L}^{\text{E},\downarrow})^T \mathbf{L}^{\text{H},\downarrow} - (\mathbf{L}^{\text{H},\downarrow})^T \mathbf{L}^{\text{E},\downarrow}, \quad (3.36c)$$

$$\mathbf{B}^{\downarrow\downarrow} = -(\mathbf{L}^{\text{E},\downarrow})^T \mathbf{L}^{\text{H},\uparrow} - (\mathbf{L}^{\text{H},\downarrow})^T \mathbf{L}^{\text{E},\uparrow}. \quad (3.36d)$$

The amplitudes of the up- or downgoing waves \mathbf{W} have a x_3 -dependence according to Eq. (3.8) of

$$\mathbf{W}(k_\beta, x_3, \omega) = \mathbf{W}(k_\beta, x_3^r, \omega) \exp[-\lambda_3^n(k_\beta, \omega)(x_3 - x_3^r)]. \quad (3.37)$$

Substitution of Eqs. (3.25a) and (3.25b) into Eqs. (3.36a)-(3.36d) shows that

$$\mathbf{B}^{\uparrow\downarrow} = -\mathbf{B}^{\downarrow\uparrow}. \quad (3.38)$$

and

$$\mathbf{B}^{\uparrow\uparrow} = \mathbf{0}, \quad (3.39a)$$

$$\mathbf{B}^{\downarrow\downarrow} = \mathbf{0}, \quad (3.39b)$$

which indicates that there is no interaction of waves propagating in the same direction and thus Eq. (3.34) is not x_3 dependent. Rewriting Eqs. (3.36a)-(3.36d) using Eqs. (3.39a) and (3.39b) we obtain

$$\begin{bmatrix} (\mathbf{L}^{\text{H},\uparrow})^T & (\mathbf{L}^{\text{E},\uparrow})^T \\ (\mathbf{L}^{\text{H},\downarrow})^T & (\mathbf{L}^{\text{E},\downarrow})^T \end{bmatrix} \begin{bmatrix} \mathbf{L}^{\text{E},\uparrow} & \mathbf{L}^{\text{E},\downarrow} \\ \mathbf{L}^{\text{H},\uparrow} & \mathbf{L}^{\text{H},\downarrow} \end{bmatrix} = \begin{bmatrix} \mathbf{B}^{\downarrow\uparrow} & \mathbf{0} \\ \mathbf{0} & -\mathbf{B}^{\downarrow\uparrow} \end{bmatrix}, \quad (3.40)$$

where we have written matrix \mathbf{B} as function of $\mathbf{B}^{\downarrow\uparrow}$ to enforce real-valued normalisation constants for \mathbf{N} . Using Eqs. (3.25) and (3.40) $\mathbf{B}^{\downarrow\uparrow}$ can be written as

$$\mathbf{B}^{\downarrow\uparrow} = 2(k_1^2 + k_2^2) \begin{bmatrix} Y & 0 \\ 0 & \bar{Y} \end{bmatrix} \mathbf{N}^{-2}. \quad (3.41)$$

There exist different ways to choose the normalisation constant contained in the matrix \mathbf{N} . One way is to choose the normalisation constants such that $\mathbf{B}^{\downarrow\uparrow}$ becomes the unity matrix. This is called energy-flux normalisation. This approach will in general result in a numerically more stable expression. Because in this thesis expressions are derived for simple two-layer media the flux normalisation is not required. By deriving Eqs. (3.25a) and (3.25b) we have implicitly chosen the normalisation constants by normalising the eigenvectors on the electric field. In this way the transmission and reflection coefficients, which will be derived are equal with results in the literature. Hence, the normalisation matrix is obtained as

$$\mathbf{N} = \sqrt{2(k_1^2 + k_2^2)} \mathbf{I}. \quad (3.42)$$

Next using Eq. (3.40), we identify the decomposition matrix \mathbf{L}^{-1} as

$$\begin{aligned}\mathbf{L}^{-1} &= \begin{bmatrix} \mathbf{B}^{\downarrow\uparrow} & \mathbf{0} \\ \mathbf{0} & -\mathbf{B}^{\downarrow\uparrow} \end{bmatrix}^{-1} \begin{bmatrix} (\mathbf{L}^{\text{H},\uparrow})^T & (\mathbf{L}^{\text{E},\uparrow})^T \\ (\mathbf{L}^{\text{H},\downarrow})^T & (\mathbf{L}^{\text{E},\downarrow})^T \end{bmatrix}, \\ &= \begin{bmatrix} (\mathbf{B}^{\downarrow\uparrow})^{-1} & \mathbf{0} \\ \mathbf{0} & -(\mathbf{B}^{\downarrow\uparrow})^{-1} \end{bmatrix} \begin{bmatrix} (\mathbf{L}^{\text{H},\uparrow})^T & (\mathbf{L}^{\text{E},\uparrow})^T \\ (\mathbf{L}^{\text{H},\downarrow})^T & (\mathbf{L}^{\text{E},\downarrow})^T \end{bmatrix}.\end{aligned}\quad (3.43)$$

where

$$\mathbf{B}^{\downarrow\uparrow} = \begin{bmatrix} Y & 0 \\ 0 & \bar{Y} \end{bmatrix}, \quad (3.44a)$$

$$(\mathbf{B}^{\downarrow\uparrow})^{-1} = \begin{bmatrix} Z & 0 \\ 0 & \bar{Z} \end{bmatrix}, \quad (3.44b)$$

and

$$Z = \frac{1}{Y}, \quad (3.45a)$$

$$\bar{Z} = \frac{1}{\bar{Y}}. \quad (3.45b)$$

As a consequence we obtain,

$$\mathbf{L}^{-1} = \frac{1}{[2(k_1^2 + k_2^2)]^{\frac{1}{2}}} \begin{bmatrix} k_1 & k_2 & k_1 Z & k_2 Z \\ -k_2 & k_1 & -k_2 \bar{Z} & k_1 \bar{Z} \\ k_1 & k_2 & -k_1 Z & -k_2 Z \\ -k_2 & k_1 & k_2 \bar{Z} & -k_1 \bar{Z} \end{bmatrix}. \quad (3.46)$$

3.4 Scattering theory

For an efficient procedure to derive the electromagnetic field in a horizontally layered space we will discuss the scattering operator. The scattering operator $\mathbf{S}(x_3^a; x_3^b)$ relates the outgoing polarisation modes to the incoming polarisation modes at the levels x_3^a and x_3^b . We will implicitly assume that the alphabetic order is representative for their relative level. For example, the use of x_3^a and x_3^b implicitly states that the level x_3^b is below x_3^a , hence $x_3^b > x_3^a$. Furthermore we will assume that at level x_3^a the medium parameters are different compared with the medium parameters at level x_3^b . This means that at a certain depth level x_3^{ab} , where $x_3^b > x_3^{ab} > x_3^a$, an interface between medium \mathbb{D}^a and \mathbb{D}^b is

present. At this interface reflection and transmission of the electromagnetic modes will occur, which are described by the scatter matrix. The short-hand notation $\mathbf{W}^\uparrow(x_3^a)$ will be used in stead of $\mathbf{W}^\uparrow(k_\beta, x_3^a, \omega)$. We uniquely define the scattering operator as

$$\begin{bmatrix} \mathbf{W}^\uparrow(x_3^a) \\ \mathbf{W}^\downarrow(x_3^b) \end{bmatrix} = \mathbf{S}(x_3^a; x_3^b) \begin{bmatrix} \mathbf{W}^\downarrow(x_3^a) \\ \mathbf{W}^\uparrow(x_3^b) \end{bmatrix}, \quad (3.47)$$

where we partition the scattering operator $\mathbf{S}(x_3^a; x_3^b)$ into the submatrices, which define the reflection and transmission matrices, i.e.

$$\mathbf{S}(x_3^a; x_3^b) = \begin{bmatrix} \mathbf{R}^\smile(x_3^a; x_3^b) & \mathbf{T}^\uparrow(x_3^a; x_3^b) \\ \mathbf{T}^\downarrow(x_3^a; x_3^b) & \mathbf{R}^\frown(x_3^a; x_3^b) \end{bmatrix}. \quad (3.48)$$

Figure 3.2 shows an illustration with an explanation of the relevant symbols. Note that $\mathbf{S}(x_3^a; x_3^b)$ describes the reflection and transmission at the interface as well as the propagation of the reflected and transmitted waves from x_3^{ab} towards x_3^a and from x_3^{ab} towards x_3^b , which will be investigated separately. For this purpose we use the following notation; when approached from above towards the interface at x_3^{ab} we have

$$\mathbf{W}(x_3^{a\downarrow}) \stackrel{\text{def}}{=} \lim_{\epsilon \downarrow 0} \mathbf{W}(x_3^{ab} - \epsilon), \quad (3.49)$$

and when approaching from below

$$\mathbf{W}(x_3^{b\uparrow}) \stackrel{\text{def}}{=} \lim_{\epsilon \downarrow 0} \mathbf{W}(x_3^{ab} + \epsilon). \quad (3.50)$$

Note that the classical boundary condition of the continuity of the field vector of Eqs. (2.7a) and (2.7b) can be expressed as

$$\mathbf{F}(x_3^{b\uparrow}) = \mathbf{F}(x_3^{a\downarrow}). \quad (3.51)$$

First the scattering operator of a homogeneous interval is discussed. In this way the propagation of the modes in domain \mathbb{D}^a from $x_3^{a\uparrow}$ towards $x_3^{a\downarrow}$ and vice versa is described. Next, the scattering operator at an interface is discussed.

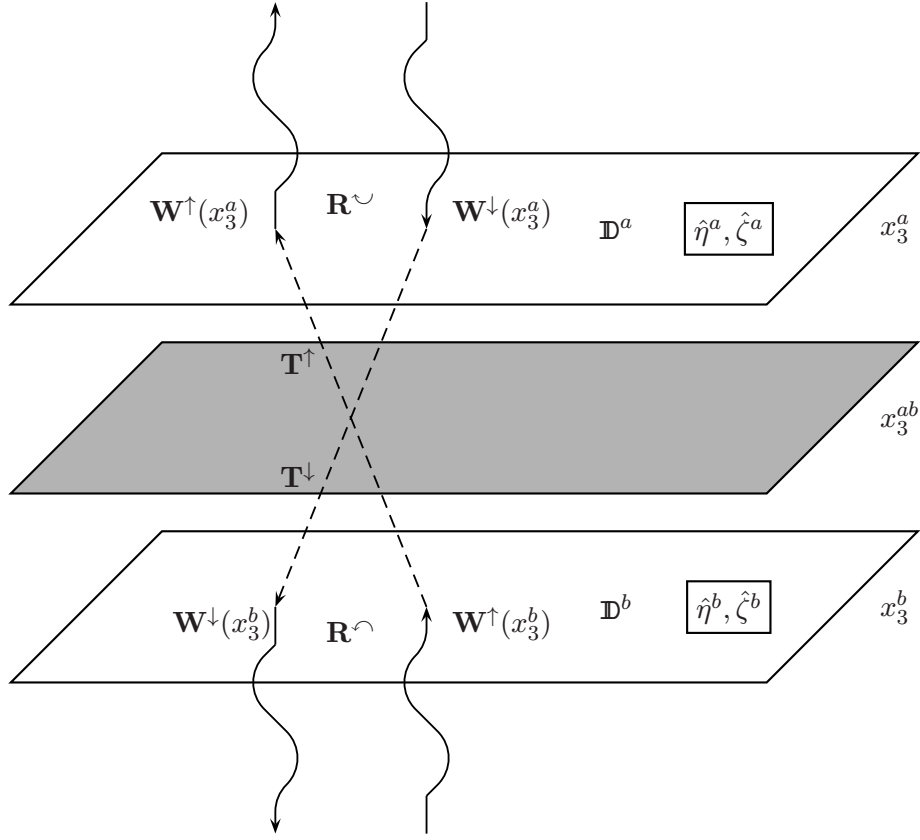


Figure 3.2: A graphical illustration of the components of the scattering operator, the reflection and transmission matrices.

3.4.1 The scattering operator of a homogeneous interval

To arrive at the scattering operator of a homogeneous interval, we start with the source-free wave equation formulated in Eq. (3.23) as

$$\partial_3 \mathbf{W} = -\Lambda \mathbf{W}. \quad (3.52)$$

Next, the scattering operator of a homogeneous interval is obtained as

$$\mathbf{S}(x_3^{a\bar{\uparrow}}; x_3^{a\downarrow}) = \begin{bmatrix} 0 & \mathbf{T}_{(a)}^\uparrow \\ \mathbf{T}_{(a)}^\downarrow & 0 \end{bmatrix}, \quad (3.53)$$

where we have introduced the one-way phase delay operators $\mathbf{T}_{(a)}^\uparrow$ and $\mathbf{T}_{(a)}^\downarrow$, defined as

$$\mathbf{T}_{(a)}^\uparrow = \exp[+\mathbf{\Lambda}^\uparrow(x_3^{a\bar{\uparrow}} - x_3^{a\downarrow})], \quad (3.54a)$$

$$\mathbf{T}_{(a)}^\downarrow = \exp[+\mathbf{\Lambda}^\downarrow(x_3^{a\downarrow} - x_3^{a\bar{\uparrow}})]. \quad (3.54b)$$

Note that both components of the one-way phase delay operators are equivalent with $\exp(-\Gamma d^a)$, where d^a is the thickness of the homogeneous layer, $d^a = x_3^{a\downarrow} - x_3^{a\bar{\uparrow}}$, since they all take into account the phase delay of a wave propagating through a homogeneous medium. However, to emphasize the direction of the propagation we have introduced two different phase delay operators, which will be used to derive inverse propagation of downgoing and upgoing waves.

3.4.2 The scattering operator of an interface

In order to obtain the scattering operator of an interface at x_3^{ab} between media \mathbb{D}^a and \mathbb{D}^b across which the constitutive parameters jump by a finite amount, we use the continuity of the field vector, which is expressed in Eq. (3.51). Note that the wave vector will be discontinuous. Equation (3.51) can be expressed in terms of the wave vector using Eq. (3.20) as

$$\mathbf{L}_{(a)}\mathbf{W}(x_3^{a\downarrow}) = \mathbf{L}_{(b)}\mathbf{W}(x_3^{b\bar{\uparrow}}), \quad (3.55)$$

where $\mathbf{L}_{(a)}$ and $\mathbf{L}_{(b)}$ are the composition matrix in media \mathbb{D}^a and \mathbb{D}^b , respectively. Next, we define the local reflection and transmission coefficients for the interface in terms of the local scattering operator of the interface $\mathbf{S}(x_3^{a\downarrow}; x_3^{b\bar{\uparrow}})$, expressed as

$$\mathbf{S}(x_3^{a\downarrow}; x_3^{b\bar{\uparrow}}) = \begin{bmatrix} \mathbf{R}_{(ab)}^\smile & \mathbf{T}_{(ab)}^\uparrow \\ \mathbf{T}_{(ab)}^\downarrow & \mathbf{R}_{(ab)}^\frown \end{bmatrix}. \quad (3.56)$$

Evaluation of the reflection and transmission coefficients using Eqs. (3.55)-(3.56) results in upward and downward reflection coefficients given by

$$\mathbf{R}_{(ab)}^\smile = \begin{bmatrix} r_{(ab)}^{TM} & 0 \\ 0 & r_{(ab)}^{TE} \end{bmatrix}, \quad (3.57a)$$

$$\mathbf{R}_{(ab)}^\frown = \begin{bmatrix} -r_{(ab)}^{TM} & 0 \\ 0 & -r_{(ab)}^{TE} \end{bmatrix}, \quad (3.57b)$$

where the transverse magnetic $r_{(ab)}^{TM}$ and the transverse electric $r_{(ab)}^{TE}$ reflection coefficients are given by

$$r_{(ab)}^{TM} = \frac{Z^b - Z^a}{Z^b + Z^a} = \frac{\hat{\eta}^a \Gamma^b - \hat{\eta}^b \Gamma^a}{\hat{\eta}^a \Gamma^b + \hat{\eta}^b \Gamma^a}, \quad (3.58a)$$

$$r_{(ab)}^{TE} = \frac{\bar{Z}^b - \bar{Z}^a}{\bar{Z}^b + \bar{Z}^a} = \frac{\hat{\zeta}^b \Gamma^a - \hat{\zeta}^a \Gamma^b}{\hat{\zeta}^b \Gamma^a + \hat{\zeta}^a \Gamma^b}. \quad (3.58b)$$

The downward and upward transmission coefficients are given by

$$\mathbf{T}_{(ab)}^\downarrow = \begin{bmatrix} t_{(ab)}^{TM} & 0 \\ 0 & t_{(ab)}^{TE} \end{bmatrix}, \quad (3.59a)$$

$$\mathbf{T}_{(ab)}^\uparrow = \begin{bmatrix} 2 - t_{(ab)}^{TM} & 0 \\ 0 & 2 - t_{(ab)}^{TE} \end{bmatrix}, \quad (3.59b)$$

where the transverse magnetic $t_{(ab)}^{TM}$ and the transverse electric $t_{(ab)}^{TE}$ transmission coefficients are given by

$$t_{(ab)}^{TM} = \frac{2Z^b}{Z^b + Z^a} = \frac{2\hat{\eta}^a \Gamma^b}{\hat{\eta}^a \Gamma^b + \hat{\eta}^b \Gamma^a}, \quad (3.60a)$$

$$t_{(ab)}^{TE} = \frac{2\bar{Z}^b}{\bar{Z}^a + \bar{Z}^b} = \frac{2\hat{\zeta}^b \Gamma^a}{\hat{\zeta}^b \Gamma^a + \hat{\zeta}^a \Gamma^b}. \quad (3.60b)$$

The nomenclature of the reflection and transmission coefficients is related to the orientation of the electric and magnetic field with respect to the plane of incidence. The TE wave is linearly polarised with the electric field vector perpendicular to the plane of incidence and is also called perpendicular polarisation. The corresponding reflection and transmission coefficients are described by the transverse electric reflection and transmission coefficients, $r_{(ab)}^{TE}$ and $t_{(ab)}^{TE}$. The TM wave is linearly polarised with the electric vector parallel to the plane of incidence and is also called parallel polarisation. The corresponding reflection and transmission coefficients are described by the transverse magnetic reflection and transmission coefficients, $r_{(ab)}^{TM}$ and $t_{(ab)}^{TM}$.

3.5 The presence of sources on an interface

To include the presence of sources and specifically a source on the interface, we use the configuration given in Figure 3.3. We now define a specific source

level present at an interface x_3^{bc} . When the interface x_3^{bc} is an artificial interface and \mathbb{D}^b and \mathbb{D}^c have equal medium properties the behaviour of the sources can be easily obtained. However, when the medium properties of \mathbb{D}^b and \mathbb{D}^c differ, we use another approach. Medium \mathbb{D}^b is replaced by medium \mathbb{D}^a and medium \mathbb{D}^c is replaced by medium \mathbb{D}^d . In between the two interfaces x_3^{ab} and x_3^{cd} we assume an artificial interface at x_3^{bc} on which the sources are located. We now can use the expressions for the source on the artificial interface. Next, we perform the limiting procedure of taking the thickness of layers \mathbb{D}^b and \mathbb{D}^c equal to zero. In this way we obtain expressions for a source which approach the interface from above or below the interface.

3.5.1 Sources at an artificial interface

First we focus on interface x_3^{bc} . In this case Eq. (3.51) results in

$$\mathbf{F}(x_3^{b\downarrow}) - \mathbf{F}(x_3^{c\uparrow}) = \mathbf{Q}(x_3^{bc}), \quad (3.61)$$

where $\mathbf{Q}(x_3^{bc})$ is given by Eq. (3.6). Note that the vertical source terms in $\mathbf{Q}(x_3^{bc})$ depend on the medium properties, which yields that the concerning factors pertain to the domain where these specific sources find their origin. This will be of importance when a limiting procedure is carried out to obtain expressions for sources present on the interface between two different media, which will be discussed later. In addition to the scatter matrix, which describes the waves propagating away from the interface in terms of the waves propagating towards the interface we have added a source term in Eq. (3.47), resulting in an expression describing the source and scattering at interface $x_3 = x_3^{bc}$,

$$\begin{bmatrix} \mathbf{W}^\uparrow(x_3^{b\downarrow}) \\ \mathbf{W}^\downarrow(x_3^{c\uparrow}) \end{bmatrix} = \begin{bmatrix} \mathbf{R}_{(bc)}^\smile & \mathbf{T}_{(bc)}^\uparrow \\ \mathbf{T}_{(bc)}^\downarrow & \mathbf{R}_{(bc)}^\frown \end{bmatrix} \begin{bmatrix} \mathbf{W}^\downarrow(x_3^{b\downarrow}) \\ \mathbf{W}^\uparrow(x_3^{c\uparrow}) \end{bmatrix} + \begin{bmatrix} \mathbf{X}^\uparrow(x_3^{b\downarrow}) \\ \mathbf{X}^\downarrow(x_3^{c\uparrow}) \end{bmatrix}. \quad (3.62)$$

We now concentrate on the determination of the source term in Eq. (3.62). When a source is present on the interface and no other interfaces are present, it is obvious that only upgoing waves are present for $x_3^b < x_3^{b\downarrow}$ ($\mathbf{W}^\downarrow(x_3^b) = 0$), and that only downgoing waves are present for $x_3^c > x_3^{c\uparrow}$ ($\mathbf{W}^\uparrow(x_3^c) = 0$). Using Eq. (3.61) this can be written as

$$\mathbf{F}(x_3^{c\uparrow}) - \mathbf{F}(x_3^{b\downarrow}) = \begin{bmatrix} -\mathbf{L}_{(b)}^{E,\uparrow} & \mathbf{L}_{(c)}^{E,\downarrow} \\ -\mathbf{L}_{(b)}^{H,\uparrow} & \mathbf{L}_{(c)}^{H,\downarrow} \end{bmatrix} \begin{bmatrix} \mathbf{X}^\uparrow(x_3^{b\downarrow}) \\ \mathbf{X}^\downarrow(x_3^{c\uparrow}) \end{bmatrix} = \mathbf{Q}(x_3^{bc}), \quad (3.63)$$

where the subscript b and c of the composition submatrices pertain to the appropriate domain in which the composition is carried out. When the above equations describe an artificial interface, below and above the interface equal medium properties are present, $(\mathbf{L}_{(b)} = \mathbf{L}_{(c)} = \mathbf{L})$ and substitution of Eq. (3.46) in Eq. (3.63) results in

$$\begin{aligned} \begin{bmatrix} \mathbf{X}^\uparrow(x_3^{a\downarrow}) \\ \mathbf{X}^\downarrow(x_3^{b\uparrow}) \end{bmatrix} &= \begin{bmatrix} -\mathbf{I} & 0 \\ 0 & \mathbf{I} \end{bmatrix} \begin{bmatrix} \mathbf{L}^{E,\uparrow} & \mathbf{L}^{E,\downarrow} \\ \mathbf{L}^{H,\uparrow} & \mathbf{L}^{H,\downarrow} \end{bmatrix}^{-1} \mathbf{Q}(x_3^{bc}), \\ &= \begin{bmatrix} -(\mathbf{B}^{\downarrow\uparrow})^{-1} & 0 \\ 0 & -(\mathbf{B}^{\downarrow\uparrow})^{-1} \end{bmatrix} \begin{bmatrix} (\mathbf{L}^{H\uparrow})^T & (\mathbf{L}^{E\uparrow})^T \\ (\mathbf{L}^{H\downarrow})^T & (\mathbf{L}^{E\downarrow})^T \end{bmatrix} \mathbf{Q}(x_3^{bc}). \end{aligned} \quad (3.64)$$

3.5.2 Sources at an interface between two different media

However, when for $x_3^{b\downarrow}$ and for $x_3^{c\uparrow}$ different media properties are present we must consider both the boundary conditions forced by the two different media and the boundary conditions forced by the presence of sources. To gain insight in the process of a source close to an interface, whether present above, beneath or on the interface, we use the four media configuration (see Figure 3.3) in which the sources are present on the artificial interface x_3^{bc} in between an upper \mathbf{D}^a and lower \mathbf{D}^d layer. The limiting procedure for $x_3^{b\uparrow} - x_3^{c\downarrow} \rightarrow 0$ is carried out to obtain expressions for the waves due to a source present on the interface, where the properties of domain \mathbf{D}^b and \mathbf{D}^c are chosen equal to domain \mathbf{D}^a or \mathbf{D}^d . The two intermediate layers, \mathbf{D}^b and \mathbf{D}^c have equal medium parameters, hence $\mathbf{T}_{(bc)}^\uparrow = \mathbf{T}_{(c)}^\uparrow$ and $\mathbf{T}_{(bc)}^\downarrow = \mathbf{T}_{(b)}^\downarrow$ and $\mathbf{R}_{(bc)}^\smile = \mathbf{R}_{(bc)}^\frown = \mathbf{0}$ and the performance of these sources is given by Eq. (3.64). Using the scatter matrices we obtain the following expressions for the upgoing wave in \mathbf{D}^a and the downgoing wave in \mathbf{D}^d

$$\begin{aligned} \mathbf{W}^\uparrow(x_3^{a\downarrow}) &= \mathbf{T}_{(ab)}^\uparrow \mathbf{T}_{(b)}^\uparrow \left(\mathbf{I} - \mathbf{T}_{(b)}^\uparrow \mathbf{T}_{(c)}^\uparrow \mathbf{R}_{(cd)}^\smile \mathbf{T}_{(c)}^\downarrow \mathbf{T}_{(b)}^\downarrow \mathbf{R}_{(ab)}^\frown \right)^{-1} \\ &\quad \times \left[\mathbf{X}^\uparrow(x_3^{b\downarrow}) + \mathbf{T}_{(c)}^\uparrow \mathbf{R}_{(cd)}^\smile \mathbf{T}_{(c)}^\downarrow \mathbf{X}^\downarrow(x_3^{c\uparrow}) \right], \end{aligned} \quad (3.65a)$$

$$\begin{aligned} \mathbf{W}^\downarrow(x_3^{d\uparrow}) &= \mathbf{T}_{(cd)}^\downarrow \mathbf{T}_{(c)}^\downarrow \left(\mathbf{I} - \mathbf{T}_{(c)}^\downarrow \mathbf{T}_{(b)}^\downarrow \mathbf{R}_{(ab)}^\frown \mathbf{T}_{(b)}^\uparrow \mathbf{T}_{(c)}^\uparrow \mathbf{R}_{(cd)}^\smile \right)^{-1} \\ &\quad \times \left[\mathbf{X}^\downarrow(x_3^{c\uparrow}) + \mathbf{T}_{(b)}^\downarrow \mathbf{R}_{(ab)}^\frown \mathbf{T}_{(b)}^\uparrow \mathbf{X}^\uparrow(x_3^{b\downarrow}) \right]. \end{aligned} \quad (3.65b)$$

We now derive expressions for two different cases. The first case is when the sources approach the interface from above and the second case is when the

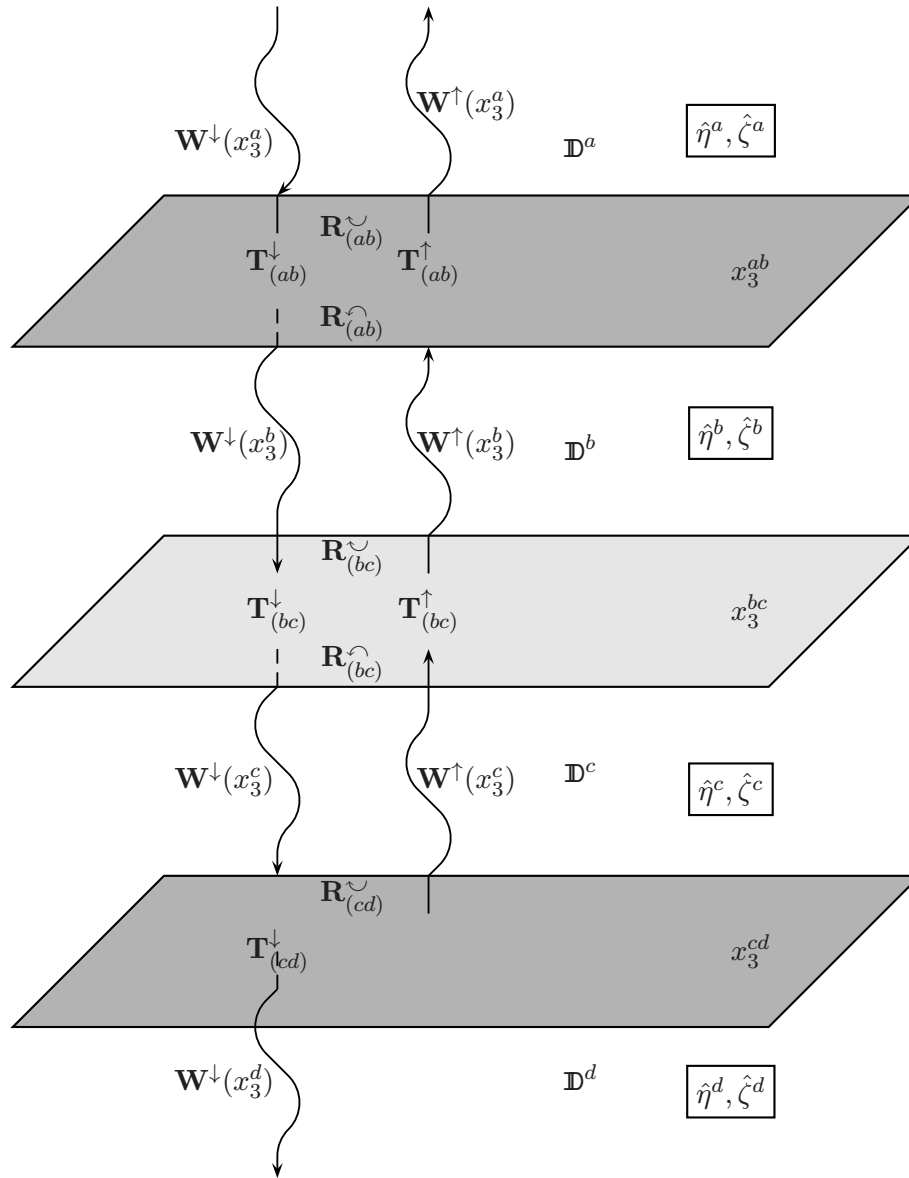


Figure 3.3: The wave fields present in a four-media configuration.

sources approach the interface from below. For the first case, the medium

parameters of \mathbf{D}^b and \mathbf{D}^c are equal to the medium parameters of \mathbf{D}^a , which results in

$$\mathbf{R}_{(ab)}^{\frown} = 0, \quad (3.66a)$$

$$\mathbf{T}_{(ab)}^{\uparrow} = \mathbf{T}_{(b)}^{\uparrow}, \quad (3.66b)$$

and Eq. (3.65) can be written as

$$\begin{aligned} \begin{bmatrix} \mathbf{W}^{\uparrow}(x_3^{a\downarrow}) \\ \mathbf{W}^{\downarrow}(x_3^{d\uparrow}) \end{bmatrix} &= - \begin{bmatrix} (\mathbf{B}^{\downarrow\uparrow})_{\{(b),(c)\}}^{-1} & 0 \\ 0 & (\mathbf{B}^{\downarrow\uparrow})_{\{(b),(c)\}}^{-1} \end{bmatrix} \begin{bmatrix} \mathbf{T}_{(b)}^{\uparrow} & 0 \\ 0 & \mathbf{T}_{(c)}^{\downarrow} \mathbf{T}_{(cd)}^{\downarrow} \end{bmatrix} \times \\ &\left[\begin{array}{cc} (\mathbf{L}_{(b)}^{\text{H},\uparrow})^T + \mathbf{T}_{(c)}^{\uparrow} \mathbf{R}_{(cd)}^{\smile} \mathbf{T}_{(c)}^{\downarrow} (\mathbf{L}_{(c)}^{\text{H},\downarrow})^T & (\mathbf{L}_{(b)}^{\text{E},\uparrow})^T + \mathbf{T}_{(c)}^{\uparrow} \mathbf{R}_{(cd)}^{\smile} \mathbf{T}_{(c)}^{\downarrow} (\mathbf{L}_{(c)}^{\text{E},\downarrow})^T \\ (\mathbf{L}_{(c)}^{\text{H},\downarrow})^T & (\mathbf{L}_{(c)}^{\text{E},\downarrow})^T \end{array} \right] \mathbf{Q}(x_3^{bc}). \end{aligned} \quad (3.67)$$

The second case is when the medium parameters of \mathbf{D}^b and \mathbf{D}^c are equal to the medium parameters of \mathbf{D}^d , which results in

$$\mathbf{R}_{(cd)}^{\smile} = 0, \quad (3.68a)$$

$$\mathbf{T}_{(cd)}^{\downarrow} = \mathbf{T}_{(c)}^{\downarrow}, \quad (3.68b)$$

and Eq. (3.65) can be written as

$$\begin{aligned} \begin{bmatrix} \mathbf{W}^{\uparrow}(x_3^{a\downarrow}) \\ \mathbf{W}^{\downarrow}(x_3^{d\uparrow}) \end{bmatrix} &= - \begin{bmatrix} (\mathbf{B}^{\downarrow\uparrow})_{\{(b),(c)\}}^{-1} & 0 \\ 0 & (\mathbf{B}^{\downarrow\uparrow})_{\{(b),(c)\}}^{-1} \end{bmatrix} \begin{bmatrix} \mathbf{T}_{(ab)}^{\uparrow} \mathbf{T}_{(b)}^{\uparrow} & 0 \\ 0 & \mathbf{T}_{(c)}^{\downarrow} \end{bmatrix} \times \\ &\left[\begin{array}{cc} (\mathbf{L}_{(b)}^{\text{H},\uparrow})^T & (\mathbf{L}_{(b)}^{\text{E},\uparrow})^T \\ (\mathbf{L}_{(c)}^{\text{H},\downarrow})^T + \mathbf{T}_{(b)}^{\downarrow} \mathbf{R}_{(ab)}^{\frown} \mathbf{T}_{(b)}^{\uparrow} (\mathbf{L}_{(b)}^{\text{H},\uparrow})^T & (\mathbf{L}_{(c)}^{\text{E},\downarrow})^T + \mathbf{T}_{(b)}^{\downarrow} \mathbf{R}_{(ab)}^{\frown} \mathbf{T}_{(b)}^{\uparrow} (\mathbf{L}_{(b)}^{\text{E},\uparrow})^T \end{array} \right] \mathbf{Q}(x_3^{bc}). \end{aligned} \quad (3.69)$$

We now carry out the limiting procedure $x_3^{b\uparrow} - x_3^{c\downarrow} \rightarrow 0$ which results in $x_3^{ab} = x_3^{bc} = x_3^{cd}$. For Eq. (3.67) this is similar to move the source from above the interface towards the interface and for Eq. (3.69) this is similar to move the source from below the interface towards the interface. No propagation appears in domain \mathbf{D}^b and \mathbf{D}^c and the modified reflection and transmission coefficients can be replaced by the original reflection and transmission coefficients.

Apart from the source vector $\mathbf{Q}(x_3^{bc})$, which must be defined in either domain \mathbf{D}^a or \mathbf{D}^d (see also Eq. (3.6)), Eqs. (3.67) and (3.69) give equal results

using the relations between the transmission and reflection coefficients. It appears that the simplest and most convenient relations are found when we use a hybrid form, that uses both expressions. For Eq. (3.67) the medium properties of \mathbb{D}^b and \mathbb{D}^c are equal to \mathbb{D}^a , while for Eq. (3.69) the medium properties of \mathbb{D}^b and \mathbb{D}^c are equal to \mathbb{D}^d . This is used to write the hybrid form as function of the medium properties of \mathbb{D}^a and \mathbb{D}^d resulting in

$$\begin{aligned}
\begin{bmatrix} \mathbf{W}^\uparrow(x_3^{\frac{a\downarrow}{-}}) \\ \mathbf{W}^\downarrow(x_3^{\frac{d\uparrow}{+}}) \end{bmatrix} &= - \begin{bmatrix} (\mathbf{B}^{\downarrow\uparrow})_{(d)}^{-1} & 0 \\ 0 & (\mathbf{B}^{\downarrow\uparrow})_{(a)}^{-1} \end{bmatrix} \begin{bmatrix} \mathbf{T}_{(ad)}^\uparrow (\mathbf{L}_{(d)}^{\text{H},\uparrow})^T & \mathbf{T}_{(ad)}^\uparrow (\mathbf{L}_{(d)}^{\text{E},\uparrow})^T \\ \mathbf{T}_{(ad)}^\downarrow (\mathbf{L}_{(a)}^{\text{H},\downarrow})^T & \mathbf{T}_{(ad)}^\downarrow (\mathbf{L}_{(a)}^{\text{E},\downarrow})^T \end{bmatrix} \mathbf{Q}(x_3^{ad}), \\
&= \frac{\sqrt{2}}{(k_1^2 + k_2^2)^{\frac{1}{2}}} \times \\
&\quad \begin{bmatrix} (-k_1 Y^d Q_1 - k_2 Y^d Q_2 - k_1 Q_3 - k_2 Q_4)/(Y^a + Y^d) \\ (k_2 \bar{Y}^d Q_1 - k_1 \bar{Y}^d Q_2 + k_2 Q_3 - k_1 Q_4)/(\bar{Y}^a + \bar{Y}^d) \\ (k_1 Y^a Q_1 + k_2 Y^a Q_2 - k_1 Q_3 - k_2 Q_4)/(Y^a + Y^d) \\ (-k_2 \bar{Y}^a Q_1 + k_1 \bar{Y}^a Q_2 + k_2 Q_3 - k_1 Q_4)/(\bar{Y}^a + \bar{Y}^d) \end{bmatrix}.
\end{aligned} \tag{3.70}$$

Using Eqs. (3.11) and (3.70), expressions are obtained for the electromagnetic field due to sources present on a half-space, which form the starting point of the analysis of the half-space response and the radiation pattern for a dipole present on the interface.

The electromagnetic field in a two-media configuration

In this chapter we will derive the electromagnetic field for electric and magnetic dipoles, which are valid when the source is present on the surface of the Earth. This is the configuration, in which electromagnetic exploration methods are usually carried out. First, Maxwell's equations are solved using the approach presented in Chapter 3, where a field vector was introduced containing only field components, which were continuous on the interfaces of horizontally layered media. We consider a field vector that contains all six field components, which is used when a (electric or magnetic) source is present on the surface of the Earth. The matrix containing the relation between the electric and magnetic field components and the electric and magnetic sources is denoted as the half-space matrix.

The half-space matrices for the different regimes are given in the wavenumber domain. Taking the medium properties to be the same for both half-spaces, the response for a homogeneous medium is obtained, in the form of closed-form expressions in x - f -domain. In case of two homogeneous half-spaces, only some of the closed-form expressions can be obtained analytically; specifically in the case when the field is evaluated at the interface. To obtain closed-form expressions for the electromagnetic field valid for the entire hemisphere an

asymptotic evaluation is inevitable. It will be shown that asymptotic expressions valid for the diffusion regime derived some 30 years ago are also valid when the displacement currents are taken appropriately into account, because these results resemble the asymptotic expressions for the electromagnetic field valid in a dielectric half-space.

4.1 Different regimes of the Maxwell's equations

Looking at Maxwell's equations, different regimes can be distinguished. Depending on the frequency used and the medium parameters, Maxwell's differential equations describe different wave phenomena, ranging from the direct current regime, towards the diffusive regime to the wave propagating regime. For the direct current regime the frequency employed equals zero. For the diffusive regime the displacement currents can be neglected compared to the conduction currents and for the wave propagation regime the displacement currents dominate the conduction currents for low loss materials. Note that in between two different regimes, both phenomena have to be taken into account. For the wave propagating regime, no approximation can be made and the full half-space matrix must be evaluated. First the different regimes are investigated whereafter the corresponding half-space matrices are derived. Using Eqs. (2.17a) and (2.17b) the propagation coefficient γ given in Eq. (3.14) can be written as

$$\gamma = j\frac{\omega}{c}\sqrt{1 - \frac{j\sigma}{\omega\varepsilon}} = j\frac{\omega}{v(\omega)} + \alpha(\omega), \text{ with } \text{Re}(\gamma) \geq 0, \quad (4.1)$$

where the wave velocity c is defined as

$$c = \frac{1}{\sqrt{\varepsilon\mu}}. \quad (4.2)$$

The imaginary part of γ is related to the travel time of the wave, while the real part of γ is related to the amount of energy that is converted into heat. The quantity $v(\omega)$ is known as the frequency-dependent propagation coefficient, while $\alpha(\omega)$ is known as the frequency-dependent attenuation factor.

We now distinguish two different ranges in which different phenomena are dominant. The first range exists for $\sigma \gg \omega\varepsilon$, where the conduction currents are dominant. When the displacements currents are neglected then the propagation constant is given by $\gamma = (1 + j)\sqrt{(\omega\sigma\mu)/2}$. In this case we have a parabolic differential equation, known as the diffusion equation. The second range exists for $\sigma \ll \omega\varepsilon$, where the displacement currents are dominant.

When the conduction currents are neglected then $\gamma = j\omega/c + \sigma\sqrt{\mu/4\epsilon}$. In this case we have an elliptic differential equation, known as the wave equation. In the intermediate regime when both displacement currents and conduction currents are present we have a lossy wave propagation. In fact we have a wave equation holding for a lossy medium.

4.2 Electromagnetic field expressions in the horizontal wavenumber domain

In Section 3.5.2 expressions are derived for the up and downgoing elementary waves due to a source present on the interface $x_3 = 0$ between two homogeneous media. Substitution of Eq. (3.70) into Eq. (3.20) and using Eqs. (3.1a) and (3.1b) results in expressions for the six up- and downgoing electromagnetic field components in the upper and lower half-spaces, respectively, which are given by

$$\begin{bmatrix} \tilde{\mathbf{E}}^\uparrow \\ \tilde{\mathbf{H}}^\uparrow \end{bmatrix} = \begin{bmatrix} \tilde{\mathbf{G}}^{\text{EJ},\uparrow} & \tilde{\mathbf{G}}^{\text{EK},\uparrow} \\ \tilde{\mathbf{G}}^{\text{HJ},\uparrow} & \tilde{\mathbf{G}}^{\text{HK},\uparrow} \end{bmatrix} \begin{bmatrix} \tilde{\mathbf{J}} \\ \tilde{\mathbf{K}} \end{bmatrix}, \quad \text{for } x_3 \leq 0, \quad (4.3a)$$

$$\begin{bmatrix} \tilde{\mathbf{E}}^\downarrow \\ \tilde{\mathbf{H}}^\downarrow \end{bmatrix} = \begin{bmatrix} \tilde{\mathbf{G}}^{\text{EJ},\downarrow} & \tilde{\mathbf{G}}^{\text{EK},\downarrow} \\ \tilde{\mathbf{G}}^{\text{HJ},\downarrow} & \tilde{\mathbf{G}}^{\text{HK},\downarrow} \end{bmatrix} \begin{bmatrix} \tilde{\mathbf{J}} \\ \tilde{\mathbf{K}} \end{bmatrix}, \quad \text{for } x_3 \geq 0. \quad (4.3b)$$

In Section 3.5.2 it was noted that the vertical electric and magnetic source must be defined in the upper or lower domain. We now restrict our analysis to sources which are defined in the upper half-space and that $\zeta = \zeta_0$ in the upper and lower half-space.

4.2.1 Electromagnetic field in two homogeneous half-spaces

Using Eqs. (3.20), (3.70), (3.1a) and (3.1b), the submatrices for the upper homogeneous half-space are obtained as

$$\tilde{\mathbf{G}}^{\text{EJ},\uparrow} = \hat{\zeta}_0 \begin{bmatrix} -k_1^2 \tilde{V}^\uparrow - \tilde{U}^\uparrow & -k_1 k_2 \tilde{V}^\uparrow & -jk_1 \hat{\eta}_1 \Gamma_0 \tilde{V}^\uparrow / \hat{\eta}_0 \\ -k_1 k_2 \tilde{V}^\uparrow & -k_2^2 \tilde{V}^\uparrow - \tilde{U}^\uparrow & -jk_2 \hat{\eta}_1 \Gamma_0 \tilde{V}^\uparrow / \hat{\eta}_0 \\ -jk_1 \Gamma_1 \tilde{V}^\uparrow & -jk_2 \Gamma_1 \tilde{V}^\uparrow & \hat{\eta}_1 (k_1^2 + k_2^2) \tilde{V}^\uparrow / \hat{\eta}_0 \end{bmatrix}, \quad (4.4a)$$

$$\tilde{\mathbf{G}}^{\text{EK},\uparrow} = \begin{bmatrix} -k_1 k_2 (\Gamma_0 - \Gamma_1) \tilde{V}^\uparrow & (\gamma_1^2 \Gamma_0 + k_2^2 [\Gamma_1 - \Gamma_0]) \tilde{V}^\uparrow & jk_2 \tilde{U}^\uparrow \\ -(\gamma_1^2 \Gamma_0 + k_1^2 [\Gamma_0 - \Gamma_1]) \tilde{V}^\uparrow & k_1 k_2 (\Gamma_0 - \Gamma_1) \tilde{V}^\uparrow & -jk_1 \tilde{U}^\uparrow \\ -jk_2 \gamma_1^2 \tilde{V}^\uparrow & jk_1 \gamma_1^2 \tilde{V}^\uparrow & 0 \end{bmatrix}, \quad (4.4b)$$

$$\tilde{\mathbf{G}}^{\text{HJ},\uparrow} = \begin{bmatrix} k_1 k_2 (\Gamma_0 - \Gamma_1) \tilde{V}^\uparrow & -(\gamma_0^2 \Gamma_1 + k_1^2 [\Gamma_1 - \Gamma_0]) \tilde{V}^\uparrow & -jk_2 \gamma_1^2 \tilde{V}^\uparrow \\ (\gamma_0^2 \Gamma_1 + k_2^2 [\Gamma_1 - \Gamma_0]) \tilde{V}^\uparrow & -k_1 k_2 (\Gamma_0 - \Gamma_1) \tilde{V}^\uparrow & jk_1 \gamma_1^2 \tilde{V}^\uparrow \\ jk_2 \tilde{U}^\uparrow & -jk_1 \tilde{U}^\uparrow & 0 \end{bmatrix}, \quad (4.4c)$$

$$\tilde{\mathbf{G}}^{\text{HK},\uparrow} = \frac{1}{\hat{\zeta}_0} \times \begin{bmatrix} k_1^2 \tilde{U}^\uparrow - [\gamma_0^2 \gamma_1^2 + k_1^2 (\gamma_0^2 + \gamma_1^2)] \tilde{V}^\uparrow & -k_1 k_2 [(\gamma_0^2 + \gamma_1^2) \tilde{V}^\uparrow + \tilde{U}^\uparrow] & -jk_1 \Gamma_0 \tilde{U}^\uparrow \\ -k_1 k_2 [(\gamma_0^2 + \gamma_1^2) \tilde{V}^\uparrow + \tilde{U}^\uparrow] & k_2^2 \tilde{U}^\uparrow - [\gamma_0^2 \gamma_1^2 + k_2^2 (\gamma_0^2 + \gamma_1^2)] \tilde{V}^\uparrow & -jk_2 \Gamma_0 \tilde{U}^\uparrow \\ -jk_1 \Gamma_1 \tilde{U}^\uparrow & -jk_2 \Gamma_1 \tilde{U}^\uparrow & (k_1^2 + k_2^2) \tilde{U}^\uparrow \end{bmatrix} \quad (4.4d)$$

for $x_3 \leq 0$,

where

$$\tilde{U}^\uparrow = \frac{\exp(\Gamma_0 x_3)}{\Gamma_0 + \Gamma_1}, \quad (4.5a)$$

$$\tilde{V}^\uparrow = \frac{\exp(\Gamma_0 x_3)}{\gamma_1^2 \Gamma_0 + \gamma_0^2 \Gamma_1}, \quad (4.5b)$$

in which $\Gamma_{\{0,1\}}$ and $\gamma_{\{0,1\}}$ are the vertical propagation coefficient and the propagation coefficient, respectively in the upper and lower halfspace, which are given in Eqs. (3.13) and 3.14) for arbitrary media. Note that only upgoing waves are present in the upper medium, which is indicated by the

propagation constant Γ_0 which is present in the exponent for the upgoing waves. The submatrices for the lower homogeneous half-space are obtained as

$$\tilde{\mathbf{G}}^{\text{EJ},\downarrow} = \hat{\zeta}_0 \begin{bmatrix} -k_1^2 \tilde{V}^\downarrow - \tilde{U}^\downarrow & -k_1 k_2 \tilde{V}^\downarrow & j k_1 \Gamma_1 \tilde{V}^\downarrow \\ -k_1 k_2 \tilde{V}^\downarrow & -k_2^2 \tilde{V}^\downarrow - \tilde{U}^\downarrow & j k_2 \Gamma_1 \tilde{V}^\downarrow \\ j k_1 \Gamma_0 \tilde{V}^\downarrow & j k_2 \Gamma_0 \tilde{V}^\downarrow & (k_1^2 + k_2^2) \tilde{V}^\downarrow \end{bmatrix}, \quad (4.6a)$$

$$\tilde{\mathbf{G}}^{\text{EK},\downarrow} = \begin{bmatrix} -k_1 k_2 (\Gamma_0 - \Gamma_1) \tilde{V}^\downarrow & -(\gamma_0^2 \Gamma_1 + k_2^2 [\Gamma_1 - \Gamma_0]) \tilde{V}^\downarrow & j k_2 \tilde{U}^\downarrow \\ (\gamma_0^2 \Gamma_1 + k_1^2 [\Gamma_1 - \Gamma_0]) \tilde{V}^\downarrow & k_1 k_2 (\Gamma_0 - \Gamma_1) \tilde{V}^\downarrow & -j k_1 \tilde{U}^\downarrow \\ -j k_2 \gamma_0^2 \tilde{V}^\downarrow & j k_1 \gamma_0^2 \tilde{V}^\downarrow & 0 \end{bmatrix}, \quad (4.6b)$$

$$\tilde{\mathbf{G}}^{\text{HJ},\downarrow} = \begin{bmatrix} k_1 k_2 (\Gamma_0 - \Gamma_1) \tilde{V}^\downarrow & (\gamma_1^2 \Gamma_0 + k_1^2 [\Gamma_0 - \Gamma_1]) \tilde{V}^\downarrow & -j k_2 \gamma_1^2 \tilde{V}^\downarrow \\ -(\gamma_1^2 \Gamma_0 + k_2^2 [\Gamma_0 - \Gamma_1]) \tilde{V}^\downarrow & -k_1 k_2 (\Gamma_0 - \Gamma_1) \tilde{V}^\downarrow & j k_1 \gamma_1^2 \tilde{V}^\downarrow \\ j k_2 \tilde{U}^\downarrow & -j k_1 \tilde{U}^\downarrow & 0 \end{bmatrix}, \quad (4.6c)$$

$$\tilde{\mathbf{G}}^{\text{HK},\downarrow} = \frac{1}{\hat{\zeta}_0} \times \begin{bmatrix} k_1^2 \tilde{U}^\downarrow - [\gamma_0^2 \gamma_1^2 + k_1^2 (\gamma_0^2 + \gamma_1^2)] \tilde{V}^\downarrow & -k_1 k_2 [(\gamma_0^2 + \gamma_1^2) \tilde{V}^\downarrow + \tilde{U}^\downarrow] & j k_1 \Gamma_1 \tilde{U}^\downarrow \\ -k_1 k_2 [(\gamma_0^2 + \gamma_1^2) \tilde{V}^\downarrow + \tilde{U}^\downarrow] & k_2^2 \tilde{U}^\downarrow - [\gamma_0^2 \gamma_1^2 + k_2^2 (\gamma_0^2 + \gamma_1^2)] \tilde{V}^\downarrow & j k_2 \Gamma_1 \tilde{U}^\downarrow \\ j k_1 \Gamma_0 \tilde{U}^\downarrow & j k_2 \Gamma_0 \tilde{U}^\downarrow & (k_1^2 + k_2^2) \tilde{U}^\downarrow \end{bmatrix} \quad (4.6d)$$

for $x_3 \geq 0$,

where

$$\tilde{U}^\downarrow = \frac{\exp(-\Gamma_1 x_3)}{\Gamma_0 + \Gamma_1}, \quad (4.7a)$$

$$\tilde{V}^\downarrow = \frac{\exp(-\Gamma_1 x_3)}{\gamma_1^2 \Gamma_0 + \gamma_0^2 \Gamma_1}. \quad (4.7b)$$

Only downgoing waves are present in the lower medium, which is indicated by the propagation constant Γ_1 , which is present in the exponent for the downgoing waves. These expressions in the horizontal Fourier domain for the electromagnetic fields in the upper and lower half-space are exact and no approximation is made.

4.2.2 Electromagnetic field in homogeneous space

For a homogeneous space, γ_1 and γ_0 are equal and abbreviated by γ , and at the same time Γ_1 and Γ_0 are equal and abbreviated by Γ . The submatrices given in Eqs. (4.4a)-(4.4d) reduce to

$$\tilde{\mathbf{G}}^{\text{EJ},\uparrow} = \hat{\zeta}_0 \begin{bmatrix} -(k_1^2/\gamma^2 + 1) & -k_1 k_2/\gamma^2 & -jk_1 \Gamma/\gamma^2 \\ -k_1 k_2/\gamma^2 & -(k_2^2/\gamma^2 + 1) & -jk_2 \Gamma/\gamma^2 \\ -jk_1 \Gamma/\gamma^2 & -jk_2 \Gamma/\gamma^2 & (k_1^2 + k_2^2)/\gamma^2 \end{bmatrix} \tilde{G}, \quad (4.8a)$$

$$\tilde{\mathbf{G}}^{\text{EK},\uparrow} = \begin{bmatrix} 0 & \Gamma & jk_2 \\ -\Gamma & 0 & -jk_1 \\ -jk_2 & jk_1 & 0 \end{bmatrix} \tilde{G}, \quad (4.8b)$$

$$\tilde{\mathbf{G}}^{\text{HJ},\uparrow} = \begin{bmatrix} 0 & -\Gamma & -jk_2 \\ \Gamma & 0 & jk_1 \\ jk_2 & -jk_1 & 0 \end{bmatrix} \tilde{G}, \quad (4.8c)$$

$$\tilde{\mathbf{G}}^{\text{HK},\uparrow} = \frac{1}{\hat{\zeta}_0} \begin{bmatrix} -(\gamma^2 + k_1^2) & -k_1 k_2 & -jk_1 \Gamma \\ -k_1 k_2 & -(\gamma^2 + k_2^2) & -jk_2 \Gamma \\ -jk_1 \Gamma & -jk_2 \Gamma & (k_1^2 + k_2^2) \end{bmatrix} \tilde{G}, \quad (4.8d)$$

for $x_3 \leq 0$,

where

$$\tilde{G} = \frac{\exp(-\Gamma|x_3|)}{2\Gamma}, \quad (4.9)$$

and the following relations exist:

$$\tilde{\mathbf{G}}^{\text{EK},\uparrow} = -\tilde{\mathbf{G}}^{\text{HJ},\uparrow}, \quad (4.10a)$$

$$\tilde{\mathbf{G}}^{\text{EJ},\uparrow} = \frac{\hat{\zeta}}{\hat{\eta}} \tilde{\mathbf{G}}^{\text{HK},\uparrow}. \quad (4.10b)$$

The submatrices given in Eqs. (4.6a)-(4.6d) reduce to

$$\tilde{\mathbf{G}}^{\text{EJ},\downarrow} = \hat{\zeta}_0 \begin{bmatrix} -(k_1^2/\gamma^2 + 1) & -k_1 k_2/\gamma^2 & j k_1 \Gamma/\gamma^2 \\ -k_1 k_2/\gamma^2 & -(k_2^2/\gamma^2 + 1) & j k_2 \Gamma/\gamma^2 \\ j k_1 \Gamma/\gamma^2 & j k_2 \Gamma/\gamma^2 & (k_1^2 + k_2^2)/\gamma^2 \end{bmatrix} \tilde{\mathbf{G}}, \quad (4.11a)$$

$$\tilde{\mathbf{G}}^{\text{EK},\downarrow} = \begin{bmatrix} 0 & -\Gamma & j k_2 \\ \Gamma & 0 & -j k_1 \\ -j k_2 & j k_1 & 0 \end{bmatrix} \tilde{\mathbf{G}}, \quad (4.11b)$$

$$\tilde{\mathbf{G}}^{\text{HJ},\downarrow} = \begin{bmatrix} 0 & \Gamma & -j k_2 \\ -\Gamma & 0 & j k_1 \\ j k_2 & -j k_1 & 0 \end{bmatrix} \tilde{\mathbf{G}}, \quad (4.11c)$$

$$\tilde{\mathbf{G}}^{\text{HK},\downarrow} = \frac{1}{\hat{\zeta}_0} \begin{bmatrix} -(\gamma^2 + k_1^2) & -k_1 k_2 & j k_1 \Gamma \\ -k_1 k_2 & -(\gamma^2 + k_2^2) & j k_2/2 \\ j k_1 \Gamma & j k_2 \Gamma & (k_1^2 + k_2^2) \end{bmatrix} \tilde{\mathbf{G}}, \quad (4.11d)$$

$$\text{for } x_3 \geq 0, \quad (4.11e)$$

and the following relations exist:

$$\tilde{\mathbf{G}}^{\text{EK},\downarrow} = -\tilde{\mathbf{G}}^{\text{HJ},\downarrow}, \quad (4.12a)$$

$$\tilde{\mathbf{G}}^{\text{EJ},\downarrow} = \frac{\hat{\zeta}}{\hat{\eta}} \tilde{\mathbf{G}}^{\text{HK},\downarrow}. \quad (4.12b)$$

Note that Eqs. (4.10a) and (4.10b) and (4.12a) and (4.12b) do not hold for a configuration consisting of two homogeneous half-spaces.

4.3 Analytical derivation of closed-form expressions in the space-frequency domain

For particular elements of the matrices given in Section 4.2 closed form expressions in the space-frequency domain can be analytically derived for the electric and magnetic field as given in Eqs. (4.3a) and (4.3b). The inverse spatial Fourier transformation as discussed in Section 2.5 has to be evaluated, which shows that the spatial derivatives can be recognized and the rule that $-j k_\nu$ transforms to ∂_ν can be applied. Next a transition to cylindrical coordinates can be applied as discussed in Section 2.6. From Eq. (4.9) it is

observed that only one elementary function must be evaluated,

$$\begin{aligned}
\hat{G}(\mathbf{x}, \omega) &= \frac{1}{2\pi} \int_{\kappa=0}^{\infty} \tilde{G}(k_1, k_2, x_3, \omega) J_0(\kappa r) \kappa d\kappa, \\
&= \frac{1}{2\pi} \int_{\kappa=0}^{\infty} \frac{\exp(-\Gamma|x_3|)}{2\Gamma} J_0(\kappa r) \kappa d\kappa, \\
&= \frac{\exp(-\gamma|\mathbf{x}|)}{4\pi|\mathbf{x}|}.
\end{aligned} \tag{4.13}$$

Equation (4.13) is also given by Sommerfeld [1949].

4.3.1 Electromagnetic field in homogeneous space

The replacement of the elementary function given in Eq. (4.13) in Eqs. (4.8a)-(4.11d) and making use of the shift invariance in a homogeneous medium shows that the different expressions for $x_3 \geq 0$ and $x_3 \leq 0$ can be combined to

$$\begin{bmatrix} \hat{\mathbf{E}} \\ \hat{\mathbf{H}} \end{bmatrix} = \begin{bmatrix} \hat{\mathbf{G}}^{\text{EJ}} & \hat{\mathbf{G}}^{\text{EK}} \\ \hat{\mathbf{G}}^{\text{HJ}} & \hat{\mathbf{G}}^{\text{HK}} \end{bmatrix} \begin{bmatrix} \hat{\mathbf{J}} \\ \hat{\mathbf{K}} \end{bmatrix}, \tag{4.14}$$

in which

$$\hat{\mathbf{G}}^{\text{EJ}} = \frac{1}{\hat{\eta}} \begin{bmatrix} \partial_1^2 - \gamma^2 & \partial_2 \partial_1 & \partial_3 \partial_1 \\ \partial_1 \partial_2 & \partial_2^2 - \gamma^2 & \partial_3 \partial_2 \\ \partial_3 \partial_1 & \partial_3 \partial_2 & -(\partial_1^2 + \partial_2^2) \end{bmatrix} \hat{G}, \tag{4.15a}$$

$$\hat{\mathbf{G}}^{\text{EK}} = \begin{bmatrix} 0 & \partial_3 & -\partial_2 \\ -\partial_3 & 0 & \partial_1 \\ \partial_2 & -\partial_1 & 0 \end{bmatrix} \hat{G}, \tag{4.15b}$$

$$\hat{\mathbf{G}}^{\text{HJ}} = \begin{bmatrix} 0 & -\partial_3 & \partial_2 \\ \partial_3 & 0 & -\partial_1 \\ -\partial_2 & \partial_1 & 0 \end{bmatrix} \hat{G}, \tag{4.15c}$$

$$\hat{\mathbf{G}}^{\text{HK}} = \frac{1}{\hat{\zeta}_0} \begin{bmatrix} \partial_1^2 - \gamma^2 & \partial_2 \partial_1 & \partial_3 \partial_1 \\ \partial_1 \partial_2 & \partial_2^2 - \gamma^2 & \partial_3 \partial_2 \\ \partial_1 \partial_3 & \partial_2 \partial_3 & -(\partial_1^2 + \partial_2^2) \end{bmatrix} \hat{G}. \tag{4.15d}$$

Using $\gamma^2 \hat{G} = (\partial_1^2 + \partial_2^2 + \partial_3^2) \hat{G}$ the results can be written as

$$\hat{G}_{kr}^{\text{EJ}} = \hat{\eta}^{-1} [\partial_k \partial_r - \gamma^2 \delta_{k,r}] \hat{G}, \quad (4.16a)$$

$$\hat{G}_{kr}^{\text{EK}} = -\epsilon_{k,m,r} \partial_m \hat{G}, \quad (4.16b)$$

$$\hat{G}_{jr}^{\text{HJ}} = \epsilon_{j,m,r} \partial_m \hat{G}, \quad (4.16c)$$

$$\hat{G}_{jp}^{\text{HK}} = \hat{\zeta}^{-1} [\partial_j \partial_p - \gamma^2 \delta_{j,p}] \hat{G}. \quad (4.16d)$$

All expressions have the propagation factor $\exp(-\gamma|\mathbf{x}|)$ in common. Due to the spatial derivatives, particular direction patterns arise, which depend on the orientation of the source and the direction of observation. Another fact that arises due to the spatial derivatives is that the field can be distinguished in three different contributions; the near field is proportional to $|\mathbf{x}|^{-3}$, the intermediate field proportional to $|\mathbf{x}|^{-2}$ and the far field proportional to $|\mathbf{x}|^{-1}$ [see also de Hoop, 1995]. These closed form representations facilitate a thorough analysis of the radiation characteristics of each separate near, intermediate- and far-field term [de Hoop, 1995]. For $|\gamma||\mathbf{x}| \gg 1$, the near and intermediate field can be neglected compared to the far-field contributions. Another definition of the far-field region, or Fraunhofer region, is based on the influence of a finite aperture of the source. The Fraunhofer region is present for $R \gg 2D^2/\lambda$ [Skolnik, 1980], where D is the size of the aperture and λ is the wavelength. We will concentrate on the amplitudes of the electric field in spherical coordinates (R, ϕ, θ) .

The electric current source is positioned at the origin and is oriented in the \mathbf{i}_1 -direction ($\phi = 0$). For different angles θ the electric field is analysed at a fixed radius. The configuration is given in Figure 4.1. The analysis is carried out in two planes; the E -plane ($\phi = 0$), and the H -plane ($\phi = \pi/2$). The E -plane is parallel to the direction of the current source dipole, while the H -plane is perpendicular to the direction of the current source dipole. In the E -plane, the electric field is always parallel to the E -plane, so no \hat{E}_2 -component will be present in the E -plane. In the H -plane, the magnetic field is always parallel to the H -plane. The electric field is perpendicular to the magnetic field, so in the H -plane only an \hat{E}_1 -component will be present in the H -plane. Note that all three components of the electric field will be present when not in the E - or H -plane. The amplitude and polarisation of the electric field in a homogeneous space at a distance of 1 meter are plotted in Figures 4.2 and 4.3 for the H - and the E -plane, respectively. The wavelength is $\lambda = 0.3$ m, for a frequency of $f = 500$ MHz.

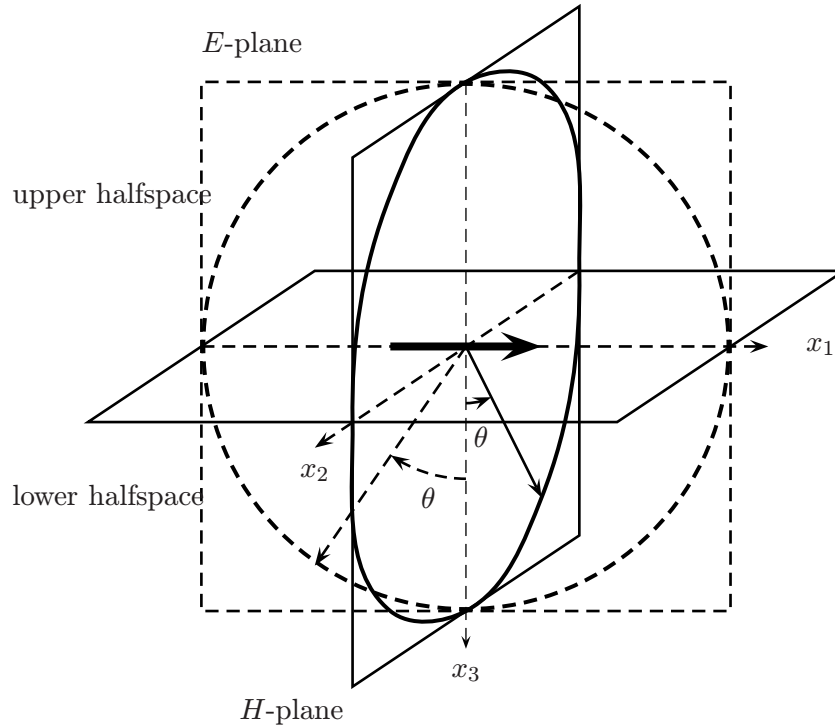


Figure 4.1: Different planes of investigation; the E -plane and the H -plane.

In Fig. 4.2 a circle is present in the origin, indicating the direction of the source, which is perpendicular to the H -plane and in Fig. 4.3 an arrow is present in the E -plane, indicating the direction of the source, which is parallel to the E -plane. The dashed line indicates the amplitude of the electric field as function of the angle θ at a fixed radius $R = 1 \text{ m} \approx 3.3\lambda$ and the dotted line indicates a line of equal amplitudes. The only component of the electric field in the H -plane is in the \hat{i}_1 -direction and is omnidirectional. The electric field components in the E -plane are in the \hat{i}_1 - and \hat{i}_3 -direction. \hat{E}_θ has a zero in the E -plane for $x_3 = 0$. The electric field shown in Figures 4.2 and 4.3 contributes to the radiated power. However, it is still important to know also the electric field in the radial direction, which is shown in Fig. 4.4. \hat{E}_R is zero in the plane $x_1 = 0$. The contribution of \hat{E}_R is proportional to $|\mathbf{x}|^2$

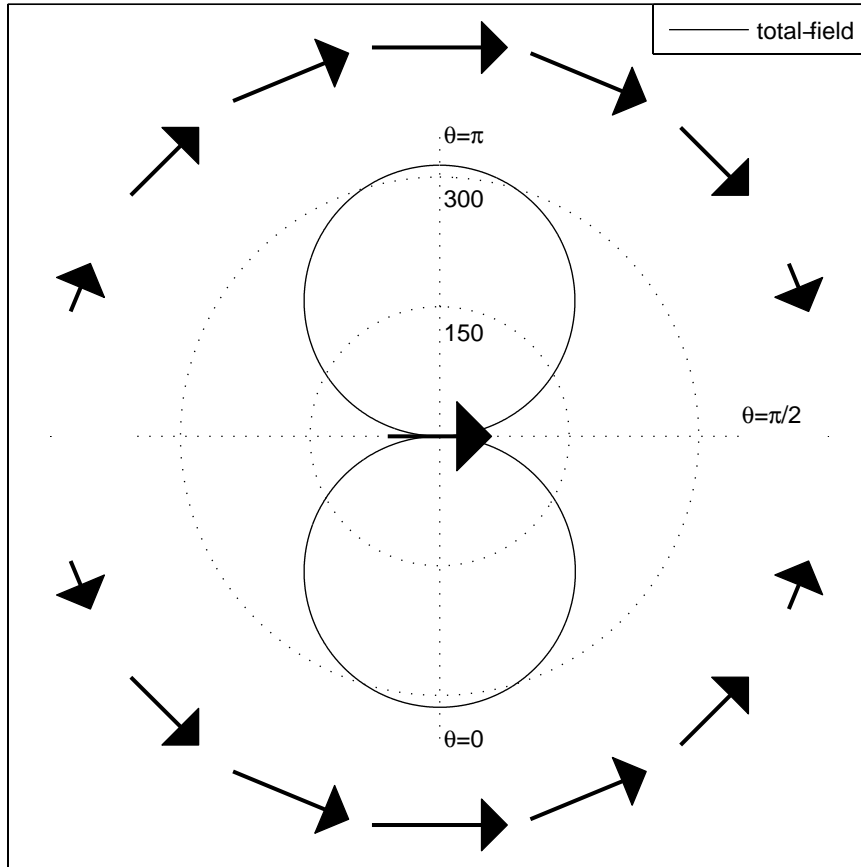


Figure 4.3: The amplitude of the total-field amplitudes for \hat{E}_θ in the E -plane for $R = 1 \text{ m} \approx 3.3\lambda$, $f = 500 \text{ MHz}$, $\sigma = 0 \text{ S/m}$ and $\varepsilon_r = 4$. The orientation of the field is indicated by an arrow.

4.3.2 Electromagnetic field in two homogeneous half-spaces at the interface

For some of the expressions in the Fourier domain given in Eqs. (4.4a)-(4.4d) and (4.6a)-(4.6d) a closed-form representation can be analytically obtained for locations at the interface ($x_3 = 0$) using the scalar Green function as

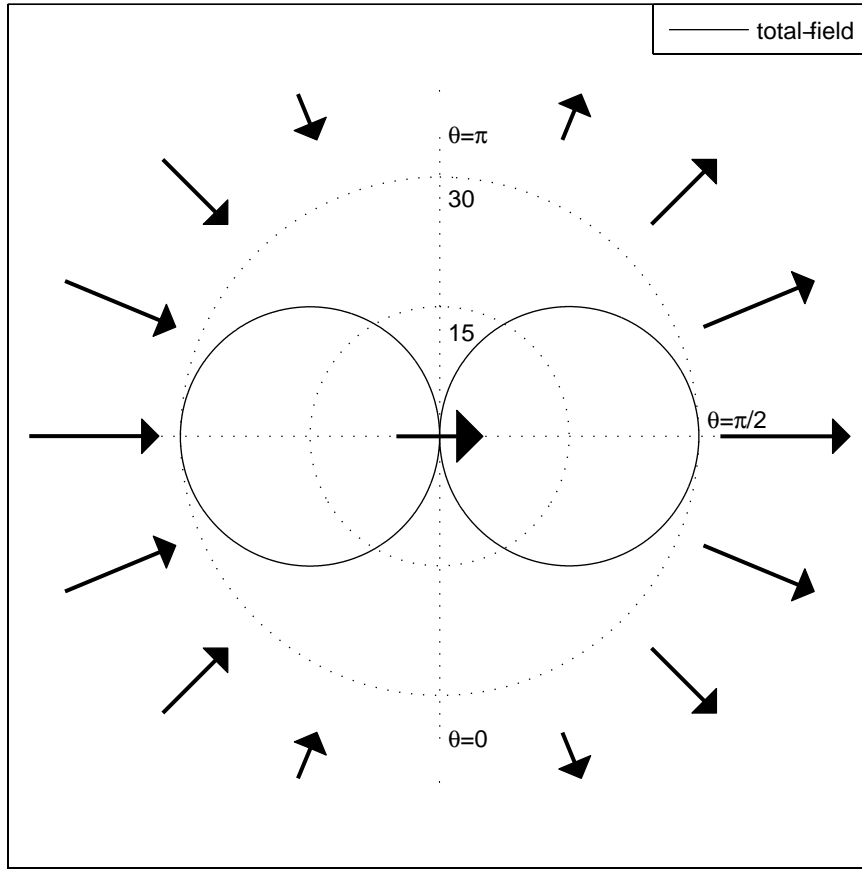


Figure 4.4: The amplitude of the total-field amplitudes for \hat{E}_R in the E -plane for $R = 1 \text{ m} \approx 3.3\lambda$, $f = 500 \text{ MHz}$, $\sigma = 0 \text{ S/m}$ and $\epsilon_r = 4$. The orientation of the field is indicated by an arrow.

given in Eq. (4.13). Rewriting Eq. (4.5a) for $x_3 = 0$, we obtain

$$\tilde{U} = \frac{1}{\Gamma_0 + \Gamma_1} = \frac{\Gamma_0 - \Gamma_1}{\gamma_0^2 - \gamma_1^2}. \quad (4.17)$$

The inverse transform of \tilde{U} is obtained as

$$\hat{U} = \frac{2}{\gamma_0^2 - \gamma_1^2} \left(\lim_{x_3 \rightarrow 0} \partial_3^2 \hat{G}_0(\mathbf{x}) - \lim_{x_3 \rightarrow 0} \partial_3^2 \hat{G}_1(\mathbf{x}) \right), \quad (4.18)$$

where

$$\hat{G}_0 = \frac{\exp(-\gamma_0|\mathbf{x}|)}{4\pi|\mathbf{x}|}, \quad (4.19a)$$

$$\hat{G}_1 = \frac{\exp(-\gamma_1|\mathbf{x}|)}{4\pi|\mathbf{x}|}. \quad (4.19b)$$

It is observed that for field components which only depend on the factor \tilde{U} a closed-form equivalent can be analytically derived in the space-frequency domain for $x_3 = 0$. The following expressions have arguments $(x_\kappa, 0)$, which is shortly indicated by (x_κ) .

$$\hat{G}_{13}^{\text{EK}}(x_\kappa) = \frac{-2\partial_2}{\gamma_1^2 - \gamma_0^2} \left\{ \lim_{x_3 \rightarrow 0} \partial_3^2 \hat{G}_1(\mathbf{x}) - \lim_{x_3 \rightarrow 0} \partial_3^2 \hat{G}_0(\mathbf{x}) \right\}, \quad (4.20a)$$

$$\hat{G}_{23}^{\text{EK}}(x_\kappa) = \frac{2\partial_1}{\gamma_1^2 - \gamma_0^2} \left\{ \lim_{x_3 \rightarrow 0} \partial_3^2 \hat{G}_1(\mathbf{x}) - \lim_{x_3 \rightarrow 0} \partial_3^2 \hat{G}_0(\mathbf{x}) \right\}, \quad (4.20b)$$

$$\hat{G}_{31}^{\text{HJ}}(x_\kappa) = \frac{-2\partial_2}{\gamma_1^2 - \gamma_0^2} \left\{ \lim_{x_3 \rightarrow 0} \partial_3^2 \hat{G}_1(\mathbf{x}) - \lim_{x_3 \rightarrow 0} \partial_3^2 \hat{G}_0(\mathbf{x}) \right\}, \quad (4.20c)$$

$$\hat{G}_{32}^{\text{HJ}}(x_\kappa) = \frac{2\partial_1}{\gamma_1^2 - \gamma_0^2} \left\{ \lim_{x_3 \rightarrow 0} \partial_3^2 \hat{G}_1(\mathbf{x}) - \lim_{x_3 \rightarrow 0} \partial_3^2 \hat{G}_0(\mathbf{x}) \right\}, \quad (4.20d)$$

$$\hat{G}_{33}^{\text{HK}}(x_\kappa) = \frac{-2(\partial_1^2 + \partial_2^2)}{\hat{\zeta}_0(\gamma_0^2 - \gamma_1^2)} \left\{ \lim_{x_3 \rightarrow 0} \partial_3^2 \hat{G}_0(\mathbf{x}) - \lim_{x_3 \rightarrow 0} \partial_3^2 \hat{G}_1(\mathbf{x}) \right\}. \quad (4.20e)$$

Note that \hat{G}_{13}^{EK} and \hat{G}_{23}^{EK} equals \hat{G}_{31}^{HJ} and \hat{G}_{32}^{HJ} , respectively. For the following, the expressions are evaluated for $x_2 = 0$ and the argument is shortly

indicated by (x_1) . Evaluating Eqs. (4.20a)-(4.20e) yields

$$\hat{G}_{13}^{\text{EK}}(x_1) = 0, \quad (4.21a)$$

$$\hat{G}_{23}^{\text{EK}}(x_1) = \frac{2}{4\pi(\gamma_1^2 - \gamma_0^2)x_1^4} \left[(3 + 3\gamma_1 x_1 + \gamma_1^2 x_1^2) \exp(-\gamma_1 |x_1|) - (3 + 3\gamma_0 x_1 + \gamma_0^2 x_1^2) \exp(-\gamma_0 |x_1|) \right], \quad (4.21b)$$

$$\hat{G}_{31}^{\text{HJ}}(x_1) = 0, \quad (4.21c)$$

$$\hat{G}_{32}^{\text{HJ}}(x_1) = \frac{2}{4\pi(\gamma_1^2 - \gamma_0^2)x_1^4} \left[(3 + 3\gamma_1 x_1 + \gamma_1^2 x_1^2) \exp(-\gamma_1 |x_1|) - (3 + 3\gamma_0 x_1 + \gamma_0^2 x_1^2) \exp(-\gamma_0 |x_1|) \right], \quad (4.21d)$$

$$\hat{G}_{33}^{\text{HK}}(x_1) = \frac{2}{4\pi\hat{\zeta}_0(\gamma_0^2 - \gamma_1^2)x_1^5} \left[(\gamma_0^3 x_1^3 + 4\gamma_0^2 x_1^2 + 9\gamma_0 x_1 + 9) \exp(-\gamma_0 |x_1|) - (\gamma_1^3 x_1^3 + 4\gamma_1^2 x_1^2 + 9\gamma_1 x_1 + 9) \exp(-\gamma_1 |x_1|) \right]. \quad (4.21e)$$

The above expressions are exact; no approximations have been made. Eq. (4.21e) may also be derived using the magnetic vector potential (Wait, 1954). For the diffusive field regime, the displacement currents in the air are neglected $\gamma_0 = 0$. An overview of closed-form expressions for the diffusive field for various sources on the surface of a homogeneous half-space are summarized by Nabighian [1991].

For ground penetrating radar we are interested in closed-form expressions in the space-frequency domain for Eqs. (4.4a) and (4.6a). However these expressions cannot be analytically obtained, because these expressions do not depend on the basic function given in Eq. (4.13). Therefore an asymptotic evaluation will be carried out to obtain closed-form expressions.

4.4 Asymptotics for electric field generated by a horizontal electric dipole on an interface

Many environmental and engineering targets of interest are located within a few wavelengths of the antennas. It is important that the behaviour of the propagation of the electromagnetic field is known in this intermediate regime. For a fast and efficient imaging algorithm, it is indispensable to have closed-form expressions of the electromagnetic field. In Section 4.3.1 it is already indicated that in a homogeneous space the contribution of the intermediate field is significant and has to be taken into account for positions relatively close to the source. Far-field asymptotic solutions for a lossless half-space as

given by Engheta et al. [1982] do not accurately describe the performance of elementary GPR antennas, horizontal electric dipoles, in the intermediate region. In this section, I attempt to obtain closed-form expressions for the electromagnetic field due to a horizontal dipole present on the interface of a dielectric medium for the intermediate region.

Using the rule that $-jk_{\{1,2\}}$ transforms to $\partial_{\{1,2\}}$, we can write the result of Eqs. (4.4a) and (4.6a) for horizontal electric current sources in the space-frequency domain as

$$\begin{bmatrix} \hat{E}_1 \\ \hat{E}_2 \\ \hat{E}_3 \end{bmatrix}^\uparrow = \hat{\zeta}_0 \begin{bmatrix} \partial_1^2 \hat{V}^\uparrow - \hat{U}^\uparrow & \partial_1 \partial_2 \hat{V}^\uparrow \\ \partial_1 \partial_2 \hat{V}^\uparrow & \partial_2^2 \hat{V}^\uparrow - \hat{U}^\uparrow \\ -\partial_1 \partial_a \hat{V}^\uparrow & -\partial_2 \partial_a \hat{V}^\uparrow \end{bmatrix} \begin{bmatrix} \hat{J}_1 \\ \hat{J}_2 \end{bmatrix}, \quad (4.22a)$$

$$\begin{bmatrix} \hat{E}_1 \\ \hat{E}_2 \\ \hat{E}_3 \end{bmatrix}^\downarrow = \hat{\zeta}_0 \begin{bmatrix} \partial_1^2 \hat{V}^\downarrow - \hat{U}^\downarrow & \partial_1 \partial_2 \hat{V}^\downarrow \\ \partial_1 \partial_2 \hat{V}^\downarrow & \partial_2^2 \hat{V}^\downarrow - \hat{U}^\downarrow \\ \partial_1 \partial_b \hat{V}^\downarrow & \partial_2 \partial_b \hat{V}^\downarrow \end{bmatrix} \begin{bmatrix} \hat{J}_1 \\ \hat{J}_2 \end{bmatrix}, \quad (4.22b)$$

Writing the expressions for \hat{U}^\uparrow and \hat{U}^\downarrow and \hat{V}^\uparrow and \hat{V}^\downarrow as particular forms of the more general integrals $\hat{\mathcal{U}}^\uparrow$ and $\hat{\mathcal{V}}^\uparrow$, we have

$$\hat{U}^\uparrow = \hat{\mathcal{U}}(0, -x_3, r), \quad (4.23a)$$

$$\hat{V}^\uparrow = \hat{\mathcal{V}}(0, -x_3, r), \quad (4.23b)$$

$$\partial_a \hat{V}^\uparrow = \left[\partial_a \hat{\mathcal{V}}(a, -x_3, r) \right]_{a=0}, \quad (4.23c)$$

$$\hat{U}^\downarrow = \hat{\mathcal{U}}(x_3, 0, r), \quad (4.23d)$$

$$\hat{V}^\downarrow = \hat{\mathcal{V}}(x_3, 0, r), \quad (4.23e)$$

$$\partial_b \hat{V}^\downarrow = \left[\partial_b \hat{\mathcal{V}}(x_3, b, r) \right]_{b=0}. \quad (4.23f)$$

The essential integrals $\hat{\mathcal{U}}^\uparrow$ and $\hat{\mathcal{V}}^\uparrow$, which have to be evaluated, are given by

$$\hat{\mathcal{U}}(a, b, r) = \frac{1}{4\pi^2} \int_{k_2=-\infty}^{\infty} dk_2 \int_{k_1=-\infty}^{\infty} \frac{\exp(-\Gamma_1 a - \Gamma_0 b - jk_\alpha x_\alpha)}{\Gamma_0 + \Gamma_1} dk_1, \quad (4.24a)$$

$$\hat{\mathcal{V}}(a, b, r) = \frac{1}{4\pi^2} \int_{k_2=-\infty}^{\infty} dk_2 \int_{k_1=-\infty}^{\infty} \frac{\exp(-\Gamma_1 a - \Gamma_0 b - jk_\alpha x_\alpha)}{\gamma_1^2 \Gamma_0 + \gamma_0^2 \Gamma_1} dk_1. \quad (4.24b)$$

Using Eq. (2.28b) as derived in Section 2.6, Eqs. (4.24a) and (4.24b) reduce

to

$$\hat{U}(a, b, r) = \frac{1}{4\pi} \int_{-\infty}^{\infty} \frac{\exp(-\Gamma_1 a - \Gamma_0 b)}{\Gamma_1 + \Gamma_0} H_0^{(2)}(\kappa r) \kappa d\kappa, \quad (4.25a)$$

$$\hat{V}(a, b, r) = \frac{1}{4\pi} \int_{-\infty}^{\infty} \frac{\exp(-\Gamma_1 a - \Gamma_0 b)}{\gamma_1^2 \Gamma_0 + \gamma_0^2 \Gamma_1} H_0^{(2)}(\kappa r) \kappa d\kappa. \quad (4.25b)$$

When asymptotic expressions for these integrals can be derived, the electric field can be obtained. Many researchers have already investigated asymptotic expressions for the electric field due to a horizontal electric dipole present on an interface.

Baños [1966] discussed the radiated diffusive electromagnetic field of a dipole in the presence of a conducting half-space and gave separate asymptotic expressions for the electromagnetic field which are valid in the vicinity of the interface or in the vicinity of the vertical axis. King and Smith [1981] investigated the validity of the expressions for field values in the vicinity of the interface which were given by Baños for the joint diffusive and propagating regime and concluded that within a certain range the asymptotic solutions were valid. Baños [1966] also gave in his Chapter 6, asymptotic expressions for the basic functions U and V , which are valid over an entire hemisphere and can be used to evaluate expressions for the intermediate and far field, which are proportional to $1/R^2$ and $1/R$, respectively. These basic functions U and V^1 are similar to the basic functions given in Eqs. (4.25a) and (4.25b). The important differences between the basic functions given by Baños [1966] and those given in this thesis are the different transformation parameters, the different definitions of the complex propagation constants and the different coordinate systems. The temporal transformation to the frequency domain used by Baños [1966] and used in this report (see Eq. (2.14)) were carried out with $\exp(-j\omega t)$ and $\exp(j\omega t)$, respectively². This results in the expressions being complex conjugates of each other in the space-frequency domain. Due to the different definitions of the complex propagation constants³, the basic function V given by Eq. (2.138) of Baños [1966] is similar to $-\hat{V}$ given in Eq. (4.25b). It can be proven that the far-field expressions of Baños are equal to the far-field expressions of Engheta et al. [1982], despite the fact that the propagation constants of Baños are valid for diffusion and the propagation constants of Engheta are valid for wave propagation in lossless media. This

¹Eqs. (2.137) and (2.138) [Baños, 1966].

²Engheta et al. [1982] used the same transformation parameters as used by Baños [1966].

³ γ_1^2 and γ_0^2 given in Eqs. (4.25b), are similar to $-k_1^2$ and $-k_2^2$ given in Eq. (2.138) of Baños [1966].

fact is also confirmed by the general correspondence principle for electromagnetic wave and diffusion fields, which is discussed by de Hoop [1996]. This indicates that the intermediate-field expressions given by Baños may be used for the lossless case.

Therefore, we will investigate the validity of the intermediate-field contributions given by Baños by comparing the asymptotic expressions with the exact numerical evaluation of the integral expressions in Section 4.6.

4.5 Numerical evaluation of the integral expressions

To check the validity of the asymptotic expressions, we have to transform Eqs. (4.4a) and (4.6a) into the space-frequency domain using Eq. (2.20). It is efficient to change to polar coordinates to reduce the number of integrals, as is done in Eqs. (2.28a). Next, selecting the horizontal source components and rewriting Eqs. (4.22a) and (4.22b) as

$$\begin{bmatrix} \hat{E}_1 \\ \hat{E}_2 \\ \hat{E}_3 \end{bmatrix}^{\{\uparrow, \downarrow\}} = \begin{bmatrix} \hat{G}_{11}^{\text{EJ}} & \hat{G}_{12}^{\text{EJ}} \\ \hat{G}_{21}^{\text{EJ}} & \hat{G}_{22}^{\text{EJ}} \\ \hat{G}_{31}^{\text{EJ}} & \hat{G}_{32}^{\text{EJ}} \end{bmatrix}^{\{\uparrow, \downarrow\}} \begin{bmatrix} \hat{J}_1 \\ \hat{J}_2 \end{bmatrix}, \quad (4.26)$$

only the integrals \hat{U} and \hat{V} and the partial derivatives which work on the Bessel functions within the integral, have to be evaluated. Writing the partial derivatives of the Bessel functions as

$$\partial_1 J_0(\kappa r) = -\frac{x_1}{r} \kappa J_1(\kappa r) = -\cos(\phi) \kappa J_1(\kappa r), \quad (4.27a)$$

$$\partial_2 J_0(\kappa r) = -\frac{x_2}{r} \kappa J_1(\kappa r) = -\sin(\phi) \kappa J_1(\kappa r), \quad (4.27b)$$

$$\partial_1 \partial_1 J_0(\kappa r) = -\frac{\kappa^2}{2} [J_0(\kappa r) - \cos(2\phi) J_2(\kappa r)], \quad (4.27c)$$

$$\partial_2 \partial_2 J_0(\kappa r) = -\frac{\kappa^2}{2} [J_0(\kappa r) + \cos(2\phi) J_2(\kappa r)], \quad (4.27d)$$

$$\partial_1 \partial_2 J_0(\kappa r) = \frac{\kappa^2}{2} \sin(2\phi) J_2(\kappa r), \quad (4.27e)$$

and

$$\hat{G}_{11}^{\text{EJ},\uparrow} = \frac{-\hat{\zeta}_0}{2\pi} \int_{\kappa=0}^{\infty} \left[\left(\tilde{U}^{\uparrow} + \frac{\kappa^2}{2} \tilde{V}^{\uparrow} \right) J_0(\kappa r) - \frac{\kappa^2}{2} \tilde{V}^{\uparrow} \cos(2\phi) J_2(\kappa r) \right] \kappa d\kappa, \quad (4.28a)$$

$$\hat{G}_{21}^{\text{EJ},\uparrow} = \frac{\hat{\zeta}_0}{2\pi} \int_{\kappa=0}^{\infty} \frac{\kappa^2}{2} \tilde{V}^{\uparrow} \sin(2\phi) J_2(\kappa r) \kappa d\kappa, \quad (4.28b)$$

$$\hat{G}_{31}^{\text{EJ},\uparrow} = \frac{-\hat{\zeta}_0}{2\pi} \int_{\kappa=0}^{\infty} \Gamma_1 \tilde{V}^{\uparrow} \cos(\phi) J_1(\kappa r) \kappa^2 d\kappa, \quad (4.28c)$$

$$\hat{G}_{12}^{\text{EJ},\uparrow} = \frac{\hat{\zeta}_0}{2\pi} \int_{\kappa=0}^{\infty} \frac{\kappa^2}{2} \tilde{V}^{\uparrow} \sin(2\phi) J_2(\kappa r) \kappa d\kappa, \quad (4.28d)$$

$$\hat{G}_{22}^{\text{EJ},\uparrow} = \frac{-\hat{\zeta}_0}{2\pi} \int_{\kappa=0}^{\infty} \left[\left(\tilde{U}^{\uparrow} + \frac{\kappa^2}{2} \tilde{V}^{\uparrow} \right) J_0(\kappa r) - \frac{\kappa^2}{2} \tilde{V}^{\uparrow} \cos(2\phi) J_2(\kappa r) \right] \kappa d\kappa, \quad (4.28e)$$

$$\hat{G}_{32}^{\text{EJ},\uparrow} = \frac{-\hat{\zeta}_0}{2\pi} \int_{\kappa=0}^{\infty} \Gamma_1 \tilde{V}^{\uparrow} \sin(\phi) J_1(\kappa r) \kappa^2 d\kappa, \quad (4.28f)$$

$$\hat{G}_{11}^{\text{EJ},\downarrow} = \frac{-\hat{\zeta}_0}{2\pi} \int_{\kappa=0}^{\infty} \left[\left(\tilde{U}^{\downarrow} + \frac{\kappa^2}{2} \tilde{V}^{\downarrow} \right) J_0(\kappa r) - \frac{\kappa^2}{2} \tilde{V}^{\downarrow} \cos(2\phi) J_2(\kappa r) \right] \kappa d\kappa, \quad (4.28g)$$

$$\hat{G}_{21}^{\text{EJ},\downarrow} = \frac{\hat{\zeta}_0}{2\pi} \int_{\kappa=0}^{\infty} \frac{\kappa^2}{2} \tilde{V}^{\downarrow} \sin(2\phi) J_2(\kappa r) \kappa d\kappa, \quad (4.28h)$$

$$\hat{G}_{31}^{\text{EJ},\downarrow} = \frac{\hat{\zeta}_0}{2\pi} \int_{\kappa=0}^{\infty} \Gamma_0 \tilde{V}^{\downarrow} \cos(\phi) J_1(\kappa r) \kappa^2 d\kappa, \quad (4.28i)$$

$$\hat{G}_{12}^{\text{EJ},\downarrow} = \frac{\hat{\zeta}_0}{2\pi} \int_{\kappa=0}^{\infty} \frac{\kappa^2}{2} \tilde{V}^{\downarrow} \sin(2\phi) J_2(\kappa r) \kappa d\kappa, \quad (4.28j)$$

$$\hat{G}_{22}^{\text{EJ},\downarrow} = \frac{-\hat{\zeta}_0}{2\pi} \int_{\kappa=0}^{\infty} \left[\left(\tilde{U}^{\downarrow} + \frac{\kappa^2}{2} \tilde{V}^{\downarrow} \right) J_0(\kappa r) - \frac{\kappa^2}{2} \tilde{V}^{\downarrow} \cos(2\phi) J_2(\kappa r) \right] \kappa d\kappa, \quad (4.28k)$$

$$\hat{G}_{32}^{\text{EJ},\downarrow} = \frac{\hat{\zeta}_0}{2\pi} \int_{\kappa=0}^{\infty} \Gamma_0 \tilde{V}^{\downarrow} \sin(\phi) J_1(\kappa r) \kappa^2 d\kappa. \quad (4.28l)$$

These integrals can in principle be evaluated numerically using standard integration routines. It is advantageous to use normalised quantities and we make the following substitution,

$$\kappa = \frac{\omega p}{c_0}. \quad (4.29)$$

An adaptive integration routine is used, which bisects each interval of integration until a certain desired accuracy is found. Eventually, a sufficient accuracy over the entire interval is obtained. In this way the algorithm automatically finds the difficult regions of integration related to branch points or strong oscillations. Analysing the expressions for the electric field, two branch points can be identified in the complex wavenumber domain. It is therefore convenient to introduce intermediate boundaries for the integration interval at $p = 1$, where a branch point is present on the real p -axis, corresponding to the branch point for the propagation constant $\gamma_0 = \sqrt{\hat{\eta}_0 \hat{\zeta}_0}$ in the upper medium. A similar intermediate boundary of the integration interval is introduced by

$$p = \operatorname{Re} \left\{ \sqrt{\varepsilon_r + \frac{\sigma}{j\omega\varepsilon_0}} \right\}, \quad (4.30)$$

which corresponds to the projection of the branch point due to the propagation constant $\gamma_1 = \sqrt{\hat{\eta}_1 \hat{\zeta}_0}$ in the lower medium.

4.6 Validation of the asymptotic expressions for the electric field

Eqs. (4.22b) and (4.22b) show that the electric field expressions depend on two basic functions, \hat{U} and \hat{V} , which can be determined in three different ways. In this section we will compare the two different asymptotic expressions for the electric field as described in Section 4.4 with the numerically evaluated integrals for the electric field as given in Section 4.5. The expressions for the far field, a combination of far- and intermediate-field and the total-field expressions are compared. Comparison will be carried out in two different ways. First, the real and imaginary part of the Cartesian components of the electric field are analysed at a fixed radius. Second, the amplitudes of the electric field of the spherical components of the electric field are plotted as a polar plot as in Figures 4.2-4.4. The configuration is given in Figure 4.1. The electric current source is positioned at the origin and is oriented in the x_1 -direction. The critical angle θ_c is given by $\theta_c = \sin^{-1}(1/\sqrt{\varepsilon_r})$ for a lossless medium. For different angles θ the different expressions for the electric field are compared. This will be carried out in two planes; the E -plane, and the H -plane. The E -plane is parallel to the direction of the current source dipole, while the H -plane is perpendicular to the direction of the current

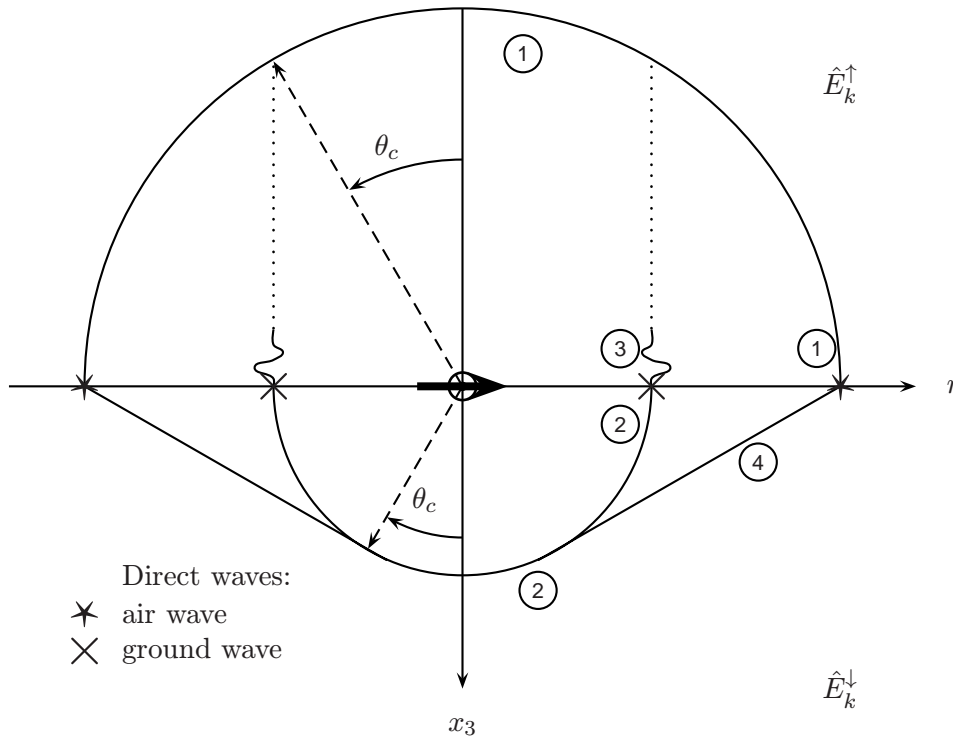


Figure 4.5: Wavefronts generated by a dipole source on the surface of a half-space earth with 1: Body wave in air, 2: Body wave in ground, 3: Inhomogeneous wave in air and 4: Head wave in ground.

source dipole. In the E -plane, the electric field is always parallel to the E -plane, so no E_2 -component will be present in the E -plane. In the H -plane, the magnetic field is always parallel to the H -plane. The electric field is perpendicular to the magnetic field, so in the H -plane only a E_1 -component will be present in the H -plane. Note that for $0 < \theta < \pi/2$ a dielectric medium is present, while for $\pi/2 < \theta < \pi$ air is present.

The different contributions to the total-field are shown in Figure 4.5. The far-field expressions only describe the body wave in air and ground and have a zero at the interface, whereas the combination of far- and intermediate-field expressions also describe the head wave in the ground and the inhomogeneous wave in air. The combination of intermediate- and far-field expressions do

not have a zero at the interface; they satisfy the boundary conditions on the interface.

In Fig. 4.6 the real and imaginary parts for the three Cartesian electric field components are evaluated using the far, far- and intermediate-field expressions and the total-field at a radius of 1 m $\approx 3.3\lambda$, $f = 500$ MHz and $\varepsilon_r = 4$. In Fig. 4.6(a) the real and imaginary parts of the three different results for the electric field in the H -plane, $E_1(0, x_2, x_3)$, are depicted. The far-field expressions do not resemble the total-field in the lower half-space. The far- and intermediate-field expressions do resemble the total-field expressions better, except for angles close to the critical angle. Near the critical angle the intermediate-field expressions are not stable. Similar results can be observed in Figures 4.6(b) and 4.6(c) for the real and imaginary parts for the electric field in the E -plane, $E_1(x_1, 0, x_3)$ and $E_3(x_1, 0, x_3)$, respectively. Near the interface the total-field is not equal to zero. The far-field expressions have a zero at the interface, whereas the combination of far- and intermediate-field expressions describe the amplitudes near the interface quite well. Note that also the boundary conditions, Eqs. (2.7a) and (2.7b) for the electric field components tangential and perpendicular to the interface are satisfied.

In Figure 4.7 the spherical electric component \hat{E}_ϕ in the H -plane and in Figures 4.8 and 4.8 the spherical electric field components \hat{E}_θ and \hat{E}_R , respectively, in the E -plane at a distance of 1 m are depicted. In the center of the figures a circle or arrow indicates the direction of the electric current source. The circle indicates that the direction of the electric field is perpendicular to the plane of reference and the arrow indicates that the electric field is parallel to the plane of reference. Note that the intermediate-field values are not bounded near the critical angle.

In Fig. 4.10 the real and imaginary part for the three Cartesian electric field components are evaluated using the far, far- and intermediate-field expressions and the total-field at a radius of 5 m $\approx 16.6\lambda$, $f = 500$ MHz and $\varepsilon_r = 4$. In Figure 4.11 the spherical electric component \hat{E}_ϕ in the H -plane and in Figures 4.12 and 4.8 the spherical electric field components \hat{E}_θ and \hat{E}_R , respectively, in the E -plane at a distance of 5 m are depicted. A comparison between the far-field expressions and the combination between far- and intermediate-field expressions with the total-field evaluation, show that interference of the body wave and head wave in the ground result in a lobed structure. For larger distances R , the travel time between body wave and head wave increases, which result in an increased number of lobes. The large contribution of the intermediate field near the critical angle causes the

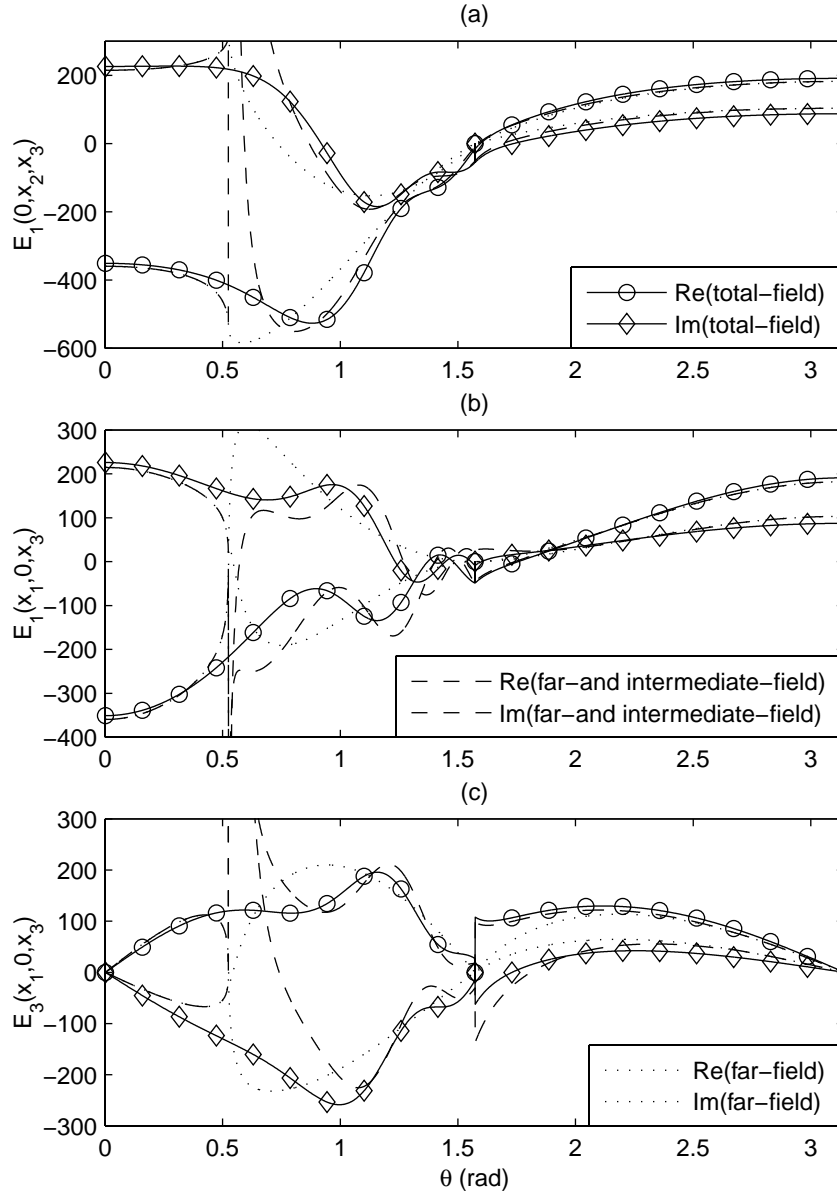


Figure 4.6: Real and imaginary part of the total-field, far-field and far- and intermediate-field amplitudes for (a) \hat{E}_1 in the H-plane, (b) \hat{E}_1 and (c) \hat{E}_3 in the E-plane for $R = 1 \text{ m} \approx 3.3\lambda$, $f = 500 \text{ MHz}$, $\sigma = 0 \text{ S/m}$ and $\epsilon_r = 4$.

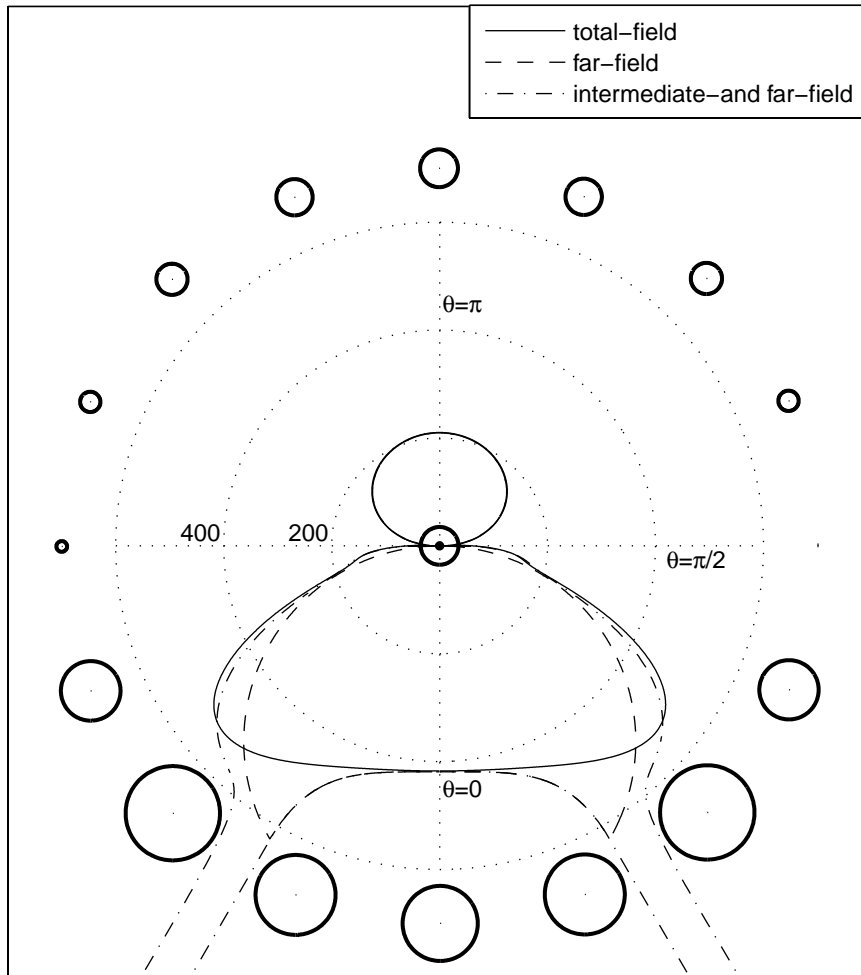


Figure 4.7: Comparison between the total-field, far-field and far- and intermediate-field amplitudes of the spherical electric field component \hat{E}_ϕ in the H-plane for $R = 1 \text{ m} \approx 3.3\lambda$, $f = 500 \text{ MHz}$, $\sigma = 0 \text{ S/m}$ and $\epsilon_r = 4$.

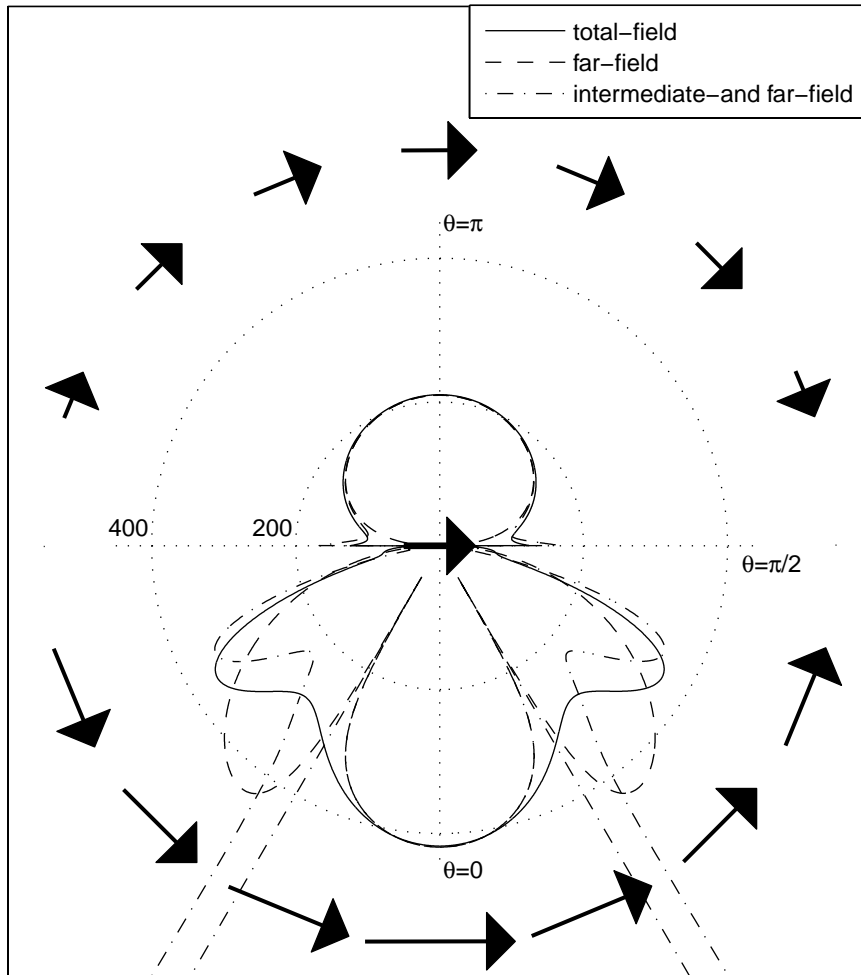


Figure 4.8: Comparison between the total-field, far-field and far- and intermediate-field amplitudes of the spherical electric field component \hat{E}_θ in the E-plane for $R = 1 \text{ m} \approx 3.3\lambda$, $f = 500 \text{ MHz}$, $\sigma = 0 \text{ S/m}$ and $\epsilon_r = 4$.

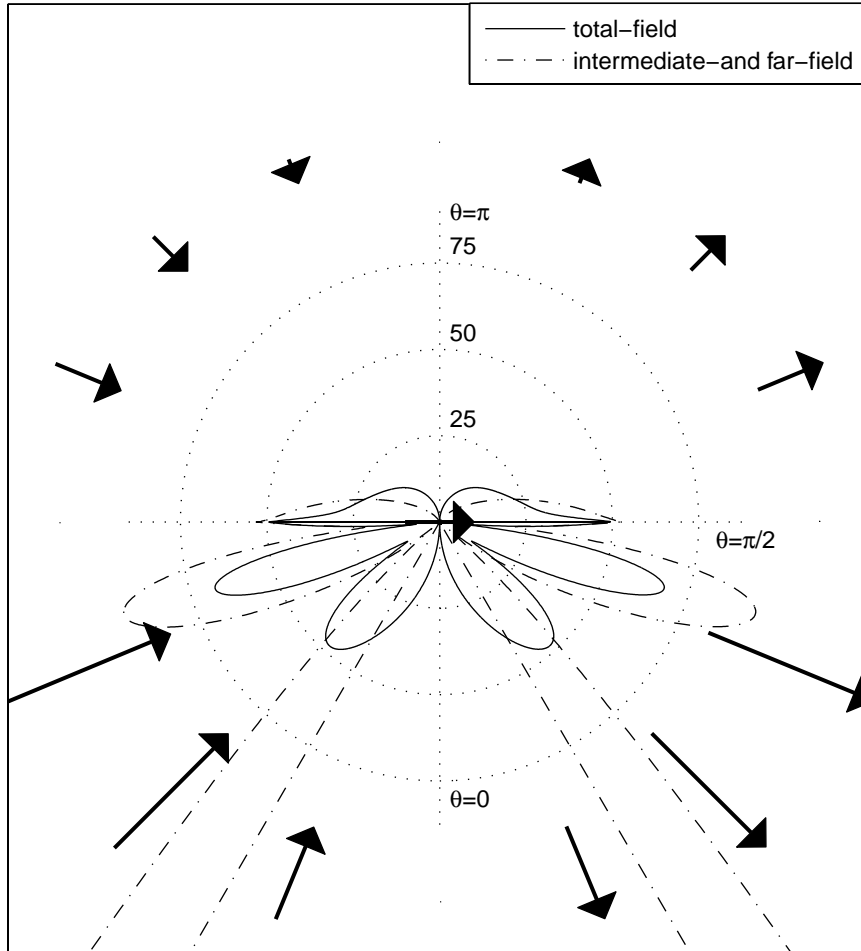


Figure 4.9: Comparison between the total-field, far-field and far- and intermediate-field amplitudes of the spherical electric field component \hat{E}_R in the E-plane for $R = 1 \text{ m} \approx 3.3\lambda$, $f = 500 \text{ MHz}$, $\sigma = 0 \text{ S/m}$ and $\epsilon_r = 4$.

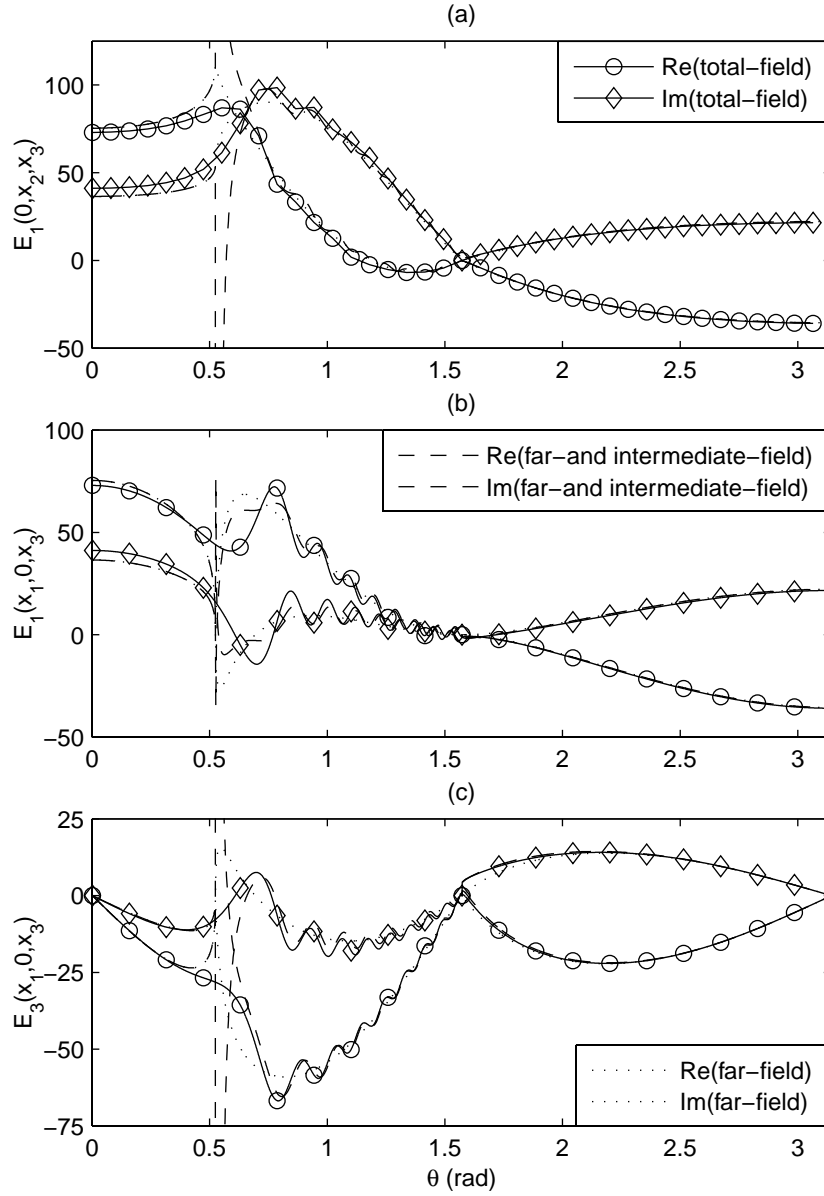


Figure 4.10: Real and imaginary part of the total-field, far-field and far- and intermediate-field amplitudes for (a) \hat{E}_1 in the H-plane, (b) \hat{E}_1 and (c) \hat{E}_3 in the E-plane for $R = 5 \text{ m} \approx 16.6\lambda$, $f = 500 \text{ MHz}$, $\sigma = 0 \text{ S/m}$ and $\epsilon_r = 4$.

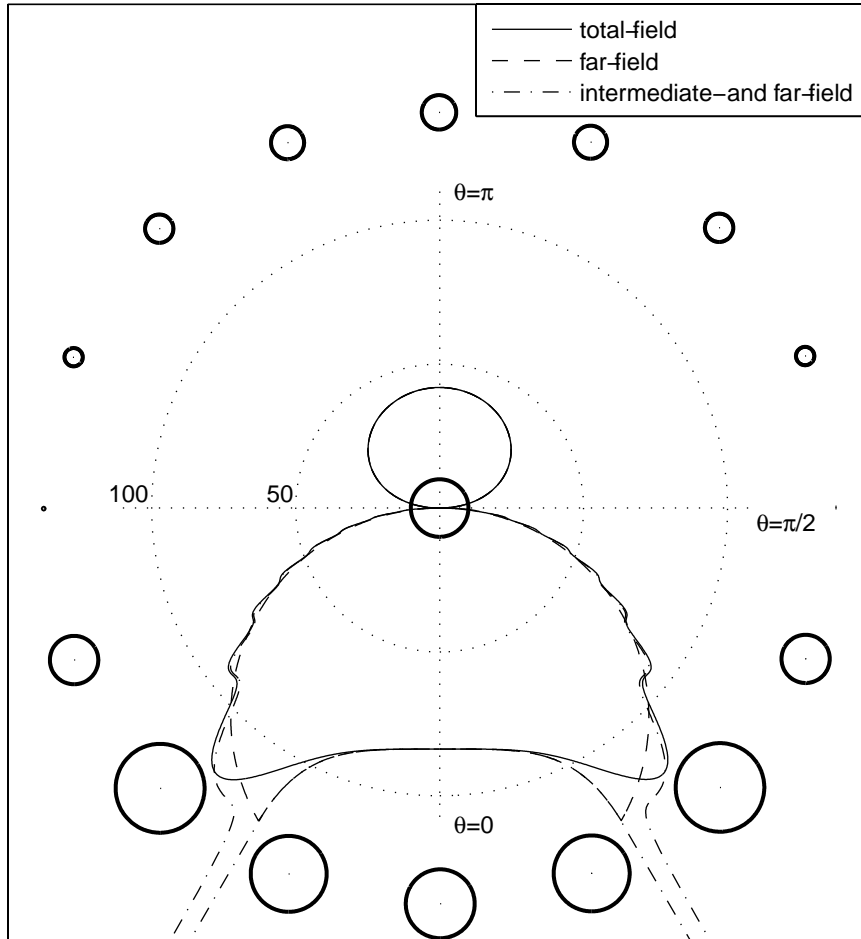


Figure 4.11: Comparison between the total-field, far-field and far- and intermediate-field amplitudes of the spherical electric field component \hat{E}_ϕ in the H-plane and for $R = 5 \text{ m} \approx 16.6\lambda$, $f = 500 \text{ MHz}$, $\sigma = 0 \text{ S/m}$ and $\epsilon_r = 4$.

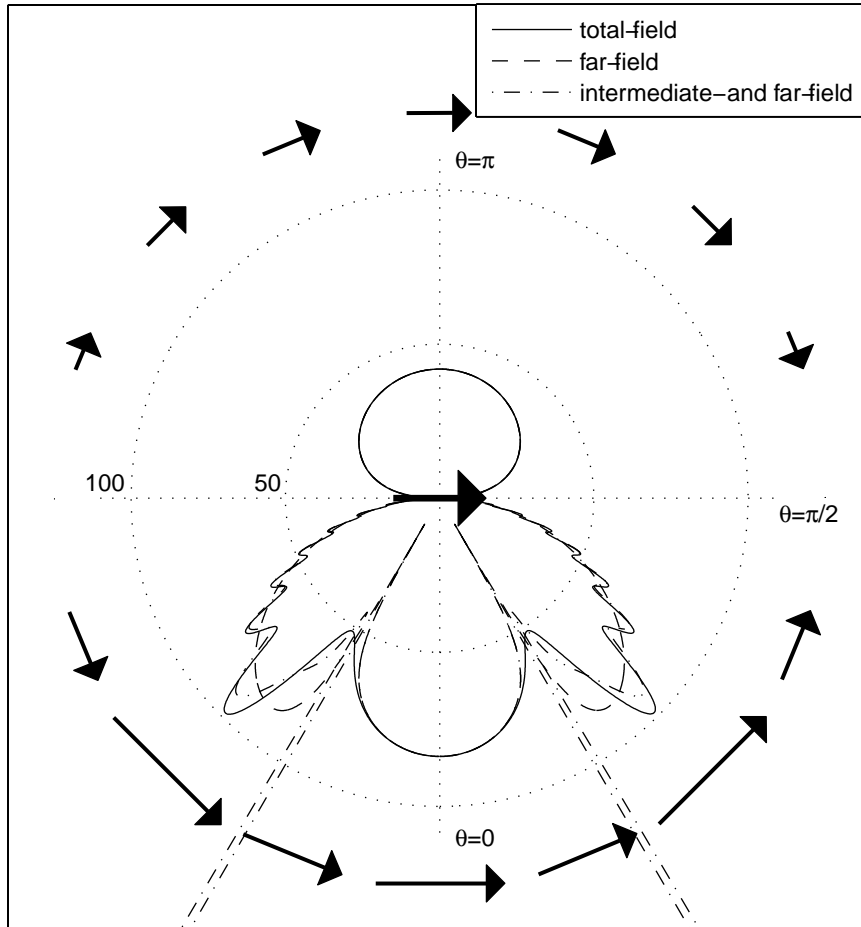


Figure 4.12: Comparison between the total-field, far-field and far- and intermediate-field amplitudes of the spherical electric field component \hat{E}_θ in the E-plane for $R = 5 \text{ m} \approx 16.6\lambda$, $f = 500 \text{ MHz}$, $\sigma = 0 \text{ S/m}$ and $\epsilon_r = 4$.

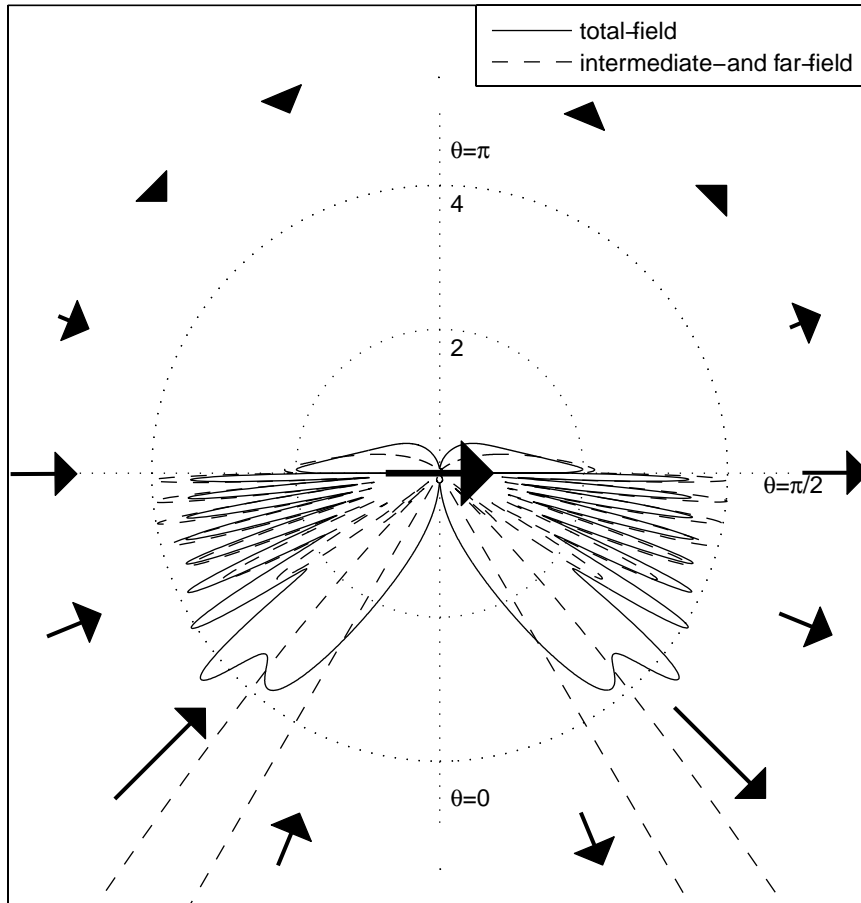


Figure 4.13: Comparison between the total-field, far-field and far- and intermediate-field amplitudes of the radial electric field components \hat{E}_R in the E -plane for $R = 5$ m $\approx 16.6\lambda$, $f = 500$ MHz, $\sigma = 0$ S/m and $\epsilon_r = 4$.

maximum of the radiation pattern not to be present at the critical angle, but at an angle larger than the critical angle. Radzevicius and Daniels [2000a] and Holliger and Bergmann [1998] compared the far-field expressions with FDTD modelling and observed a similar phenomenon.

■

In this chapter the electric field radiated by a horizontal dipole present on a dielectric medium, and the different wave phenomena which occur, are discussed. A comparison between the far-field expressions and the combination of far- and intermediate-field expressions with the total-field evaluation, show that interference of the body wave and head wave in the ground result in a lobed structure. For larger distances R , the travel time difference between body wave and head wave increases, which result in an increased number of lobes. It has been observed that the intermediate field has a significant contribution, especially near the critical angle at a few wavelengths away from the source. Also at a distance of more than 10 wavelengths away, the relative amplitude of the intermediate field can be still significant.

Comparison of the results indicate that a combination of the far- and intermediate-field expressions describes the electric field quite well. However, the intermediate-field expressions are not bounded at the critical angle. For increasing distance, a decreasing region of angles is observed where the intermediate-field expressions are not bounded and the error between the total-field and the combination of the far- and intermediate field results decreases.

Because the obtained expressions for the intermediate-field expressions are not bounded, they cannot be used for our imaging scheme. Further research is needed to obtain bounded expressions for the intermediate field. The far-field expressions discussed in this chapter form the basis for the scattering formalism discussed in Chapter 5. This scattering formalism will form the basis for the imaging algorithms derived in Chapter 6.

Theory of a ground penetrating radar survey

In this chapter the theory of a ground penetrating radar survey is discussed. First, the forward (or direct) source problem is dealt with, which shows that the emitted electromagnetic field from known sources in a known medium can be calculated once the fields radiated by appropriate point sources have been calculated (see Chapter 4). Next, the forward (or direct) scattering problem is formulated. Basic integral equations are derived for the scattering of the electromagnetic field by a contrasting domain of bounded extent in a known background medium as a function of contrast source densities. For a spherical diffractor explicit expressions for the contrast source densities can be derived when the radius of this spherical scatterer goes to zero. For a small contrast, these expressions reduce to the well-known Born approximation. This linearised scattering formalism constitutes the basis for the multi-component algorithm, which is derived in Chapter 6 for lossless media. In principal, the influence of the losses (σ) on the frequency-dependent propagation coefficient has to be taken into account. Frequency-dependent medium properties can be obtained from a CMP measurement as is done by van der Kruk and Slob [1998]. Turner [1994], Turner and Siggins [1994] and Irving and Knight [2000] also corrected for the wavelet dispersion in GPR

data. For the imaging in a lossy medium, where a strong frequency dependent propagation coefficient is present, it is a requirement that this frequency dependent propagation coefficient is known. However, our imaging algorithm is limited to the lossless case, but can be easily extended for the lossy case when the frequency dependent medium properties are known. Next, the acquisition set-up is discussed. Due to the finite length of the antennas, only horizontal directions are possible for the source and receiver antennas for a sufficient coupling of the energy into the subsurface. The common-offset and the common-midpoint set-up are discussed. For a zero-offset measurement, four antenna combinations are possible. The offset between the source and receiver is also a parameter.

Because the imaging algorithm will be carried out in the spatial Fourier domain, it is investigated what region of support can be used by the imaging algorithm. Different factors, like the spatial and temporal bandwidth, influence this region of support.

Together with the orientation of a scatterer, a qualitative indication of the sensitivity for reflections is obtained by analysing the radiation characteristics and the vectorial scattering formalism. These results show how to increase the sensitivity of subsurface reflections. On the other hand, these results also show how to reduce the measurement of unwanted reflections from objects on or above the soil. Synthetic data are presented which indicate that for appropriate 3D imaging of the subsurface the vectorial character of the electromagnetic field must be taken into account.

5.1 Forward source problem

The configuration for the forward source problem consists of an unbounded inhomogeneous medium with known electromagnetic properties. In this medium sources are present that occupy the bounded domain \mathbb{D}^e , being a subdomain of \mathbb{D} . To arrive at representations that express the electromagnetic field in all space in terms of the source distributions, we apply the reciprocity theorem and extend the validity of the reciprocity relation to \mathbb{D} , as is done in Section 2.7.2. Then the reciprocity relation in Eq. (2.33) reduces to,

$$\int_{\mathbf{x} \in \mathbb{D}} [(\hat{\zeta}^B - \hat{\zeta}^A) \hat{H}_j^A \hat{H}_j^B - (\hat{\eta}^B - \hat{\eta}^A) \hat{E}_k^A \hat{E}_k^B] dV + \int_{\mathbf{x} \in \mathbb{D}} (\hat{J}_r^{e;A} \hat{E}_r^B - \hat{J}_k^{e;B} \hat{E}_k^A + \hat{K}_j^{e;B} \hat{H}_j^A - \hat{K}_p^{e;A} \hat{H}_p^B) dV = 0. \quad (5.1)$$

State A is identified with the actual field that is generated by the sources. It is represented by

$$\begin{aligned} \{\hat{E}_k^A, \hat{H}_j^A\} &= \{\hat{E}_k, \hat{H}_j\}(\mathbf{x}, \omega), \\ \{\hat{J}_r^{e;A}, \hat{K}_p^{e;A}\} &= \{\hat{J}_r^e, \hat{K}_p^e\}(\mathbf{x}, \omega), \\ \{\hat{\eta}^A, \hat{\zeta}^A\} &= \{\hat{\eta}, \hat{\zeta}\}(\mathbf{x}, \omega), \end{aligned} \quad (5.2)$$

where we have taken $s \rightarrow j\omega$ and $\hat{\eta}$ and $\hat{\zeta}$ are given by Eqs. (2.17a) and (2.17b). In State A the constitutive parameters and the external sources are known; the field strengths are unknown. State B is chosen such that the application of Eq. (5.1) leads to the values of the actual electric and magnetic field strengths at any point in space. Inspection of Eq. (5.1) reveals that this is accomplished when the media in the two states are each others' adjoint: in State B , we first take a point source of the electric-current type while the source of the magnetic-current type is zero, and then take a point source of the magnetic-current type while the source of the electric-current type is zero. This yields the desired representations for the electric and magnetic field strengths, respectively. State B is represented by

$$\begin{aligned} \{\hat{E}_r^B, \hat{H}_p^B\} &= \{\hat{E}_r^{GJ}, \hat{H}_p^{GJ}\}(\mathbf{x}|\mathbf{x}^R, \omega), \\ \{\hat{J}_k^{e;B}, \hat{K}_j^{e;B}\} &= \{\hat{S}^J(\omega)\delta(\mathbf{x} - \mathbf{x}^R)b_k^J, 0\}, \\ \{\hat{\eta}^B, \hat{\zeta}^B\} &= \{\hat{\eta}, \hat{\zeta}\}(\mathbf{x}, \omega), \end{aligned} \quad (5.3)$$

and

$$\begin{aligned} \{\hat{E}_r^B, \hat{H}_p^B\} &= \{\hat{E}_r^{GK}, \hat{H}_p^{GK}\}(\mathbf{x}|\mathbf{x}^R, \omega), \\ \{\hat{J}_k^{e;B}, \hat{K}_j^{e;B}\} &= \{0, \hat{S}^K(\omega)\delta(\mathbf{x} - \mathbf{x}^R)b_j^K\}, \\ \{\hat{\eta}^B, \hat{\zeta}^B\} &= \{\hat{\eta}, \hat{\zeta}\}(\mathbf{x}, \omega), \end{aligned} \quad (5.4)$$

respectively. The superscripts $\{GJ, GK\}$ refer to the fact that the relevant field quantities are associated with either a source of the electric-current type or a source of the magnetic-current type. These field quantities are also denoted as the Green's states. The three-dimensional unit impulse (Dirac distribution) operative at the point $\mathbf{x} = \mathbf{x}^R$ is represented by $\delta(\mathbf{x} - \mathbf{x}^R)$, $\hat{S}^J(\omega)$ and $\hat{S}^K(\omega)$ contain the source wavelet and depend on ω , while b_k^J and b_j^K are arbitrary vector functions indicating the orientation for the electric- and magnetic-current density, respectively. In view of the configuration and

the choices for the States A and B we can use the reciprocity relation of Eq. (5.1) to determine the two situations discussed above

$$\int_{\mathbf{x} \in \mathbf{D}} [\hat{J}_r^e \hat{E}_r^{GJ} - \hat{S}^J(\omega) \delta(\mathbf{x} - \mathbf{x}^R) b_k^J \hat{E}_k - \hat{K}_p^e \hat{H}_p^{GJ}] dV = 0, \quad (5.5a)$$

$$\int_{\mathbf{x} \in \mathbf{D}} [\hat{J}_r^e \hat{E}_r^{GK} + \hat{S}^K(\omega) \delta(\mathbf{x} - \mathbf{x}^R) b_j^K \hat{H}_j - \hat{K}_p^e \hat{H}_p^{GK}] dV = 0. \quad (5.5b)$$

The representations for the electromagnetic field are arrived at by taking into account the fact that the fields are linearly related to the sources, expressed as

$$\{\hat{E}_r^{GJ}, \hat{H}_p^{GJ}\}(\mathbf{x}|\mathbf{x}^R, \omega) = \hat{S}^J(\omega) \{\hat{G}_{rk}^{EJ}, \hat{G}_{pk}^{HJ}\}(\mathbf{x}|\mathbf{x}^R, \omega) b_k^J, \quad (5.6a)$$

$$\{\hat{E}_r^{GK}, \hat{H}_p^{GK}\}(\mathbf{x}|\mathbf{x}^R, \omega) = \hat{S}^K(\omega) \{\hat{G}_{rj}^{EK}, \hat{G}_{pj}^{HK}\}(\mathbf{x}|\mathbf{x}^R, \omega) b_j^K. \quad (5.6b)$$

The Green's tensor functions for a homogeneous space are given in Section 4.3.1. Using reciprocity for the Green's tensor functions on the right-hand side of Eqs. (5.6a)-(5.6b), we find

$$\hat{G}_{rk}^{EJ}(\mathbf{x}|\mathbf{x}^R, \omega) = \hat{G}_{kr}^{EJ}(\mathbf{x}^R|\mathbf{x}, \omega), \quad (5.7a)$$

$$\hat{G}_{pk}^{HJ}(\mathbf{x}|\mathbf{x}^R, \omega) = -\hat{G}_{kp}^{EK}(\mathbf{x}^R|\mathbf{x}, \omega), \quad (5.7b)$$

$$\hat{G}_{pj}^{HK}(\mathbf{x}|\mathbf{x}^R, \omega) = \hat{G}_{jp}^{HK}(\mathbf{x}^R|\mathbf{x}, \omega). \quad (5.7c)$$

Further, using the fact that $\{\hat{S}^J(\omega) b_k^J, \hat{S}^K(\omega) b_j^K\}$ are arbitrary, we arrive at

$$\hat{E}_k(\mathbf{x}^R, \omega) = \int_{\mathbf{x} \in \mathbf{D}^e} [\hat{G}_{kr}^{EJ}(\mathbf{x}^R|\mathbf{x}, \omega) \hat{J}_r^e(\mathbf{x}, \omega) + \hat{G}_{kp}^{EK}(\mathbf{x}^R|\mathbf{x}, \omega) \hat{K}_p^e(\mathbf{x}, \omega)] dV, \quad (5.8a)$$

$$\hat{H}_j(\mathbf{x}^R, \omega) = \int_{\mathbf{x} \in \mathbf{D}^e} [\hat{G}_{jr}^{HJ}(\mathbf{x}^R|\mathbf{x}, \omega) \hat{J}_r^e(\mathbf{x}, \omega) + \hat{G}_{jp}^{HK}(\mathbf{x}^R|\mathbf{x}, \omega) \hat{K}_p^e(\mathbf{x}, \omega)] dV, \quad (5.8b)$$

where $\mathbf{x}^R \in \mathbf{D}$. In case $\mathbf{x}^R \in \mathbf{D}^e$ the integrals are to be interpreted as their Cauchy principal values. Eqs. (5.8a) and (5.8b) show that the electromagnetic field from known sources in a known medium can be calculated in all space once the fields radiated by appropriate point sources (the Green's tensor functions) have been calculated. The right-hand sides of the representations express the field values as a superposition of the fields radiated by elementary volume sources, from which the distributed sources can be constructed.

5.2 Forward scattering problem

We investigate the scattering of electromagnetic fields by a contrasting domain of bounded extent present in an unbounded medium. Let \mathbf{D}^s be the bounded domain occupied by the scatterer and let $\sigma^s(\mathbf{x})$ be its conductivity, $\varepsilon^s(\mathbf{x})$ its permittivity and $\mu^s(\mathbf{x})$ its permeability. The embedding medium occupies the domain $\bar{\mathbf{D}}^s$ and has a conductivity $\sigma(\mathbf{x})$, permittivity $\varepsilon(\mathbf{x})$ and permeability $\mu(\mathbf{x})$. We decompose the total electromagnetic field $\{\hat{E}_k, \hat{H}_j\}$ into the incident field $\{\hat{E}_k^i, \hat{H}_j^i\}$ and the scattered field $\{\hat{E}_k^s, \hat{H}_j^s\}$. The incident field is taken as the field that would be present if the scattering domain \mathbf{D}^s would show no contrast with its embedding medium. The scattered field is the difference between the total field and the incident field. To arrive at the electromagnetic field equations satisfied by the scattered field we substitute

$$\hat{E}_k = \hat{E}_k^i + \hat{E}_k^s, \quad (5.9a)$$

$$\hat{H}_j = \hat{H}_j^i + \hat{H}_j^s, \quad (5.9b)$$

into Eqs. (2.16a) and (2.16b). Taking into account that the incident field satisfies Maxwell's equations we obtain for the scattered field

$$-\epsilon_{kmp}\partial_m\hat{H}_p^s + \hat{\eta}\hat{E}_k^s = \{-\hat{J}_k^s, 0\} \quad \text{for } \mathbf{x} \in \{\mathbf{D}^s, \bar{\mathbf{D}}^s\}, \quad (5.10a)$$

$$\epsilon_{jmr}\partial_m\hat{E}_r^s + \hat{\zeta}\hat{H}_j^s = \{-\hat{K}_j^s, 0\} \quad \text{for } \mathbf{x} \in \{\mathbf{D}^s, \bar{\mathbf{D}}^s\}, \quad (5.10b)$$

where $\bar{\mathbf{D}}^s$ is the complement of \mathbf{D}^s in \mathbb{R} . The contrast source volume densities $\{\hat{J}_k^s, \hat{K}_j^s\}$ of electric and magnetic current, also denoted as scatter sources, are given by

$$\hat{J}_k^s = \chi^{\hat{\eta}}(\hat{E}_k^i + \hat{E}_k^s), \quad (5.11a)$$

$$\hat{K}_j^s = \chi^{\hat{\zeta}}(\hat{H}_j^i + \hat{H}_j^s), \quad (5.11b)$$

in which the medium contrast functions are found as

$$\chi^{\hat{\eta}} = \hat{\eta}^s - \hat{\eta} = (\sigma^s - \sigma) + j\omega(\varepsilon^s - \varepsilon), \quad (5.12a)$$

$$\chi^{\hat{\zeta}} = \hat{\zeta}^s - \hat{\zeta} = j\omega(\mu^s - \mu). \quad (5.12b)$$

Note that the total field strengths inside the scatterer must be determined before the values of the scattered fields can be calculated. Once the total field strengths are known, Eqs. (5.10a) and (5.10b) constitute an electromagnetic radiation problem as discussed in the forward source problem. The scattered

field values in all space can then be obtained upon substituting the relevant quantities into Eqs. (5.8a) and (5.8b), hence we may write

$$\hat{E}_k^s(\mathbf{x}^R, \omega) = \int_{\mathbf{x} \in \mathbf{D}^s} [\hat{G}_{kr}^{EJ}(\mathbf{x}^R | \mathbf{x}, \omega) \hat{J}_r^s(\mathbf{x}, \omega) + \hat{G}_{kp}^{EK}(\mathbf{x}^R | \mathbf{x}, \omega) \hat{K}_p^s(\mathbf{x}, \omega)] dV, \quad (5.13a)$$

$$\hat{H}_j^s(\mathbf{x}^R, \omega) = \int_{\mathbf{x} \in \mathbf{D}^s} [\hat{G}_{jr}^{HJ}(\mathbf{x}^R | \mathbf{x}, \omega) \hat{J}_r^s(\mathbf{x}, \omega) + \hat{G}_{jp}^{HK}(\mathbf{x}^R | \mathbf{x}, \omega) \hat{K}_p^s(\mathbf{x}, \omega)] dV. \quad (5.13b)$$

In case $\mathbf{x}^R \in \mathbf{D}^s$ the integrals are to be interpreted as their Cauchy principal values. To arrive at the integral equations for the unknown total field strengths, we employ Eqs. (5.9a)-(5.9b), (5.11a)-(5.11b) and substitute the results into Eqs. (5.13a)-(5.13b). We obtain

$$\begin{aligned} \hat{E}_k^i(\mathbf{x}, \omega) &= \hat{E}_k(\mathbf{x}, \omega) \\ &- \int_{\mathbf{x}' \in \mathbf{D}^s} [\hat{G}_{kl}^{EJ}(\mathbf{x} | \mathbf{x}', \omega) \chi^{\hat{\eta}}(\mathbf{x}') \hat{E}_l(\mathbf{x}', \omega) + \hat{G}_{kq}^{EK}(\mathbf{x} | \mathbf{x}', \omega) \chi^{\hat{\zeta}}(\mathbf{x}') \hat{H}_q(\mathbf{x}', \omega)] dV, \end{aligned} \quad (5.14a)$$

$$\begin{aligned} \hat{H}_j^i(\mathbf{x}, \omega) &= \hat{H}_j(\mathbf{x}, \omega) \\ &- \int_{\mathbf{x}' \in \mathbf{D}^s} [\hat{G}_{jl}^{HJ}(\mathbf{x} | \mathbf{x}', \omega) \chi^{\hat{\eta}}(\mathbf{x}') \hat{E}_l(\mathbf{x}', \omega) + \hat{G}_{jq}^{HK}(\mathbf{x} | \mathbf{x}', \omega) \chi^{\hat{\zeta}}(\mathbf{x}') \hat{H}_q(\mathbf{x}', \omega)] dV, \end{aligned} \quad (5.14b)$$

$$\text{for } \mathbf{x} \in \mathbf{R}^3.$$

To solve this system of integral equations, first \hat{E}_k and \hat{H}_j can, in principle, be determined by taking $\mathbf{x} \in \mathbf{D}^s$ in Eqs. (5.14a) and (5.14b), where the integrals are to be interpreted as their Cauchy principal values, i.e., the integrals are, when necessary, calculated by a limiting procedure that excludes a singularity in the integrand by a ball with radius $\delta > 0$, and $|\mathbf{x}' - \mathbf{x}| < \delta$, around the singular point \mathbf{x}' , after which the limit $\delta \downarrow 0$ is taken. This procedure will be carried out in Section 5.3 to obtain exact expressions for an effective point scatterer. Once these quantities have been determined, the total wave field can be calculated in the entire configuration by reusing Eqs. (5.14a) and (5.14b) for all $\mathbf{x} \in \mathbf{R}^3$.

An efficient 3D implementation has been given by Zwamborn and van den Berg [1992]. However, for real-time imaging, such an approach is not feasible. For a point scatterer, however, the two integral equations can be solved. This will be discussed in the next section.

5.3 Scattering by a point scatterer

When $\mathbf{x} \in \mathbb{D}^s$, the evaluation of the domain integrals of Eqs. (5.14a) and (5.14b) have to be interpreted as their Cauchy principal value, where the contribution around the singular point $\mathbf{x} = \mathbf{x}'$, is excluded and calculated analytically [Lee et al., 1980]. To this end, we consider a point diffractor which is defined as a small spherical scatterer occupying the domain \mathbb{D}^δ with radius δ and origin $\mathbf{x}^{psc} = \mathbf{x}'$ in the limit of $\delta \downarrow 0$. The embedding medium is homogeneous and isotropic with constitutive parameters ε , σ and μ . The field incident on the point diffractor is generated by an electric dipole or magnetic dipole located at the origin \mathcal{O} . Inside \mathbb{D}^δ , the quantities $\hat{\eta}^s$ and $\hat{\zeta}^s$ consist of the homogeneous isotropic material parameters $\varepsilon^s, \sigma^s, \mu^s$. Using these definitions, the total electric and magnetic field at the location of the point diffractor $\mathbf{x} = \mathbf{x}^{psc}$ are calculated by applying Eqs. (5.14a)-(5.14b). When we carry out the limiting procedure for the contrast source densities this results in

$$\begin{aligned} \hat{E}_k^i(\mathbf{x}^{psc}, \omega) &= \hat{E}_k(\mathbf{x}^{psc}, \omega) \\ &- \chi^{\hat{\eta}} \hat{E}_r(\mathbf{x}^{psc}, \omega) \lim_{\delta \downarrow 0} \lim_{|\mathbf{x} - \mathbf{x}^{psc}| \downarrow 0} \int_{\mathbf{x}' \in \mathbb{D}^\delta} \hat{G}_{kr}^{EJ}(\mathbf{x}|\mathbf{x}', \omega) dV \\ &- \chi^{\hat{\zeta}} \hat{H}_r(\mathbf{x}^{psc}, \omega) \lim_{\delta \downarrow 0} \lim_{|\mathbf{x} - \mathbf{x}^{psc}| \downarrow 0} \int_{\mathbf{x}' \in \mathbb{D}^\delta} \hat{G}_{kr}^{EK}(\mathbf{x}|\mathbf{x}', \omega) dV \end{aligned} \quad (5.15a)$$

$$\begin{aligned} \hat{H}_j^i(\mathbf{x}^{psc}, \omega) &= \hat{H}_j(\mathbf{x}^{psc}, \omega) \\ &- \chi^{\hat{\zeta}} \hat{H}_p(\mathbf{x}^{psc}, \omega) \lim_{\delta \downarrow 0} \lim_{|\mathbf{x} - \mathbf{x}^{psc}| \downarrow 0} \int_{\mathbf{x}' \in \mathbb{D}^\delta} \hat{G}_{jp}^{HK}(\mathbf{x}|\mathbf{x}', \omega) dV \\ &- \chi^{\hat{\eta}} \hat{E}_r(\mathbf{x}^{psc}, \omega) \lim_{\delta \downarrow 0} \lim_{|\mathbf{x} - \mathbf{x}^{psc}| \downarrow 0} \int_{\mathbf{x}' \in \mathbb{D}^\delta} \hat{G}_{jr}^{HJ}(\mathbf{x}|\mathbf{x}', \omega) dV, \end{aligned} \quad (5.15b)$$

The Green's states occurring in Eqs. (5.15a)-(5.15b) are given in Section 4.3.1. The exact solution is now obtained by evaluating the integrals by first letting $|\mathbf{x} - \mathbf{x}^{psc}| \downarrow 0$ and then taking the limit of $\delta \downarrow 0$. The differentiations occurring in the Green's states act on \mathbf{x} and the integrals are to be interpreted with the differentiations taken in front of the integrals. There is essentially one integral left, viz.,

$$\hat{\Gamma}^\delta(\mathbf{x}|\mathbf{x}', \omega) = \int_{\mathbf{x}' \in \mathbb{D}^\delta} \frac{1}{4\pi|\mathbf{x} - \mathbf{x}'|} dV, \quad (5.16)$$

where the exponential factor occurring in the Green's function is replaced by unity. The simplest way to evaluate this integral is to introduce spherical coordinates with center \mathbf{x}^{psc} and the direction $\mathbf{x} - \mathbf{x}^{psc}$ as the polar axis. Let $R = |\mathbf{x}^{psc} - \mathbf{x}'|$ and θ be the polar angle between $\mathbf{x} - \mathbf{x}^{psc}$ and $\mathbf{x}' - \mathbf{x}^{psc}$, then the range of integration is $0 \leq R \leq \delta, 0 \leq \theta \leq \pi$ and $0 \leq \phi \leq 2\pi$, where ϕ is the azimuth angle in the plane perpendicular to $\mathbf{x} - \mathbf{x}^{psc}$. Let further $\mathbf{y} = \mathbf{x} - \mathbf{x}^{psc}$. Then in the integral we have

$$|\mathbf{x} - \mathbf{x}'| = \sqrt{|\mathbf{y}|^2 + R^2 - 2R|\mathbf{y}| \cos(\theta)} \quad (5.17)$$

and $dV = R^2 \sin(\theta) dR d\theta d\phi$. In the resulting integral we first carry out the integration with respect to ϕ which merely amounts to a multiplication by a factor of 2π . Next we carry out the integration with respect to θ which is elementary. After this we have

$$\begin{aligned} \hat{\Gamma}^\delta(\mathbf{x}^{psc} + \mathbf{y}, \omega) &= \frac{1}{2|\mathbf{y}|} \int_{R=0}^{\delta} [(|\mathbf{y}| + R) - (|\mathbf{y}| - R)] R dR, \\ &= \frac{1}{2}\delta^2 - \frac{1}{6}|\mathbf{y}|^2. \end{aligned} \quad (5.18)$$

Letting $|\mathbf{y}| \downarrow 0$ and then taking the limit $\delta \downarrow 0$ we arrive at

$$\hat{\Gamma}^\delta(\mathbf{x}^{psc}, \omega) = 0 \quad \text{as } \delta \downarrow 0. \quad (5.19)$$

The other terms occurring in the Green's states integrated over \mathbf{D}^δ are evaluated by taking, respectively, one and two spatial derivatives of Eq. (5.18) with respect to \mathbf{x} , viz.

$$\partial_m \hat{\Gamma}^\delta(\mathbf{x}^{psc} + \mathbf{y}, \omega) = -\frac{1}{3}y_m, \quad (5.20a)$$

$$\partial_k \partial_r \hat{\Gamma}^\delta(\mathbf{x}^{psc} + \mathbf{y}, \omega) = -\frac{1}{3}\delta_{kr}. \quad (5.20b)$$

Letting $|\mathbf{y}| \downarrow 0$ and then taking the limit $\delta \downarrow 0$ in Eqs. (5.20a)-(5.20b) yield

$$\partial_m \hat{G}^\delta(\mathbf{y}, \omega)|_{|\mathbf{y}| \downarrow 0} = 0, \quad (5.21a)$$

$$\partial_k \partial_r \hat{G}^\delta(\mathbf{y}, \omega)|_{|\mathbf{y}| \downarrow 0} = -\frac{1}{3}\delta_{kr}. \quad (5.21b)$$

The results of Eqs. (5.19), (5.21a) and (5.21b) are also found in Fokkema and van den Berg [1993]; Slob [1994]. Using these results in the Green's states

integrated over \mathbb{D}^δ in Eqs. (5.15a) and (5.15b), we arrive at the solution of the scattering problem for the point diffractor, viz.,

$$\hat{E}_k^i(\mathbf{x}^{psc}, \omega) = \hat{E}_k(\mathbf{x}^{psc}, \omega) + \chi^{\hat{\eta}}/(3\hat{\eta})\hat{E}_k(\mathbf{x}^{psc}, \omega), \quad (5.22a)$$

$$\hat{H}_j^i(\mathbf{x}^{psc}, \omega) = \hat{H}_j(\mathbf{x}^{psc}, \omega) + \chi^{\hat{\zeta}}/(3\hat{\zeta})\hat{H}_j(\mathbf{x}^{psc}, \omega). \quad (5.22b)$$

The expressions for the contrast source densities, also denoted as contrast sources, reduce to

$$\hat{J}_k^s(\mathbf{x}^{psc}, \omega) = \bar{\chi}^{\hat{\eta}}\hat{E}_k^i(\mathbf{x}^{psc}, \omega), \quad (5.23a)$$

$$\hat{K}_j^s(\mathbf{x}^{psc}, \omega) = \bar{\chi}^{\hat{\zeta}}\hat{H}_j^i(\mathbf{x}^{psc}, \omega), \quad (5.23b)$$

where

$$\bar{\chi}^{\hat{\eta}} = 3\hat{\eta}\frac{\chi^{\hat{\eta}}}{\chi^{\hat{\eta}} + 3\hat{\eta}}, \quad (5.24a)$$

$$\bar{\chi}^{\hat{\zeta}} = 3\hat{\zeta}\frac{\chi^{\hat{\zeta}}}{\chi^{\hat{\zeta}} + 3\hat{\zeta}}. \quad (5.24b)$$

The resulting representations for the scattered electric and magnetic fields can be obtained by substitution of Eqs. (5.23a) and (5.23b) in Eqs. (5.13a) and (5.13b).

5.4 Scattering from an ensemble of point scatterers

Let us now consider the scattering domain to be composed of a superposition of point scatterers, while neglecting the mutual interaction between the point scatterers. Hence, in this approximation we substitute Eqs. (5.23a) and (5.23b) into Eqs. (5.13a) and (5.13b) which yields

$$\begin{aligned} \hat{E}_k^s(\mathbf{x}^R, \omega) = & \int_{\mathbf{x} \in \mathbb{D}^s} [\hat{G}_{kr}^{EJ}(\mathbf{x}^R|\mathbf{x}, \omega)\bar{\chi}^{\hat{\eta}}(\mathbf{x})\hat{E}_r^i(\mathbf{x}, \omega) \\ & + \hat{G}_{kp}^{EK}(\mathbf{x}^R|\mathbf{x}, \omega)\bar{\chi}^{\hat{\zeta}}(\mathbf{x})\hat{H}_p^i(\mathbf{x}, \omega)]dV, \end{aligned} \quad (5.25a)$$

$$\begin{aligned} \hat{H}_j^s(\mathbf{x}^R, \omega) = & \int_{\mathbf{x} \in \mathbb{D}^s} [\hat{G}_{jr}^{HJ}(\mathbf{x}^R|\mathbf{x}, \omega)\bar{\chi}^{\hat{\eta}}(\mathbf{x})\hat{E}_r^i(\mathbf{x}, \omega) \\ & + \hat{G}_{jp}^{HK}(\mathbf{x}^R|\mathbf{x}, \omega)\bar{\chi}^{\hat{\zeta}}(\mathbf{x})\hat{H}_p^i(\mathbf{x}, \omega)]dV. \end{aligned} \quad (5.25b)$$

Note that in these representations we have taken into account the polarisation effects of the electromagnetic field while neglecting the multiple scattering

between the constituent point scatterers. For small contrasts, we observe that

$$\bar{\chi}^{\hat{\eta}} \approx \chi^{\hat{\eta}}, \quad (5.26a)$$

$$\bar{\chi}^{\hat{\zeta}} \approx \chi^{\hat{\zeta}}, \quad (5.26b)$$

and we observe that the expressions of Eqs. (5.25a) and (5.25b) coincide with the representations obtained by using the so-called first-Born approximation [see Born and Wolf, 1965], where we assume that

$$\hat{J}_k^s(\mathbf{x}^{psc}, \omega) \approx \chi^{\hat{\eta}} \hat{E}_k^i(\mathbf{x}^{psc}, \omega), \quad (5.27a)$$

$$\hat{K}_j^s(\mathbf{x}^{psc}, \omega) \approx \chi^{\hat{\zeta}} \hat{H}_j^i(\mathbf{x}^{psc}, \omega), \quad (5.27b)$$

which also follows from Eqs. (5.23a) and (5.23b). We therefore denote the Eqs. (5.25a) and (5.25b) as the modified Born approximation, which takes into account the vectorial nature of the electromagnetic field.

5.5 Scattering formalism using the modified Born approximation

In this section, we will reduce the expressions of the exact scattered field to linearised expressions of the scattered field which will be amenable to use as a starting point of the imaging procedure which will be derived in Chapter 6. We assume that the incident electromagnetic field is generated by external point sources $\hat{J}_k^e = \hat{S}^J(\omega)\delta(\mathbf{x} - \mathbf{x}^S)b_k^J$ and $\hat{K}_j^e = \hat{S}^K(\omega)\delta(\mathbf{x} - \mathbf{x}^S)b_j^K$. The incident field generated by these point sources can be written similar to Eqs. (5.6a) and (5.6b) as

$$\hat{E}_r^i(\mathbf{x}^c, \omega) = \hat{G}_{rt}^{EJ}(\mathbf{x}^c|\mathbf{x}^S, \omega)\hat{S}^J(\omega)b_t^J + \hat{G}_{rp}^{EK}(\mathbf{x}^c|\mathbf{x}^S, \omega)\hat{S}^K(\omega)b_p^K, \quad (5.28a)$$

$$\hat{H}_p^i(\mathbf{x}^c, \omega) = \hat{G}_{pr}^{HJ}(\mathbf{x}^c|\mathbf{x}^S, \omega)\hat{S}^J(\omega)b_r^J + \hat{G}_{ps}^{HK}(\mathbf{x}^c|\mathbf{x}^S, \omega)\hat{S}^K(\omega)b_s^K. \quad (5.28b)$$

Substitution of Eqs. (5.28a) and (5.28b) and the expressions for the scatter sources, Eqs. (5.23a) and (5.23b), into Eqs. (5.13a) and (5.13b) yields the

expressions for the scattered field

$$\begin{aligned} \hat{E}_k^s(\mathbf{x}^R, \mathbf{x}^S, \omega) = & \int_{\mathbf{x}^c \in \mathbb{D}^s} \left\{ \hat{G}_{kr}^{EJ}(\mathbf{x}^R | \mathbf{x}^c, \omega) \bar{\chi}^{\hat{\eta}}(\mathbf{x}^c) \right. \\ & \times \left[\hat{S}^J(\omega) \hat{G}_{rt}^{EJ}(\mathbf{x}^c | \mathbf{x}^S, \omega) b_t^J + \hat{S}^K(\omega) \hat{G}_{rp}^{EK}(\mathbf{x}^c | \mathbf{x}^S, \omega) b_p^K \right] \\ & + \hat{G}_{kp}^{EK}(\mathbf{x}^R | \mathbf{x}^c, \omega) \bar{\chi}^{\hat{\zeta}}(\mathbf{x}^c) \\ & \left. \times \left[\hat{S}^J(\omega) \hat{G}_{pr}^{HJ}(\mathbf{x}^c | \mathbf{x}^S, \omega) b_r^J + \hat{S}^K(\omega) \hat{G}_{ps}^{HK}(\mathbf{x}^c | \mathbf{x}^S, \omega) b_s^K \right] \right\} dV, \end{aligned} \quad (5.29a)$$

$$\begin{aligned} \hat{H}_j^s(\mathbf{x}^R, \mathbf{x}^S, \omega) = & \int_{\mathbf{x}^c \in \mathbb{D}^s} \left\{ \hat{G}_{jr}^{HJ}(\mathbf{x}^R | \mathbf{x}^c, \omega) \bar{\chi}^{\hat{\eta}}(\mathbf{x}^c) \right. \\ & \times \left[\hat{S}^J(\omega) \hat{G}_{rt}^{EJ}(\mathbf{x}^c | \mathbf{x}^S, \omega) b_t^J + \hat{S}^K(\omega) \hat{G}_{rp}^{EK}(\mathbf{x}^c | \mathbf{x}^S, \omega) b_p^K \right] \\ & + \hat{G}_{jp}^{HK}(\mathbf{x}^R | \mathbf{x}^c, \omega) \bar{\chi}^{\hat{\zeta}}(\mathbf{x}^c) \\ & \left. \times \left[\hat{S}^J(\omega) \hat{G}_{pr}^{HJ}(\mathbf{x}^c | \mathbf{x}^S, \omega) b_r^J + \hat{S}^K(\omega) \hat{G}_{ps}^{HK}(\mathbf{x}^c | \mathbf{x}^S, \omega) b_s^K \right] \right\} dV, \end{aligned} \quad (5.29b)$$

where \mathbb{D}^s is the scattering domain. The Green's tensor functions $\hat{G}_{rt}^{EJ}(\mathbf{x}^c | \mathbf{x}^S)$ and $\hat{G}_{pr}^{HJ}(\mathbf{x}^c | \mathbf{x}^S)$ describe the propagation of the electric and magnetic field from the primary electric-current source at \mathbf{x}^S towards the scatterer at \mathbf{x}^c , and $\hat{G}_{rp}^{EK}(\mathbf{x}^c | \mathbf{x}^S)$ and $\hat{G}_{ps}^{HK}(\mathbf{x}^c | \mathbf{x}^S)$ describe the propagation of the electric and magnetic field from the primary magnetic-current source at \mathbf{x}^S towards the scatterer at \mathbf{x}^c . Similarly, the Green's tensor functions $\hat{G}_{kr}^{EJ}(\mathbf{x}^R | \mathbf{x}^c)$ and $\hat{G}_{jr}^{HJ}(\mathbf{x}^R | \mathbf{x}^c)$ describe the propagation of the electric and magnetic field from the secondary electric-current source present at \mathbf{x}^c towards the receiver located at \mathbf{x}^R , and $\hat{G}_{kp}^{EK}(\mathbf{x}^R | \mathbf{x}^c)$ and $\hat{G}_{jp}^{HK}(\mathbf{x}^R | \mathbf{x}^c)$ describe the propagation of the electric and magnetic field from the secondary magnetic-current source present at \mathbf{x}^c towards the receiver located at \mathbf{x}^R .

We will now concentrate on the measured electric field scattered by a contrast in electrical properties due to an electric-current source. Eq. (5.29a) reduces to

$$\hat{E}_k^s(\mathbf{x}^R, \mathbf{x}^S, \omega) = \hat{S}^J(\omega) \int_{\mathbf{x}^c \in \mathbb{D}^s} \hat{G}_{kr}^{EJ}(\mathbf{x}^R | \mathbf{x}^c, \omega) \bar{\chi}^{\hat{\eta}}(\mathbf{x}^c) \hat{G}_{tr}^{EJ}(\mathbf{x}^S | \mathbf{x}^c, \omega) b_t^J dV, \quad (5.30)$$

where we have used Eq. (5.7a),

$$\hat{G}_{rt}^{EJ}(\mathbf{x}^c | \mathbf{x}^S, \omega) = \hat{G}_{tr}^{EJ}(\mathbf{x}^S | \mathbf{x}^c, \omega). \quad (5.31)$$

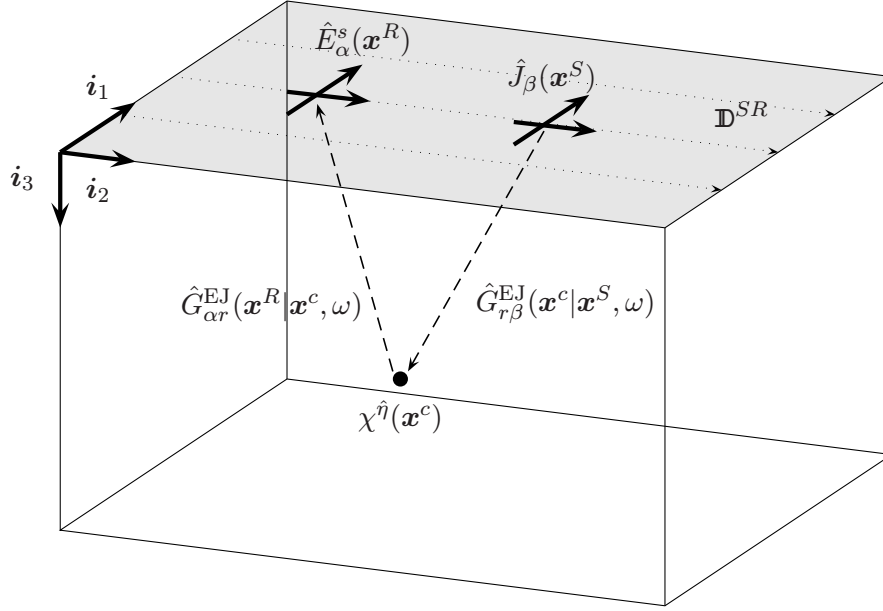


Figure 5.1: The configuration of the four possible source receiver setups.

We stress again that we have only assumed that each point in the subsurface acts as an independent point diffractor and no multiples are assumed to be present in the data.

Taking into account the practical limitation of finite length source and receiver antennas, the fact that the orientation of the source and receiver is parallel to the interface to obtain a better coupling, four different source-receiver combinations are possible. Eq. (5.30) reduces to

$$\hat{E}_\alpha^s(\mathbf{x}^R, \mathbf{x}^S, \omega) = \hat{S}^J(\omega) \int_{\mathbf{x}^c \in \mathcal{D}^s} \bar{\chi}^{\hat{\eta}}(\mathbf{x}^c) \hat{G}_{\alpha r}^{\text{EJ}}(\mathbf{x}^R | \mathbf{x}^c, \omega) \hat{G}_{\beta r}^{\text{EJ}}(\mathbf{x}^S | \mathbf{x}^c, \omega) b_\beta^J dV, \quad (5.32)$$

where $\{\alpha, \beta\} = \{1, 2\}$. We assume that the source and receiver are present on the same horizontal plane, $\{\mathbf{x}^S, \mathbf{x}^R\} \in \mathcal{D}^{SR}$, where $x_3^S = x_3^R = 0$. The configuration is depicted in Figure 5.1. The source and receiver coordinates are now written as $\mathbf{x}^S = \mathbf{x}^M - \mathbf{x}^H$ and $\mathbf{x}^R = \mathbf{x}^M + \mathbf{x}^H$. Because four different source-receiver combinations are possible, we introduce $\hat{E}_{\alpha\beta}^s(\mathbf{x}^M, \mathbf{x}^H, \omega)$,

where

$$\hat{E}_\alpha^s(\mathbf{x}^M, \mathbf{x}^H, \omega) = \hat{E}_{\alpha\beta}(\mathbf{x}^M, \mathbf{x}^H, \omega) b_\beta^J, \quad (5.33)$$

and $\hat{E}_{\alpha\beta}$ is given by

$$\begin{aligned} \hat{E}_{\alpha\beta}(\mathbf{x}^M, \mathbf{x}^H, \omega) = \hat{S}^J(\omega) \int_{\mathbf{x}^c \in \mathbf{D}^s} \bar{\chi}^{\hat{\eta}}(\mathbf{x}^c) \hat{G}_{\alpha r}^{\text{EJ}}(\mathbf{x}^M + \mathbf{x}^H | \mathbf{x}^c, \omega) \\ \times \hat{G}_{\beta r}^{\text{EJ}}(\mathbf{x}^M - \mathbf{x}^H | \mathbf{x}^c, \omega) dV, \end{aligned} \quad (5.34)$$

where α and β indicate the orientation of the receiver and the source, respectively. This notation is convenient when discussing the four different measurements separately.

Note that in this linearised scattering formalism, the measured scattered field consist of an inner product of two vectorial Greens functions. This linearised expression will be the starting point of the imaging algorithm which is derived in Chapter 6.

5.6 Acquisition set-up of a GPR survey

Different acquisition set-ups can be used to obtain information of the subsurface. First, the different orientations of the source and receiver are discussed. Then, the common-offset measurement and the common-midpoint measurement are discussed.

5.6.1 Orientations of the source and receiver antennas

As already indicated, the source and receiver antennas can only be oriented in a horizontal direction. For inline orientations, both source and receiver antennas are present on the survey line and the offset between the source and receiver is parallel to the survey line. For the crossline orientations, both source and receiver antennas are not present on the survey line and the offset between the source and receiver is perpendicular to the survey line. The possible inline and crossline orientations for the source and receiver antennas are depicted in Figures 5.2 and 5.3, respectively. In each figure, four different orientations are shown, resulting in eight possible orientations along a survey line. The survey line is indicated with a dotted line.

Two different terminologies to indicate the orientation of the source and receiver can be used. One option is to use the term broadside and endfire to indicate the orientation of two antennas with respect to each other preceded

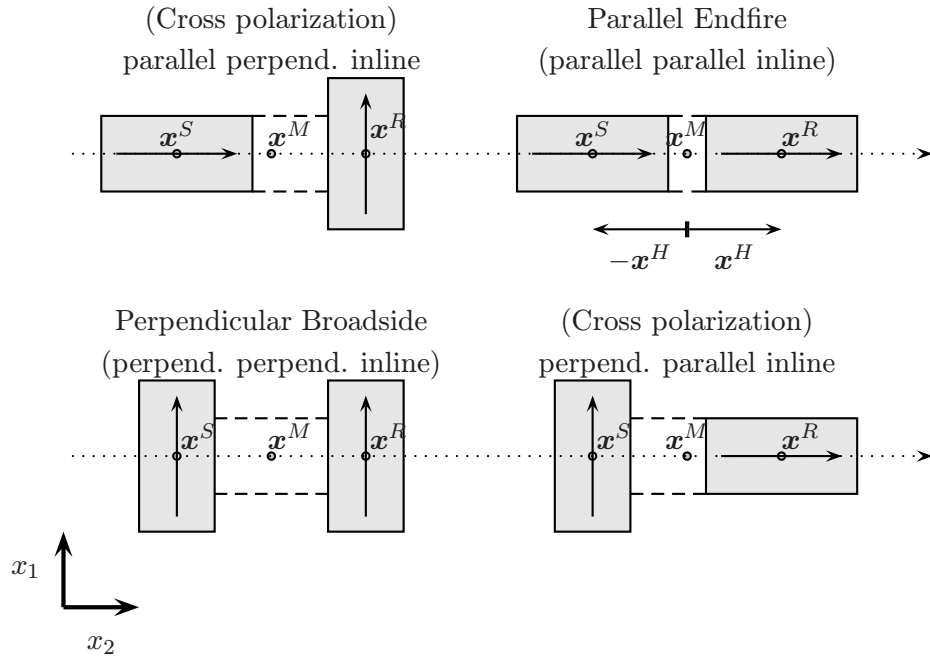


Figure 5.2: Possible inline orientations of the source and receiver antennas.

by the term Perpendicular or Parallel, which indicates that the offset is perpendicular or parallel to the survey line. When the antennas are oriented parallel to each other, but perpendicular to the offset between the antennas, we speak of broadside. When the antennas are oriented parallel to each other and also parallel to the offset between the antennas, we speak of end-fire. When the antennas are oriented perpendicular to each other, we speak of cross polarisation. In Figures 5.2 and 5.3 it can be observed that two different cross polarisations are present. To distinguish between these two cross polarisations we use the second terminology to indicate the polarisation set-up of the source and receiver relative to the survey line. First the orientation of the source, then the orientation of the receiver relative to the survey line is given; parallel or perpendicular, followed by the orientation of the offset between the source and receiver. When the offset ($2\mathbf{x}^H$) is parallel or perpendicular to the survey line the set-up is indicated by inline or crossline, respectively. Throughout this thesis a hybrid terminology will be used which uniquely describes the orientation of both antennas relative to

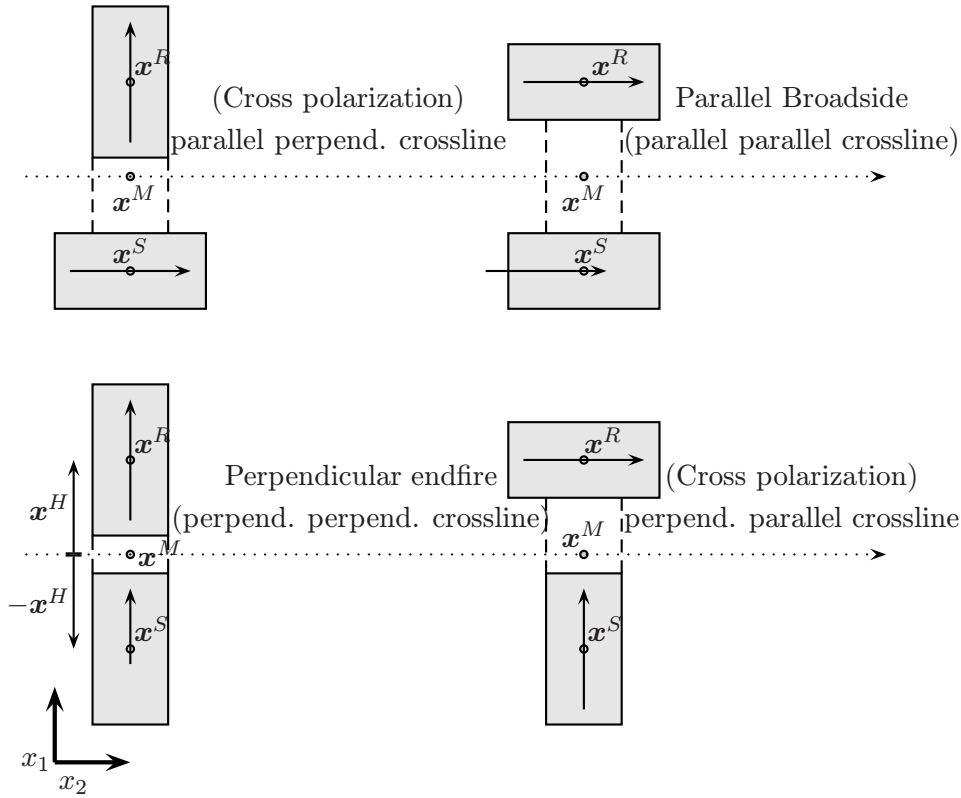


Figure 5.3: Possible crossline orientations of the source and receiver antennas.

the survey line. The used terminology is given in Figures 5.2 and 5.3 without brackets.

We will see in section 5.6.4 that for a 3D survey with equal sampling in both directions the crossline set-up can be obtained by a reorientation of the survey lines of the inline set-up.

5.6.2 Common-offset measurement (profiling)

To detect objects or to investigate the lateral and vertical changes in the subsurface, a GPR system is used in a common-offset configuration. The source and receiver antennas are separated by a fixed distance ($2x^H$), and measurements are carried out by moving the system along a line, see Figure 5.4. Measurements can be taken semi-continuously by moving the system a

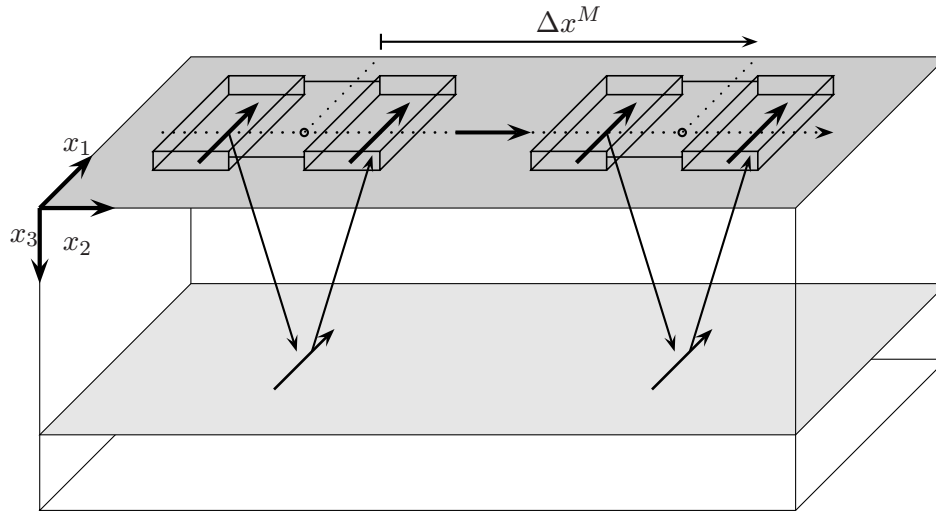


Figure 5.4: Common-offset measurement in the perpendicular-broadside configuration.

fixed distance ($\Delta \mathbf{x}^M$) taking a measurement and repeating this along the line. This method is fast and therefore relatively cheap, but a major drawback can be the lack of wave speed information of the subsurface that can be obtained from the measurements. However, when an object is present in the subsurface, a hyperbolic reflection pattern occurs in the data. From this hyperbola, the wave speed in the subsurface can be estimated as in van der Kruk and Slob [1999].

5.6.3 Common-midpoint measurement

The wave speed in layers can be obtained by the Common-MidPoint measurement (CMP). In this mode, the offset of both the source and receiver ($\Delta \mathbf{x}^H$) is increased where the reference is the fixed midpoint between source and receiver (\mathbf{x}^M). Expecting a horizontally layered earth, the information will be obtained from the line vertically below the chosen midpoint, see Figure 5.5. When a CMP measurement is carried out, different events can be distinguished and the velocities with which the events have travelled can be determined. Together with the expressions for the groundwave, valuable information about the properties of the subsurface can be obtained as in

van der Kruk and Slob [1998].

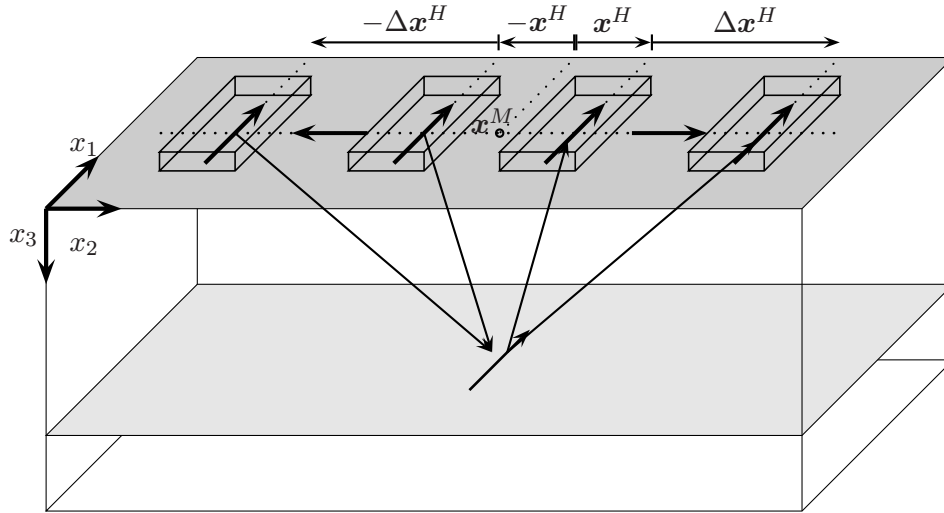


Figure 5.5: Common-midpoint configuration using the perpendicular-broadside set-up.

5.6.4 3D survey measurements

From a 3D measurement, the vertical and lateral dimensions of objects or structures present in the subsurface may be made visible. In practice, several parallel survey lines are measured. For common-offset measurements, an offset is present between the source and receiver antenna. This offset can be in the inline direction (parallel to the survey line) or in the crossline direction (perpendicular to the survey line). So the total number of possible configurations of a 3D multi-component survey is eight (see Section 5.6.1). When the inline sampling, the spatial sampling on each survey line is equal to the distance between each survey line, then a reorientation of the measurements results in equivalent measurements using only four different polarisation set-ups. This is depicted in Figure 5.6. When parallel lines are measured, the measurements for configuration E,F,G and H equal the results for I, J, K and L, respectively.

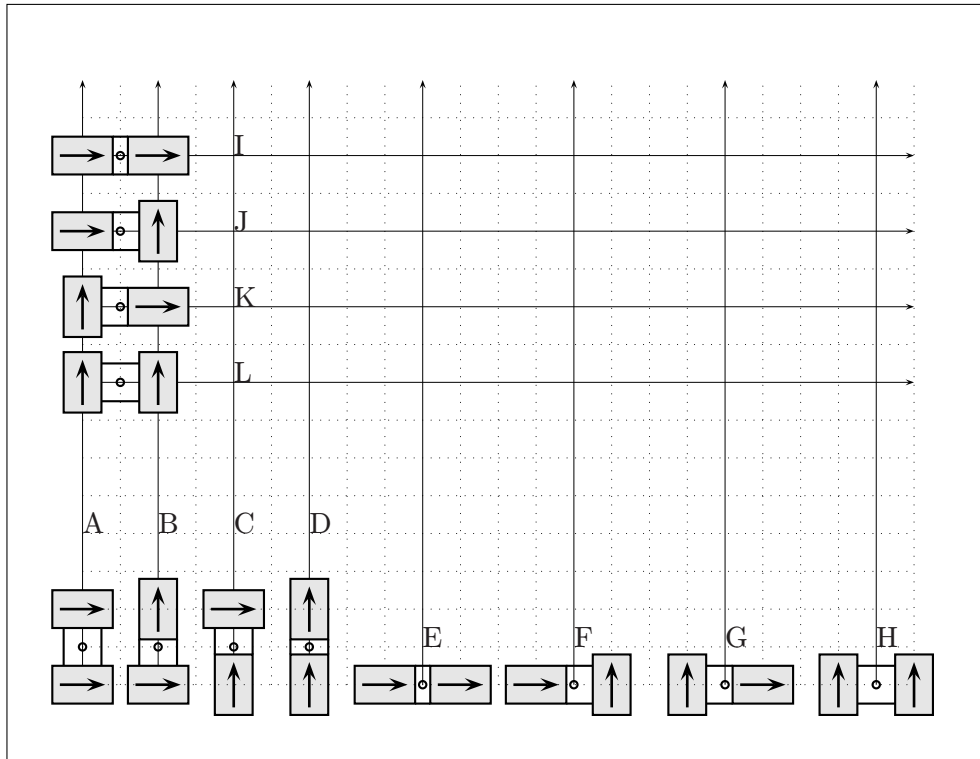


Figure 5.6: *Different configuration setups for a common offset 3D survey.*

5.7 Temporal and spatial sampling

To obtain a three-dimensional image of the subsurface numerous measurements have to be carried out along parallel survey lines to acquire reflected and diffracted electromagnetic waves. For an accurate measurement of these reflected and diffracted waves, the inline and crossline sampling interval must be chosen correctly, such that the reflected and diffracted waves are uniquely described by the sampled measurements. For a successful and efficient survey design, it is important to measure all available information, which is carried by the reflected and diffracted electromagnetic waves, by using correct temporal and spatial sampling values. This means that the sampling interval should not be chosen too sparse, resulting in a loss of information, and that the sampling interval should not be chosen too small resulting in superfluous

data which contain no additional information.

In time and space, the measured samples must satisfy the temporal sampling criterion and spatial sampling criterion, respectively. The spatial sampling criterion is derived for a point diffractor, and the influence of the radiation pattern and the acquisition surface on the spatial sampling criterion is investigated. These results are combined and the available correctly sampled information, also indicated by the temporal and spatial bandwidth, is determined, which can be used for the imaging procedure.

5.7.1 Temporal sampling

A continuous signal in time is sampled with a sampling interval of Δt . In this way, a bandlimited signal with a maximum frequency f^{max} is uniquely determined in terms of its samples, provided that the temporal sampling criterion is met, which is given by

$$\Delta t \leq \frac{1}{2f^{max}} = \frac{T^{min}}{2}, \quad (5.35)$$

where T^{min} is the period of one cycle for the frequency f^{max} . This indicates that at least two samples per cycle are required. Where there are fewer than two samples per cycle, an input signal at one frequency yields the same sample values as another frequency at the output, resulting in overlapping frequency samples, such that the original signal cannot be recovered. This effect is called aliasing. The boundary frequency f_{max} is often referred to as the Nyquist frequency. Frequencies greater than the Nyquist frequency will alias as lower frequencies from which they will be indistinguishable.

5.7.2 Spatial sampling

The sampling criterion will be discussed for one horizontal direction x_2 , whereas the sampling in the other horizontal direction x_1 can be obtained by a substitution of x_2 by x_1 and vice versa. From a practical point of view, subsequent measurements must be carried out in such a way that events on separate traces can be correlated as coming from the same horizon or reflection point in the subsurface [see Yilmaz, 1987]. For a given frequency component, the time delay between subsequent measurements can be at most half the period ($T/2$) of that frequency component to enable a correlation of two measured reflections as coming from the same horizon.

To enable a more thorough analysis of the factors which influence the spatial sampling criterion, it is advantageous to introduce the apparent wave speed c_2 , which describes the horizontal wave speed of a plane wave in the x_2 -direction, and is defined by

$$c_2 = \left[\frac{dt(x_2)}{dx_2} \right]^{-1}. \quad (5.36)$$

The maximum time delay between two subsequent measurements depends on the spatial sampling Δx_2^M and the minimum apparent wave speed c_2^{min} and is given by $\Delta x_2^M / c_2^{min}$. For a correct spatial sampling of the measured data this time delay can be at most half the period $T^{min}/2 = 1/(2f^{max})$ of the maximum frequency of the measured signal. The spatial sampling criterion between subsequent measurements is then given by

$$\Delta x_2^M \leq \frac{c_2^{min} T^{min}}{2} = \frac{c_2^{min}}{2f^{max}}, \quad (5.37)$$

where c_2^{min} is the minimum apparent wave speed in the wave field to be recorded aliasfree. Note that with the introduction of $c_2^{min} T^{min} = \lambda_2^{min}$, where λ_2^{min} is the minimum apparent wavelength, and using $k_2 = 2\pi/\lambda_2^{min}$, we obtain

$$\Delta x_2^M \leq \frac{\lambda_2^{min}}{2} = \frac{\pi}{k_2^{max}}, \quad (5.38)$$

which describes the relation between the spatial sampling and the maximum spatial frequency k_2^{max} . Note that this expression is similar to Eq. (5.35). The spatial bandwidth is given by $-k_2^{max} < k_2 < k_2^{max}$. Next, the influence of the acquisition surface and the radiation characteristics are discussed by analysing the minimum apparent wave speed. The required spatial sampling criterion is obtained by substitution of the obtained minimum apparent wave speed in Eq. (5.37).

5.7.3 Spatial sampling criterion for a point diffractor

The minimum apparent wave speed of a possible reflection or diffraction depends on several factors. First, there is the finite acquisition surface on which the reflections are measured. Second, there is the radiation pattern which limits the minimum apparent wave speed. To discuss the influence of these two factors, the apparent wave speed for the scattered field from a point

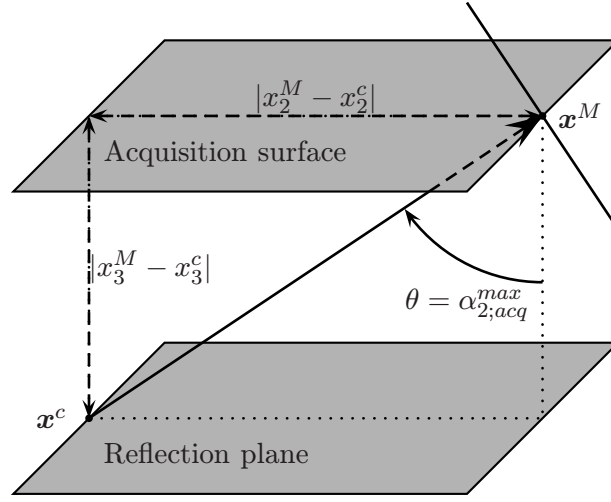


Figure 5.7: Determination of the minimum apparent velocity due to a limited acquisition surface.

diffractor is investigated. For a zero offset configuration ($\mathbf{x}^H = 0$), where the source and receiver are located at position \mathbf{x}^M , the two way traveltime of a signal to and from a point diffractor at location $\mathbf{x}^c = (x_1^c, x_2^c, x_3^c)$ is given by

$$t(\mathbf{x}^M) = \frac{2\sqrt{(x_2^M - x_2^c)^2 + (x_1^M - x_1^c)^2 + (x_3^M - x_3^c)^2}}{c}. \quad (5.39)$$

Using Eq. (5.36) the apparent wave speed c_2 as a function of the acquisition location \mathbf{x}^M is obtained as

$$c_2(\mathbf{x}^M) = \frac{c}{2} \sqrt{\frac{(x_1^M - x_1^c)^2 + (x_3^M - x_3^c)^2}{(x_2^M - x_2^c)^2} + 1}. \quad (5.40)$$

Influence of acquisition surface on apparent wave speed

For most applications, we are interested in the reflections coming from the volume present beneath the acquisition plane, which has equal dimensions as the acquisition surface (see Figure 5.7). Because the spatial sampling criterion depends on the minimum apparent wave speed, (see Eq. (5.37)), the minimum apparent wave speed c_2^{min} is obtained for $x_1^M - x_1^c = 0$. Substitution

of $x_1^M - x_1^c = 0$ in Eq. (5.40) yields

$$\begin{aligned} c_{2;acq}^{min} &= \frac{c}{2} \sqrt{\frac{(x_3^M - x_3^c)^2}{(x_2^M - x_2^c)^2} + 1}, \\ &= \frac{c}{2 \sin(\alpha_{2;acq}^{max})}, \end{aligned} \quad (5.41)$$

which shows that the minimum apparent wave speed $c_{2;acq}^{min}$ depends on the depth and is present for reflected waves, which are measured at the widest angle $\alpha_{2;acq}^{max}$ possible. For an infinitely large acquisition plane the minimum apparent wave speed is obtained for $x_3^M - x_3^c = 0$ and yields $c_{2;acq}^{min} = c/2$. Note that reflected waves measured by a zero-offset configuration have apparent velocities that are half the value that would be obtained for a single wavefront moving along the surface.

Influence of the radiation pattern on apparent wave speed

Analysing the radiation pattern of a horizontal dipole present on the interface of a dielectricum we observe that a maximum amplitude is present for an angle θ_c in the H -plane, while a notch is present at the same angle in the E -plane (see Section 4.6). For θ close to $\pi/2$ the amplitude of the electric far-field is negligible in both the E - and the H -plane. Similar to Eq. (5.41) we state that we can neglect reflections occurring at and beyond an angle $\alpha_{2;rad}^{max}$. At this angle a threshold a equals the ratio of the amplitude of the electric field to the maximum amplitude at θ_c . The reflections, that have a ratio of their amplitude to the maximum amplitude at θ_c which is smaller than the threshold a , are neglected.

For a dipole present on the interface between two homogeneous half-spaces and oriented in the x_1 -direction, Eq. (69)¹ of Engheta et al. [1982] describes the far-field in the H -plane. For the ratio where the amplitude of the electric field to the maximum amplitude at θ_c equals a , we obtain for the angle $\alpha_{2;rad}^{max}$

$$\sin(\alpha_{2;rad}^{max}) = \sqrt{1 - a^2 + \frac{a^2}{n^2}}. \quad (5.42a)$$

The apparent wave speed as a function of the relative permittivity (n^2) and

¹Note the different coordinate systems.

the radiation amplitude threshold a is obtained as

$$\begin{aligned} c_{2;rad}^{min} &= \frac{c}{2 \sin(\alpha_{2;rad}^{max})}, \\ &= \frac{c}{2\sqrt{1 - a^2 + \frac{a^2}{n^2}}}. \end{aligned} \quad (5.43)$$

The latter formula indicates that a small threshold $a \rightarrow 0$ results in an apparent wave speed of $c_{2;rad}^{min} = c/2$. The larger the threshold, the larger the apparent wave speed and the larger the spatial sampling interval can be. The smaller the relative permittivity, the larger the apparent wave speed and the larger the spatial sampling can be. It is not feasible to obtain closed-form expressions for the minimum apparent wave speed as function of a threshold a for a scatterer in the E -plane. This can only be carried out in numerical sense. For a homogeneous space $\alpha_{2;rad}^{max}$ equals $\pi/2$ and is independent of a and n in the H -plane, while for the E -plane $\alpha_{2;rad}^{max} < \pi/2$.

When both antennas are present in the air the lowest apparent wave speed is the wave speed of light. This indicates that the spatial sampling for these measurements can be less dense compared with measurements where the source and receiver are present on the interface.

5.7.4 Temporal and spatial bandwidth

The temporal and spatial bandwidth indicates the usable range in the frequency domain and in the spatial Fourier domain, which can be used to perform the imaging procedure. In the preceding sections the influence of the frequency, the acquisition surface and the radiation pattern on the temporal and spatial sampling criterion was discussed. These factors inherently influence the temporal and spatial bandwidth. Another factor which influences the spatial bandwidth is the evanescent field. These factors and their influence on the temporal and spatial bandwidth are discussed.

Neglecting evanescent waves

For a medium without losses, we can substitute $\sigma = 0$ in Eq. (4.1), which enables the introduction of the real valued wavenumber k , which is related to the propagation coefficient γ as,

$$\gamma = jk, \quad (5.44)$$

where

$$k = \omega/c. \quad (5.45)$$

It is already indicated that the measured reflected waves for a zero offset measurement have an apparent wave speed of half the original speed. Making a substitution of $c \rightarrow c/2$ into Eqs. (5.44), (5.45) and (3.13), it is convenient to introduce the vertical wavenumber k_3 ,

$$k_3 = \begin{cases} \sqrt{4k^2 - k_1^2 - k_2^2}, & \text{for } k_1^2 + k_2^2 \leq 4k^2, \\ -j\sqrt{k_1^2 + k_2^2 - 4k^2}, & \text{for } k_1^2 + k_2^2 > 4k^2, \end{cases} \quad (5.46)$$

where $k_1^2 + k_2^2 < 4k^2$ represents propagating waves and $k_1^2 + k_2^2 > 4k^2$ represents evanescent waves. Note that the evanescent waves are exponentially attenuating. For $k_1 = 0$ the areas which represent the propagating and evanescent waves are indicated in Figure 5.8. The evanescent field is usually neglected when performing the imaging procedure, because that will result in an unstable imaging operator (see Section 6.5.1). This evanescent property of wave fields is a fundamental spatial bandwidth limitation

Neglecting aliased spatial frequency components

The maximum wavenumber which is sampled correctly is given by the spatial sampling criterion (see Eq. (5.37))

$$|k_2^{max}| = \frac{\pi}{\Delta x_2^M}. \quad (5.47)$$

The periodic property of Fourier transformed discrete signals, results in a wrap around of the spatial frequency components for wavenumbers which are larger than $|k_2^{max}|$, also called aliasing. Migration of these aliased spatial frequency components will move these contributions in the wrong direction. The aliased spatial frequency components are identified by

$$|k_2| > \frac{2\pi}{\Delta x_2^M} - 2k. \quad (5.48)$$

In Figure 5.8 the wavenumber area for a given wave speed c and detector spacing Δx_2^M is indicated. Areas 1 and 3 indicate the aliased wavenumbers which are wrongly mapped into areas 2 and 4, respectively [see also Berkhout, 1984]. The wavenumber area which can be used for the imaging excludes the

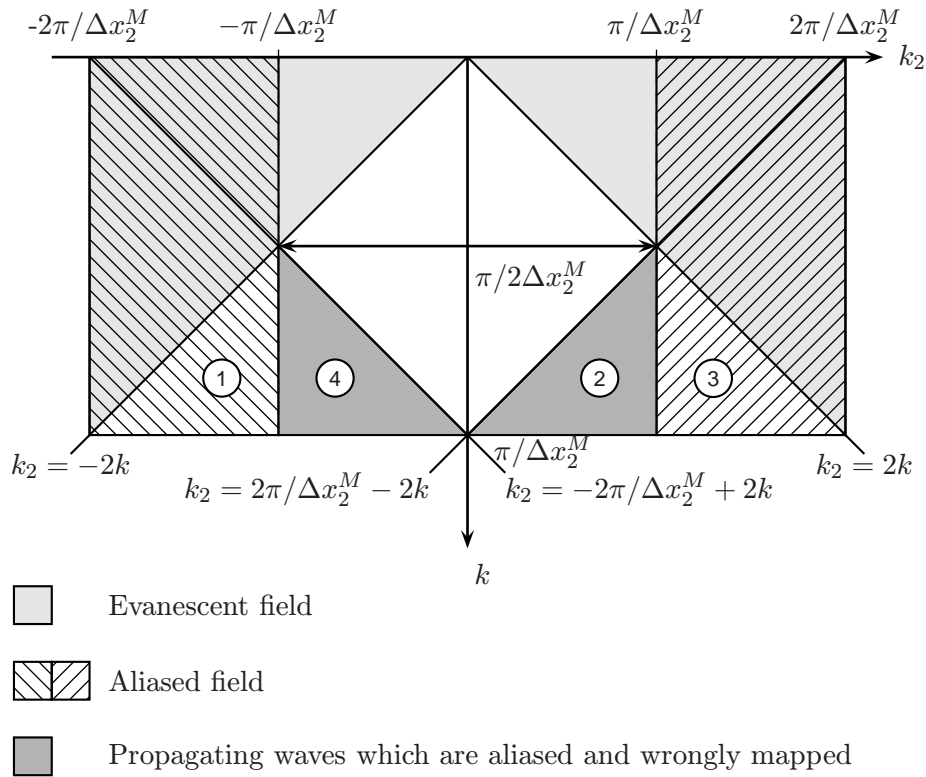


Figure 5.8: Wavenumber area of practical interest for a given velocity c and spatial sampling Δx_2^M .

evanescent field and the wrongly mapped aliased field. This is indicated in Figure 5.8.

Note the different scales of the k - and k_2 -axis. Compared with a one way analysis of the spatial sampling [Berkhout, 1984] the k -axis is divided in two, which results in a halving of the usable frequency band. This is caused by the fact that we analysed the measured reflections for a zero-offset configuration. The frequencies up to $f = ck/(2\pi) = c/(4\Delta x_2^M)$ are not aliased. For frequencies larger than $f = c/(4\Delta x_2^M)$ the highest spatial frequencies are aliased and migration or imaging will move these spatially aliased spatial

frequency components in the wrong direction.

Boundaries due to the frequency content of the measured signal

Due to the limited bandwidth of the measured signal the boundaries of the usable range lies between $f_1 < f < f_4$, which is indicated in Figure 5.9. In this figure the frequencies are indicated along the k -axis, which is possible due to the linear relation $k = 2\pi f/c$.

Boundaries due to the radiation pattern and the finite acquisition plane

Both the radiation pattern and the finite acquisition plane limit the spatial bandwidth. The minimum apparent velocity determined by the radiation pattern is given by Eq. (5.43) and depends on the angle $\alpha_{2;rad}^{max}$, while the minimum apparent velocity determined by the finite acquisition plane is given in Eq. (5.41) and depends on the angle $\alpha_{2;acq}^{max}$. The limiting factor which determines the spatial bandwidth is determined by the maximum angle α_2^{max} given by

$$\alpha_2^{max} = \max\{\alpha_{2;acq}^{max}, \alpha_{2;rad}^{max}\}, \quad (5.49)$$

and consequently the minimum apparent wave speed is given by

$$c_2^{min} = \min\{c_{2;acq}^{min}, c_{2;rad}^{min}\}. \quad (5.50)$$

Using Eqs. (5.37) and (5.38) the maximum horizontal wavenumber is obtained as

$$|k_2^{max}| \leq \frac{4\pi f \sin(\alpha_2^{max})}{c}. \quad (5.51)$$

Summarizing the results which are dictated by the limited acquisition plane, the radiation characteristics and neglect the aliased spatial frequency components, the maximum horizontal wavenumber which is recorded unaliased must satisfy

$$|k_2| \leq \frac{2\pi}{\Delta x_2^M} - 2k, \quad (5.52a)$$

$$|k_2| \leq 2k \sin(\alpha_2^{max}). \quad (5.52b)$$

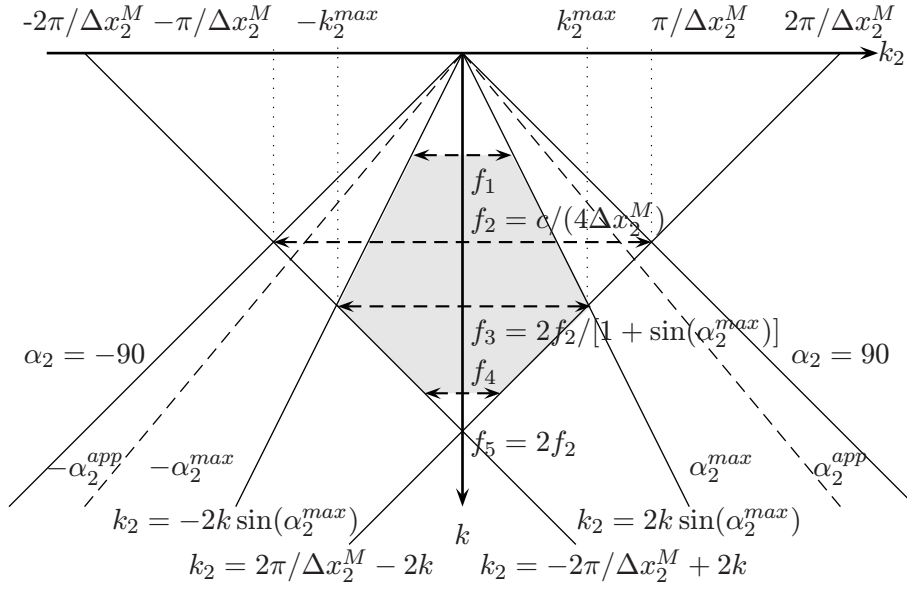


Figure 5.9: The influence on the apparent velocity and the radiation pattern on the information in the $k_2 - k$ -space.

The maximum horizontal wavenumber, which is recorded unaliased, k_2^{max} is given by

$$k_2^{max} = \frac{\sin(\alpha_2^{max})}{1 + \sin(\alpha_2^{max})} \frac{2\pi}{\Delta x_2^M}. \quad (5.53)$$

The temporal frequency for k_2^{max} is given by

$$f_3 = \frac{c}{2[1 + \sin(\alpha_2^{max})]\Delta x_2^M}. \quad (5.54)$$

The spatial sampling which is needed for unaliased recording of data with a temporal frequency f^{max} is given by

$$\Delta x_2^M = \frac{c}{2[1 + \sin(\alpha_2^{max})]f^{max}}. \quad (5.55)$$

With these results the spatial and temporal bandwidth of the measured field associated with a point scatterer in a homogeneous background is determined.

5.8 Modelling results

In Chapter 4, the electric field generated by a point source of electric current was depicted in the frequency domain. The source wavelet was assumed to have unit amplitude. In this chapter, time domain results are investigated for the scattering of a point scatterer using the Born approximation. In this way the influence of the vector character of the electromagnetic wave propagation and the radiation characteristics of the source and receiver antenna is investigated.

Synthetic results will be presented for different measurement set-ups. First, the results of a single measurement are discussed for different polarisations. Second, the results of a survey line are discussed. Finally the results of a 3D survey are discussed. These measured reflections on an acquisition plane are also transformed to the spatial Fourier domain to investigate the influence of the vector character of the measured electric field and the radiation characteristics of the source and receiver. This indicates the usable temporal and spatial bandwidth which can be used for the imaging procedure, which will be derived in Chapter 6.

5.8.1 The source wavelet

As input wavelet, we have chosen a Gaussian current distribution, because the derivatives of a Gaussian function can be easily distinguished. The source wavelet is given by

$$S^J(t) = \exp[-f_0^2 \pi^2 (t - \tau)^2], \quad (5.56a)$$

$$\hat{S}^J(\omega) = \frac{\sqrt{\pi}}{f_0} \exp\left(\frac{-\omega^2}{4\pi^2 f_0^2}\right) \exp(-j\omega\tau), \quad (5.56b)$$

where $\tau = 0.9/f_0$ is used to obtain an almost causal wavelet. The center frequency of the first and second order derivatives are given by $f_0/\sqrt{2}$ Hz and f_0 Hz, respectively. Information can be obtained by analysing the measured wavelet with respect to the order of differentiation on the initial input wavelet. The initial wavelet and its accompanying first, second and third order derivatives are shown in Figure 5.10 for $f_0 = 450$ MHz.

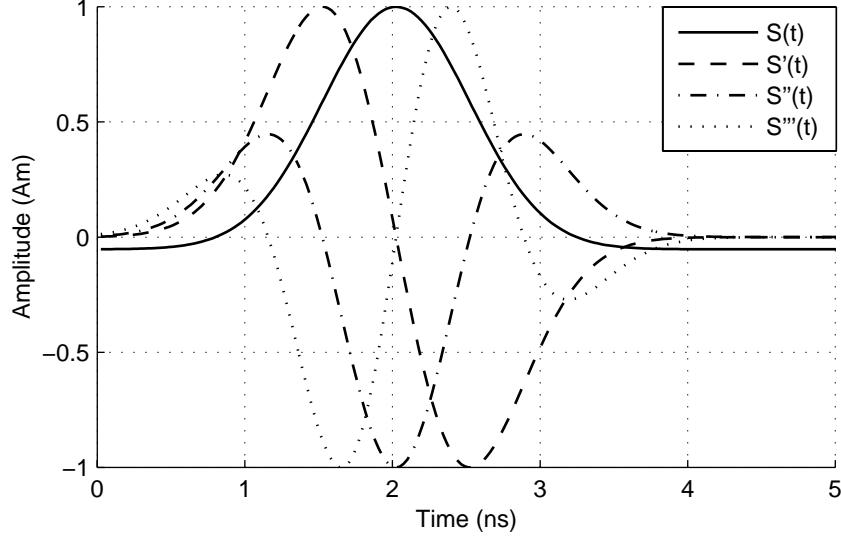


Figure 5.10: Initial input wavelet and its accompanying first, second and third order derivatives for $f_0 = 450$ MHz.

5.8.2 Measurement of different component of the scatter source

The source, which can have two orientations, generates an incident field. This incident field generates a secondary scatter-source at the location of the scatterer. For an isotropic homogeneous scatterer, this scatter source has the direction of the incident electric field at the position of this scatterer (cf. Eq. (5.23a)). So the scatter source consists of three components, which all separately contribute to the finally obtained measured electric field measured by the receiver. This receiver also can have two orientations, which results in a certain selection for the measurement of one specific electric field component. The finally obtained measured electric field is given by

$$\hat{E}_{\alpha\beta}(\mathbf{x}^R|\mathbf{x}^S, \omega) = \sum_{k=1}^3 \hat{E}_{\alpha\beta}^k(\mathbf{x}^R|\mathbf{x}^S, \omega), \quad (5.57)$$

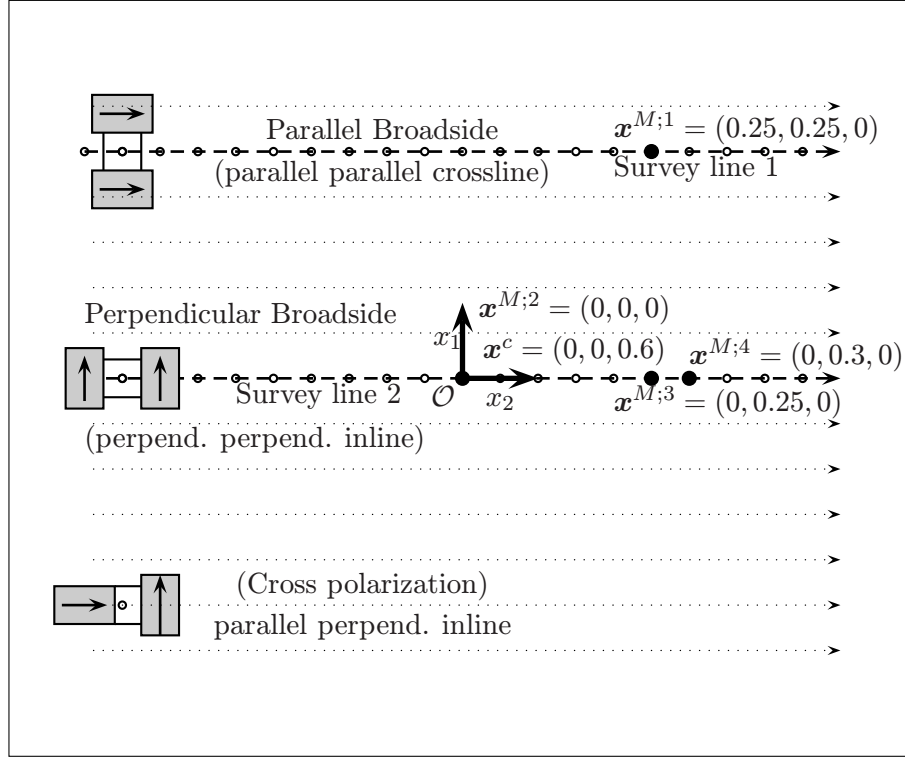


Figure 5.11: Planview of the configuration for a buried point scatterer vertically below the origin \mathcal{O} : $(0, 0, 0.6)$

where the separate contributions of the three components of the scatter source \hat{J}_k^s are given by

$$\hat{E}_{\alpha\beta}^1(\mathbf{x}^R|\mathbf{x}^S, \omega) = \bar{\chi}^{\hat{\eta}} \int_{\mathbf{x}^c \in \mathbf{D}^s} \hat{G}_{\alpha 1}^{\text{EJ}}(\mathbf{x}^R|\mathbf{x}^c, \omega) \hat{G}_{1\beta}^{\text{EJ}}(\mathbf{x}^c|\mathbf{x}^S, \omega) dV, \quad (5.58a)$$

$$\hat{E}_{\alpha\beta}^2(\mathbf{x}^R|\mathbf{x}^S, \omega) = \bar{\chi}^{\hat{\eta}} \int_{\mathbf{x}^c \in \mathbf{D}^s} \hat{G}_{\alpha 2}^{\text{EJ}}(\mathbf{x}^R|\mathbf{x}^c, \omega) \hat{G}_{2\beta}^{\text{EJ}}(\mathbf{x}^c|\mathbf{x}^S, \omega) dV, \quad (5.58b)$$

$$\hat{E}_{\alpha\beta}^3(\mathbf{x}^R|\mathbf{x}^S, \omega) = \bar{\chi}^{\hat{\eta}} \int_{\mathbf{x}^c \in \mathbf{D}^s} \hat{G}_{\alpha 3}^{\text{EJ}}(\mathbf{x}^R|\mathbf{x}^c, \omega) \hat{G}_{3\beta}^{\text{EJ}}(\mathbf{x}^c|\mathbf{x}^S, \omega) dV, \quad (5.58c)$$

where the superscript of $\hat{E}_{\alpha\beta}$ indicates the direction of the scatter source. In Figure 5.11 the configuration is depicted. A buried point diffractor is located vertically below the origin at a depth of 0.6 m ($\mathbf{x}^c = (0, 0, 0.6)$). For

simplicity we use the Born approximation $\bar{\chi}^{\hat{n}} = \chi^{\hat{n}}$ to calculate the scattered electric field. In this way the tensorial wave propagation effects can be analysed. At two locations, $\mathbf{x}^{M;1} = (0.25, 0.25, 0)$ and $\mathbf{x}^{M;2} = (0, 0, 0)$ the scattered field is calculated using the scattered field of an effective point diffractor with a conductivity contrast of unit amplitude for different orientations of the source and receiver. A comparison is made between the modelling results using the far field expressions as described in Section 4.4 and the total field as described in Section 4.5.

Synthetic data are presented in Figures 5.12 and 5.13 for the perpendicular-broadside and the parallel-perpendicular inline-configuration, respectively at offline position $\mathbf{x}^{M;1}$. The offset ($2\mathbf{x}^H$) between the source and receiver is 0 m. The relative permittivity of the lower half-space equals $\varepsilon_r = 6$ and the conductivity equals $\sigma = 0$. For each scatter source component J_k^s the contribution to the measured electric field $\{E_{11}^k, E_{12}^k\}$ is depicted together with the total electric field $\{E_{11}, E_{12}\}$, which is a sum of the separate contributions. The largest contribution for the perpendicular-broadside configuration in Figure 5.12 is given by the E_{11}^1 , while for the parallel-perpendicular configuration in Figure 5.13 the largest contribution is given by E_{12}^1 and E_{12}^2 . Note that E_{12}^1 and E_{12}^2 are equal, which is caused by the cross-polarisation set-up and the inner product of complementary radiation characteristics for both J_1^s and J_2^s scatter sources. It can also be observed that the shape of the measured electric field at the receiver has a wavelet which is similar to the second derivative of the Gaussian source wavelet in Figure 5.10. This can also be explained more theoretically by analysing the radiation characteristics of a dipole. The electric field generated by a dipole is basically a derivative of the source wavelet (Gaussian current distribution). This is indicated by the $\hat{\zeta}_0$ -factor in the Greens function in Eq. (4.22b), which indicates a time derivative and a multiplication with the permeability μ_0 . The scattered field is an inner product of two Greens functions, which results in a second derivative. The second derivative of a Gaussian current distribution with $f_0 = 450$ MHz has a center frequency of 450 MHz as given in Section 5.8.1. Note that for a permittivity contrast using the Born approximation we would obtain a source wavelet similar to the third derivative of the initial Gaussian current distribution.

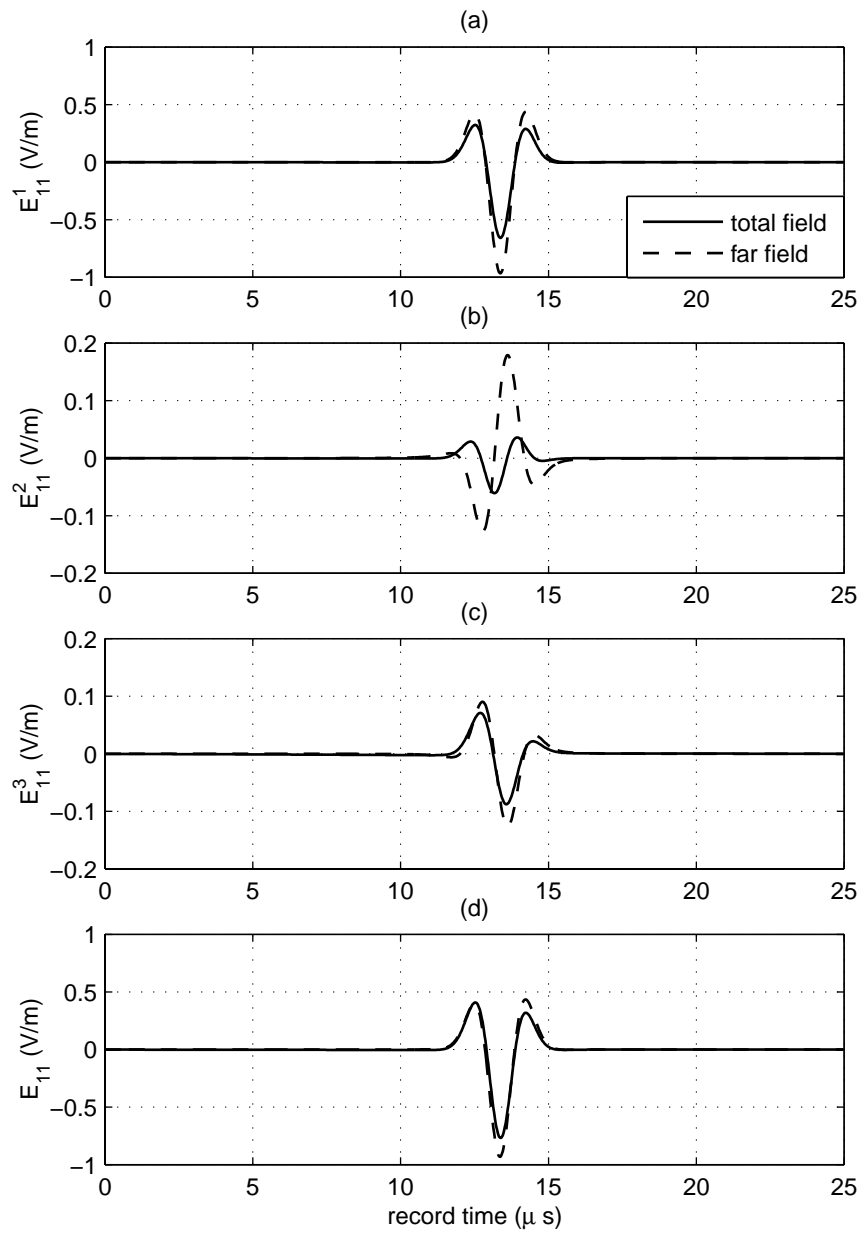


Figure 5.12: Comparison between total field and far field of an offline σ -contrast using a perpendicular-broadside configuration for (a) E_{11}^1 , (b) E_{11}^2 , (c) E_{11}^3 , (d) E_{11} .

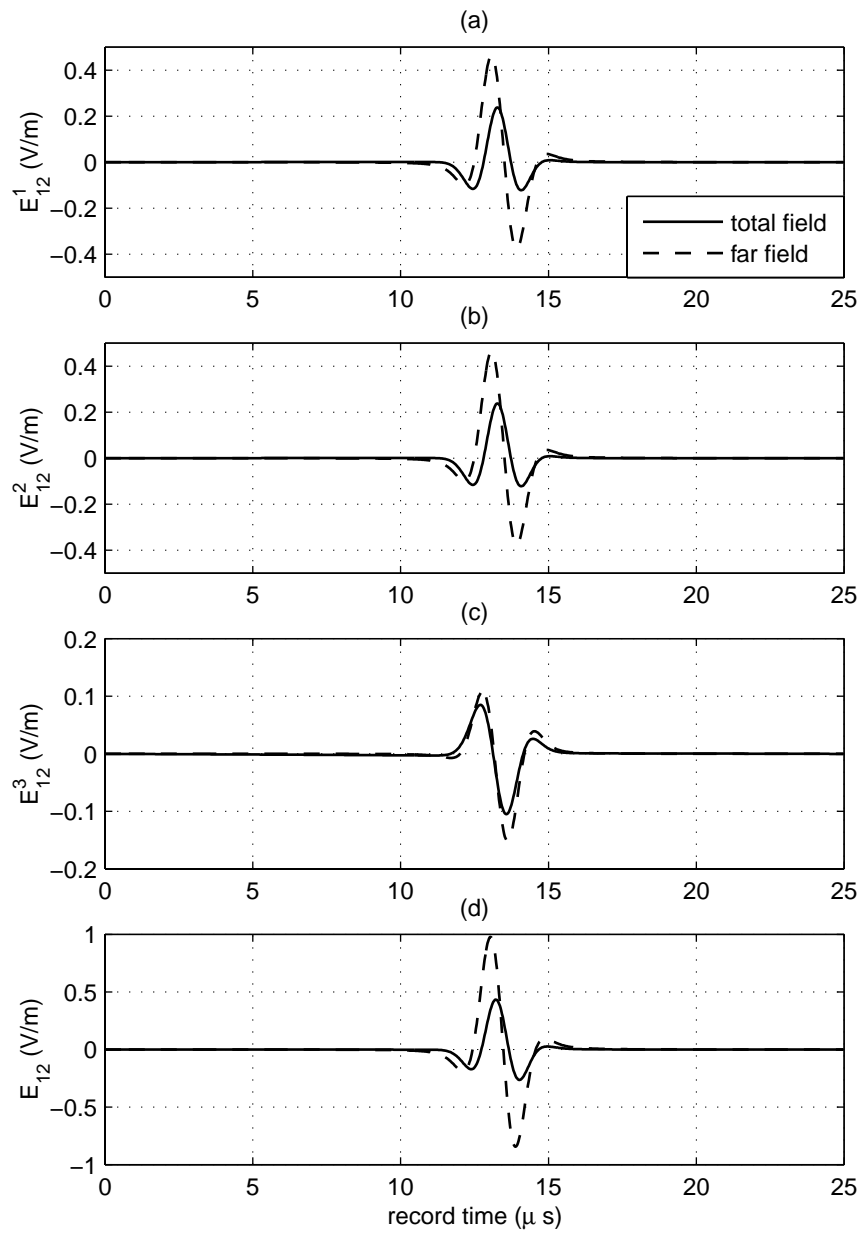


Figure 5.13: Comparison between total and far field of an offline σ -contrast using a parallel-perpendicular inline-configuration for (a) E_{12}^1 , (b) E_{12}^2 , (c) E_{12}^3 , (d) E_{12} .

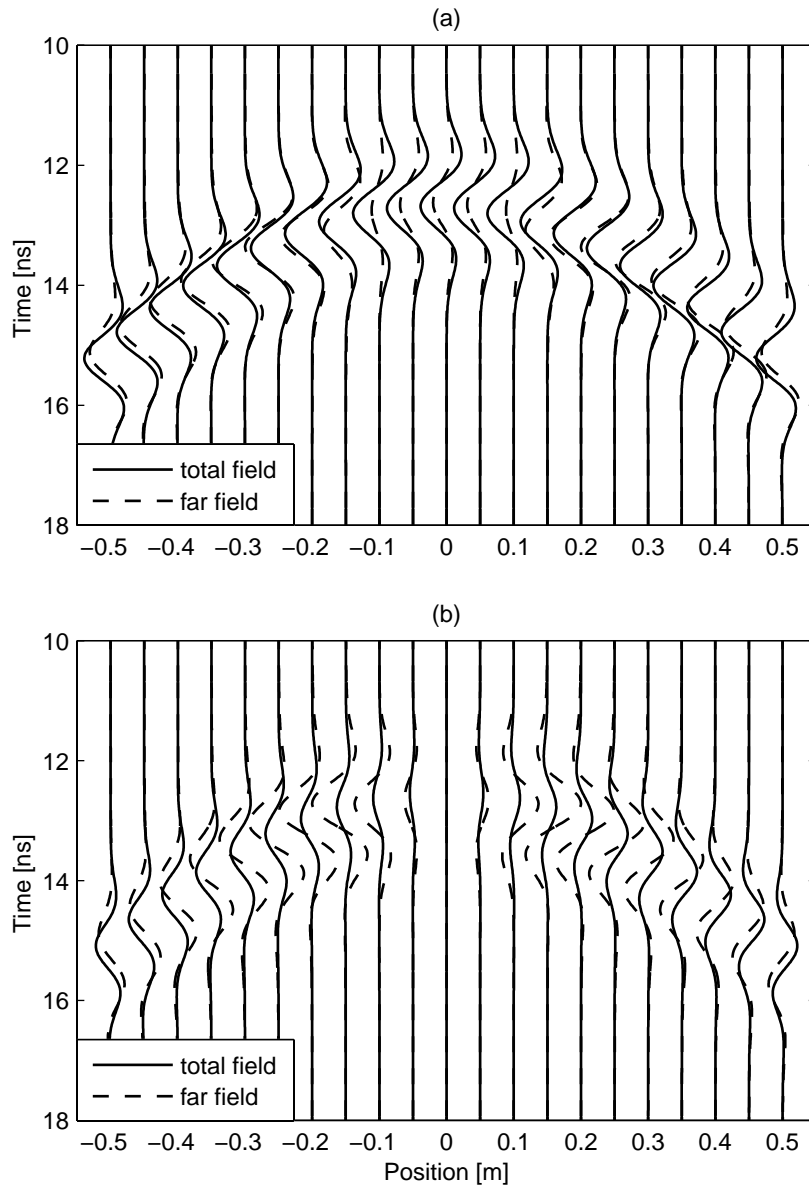


Figure 5.14: Comparison between total-field and far-field on survey line 1 for a σ -contrast using a (a) perpendicular-broadside configuration, (b) parallel-perpendicular inline-configuration.

5.8.3 Measurements along an acquisition line

Along survey line 1 (see Figure 5.11) 21 measurements were made with a step-size $\Delta \mathbf{x}^M = (0, 0.05, 0)$ m, zero-offset configuration ($\mathbf{x}^H = (0, 0, 0)$) and starting at position $(0.25, -0.5, 0)$. For survey line 1 results are presented for the perpendicular-broadside - and the parallel-perpendicular inline-configuration in Figure 5.14. Due to the fact that for the parallel-perpendicular inline-configuration at position $(0.25, 0, 0)$ a scatter source J_2^s is present at $(0, 0, 0.6)$ for a J_2 source at $(0.25, 0, 0)$. This scatter source results in only a E_2 -component at $(0.25, 0, 0)$ which is not measured by a J_1 receiver. So at position $(0.25, 0, 0)$ no reflection is measured from the point scatterer. It is stressed that the measured reflections for positive and negative positions differ in sign [see also Lehmann, 1999]. Note that the separate contributions of the different components of the scatter source for position $(0.25, 0.25, 0)$ are depicted in Figures 5.12 and 5.13 for the perpendicular-broadside and the parallel-perpendicular inline-configuration, respectively.

Along survey line 2 in Figure 5.11, 21 measurements were made with a step-size $\Delta \mathbf{x}^M = (0, 0.05, 0)$ m, $\mathbf{x}^H = (0, 0, 0)$ and starting at position $(0, -0.5, 0)$. Results are presented for the perpendicular-broadside and the parallel-broadside configuration in Figure 5.15. Note that the scatter source for the perpendicular-broadside configuration has only a J_1^s -component at survey line 2, while for the parallel-broadside configuration the scatter source has both a J_2^s and a J_3^s -component. The cross-polarised configuration did not measure a reflection, caused by the fact that the source generates an equivalent scatter source, which results in an electric field perpendicular to the receiver for survey line 2, which is similar to the discussion of the measured electric field for the parallel-perpendicular configuration at position $(0.25, 0, 0)$.

It can be observed that the similarity between the far field and total field is better when the source-receiver location is close to the object. In both Figures 5.15(a) and (b) an increasing error between the far field and total measured field is observed around position ± 0.25 m. We recall that the largest error between the far field and total field of the radiation characteristic occurs at the critical angle. This critical angle occurs in this configuration when the scatterer is present at $\theta_c = \arcsin(1/\sqrt{\varepsilon_r})$, which is equal to $x_2 = 0.268$ m for $\varepsilon_r = 6$. In Figure 5.16 the far field and total field contributions of the scatter sources J_2^s and J_3^s for position $\mathbf{x}^{M;3}$ and $\mathbf{x}^{M;4}$ (see Figure 5.11) are depicted. At position $\mathbf{x}^{M;3}$ the total field and far field contributions of J_2^s and J_3^s differ in amplitude, while for position $\mathbf{x}^{M;4}$ the contribution of scatter source J_2^s

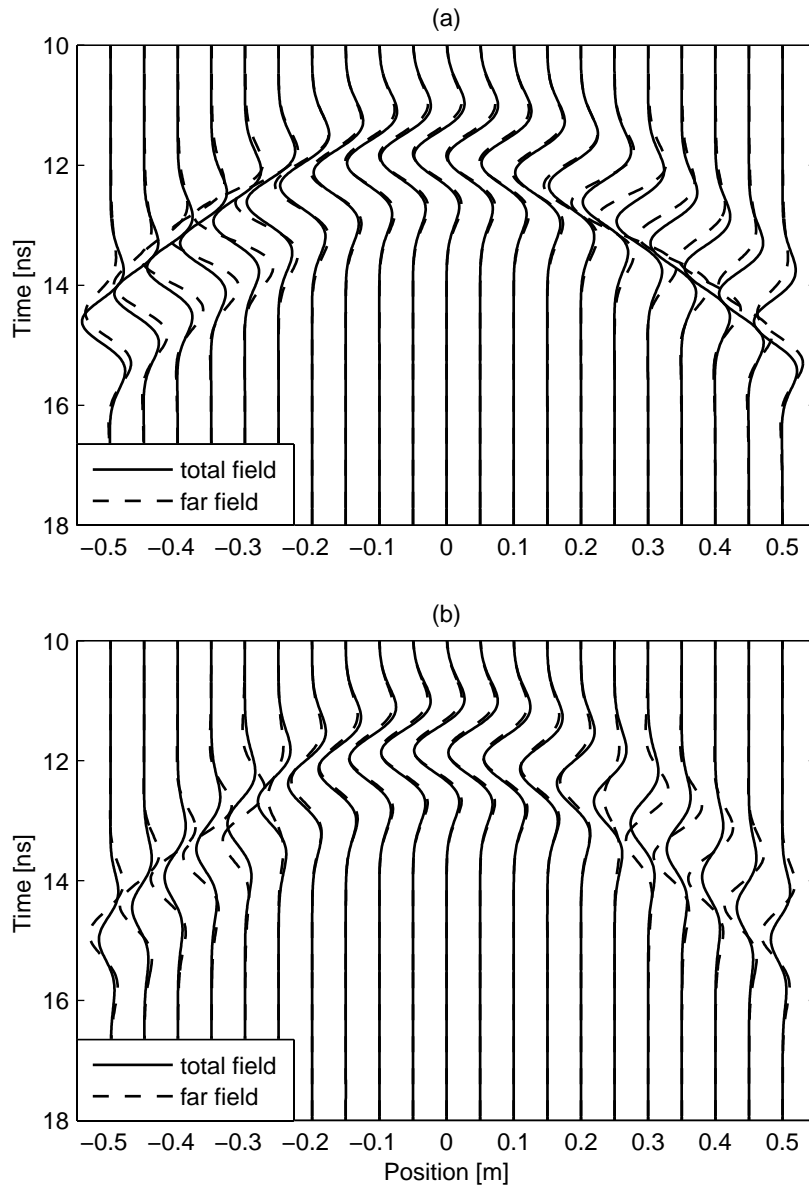


Figure 5.15: Comparison between total field and far field on survey line 2 for a σ -contrast using a (a) perpendicular-broadside configuration, (b) parallel-broadside configuration.

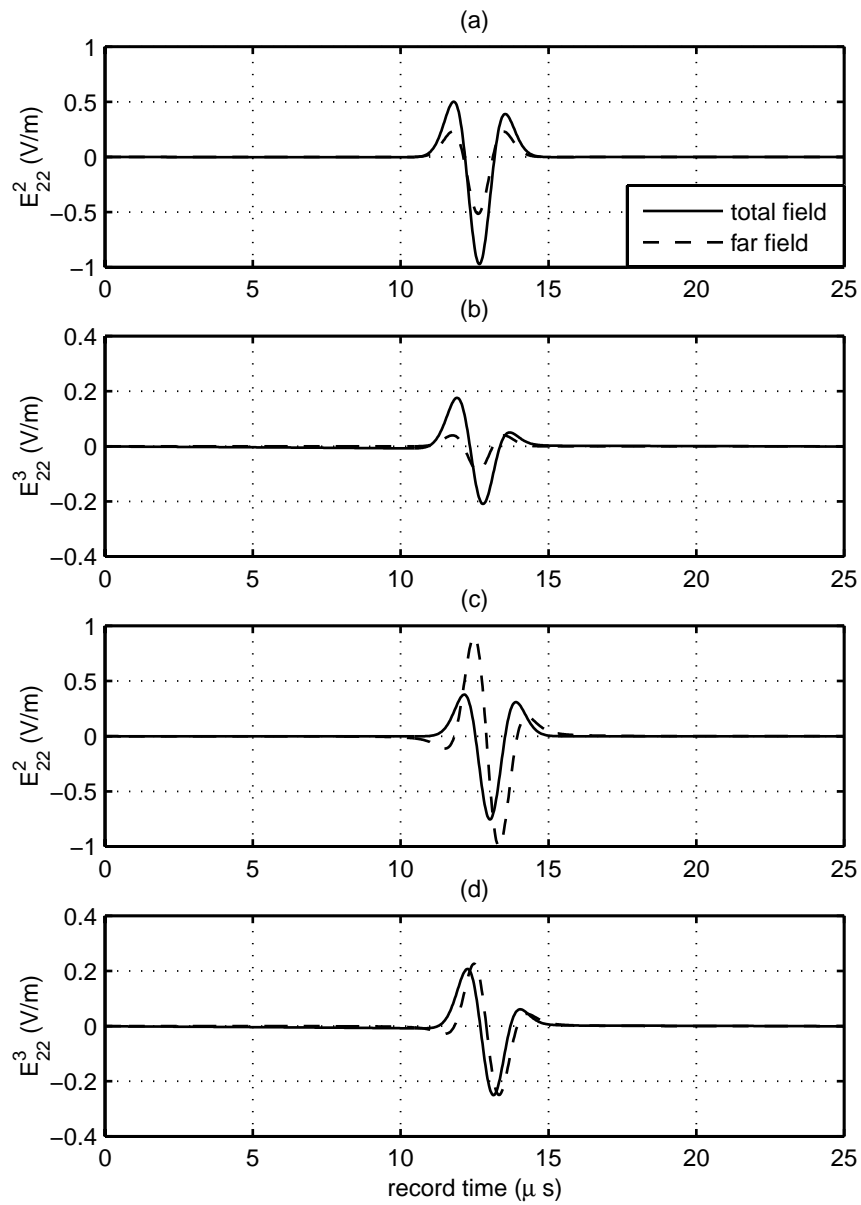


Figure 5.16: Total-field and far-field contribution of the components E_{22}^2 and E_{22}^3 of the scatter source on survey line 2 of a σ -contrast using a parallel-broadside configuration at (a) and (b) position $\mathbf{x}^{M;3}$ and (c) and (d) position $\mathbf{x}^{M;4}$.

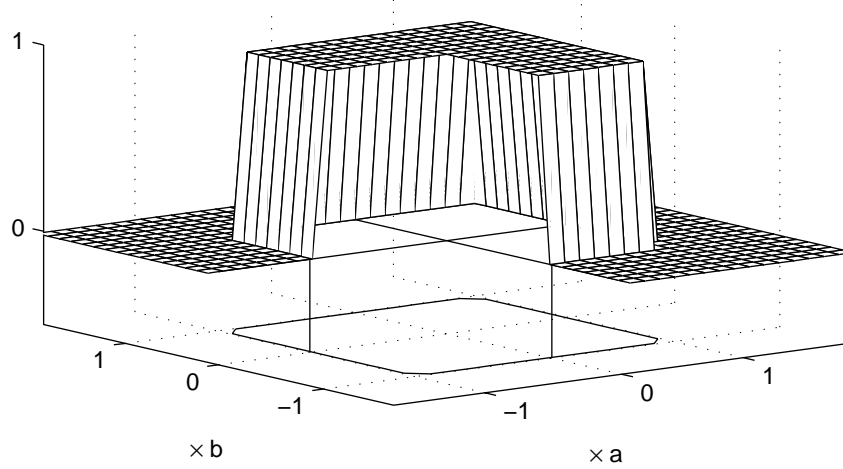


Figure 5.17: Limited region of the acquisition surface.

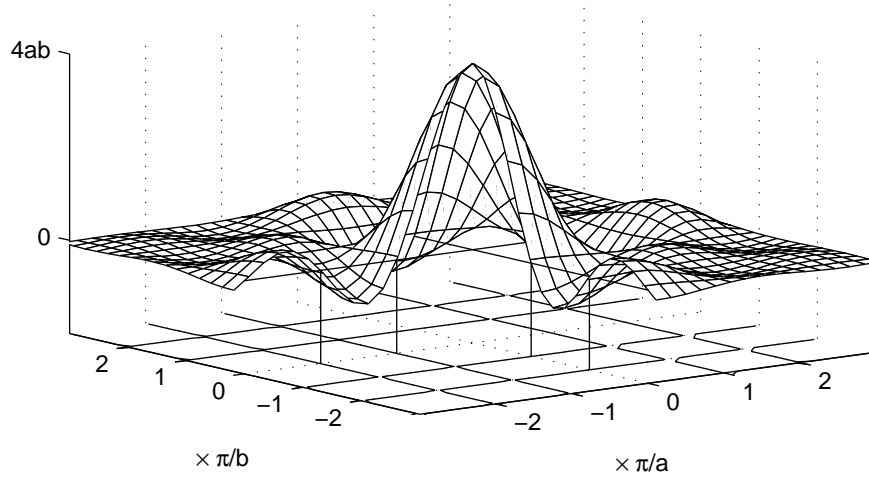


Figure 5.18: Transformation of the limited acquisition surface to the spatial Fourier domain.

differ in amplitude and also in phase and the contribution of scatter source J_3^s is well approximated by the far field.

In Figure 1.3 the reflection of a gaspipe measured by a perpendicular-broad-side configuration is depicted in a grayscale plot. At position 5 the apex of the hyperbola of the gaspipe is present. The correlation of the separate measured reflections on the different positions is evident. At position 8.5 m a near surface diffraction is depicted. It is observed that the correlation of the separate measured reflections at the different positions is not that obvious anymore. This correlation would be impossible when the results were plotted using wiggles. This indicates that for the shallow scatterer the spatial sampling was too sparse. The reflections of the shallow scatterer have a much lower apparent wave speed compared with the reflections coming from the deeper scatterer. For the shallow scatterer, a denser spatial sampling is needed for unaliased recording, compared with the deeper scatterer, as indicated by Eqs. (5.37) and (5.41). Note also that the lower frequency content of the deeper reflection compared with the high frequency content of the shallow scatterer results in a less dense spatial sampling for the deeper scatterer compared with the shallow scatterer (see also Eq. (5.37)).

5.8.4 Measurements on an acquisition surface

Due to the limited nature of the acquisition plane, the spatial bandwidth is limited compared with an infinite acquisition plane. In Section 5.7.4, the resulting bandwidth in spatial Fourier domain is determined using a high frequency approximation. When a square domain of unit amplitude is transformed to the spatial Fourier domain as in Figure 5.17, a sinc-function is obtained in the two directions in the spatial Fourier domain as in Figure 5.18. When a measurement is carried out using a limited acquisition plane, this means that a multiplication is carried out in the space domain, which results in a convolution with a sinc-function in both directions in the spatial Fourier domain. The boundaries of the acquisition plane result in discontinuities in the representation of the measured scattered field in the space domain, resulting in an oscillating nature of the synthesized result in the transformed domain. This oscillating nature can be reduced by tapering the discontinuity. Different tapers will be discussed in Section 6.3.

For a buried point diffractor at $\mathbf{x} = (0, 0, 0.5)$, the scattered field is calculated at intervals of $\Delta x_1^M = \Delta x_2^M = 0.05$ m in both horizontal directions using the far field expressions for an acquisition surface $-1.6 < x_1^M < 1.6$, $-1.6 < x_2^M < 1.6$ m and $x_3^M = 0$ m for a frequency of 500 MHz in a homogeneous

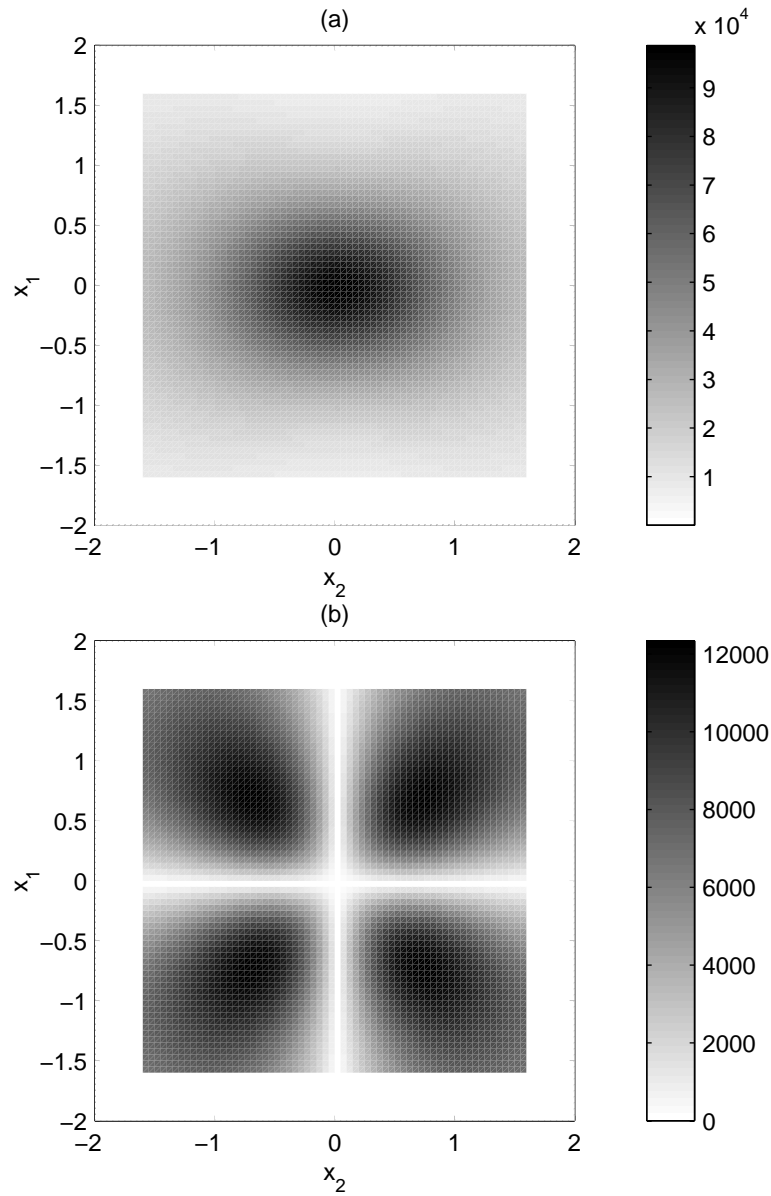


Figure 5.19: Response for $f = 500$ MHz obtained from a buried point scatterer in a homogeneous space on a limited acquisition surface for (a) perpendicular-broadside configuration, \hat{E}_{11} and (b) parallel-perpendicular configuration, \hat{E}_{12} .

space and a homogeneous half-space ($\varepsilon_r = 4$) for a zero-offset source-receiver configuration (see also Figure 5.11).

In Figure 5.19 the measured results of \hat{E}_{11} and \hat{E}_{12} are given for a homogeneous space. The boundary of the acquisition plane can be observed for $\{|x_1|, |x_2|\} = 1.6$. Note that zero's are added in the acquisition plane to prevent circular repetition of the data. Due to the radiation patterns of the source and receiver, more information is obtained for larger $|x_2|$ compared with $|x_1|$ for the perpendicular-broadside configuration, see also Section 4.3.1. The parallel-perpendicular configuration shows a zero for $\{x_1, x_2\} = 0$.

In Figure 5.20 the corresponding spatial bandwidth is displayed for the measurements, which are depicted in Figure 5.19. The boundary between propagating and evanescent waves is indicated by the circle where $k_1^2 + k_2^2 = (2k)^2$ and the maximum spatial bandwidth, which is determined by the limited acquisition plane is indicated by the square where $|k_1| = k^{max}$ and $|k_2| = k^{max}$. The spatial bandwidth for the perpendicular-broadside configuration is limited in the k_1 -direction by the radiation pattern of the source and receiver (see Figure 4.3). The minimum apparent wave speed is given by $c_1^{min} = c_{1;rad} < c_{1;acq}$, while the spatial bandwidth in the k_2 -direction is limited by the limited acquisition plane (k_2^{max}). The minimum apparent wave speed is given by $c_2^{min} = c_{2;acq} < c_{1;rad}$, see Section 5.7.4. For the parallel-perpendicular configuration no information is present for $\{k_1, k_2\} = 0$, which agrees with the results in Figure 5.19. For $k_1 = \pm k_2$ the spatial bandwidth is limited by the boundary between propagating and evanescent waves, while for $\{k_1, k_2\} = 0$ the spatial bandwidth is limited by the radiation pattern of the source and receiver. Note that also the convolutional structure with the sinc functions (see Figure 5.18) is visible in the obtained results.

In Figure 5.21 the measured results of \hat{E}_{11} and \hat{E}_{12} are given for a homogeneous half-space. Again, the boundary of the acquisition plane can be observed for $\{|x_1|, |x_2|\} = 1.6$. Due to the radiation pattern of the source and receiver a maximum occurs at the critical angle for $x_1 = 0$, while a minimum occurs at the critical angle for $x_2 = 0$, see also Section 4.6. The parallel-perpendicular configuration shows again a zero for $\{x_1, x_2\} = 0$. This was already observed at survey line 1 in Figure 5.14.

In Figure 5.22 the corresponding spatial bandwidth is displayed for the measurements depicted in Figure 5.21. The spatial bandwidth for the perpendicular-broadside configuration is limited in the k_1 - and k_2 -direction by the radiation pattern of the source and receiver (see Figures 4.7 and 4.8). The minimum apparent wave speed is given by $c_2^{min} = c_{\beta;rad} < c_{\beta;acq}$, see Section

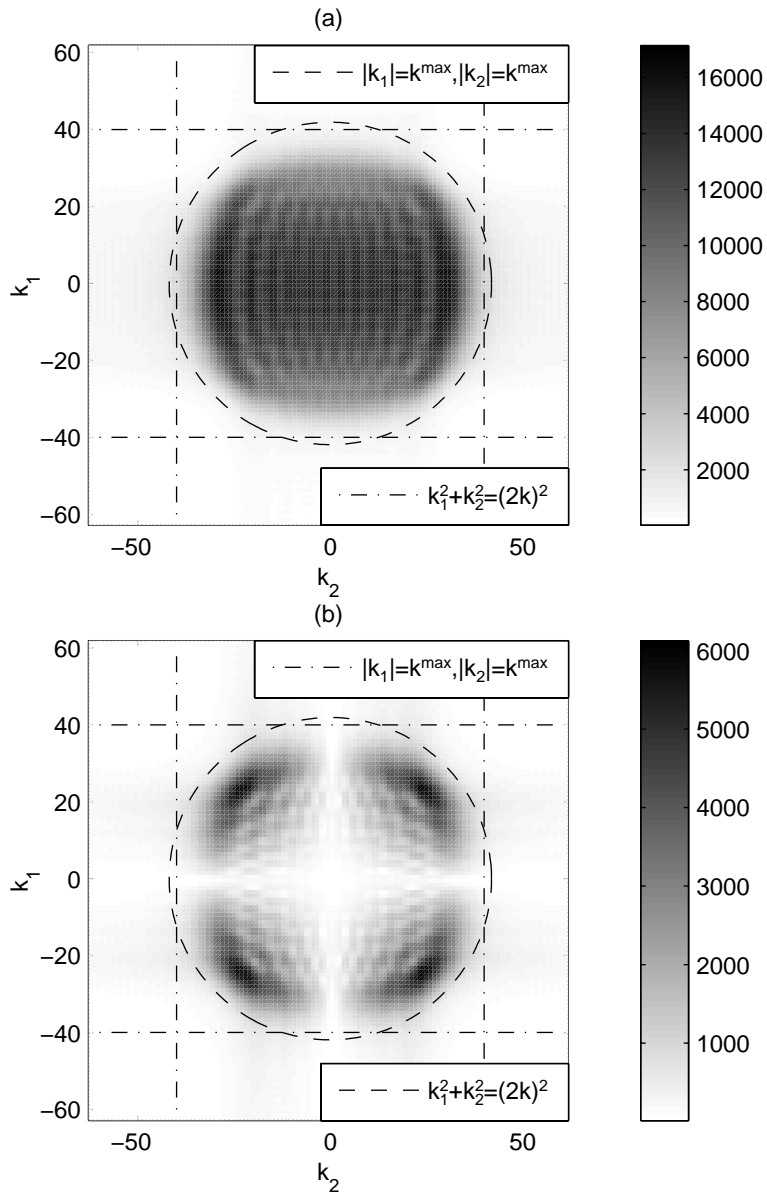


Figure 5.20: Spatial bandwidth for $f = 500$ MHz obtained from a buried point scatterer in a homogeneous space on a limited acquisition surface for (a) perpendicular-broadside configuration, \tilde{E}_{11} and (b) parallel-perpendicular configuration, \tilde{E}_{12} .

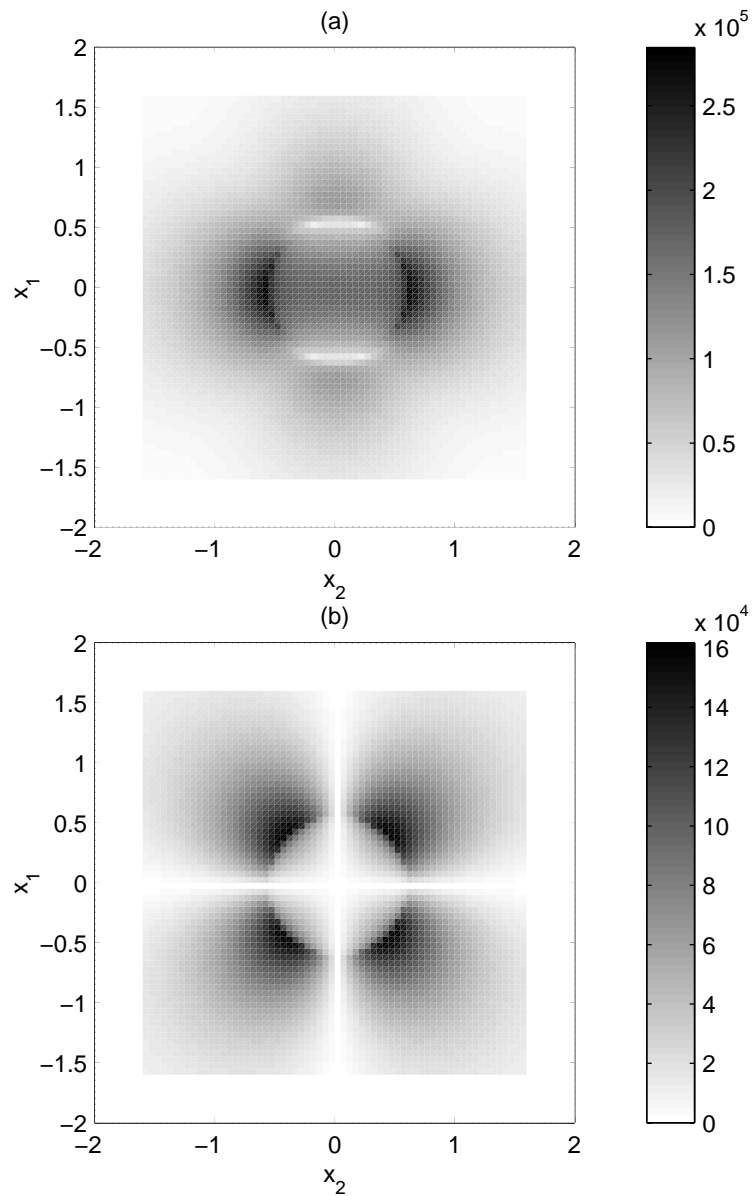


Figure 5.21: Response for $f = 500$ MHz obtained from a buried point scatterer in a homogeneous half-space on a limited acquisition surface for (a) perpendicular-broadside configuration, \hat{E}_{11} and (b) parallel-perpendicular configuration, \hat{E}_{12} .

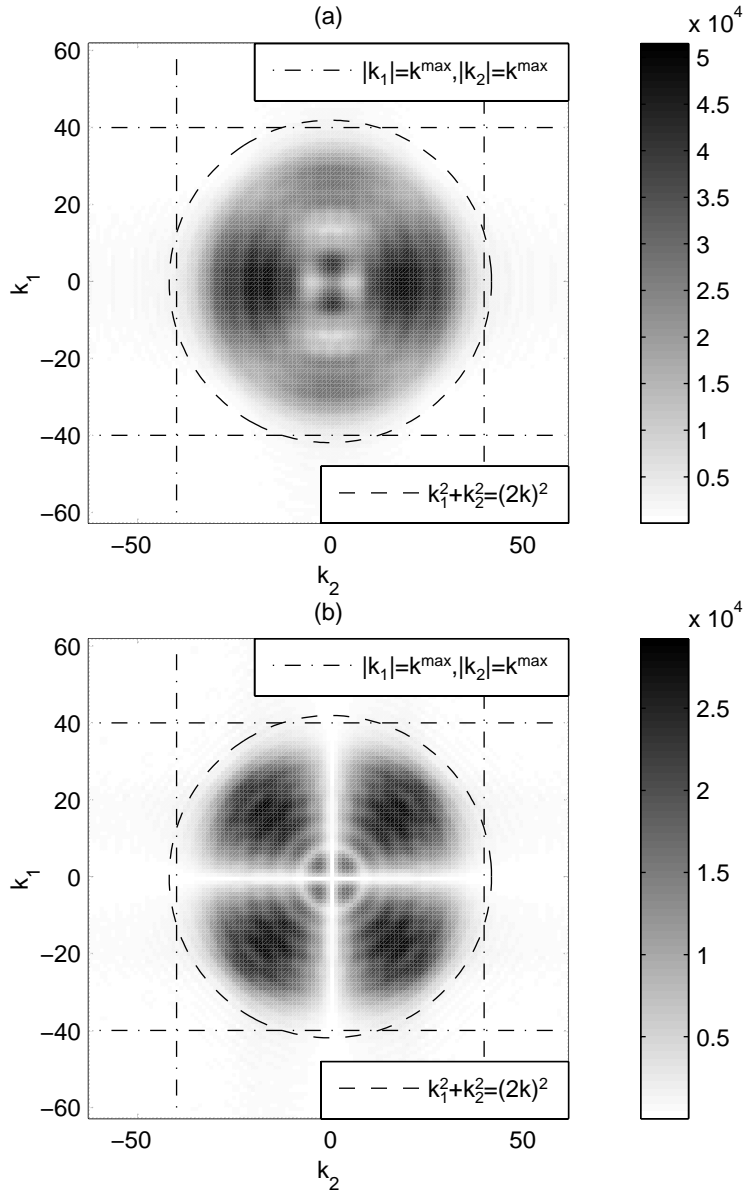


Figure 5.22: Spatial bandwidth for $f = 500$ MHz obtained from a point scatterer in a homogeneous half-space on a limited acquisition surface for (a) perpendicular-broadside configuration, \tilde{E}_{11} and (b) parallel-perpendicular configuration, \tilde{E}_{12} .

5.7.4. For the parallel-perpendicular configuration no information is present for $\{k_1, k_2\} = 0$ which agrees with the results in Figure 5.21. It can be concluded that the high-frequency approximation of the available bandwidth using the apparent wave speed is valid for the used configuration. Note that the scattered electric field is only approximately described by the Born approximation, see also Eqs. (5.23a)-(5.27b). Using the Born approximation and taking into account the proper propagation characteristics of the electric field we are able to map the reflections at the location where they originally came from.

5.9 Reduction of unwanted reflections from above surface objects

During a ground penetrating radar (GPR) survey, special attention must be paid to objects which are present above the earth's surface. As already observed in Figures 4.11 and 4.12, elementary dipole antennas emit electromagnetic waves into the air. When an electrical contrast is present in the air, a reflected wave occurs and can be recorded by the receiver antenna. Due to the low losses in air and the high wave speed, these reflected waves can obscure the data and can make the interpretation of GPR data a difficult task. Especially in an urban area it is important to know the origin of these reflections and how to reduce the influence of these unwanted reflections. In practice, this signal emission into air can be reduced by shielding the antennas. This shielding has proven practical at high frequencies. However, the physical size and portability considerations generally limit the shield effectiveness for low frequencies.

Several publications show how to deal with these unwanted reflections and how to remove them from the data. However, erroneous interpretations are still made, which demonstrates that the recognition of these unwanted reflections is mainly based on experience. A distinction between reflections coming from the subsurface and coming from objects from above the surface can be made using techniques based on the difference in wave speed of the waves coming from above the surface and waves coming from the subsurface. To identify a diffractor present above the surface, like a tree, is quite easy; the reflections will result in a hyperbolic event with a much smaller slope compared with reflections coming from the subsurface. Migration with a wave speed of $c_0 = 0.3$ m/ns will result in the collapse of a hyperbolic event showing that this event was travelling with the wave speed of c_0 . Bano

et al. [1999] applied a filter in amplitude (threshold) to the migrated data to preserve only the large amplitudes of the focused hyperbola. Diffraction of these results with the wave speed of free space resulted in synthetic air diffractions, which were used as a mask to remove the diffractions. Another option to remove reflections of above-surface events is to flatten the scattered event, apply a spatial low-pass filter, subtract and undo the flattening [Sun and Young, 1995]. This algorithm is successfully used by Dunbar et al. [1997] to remove unwanted diffractions from GPR data. More difficult to recognize are reflections coming from larger objects present above the surface parallel to the survey line. These reflections will result in subhorizontal events, which are difficult to identify. For these types of reflection a combined common-offset and common-midpoint analysis has to be carried out. Analysing the move-out in a common-midpoint measurement, allows reflections that have traveled through the air or through the subsurface to be distinguished. First, the results of a field survey are discussed in which reflections from above the surface are present. Subhorizontal events are identified as reflections from above surface objects using a combined common-midpoint and common-offset measurement. Second, the radiation characteristics of a horizontal dipole are investigated to determine the sensitivity for reflections coming from an object which is present above the surface. Both the amplitude and polarisation of the electric field play an important role. It is shown that the presence of the soil leads to relatively strong reflections from vertical objects, which are present in a specific plane relative to the antennas. This analysis indicates that a reduction of the amplitude of unwanted reflections is possible by changing the acquisition parameters. Finally, a validation of these expectations is carried out by numerical modelling using a 3D modelling package for different objects present above the surface, which confirms the former expectations that the amplitude of unwanted reflections can be reduced by choosing a proper orientation of the source and receiver. To prevent erroneous interpretations, the acquisition parameters of a field survey can be altered to reduce the recording of unwanted reflections.

5.9.1 Field survey in Delft

Measurements were carried out in Delft using unshielded (pE100) antennas with a specified center frequency of 200 MHz. The plan view of the location is depicted in Figure 5.23. The wave speed of the electromagnetic waves in the subsurface is $c = 0.08$ m/ns. Several pipes were present in the subsurface, but also some trees were located near the survey line. The measured reflections

are depicted in the common-offset section on the left side in Figure 5.23. Clear hyperbolic features are present in the data. It can be seen that two different hyperbolas are present. The tails of the hyperbolas of which the apices are present at 15 and 30 m are slowly dipping. These small slopes of the tails indicate that the reflected waves have traveled with high speed. Migration with a wave speed of $c_0 = 0.3$ m/ns resulted in a collapsing of the large hyperbolas (the result is not shown). The tails of the small hyperbolas with apices at 22, 29, 33 and 35 m are steeply dipping. These steep slopes indicate that the reflected waves have traveled with a low speed. Hence, by looking at the slopes of the tails of the hyperbolas, the reflections can be identified as coming from the subsurface or coming from above the surface. However, also (sub)-horizontal events are present in the data. To determine the wave speed with which these reflections have travelled, a combined common-offset and common-midpoint (CMP) analysis must be carried out. On the right side of Figure 5.23, the CMP results are depicted. The air and ground wave can be recognised (events 1 and 2). The small move-outs of events 3 and 4 show that these reflections have traveled with a high wave speed from above the surface. In this way, subhorizontal events from a common-offset measurements can be identified as coming from the subsurface or coming from above the surface. Hence, subhorizontal reflections from above surface objects can be identified in a common-offset section by analysing a CMP measurement.

5.9.2 Sensitivity for unwanted reflections from above surface objects

To determine the sensitivity of the measurement to reflections coming from above the surface, the radiation pattern of a horizontal electric dipole is investigated. Most unwanted reflections occur from objects present on the surface. Therefore, the radiated electromagnetic field close to the interface is important to determine the sensitivity for these unwanted reflections.

The amplitude and polarisation of the electric field in a homogeneous space at a distance of 1 meter are plotted in Figures 4.2, 4.3 and 4.4 for \hat{E}_ϕ in the H -plane and \hat{E}_θ and \hat{E}_R in the E -plane, respectively. Both the radiated amplitude and the polarisation are plotted in one figure, which simplifies the analysis of the origin of reflections from above surface objects. In a homogeneous space, a horizontal electric dipole generates a horizontal electric field at the (artificial) interface in the H -plane. The amplitude of the electric far-field in the E -plane has only a radial component at the (artificial) interface, which belongs to the intermediate field and does not contribute to the

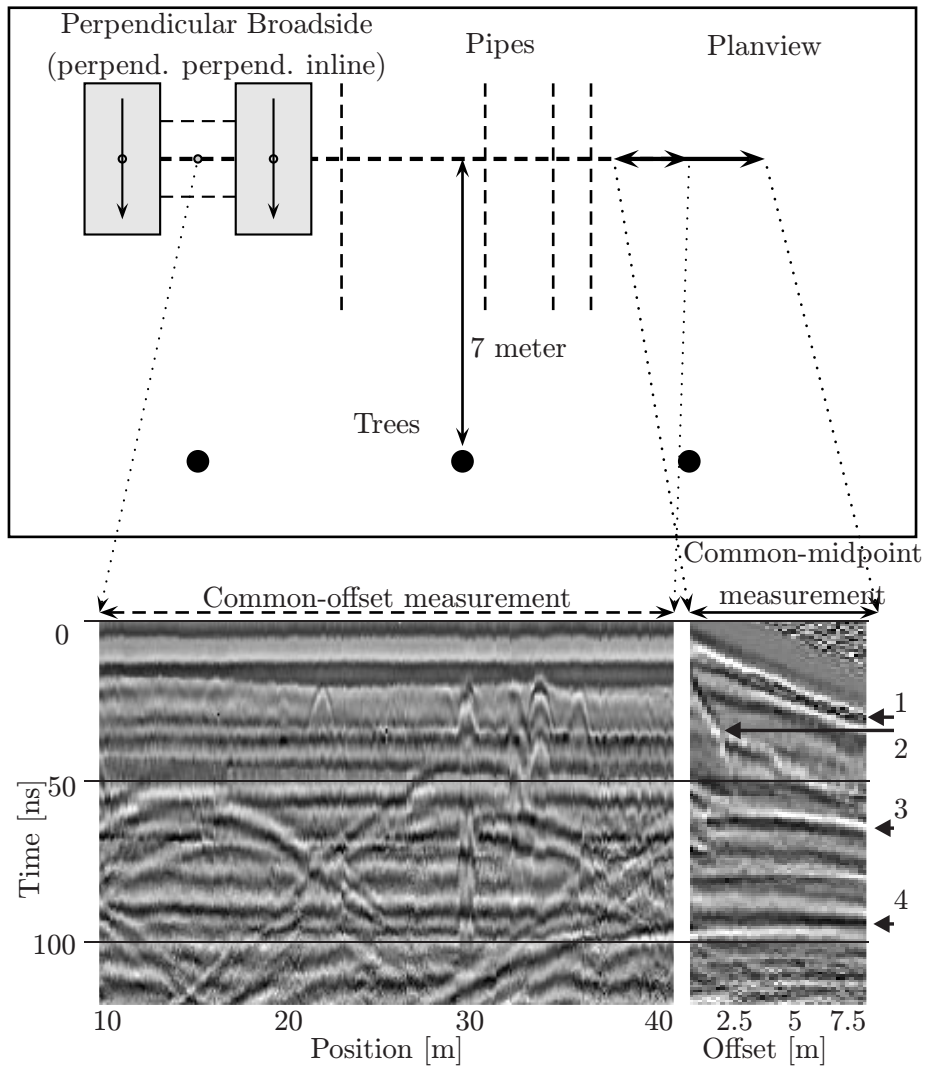


Figure 5.23: Planview of the survey line in Delft with the corresponding common-offset results and the common-midpoint results.

radiated power. The amplitude and polarisation of the electric field in a homogeneous half-space at a distance of 1 meter are plotted in Figures 4.7, 4.8 and 4.9 for \hat{E}_ϕ in the H -plane and \hat{E}_θ and \hat{E}_R in the E -plane, respectively. In the H -plane, a relatively small electric field is present at the interface and in the E -plane near the interface in the upper half-space (air), a relatively large vertical electric field component is present. Note that these results are calculated for a frequency of 500 MHz. For high frequencies, shielding can be effectively applied to reduce the signal emission into air. In Figure 5.24, the total field is depicted for different frequencies at a distance of 2.5 m for a horizontal dipole present on an interface. The amplitudes are normalised with respect to their maximum.

For 50 MHz, the amplitude of the vertical electric field is relatively large compared with the amplitude for 250 MHz. For the H -plane, a horizontal electric field is present near the interface, which is smaller than the vertical electric field in the E -plane. Comparison with the results for a homogeneous space shows that the presence of the soil results in a large vertical polarised electric field close to the interface in the E -plane. When the height of the antennas is increased, it can be expected that the amplitude of the vertical polarised electric field close to the interface in the E -plane will decrease and that the amplitude of the horizontal polarised electric field in the H -plane will increase.

The largest reflections occur when the polarisation of the electric field is parallel to the object causing the reflection, so it can be expected that a vertical object present above the surface, like a tree, will result in a larger unwanted reflection in the E -plane than in the H -plane. Conversely, a horizontal object will result in a larger unwanted reflection in the H -plane than in the E -plane. In conclusion, the radiation patterns indicate the orientation and location of possible unwanted reflections coming from above the surface relative to the antenna orientation. This knowledge can be used to identify unwanted reflectors during the acquisition and to adapt the acquisition parameters to prevent these unwanted reflections.

5.9.3 Numerical modelling of reflections from above surface objects.

A validation of these expectations is carried out by numerical modelling using a three-dimensional modelling package [Remis, 1998]. The relative permittivity of the lower half-space was $\epsilon_r = 6$, the conductivity equals 0.001 S/m and the center frequency of the wavelet is $f_c = 50$ MHz. The spatial discretization in the 3D model is 0.25 m. Three different objects were modelled

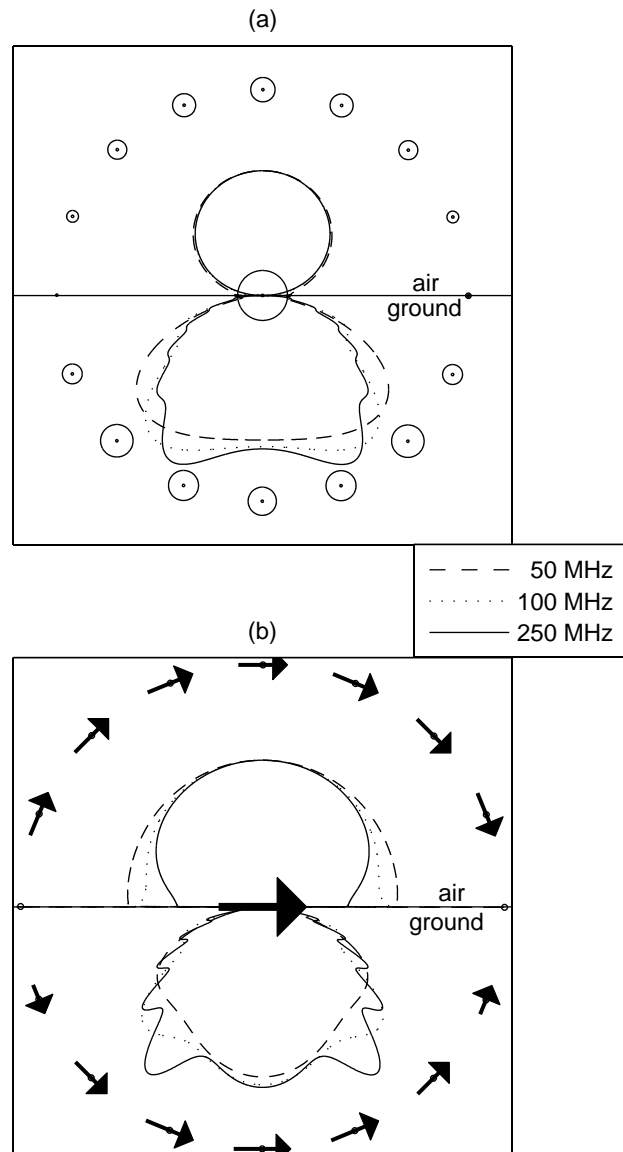


Figure 5.24: Relative amplitudes (lines) of the exact evaluation of the radiation pattern for a horizontal electric dipole present on an interface at a radius of 2.5 m. in (a) the H-plane and (b) the E-plane for different frequencies.

(see Figure 5.25), a vertical plane with a relative permittivity of $\epsilon_r = 40$, representing a wall (a), a horizontal object with a conductivity of $\sigma = 1000$ S/m, representing a wire (b) and a vertical object with a relative permittivity of $\epsilon_r = 40$, representing a tree (c). The measured field is calculated for two different source-receiver configurations; the perpendicular-broadside configuration, where the objects are present in the E -plane of the antennas and the parallel-broadside configuration, where the objects are present in the H -plane of the antennas. The source and receiver are present on the interface. At the location of the object, the electric field is vertically polarised for the perpendicular-broadside configuration and horizontally polarised for the parallel-broadside configuration. When the object is parallel to the polarisation of the electric field, it is expected that the amplitude of the reflection is larger than the reflection when the object is perpendicular to the polarisation of the electric field. We can expect that the wire will give the largest reflection for the parallel-broadside configuration, the tree will give the largest reflection for the perpendicular-broadside configuration and the wall will give the largest reflection for the perpendicular-broadside configuration. The latter can be expected because the amplitude near the interface in the E -plane is larger than the amplitude in the H -plane (see Figure 5.24).

In Figure 5.25(d), the reflections from a wall are depicted for the perpendicular-broadside and parallel-broadside configuration. For the perpendicular-broadside configuration, the measured reflection was 2.7 times larger than the reflection for the parallel-broadside configuration. In Figure 5.25(e) the reflections from a wire are depicted for the perpendicular-broadside and parallel-broadside configuration. For the parallel-broadside configuration, the measured reflection was 5 times larger than the reflection for the perpendicular-broadside configuration. In Figure 5.25(f) the reflections from a tree are depicted for the perpendicular-broadside and parallel-broadside configuration. For the perpendicular-broadside configuration, the measured reflection was 21 times larger than the reflection for the parallel-broadside configuration.

When the height of the antennas above the interface is increased, the measured amplitude for the parallel-broadside configuration increases, while the measured amplitude for the perpendicular-broadside configuration decreases. This indicates that the presence of the soil results in a relatively large vertical polarised vertical electric field close to the interface in the E -plane. This can be understood from the fact that the vertical electric displacement current must be continuous across the air/earth interface causing a jump discontinuity in the vertical electric field strength which then has a relatively high

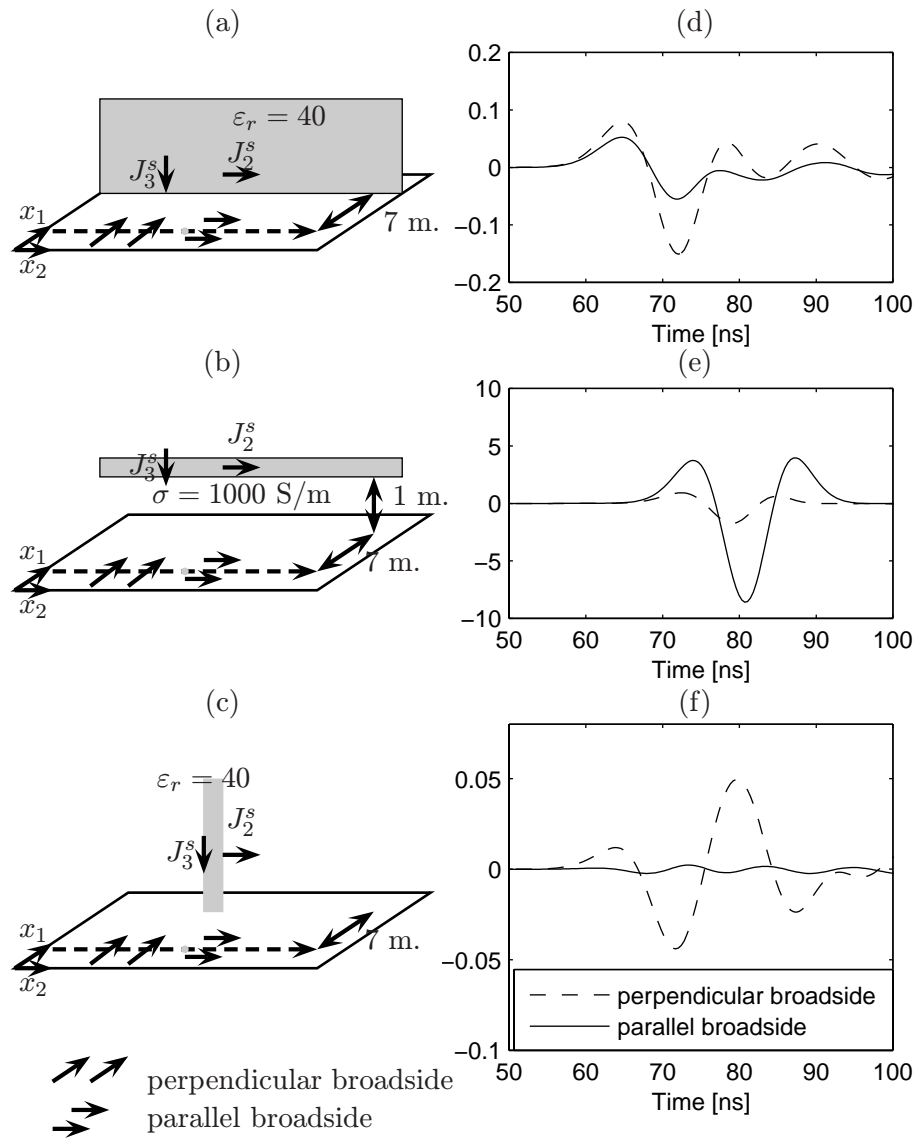


Figure 5.25: Three configurations of above surface objects (a), (b) and (c) and the corresponding calculated reflections (d), (e) and (f), respectively, for the perpendicular- and parallel-broadside configuration

Table 5.1: Influence of top layer soil of 25 cm thickness on the time pulse reflection amplitude from a modelled tree present in the H -plane (perpendicular-broadside configuration) and E -plane (parallel-broadside configuration). The center frequency of the transmitter time pulse is 50 MHz.

Model	Maximum Amplitude		Amplitude Ratio
	H -plane	E -plane	
$\varepsilon_r = 6, \sigma = 10^{-3} \text{ S/m}$	495	24	20.6
$\varepsilon_r = 3, \sigma = 10^{-4} \text{ S/m}$	579	48	12.1
$\varepsilon_r = 6, \sigma = 10^{-3} \text{ S/m}$ $\varepsilon_r = 3, \sigma = 10^{-4} \text{ S/m}$	477	23	20.7
$\varepsilon_r = 3, \sigma = 10^{-4} \text{ S/m}$ $\varepsilon_r = 6, \sigma = 10^{-3} \text{ S/m}$	547	41	13.3

value just above the interface in air. Another aspect of the analysis is to investigate the effect of a thin layer with a different permittivity than the rest of the earth. During dry periods for instance, the upper part of sand will have a low relative permittivity compared with the sand which is present deeper in the subsurface due to the evaporation of pore water in the upper layer. After a shower, the precipitation influences first the upper layer and penetrates deeper into the subsurface, depending on the presence of sand or clay, or remains in the shallow part of the subsurface, respectively. This will cause the upper layer to have a larger relative permittivity than the rest of the earth. For both possible situations, we have modelled the response of a tree in the same acquisition configurations as for the two half-space cases. Now we have a 25 cm thick layer inserted between the two half-spaces, one with a relative permittivity of the thin layer of $\varepsilon_r = 6$, followed by a lower half-space with $\varepsilon_r = 3$ and the second with $\varepsilon_r = 3$, followed by a lower half-space with $\varepsilon_r = 6$. We have summarised the results in Table 5.1, which shows that the influence on the amplitude ratio is limited to the upper part of the subsurface, because the presense of the lower halfspace in the case of a three layer medium does not influence the amplitude ratio. This indicates that the amplitude ratio mainly is determined by the top 25 cm for these examples which have a dominant wavelength of 6 m in air.

5.9.4 Identification and reduction of unwanted reflections from above surface objects

The interpreter of ground penetrating radar (GPR) data should keep in mind that reflections coming from objects above the surface can be present in the data. Horizontal events in GPR data coming from above the surface can be identified using a combined common-offset common-midpoint measurement by analysing the wave speed of the reflection in the common-midpoint measurement.

The radiation characteristics of a horizontal dipole present on a dielectric medium shows the amplitude and the polarisation of the emitted and received electric field and is indispensable for the analysis of the origin of reflections from above surface objects. The largest reflections occur when the polarisation of the electric field is parallel to the object causing the reflection. To reduce the unwanted above surface reflections, the antenna configuration should be chosen such that the emitted electric field is polarised perpendicular to the objects which are present along the survey line; Vertical objects should be present in the H -plane and horizontal objects should be present in the E -plane of the source and receiver antennas to minimize the effect of unwanted reflections in GPR data. Three-dimensional numerical modelling shows that the unwanted reflections from a vertical object (tree) can be reduced by a factor 20 by choosing a proper orientation of the source and receiver antennas.

In reality, the top soil is often different from the soil which is present deeper in the subsurface due to e.g. a dry period or recent precipitation. It can be expected that the presence of a thin top soil will result in different amplitudes of the unwanted reflections. We have simulated two of those situations, a low permittivity thin layer followed by a higher permittivity half-space and vice versa. The simulated results show that the shallow top layer mainly determines the amplitude ratio of the perpendicular-broadside and parallel-broadside configuration.

■

In this chapter, the 3D vectorial scattering formalism of an elementary point scatterer using elementary dipole antennas on the interface of two homogeneous half-spaces is discussed. Several independent point scatterers are considered to represent a bounded contrasting domain. The appropriate acquisition set-up for a three-dimensional survey is analysed by discussing the

temporal and spatial sampling criteria and the possible polarisation of the source and receiver. Synthetic data are presented, which clearly reflect the influence of the polarisation and the amplitude characteristics of the source and receiver. Together with the orientation of the scatterer, a qualitative indication of the sensitivity for reflections is obtained by analysing the radiation characteristics and the vectorial scattering formalism. These results show how to increase the sensitivity for wanted reflections. On the other hand, these results also show how to reduce the measurement of unwanted reflections from objects on or above the surface. The scattering formalism will serve as a starting point to derive the three-dimensional imaging algorithm, which is derived in Chapter 6.

Three-Dimensional Multi-Component Imaging

Three-dimensional imaging of ground penetrating radar data is a challenging task. Most imaging procedures are based on scalar algorithms such as the Synthetic Aperture Radar (SAR) [Curlander and McDonough, 1991] and the Gazdag phase shift [Gazdag, 1978] methods. The three important parameters, which are needed to obtain a good image of the subsurface are, in order of importance, the wave speed, the polarisation and the amplitude, which shows that for electromagnetic imaging the vectorial character of the emitted field and the radiation characteristics of the source and the receiver play an important role. Based on the vectorial scattering formalism as given in Chapter 5, algorithms are derived for the three-dimensional imaging of GPR data. The objective is to obtain an imaging algorithm, which takes into account the vectorial character of the electromagnetic waves and the radiation characteristics of the source and receiver antennas. This leads to a new multi-component imaging algorithm, which is dedicated to the electromagnetic case. The performances of the scalar imaging algorithms and the multi-component imaging algorithm are investigated by imaging a point scatterer present in a homogeneous space and in a homogeneous halfspace for one single frequency, which results in a resolution function.

6.1 Introduction

For seismic exploration, extensive research is carried out to image seismic data. The migration technique for imaging of seismic data was originally developed by Haagedoorn [1954]. In a literal sense, migration is the transformation of a reflection location, found by vertical plotting of the measured reflections at each position as a function of time in the data domain, to the true reflection location in depth in the image domain. This can be carried out by determining the surfaces of equal reflection times in the data domain, belonging to each location in the image domain. For the wavefield measured along a line, which is scattered by a point scatterer, a hyperbolic event is obtained when the measured data are plotted for each position as function of time (see also Figure 1.3). An appropriate transformation of these measurements will yield an energy concentration at the location of the apex of the hyperbola in the image domain. A possible transformation, which is only based on geometrical considerations, consists of a summation of all values of each separate trace at the point where it intersects a semi-hyperbola. The resulting amplitude is placed at the apex of the semi-hyperbola in the image domain. In this way, all in-phase field values add in phase whereas noncoherent field values are usually out of phase and tend to zero. The only parameter which has to be known, to realise this transformation, is the wave speed. The SAR algorithm, for example, is based on geometrical considerations and transforms reflections to the true reflection position. In non-destructive testing applications, these (time domain) backpropagation schemes (SAR) are well-known under the acronym SAFT, which stands for Synthetic Aperture Focussing Technique [see Herman et al., 1987]. Note that this approach assumes equal phase characteristics for the measured reflections which are present on the semi-hyperbola. The vectorial character of the measured electric wavefield shows that this assumption is not valid for the electromagnetic case (see e.g. Figure 5.14b).

Commonly used imaging strategies for GPR data used in the literature are similar to the (scalar) seismic processing algorithms. A tutorial paper by Berkhout [1981] mentions that three methods of wavefield extrapolation, which describe the propagation effects of the wavefield, are commonly used in seismics, i.e., the Kirchhoff-summation approach [Schneider, 1978], the plane-wave method (k - f method) described by Gazdag [1978], and the finite-difference technique. The forward and inverse wavefield extrapolation of single- and multi-component seismic data is discussed by Wapenaar and Berkhout [1989]. The presence of the source and receivers away from the in-

interface, cause effects which can be severe and degrades the quality of seismic prospecting. To remove these effects a decomposition of up- and downgoing waves has to be carried out [van Borselen, 1995]. Recently, more and more multi-component seismic experiments are being carried out. When multi-component seismic data are acquired, the upgoing and downgoing P- and S-waves must be separated [Dankbaar, 1985; Wapenaar et al., 1990; Amundsen and Reitan, 1995; Schalkwijk et al., 1998]. The decomposition of up- and down-going waves can only be carried out because a number of sources and a number of receivers are used, also called multi-offset measurements. A prestack multi-component elastic migration algorithm is discussed by Zhe and Greenhalgh [1997]. The potential of multi-component seismology is shown by Shuck et al. [1996].

Whereas for a seismic survey multi-offset measurements are used, a GPR survey is usually carried out with one source and one receiver at a fixed distance, also called a common-offset measurement. In the case of a GPR measurement, the source and receiver are present on the interface between air and ground. The assumption of a simple background model makes the decomposition of upgoing and downgoing electromagnetic waves superfluous and is not required as a preprocessing step before the actual imaging procedure. Note that when a decomposition of upgoing and downgoing electromagnetic waves is required multi-offset measurements of multi-component measurements are needed [van der Kruk, 1993].

Numerous algorithms are used to image GPR data [e.g. Mast and Johansson, 1994; Johansson and Mast, 1994; Grasmueck, 1996; Binningsbø et al., 2000; Lopez-Sanchez and Fortuny-Guasch, 2000]. Recently, the radiation characteristics of elementary GPR antennas for GPR data imaging have been taken into account. Moran et al. [2000] used a modified Kirchhoff integral by inclusion of a half-space interfacial radiation pattern. Lehmann et al. [2000] combined coincidental georadar data sets with two pairs of parallel source-receiver antennas, one oriented perpendicular to the other to obtain a "pseudo scalar" wavefield. Next, this pseudo scalar wavefield was imaged using a standard 3D Kirchhoff time-migration scheme. Van Gestel and Stoffa [2000] modified a regular Kirchhoff migration by limiting the migration to those paths that are within the predicted angle of orientation. However, all these algorithms were still adapted from scalar imaging algorithms and use the knowledge of the radiation characteristics of elementary GPR antennas heuristically to obtain a better image. Wang and Oristaglio [2000] derived a vectorial GPR imaging algorithm using the generalized Radon transform. However, the am-

plitude characteristics are approximated in the forward model, which is used to obtain an imaging operator.

We will discuss two of the scalar imaging algorithms; the SAR imaging algorithm and the Gazdag phase shift method. These will be compared with the multi-component imaging algorithm, derived later in this chapter. Note that the SAR and Gazdag imaging algorithms are based on the scalar scattering representation. It is obvious that for the imaging of GPR data, the obtained image can be improved by taking into account the polarisation of the emitted and measured wavefield and the radiation characteristics of the source and receiver.

An imaging algorithm basically consists of two steps; the first step corrects for propagation effects for each separate frequency component (inverse wavefield extrapolation). The second step involves a time zero selection for each position, which is carried out by adding all (positive and negative) frequencies. This operation is known as the imaging principle [Claerbout, 1971]. For all discussed migration algorithms, the imaging principle is equivalent. The discussion of the inverse wavefield extrapolators is thus our main concern. To investigate the performance of scalar inverse extrapolators and to derive systematically a bounded inverse extrapolator dedicated to the electromagnetic case, we first discuss the forward wavefield extrapolation.

6.2 Two-way wavefield extrapolator

We start by repeating the linearised expression for the scattering representation, which is given by Eq. (5.34),

$$\hat{E}_{\alpha\beta}(\mathbf{x}^M, \mathbf{x}^H, \omega) = \hat{S}^J(\omega) \int_{\mathbf{x}^c \in \mathbb{D}^s} \bar{\chi}^{\hat{\eta}}(\mathbf{x}^c) \hat{G}_{\alpha r}^{\text{EJ}}(\mathbf{x}^M + \mathbf{x}^H - \mathbf{x}^c, \omega) \times \hat{G}_{\beta r}^{\text{EJ}}(\mathbf{x}^M - \mathbf{x}^H - \mathbf{x}^c, \omega) dV. \quad (6.1)$$

It is convenient to combine the propagation of the vector electric field from the source towards the scatterer and from the scatterer back to the receiver by introducing the wavefield extrapolator $\hat{D}_{\alpha\beta}$, which describes the inner product between the two Green's functions. Eq. (6.1) can be written as

$$\hat{E}_{\alpha\beta}(\mathbf{x}^M, \mathbf{x}^H, \omega) = \hat{S}^J(\omega) \int_{\mathbf{x}^c \in \mathbb{D}^s} \bar{\chi}^{\hat{\eta}}(\mathbf{x}^c) \hat{D}_{\alpha\beta}(\mathbf{x}^M, \mathbf{x}^H | \mathbf{x}^c, \omega) dV, \quad (6.2)$$

where the wavefield extrapolator $\hat{D}_{\alpha\beta}$ is given by

$$\hat{D}_{\alpha\beta}(\mathbf{x}^M, \mathbf{x}^H | \mathbf{x}^c, \omega) = \hat{G}_{\alpha r}^{\text{EJ}}(\mathbf{x}^M + \mathbf{x}^H - \mathbf{x}^c, \omega) \hat{G}_{\beta r}^{\text{EJ}}(\mathbf{x}^M - \mathbf{x}^H - \mathbf{x}^c, \omega). \quad (6.3)$$

The wavefield extrapolator $\hat{D}_{\alpha\beta}$ will be denoted as the two-way wavefield extrapolator. It describes the inner product of the Green's function accounting for the downward propagation from the source towards the scatterer and the Green's function taking care for the upward propagation from scatterer towards receiver. This nomenclature must not be confused with the two-way wave equations, which are used by Berkhout and Wapenaar [1989], and also describes possible multiples which are present in a layered medium.

To make an analytical discussion possible, we will first determine the forward wavefield extrapolators in a homogeneous space for a zero-offset configuration, $\mathbf{x}^H = 0$ and $\mathbf{x}^S = \mathbf{x}^R = \mathbf{x}^M$. Furthermore, we require that the measurements are carried out for $x_3^M = 0$. For a homogeneous space, we repeat the expressions for $\hat{G}_{kr}^{\text{EJ}}(\mathbf{x}, \omega)$ given in Eqs. (4.13) and (4.16a),

$$\hat{G}_{kr}^{\text{EJ}}(\mathbf{x}, \omega) = \hat{\eta}^{-1}[\partial_k \partial_r + k^2 \delta_{kr}] \hat{G}(R, \omega), \quad (6.4a)$$

$$\hat{G}(R, \omega) = \frac{\exp(-jkR)}{4\pi R}, \quad (6.4b)$$

$$R = |\mathbf{x}|, \quad (6.4c)$$

where $k = \omega/c$. It is convenient to rewrite the two-way wavefield extrapolator for zero-offset, which is given by $\hat{D}_{\alpha\beta}(\mathbf{x}^M, \mathbf{0}|\mathbf{x}^c, \omega) = \hat{D}_{\alpha\beta}(\mathbf{x}^M - \mathbf{x}^c, \omega)$, by separating the phase delay and the corresponding amplitude factor as

$$\hat{D}_{\alpha\beta}(\mathbf{x}^M - \mathbf{x}^c, \omega) = \hat{G}_{\alpha r}^{\text{EJ}}(\mathbf{x}^M - \mathbf{x}^c, \omega) \hat{G}_{\beta r}^{\text{EJ}}(\mathbf{x}^M - \mathbf{x}^c, \omega), \quad (6.5)$$

$$= \hat{A}_{\alpha\beta}(\mathbf{x}^M - \mathbf{x}^c, \omega) \exp(-2jk|\mathbf{x}^M - \mathbf{x}^c|). \quad (6.6)$$

Because the wavefield extrapolator in Eq. (6.6) is derived for a zero-offset measurement, a factor of 2 occurs in the two-way phase delay, $\exp(-2jkR)$, which indicates that the wavefield has traveled twice along the same path. The separate elements of $\hat{A}_{\alpha\beta}$ in Eq. (6.6) are evaluated for the far-field contributions using Eqs. (6.4a)-(6.4c) and can be written as

$$\hat{A}_{11}(\mathbf{x}, \omega) = \frac{R^2 - x_1^2}{R^4} C(\omega), \quad (6.7a)$$

$$\hat{A}_{12}(\mathbf{x}, \omega) = -\frac{x_1 x_2}{R^4} C(\omega), \quad (6.7b)$$

$$\hat{A}_{21}(\mathbf{x}, \omega) = -\frac{x_1 x_2}{R^4} C(\omega), \quad (6.7c)$$

$$\hat{A}_{22}(\mathbf{x}, \omega) = \frac{R^2 - x_2^2}{R^4} C(\omega), \quad (6.7d)$$

where

$$C(\omega) = \frac{k^4}{\eta^2(4\pi)^2}. \quad (6.8)$$

The zero-offset assumption in a homogeneous space enables a thorough analytical discussion of the performance of the different inverse wavefield extrapolators. In the following sections, the zero-offset assumption will hold.

6.3 Wavefield extrapolator in horizontal spatial Fourier domain

To determine the inverse wavefield extrapolator in the horizontal spatial Fourier domain, the horizontal spatial Fourier transformation (see Eq. (2.19)) of $\hat{D}_{\alpha\beta}$ must be carried out, yielding

$$\tilde{D}_{\alpha\beta}(k_1, k_2, x_3, \omega) = \int_{(x_1, x_2) \in \mathbb{R}^2} \hat{D}_{\alpha\beta}(\mathbf{x}, \omega) \exp[j(k_1 x_1 + k_2 x_2)] dA. \quad (6.9)$$

To continue the analytical discussion in the horizontal spatial Fourier domain, the method of stationary phase for the evaluation of both integrals is used to obtain closed-form expressions in the spatial Fourier domain. Using Eq. (6.6) we can rewrite Eq. (6.9) as

$$\tilde{D}_{\alpha\beta}(k_1, k_2, x_3, \omega) = \int_{(x_1, x_2) \in \mathbb{R}^2} \hat{A}_{\alpha\beta}(\mathbf{x}, \omega) \exp\left[\frac{j\omega\phi(\mathbf{x})}{c}\right] dA, \quad (6.10)$$

where the phase of the exponential term is given by

$$\phi(\mathbf{x}) = -2R(\mathbf{x}) + \frac{k_1}{k}x_1 + \frac{k_2}{k}x_2. \quad (6.11)$$

Using the method of stationary phase, derived in Appendix A, Eq. (6.10) can be approximated for large ω [see Felsen and Marcuvitz, 1973; Bleistein, 1984]. Using this stationary phase approximation the expression for $\tilde{D}_{\alpha\beta}(k_1, k_2, x_3, \omega)$ is obtained as

$$\tilde{D}_{\alpha\beta}(k_1, k_2, x_3, \omega) = \tilde{d}_{\alpha\beta} \exp(-jk_3|x_3|), \quad (6.12)$$

where k_3 is given by

$$k_3 = \begin{cases} \sqrt{4k^2 - k_1^2 - k_2^2}, & \text{for } k_1^2 + k_2^2 \leq 4k^2, \\ -j\sqrt{k_1^2 + k_2^2 - 4k^2}, & \text{for } k_1^2 + k_2^2 > 4k^2, \end{cases} \quad (6.13)$$

and

$$\tilde{d}_{11}(k_1, k_2, x_3, \omega) = -\frac{2\pi j C(\omega)}{(2k)^3 |x_3|} [(2k)^2 - k_1^2], \quad (6.14a)$$

$$\tilde{d}_{12}(k_1, k_2, x_3, \omega) = \frac{2\pi j C(\omega)}{(2k)^3 |x_3|} k_1 k_2, \quad (6.14b)$$

$$\tilde{d}_{21}(k_1, k_2, x_3, \omega) = \frac{2\pi j C(\omega)}{(2k)^3 |x_3|} k_1 k_2, \quad (6.14c)$$

$$\tilde{d}_{22}(k_1, k_2, x_3, \omega) = -\frac{2\pi j C(\omega)}{(2k)^3 |x_3|} [(2k)^2 - k_2^2]. \quad (6.14d)$$

Note that the amplitude of $\tilde{D}_{11}(k_1, k_2, x_3, \omega)$ is constant for fixed k_1 , and that the amplitude of $\tilde{D}_{22}(k_1, k_2, x_3, \omega)$ is constant for fixed k_2 . This is equivalent for the results in the space domain observed in Section 6.2. Note that the spatial bandwidth in the spatial Fourier domain, which has been observed in Figure 5.20 for the measurement of a buried point scatterer, can be obtained by analysing Eqs. (6.12)-(6.14d). It is important to know the available spatial bandwidth in the spatial Fourier domain as is discussed in Section 5.7.4 for optimal usage of the available information in the imaging algorithm.

In Figures 6.1 and 6.2, the two-way wavefield operators derived using the stationary phase approximation, indicated with SPA(D), are compared with the numerically calculated two-way wavefield operator, indicated with FFT(D). To prevent oscillations in the transformed domain, as already discussed in Section 5.8.4, these numerical results are tapered in the original domain. Different tapers are used, linear filters indicated with 0 and 0.1 (the length of the taper relative to the length of the acquisition plane) and a cosine filter, indicated with cos (equivalent with a cos taper over the acquisition domain). It can be observed that for $k_2 = 0$, the stationary phase approximation for $\tilde{D}_{11}(k_1, 0, x_3)$ is quite good, while for $k_1 = 0$ the approximation is less accurate. This is mainly caused by the fact that the stationary phase approximation is derived for an infinite acquisition plane, which is not valid in this case.

6.4 Scalar inverse wavefield extrapolators

In this section, several scalar inverse wavefield extrapolators are discussed. The symbol \hat{H} is used to describe the different inverse wavefield extrapolators. We limit the number of extrapolators by only discussing imaging algorithms defined in the space-frequency or the spatial Fourier (wavenumber-frequency)

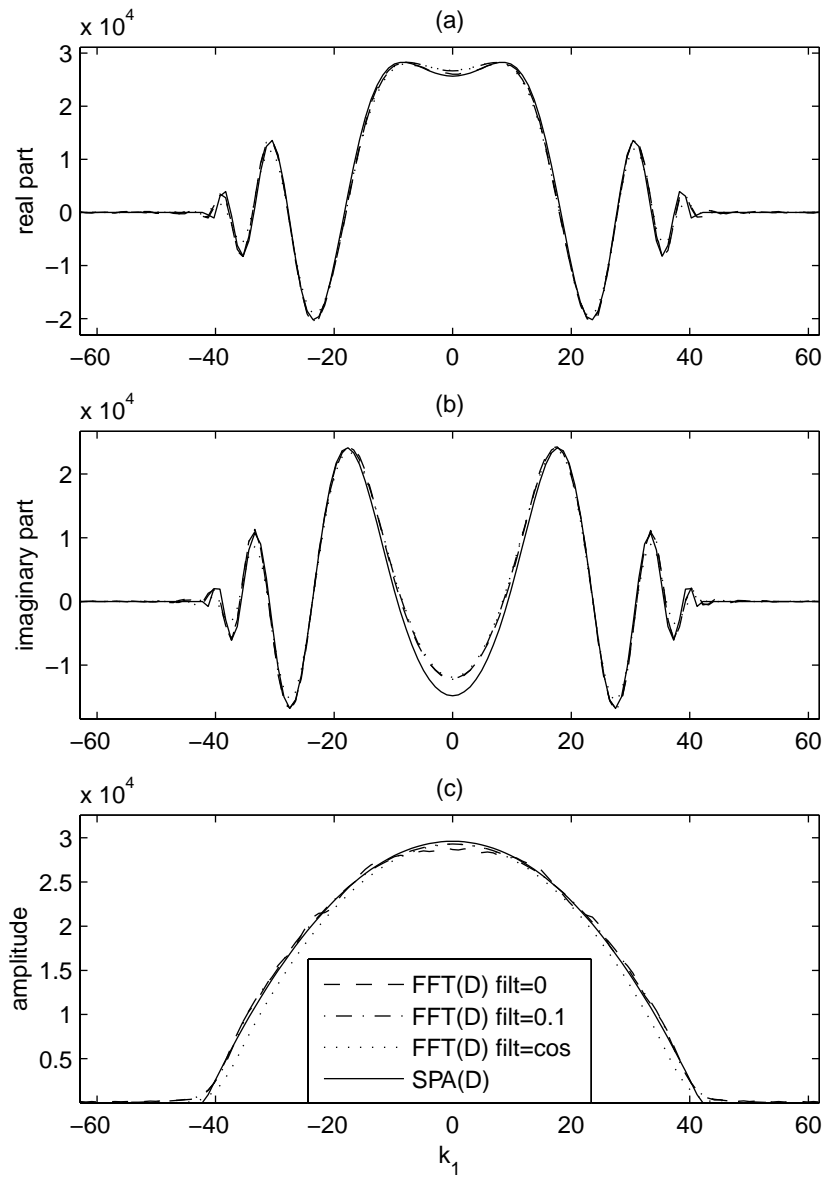


Figure 6.1: Real part (a), Imaginary part (b) and Amplitude (c) of the forward wavefield extrapolator for $k_2 = 0$.

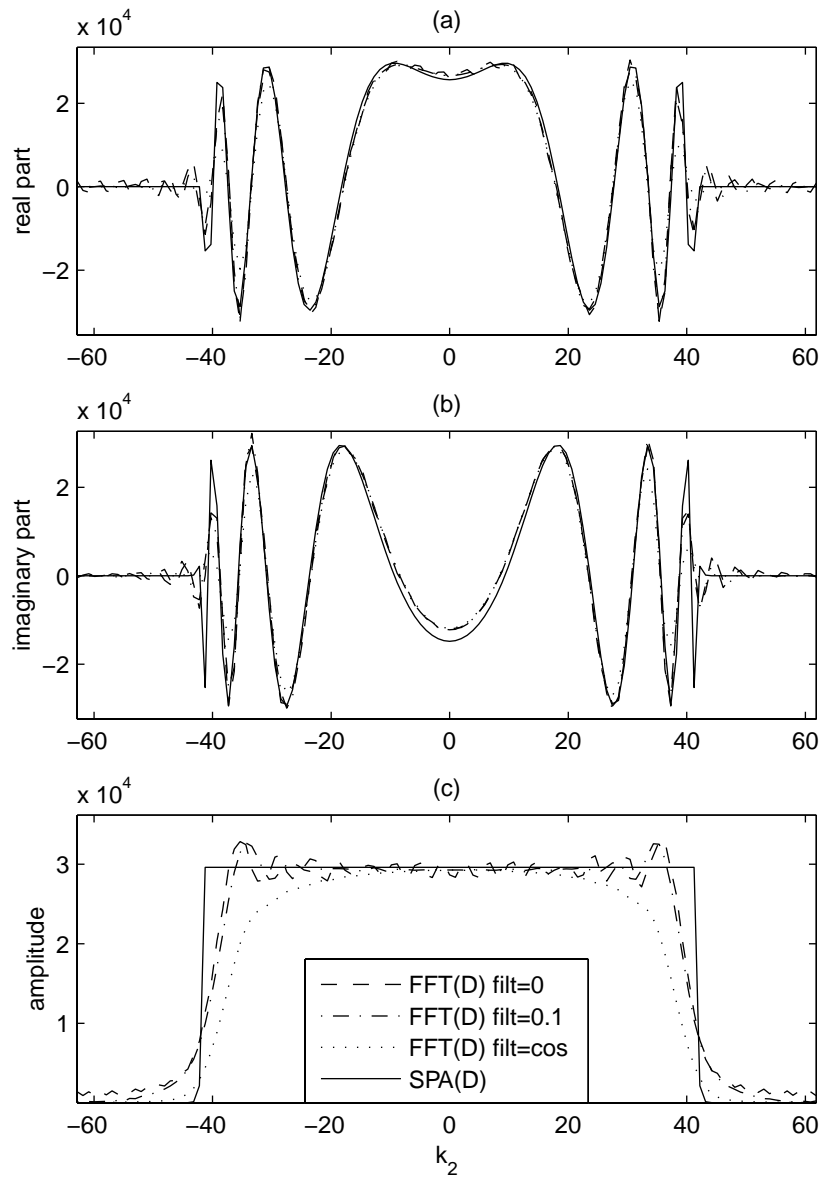


Figure 6.2: Real part (a), Imaginary part (b) and Amplitude (c) of the forward wavefield extrapolator for $k_1 = 0$.

domain. In Section 4.3.1 and 4.4, the propagation of the wavefield in the space-frequency domain is described by an amplitude factor times a phase shift in a homogeneous space and in two homogeneous half-spaces. In Section 4.2.1 and 4.2.2, the propagation of the wavefield in the spatial Fourier domain is also described by an amplitude factor times a phase shift in a homogeneous space and in two homogeneous half-spaces, respectively. For a zero-offset measurement, the scattered field can be expressed as an amplitude factor and a different phase shift in both the space-frequency and spatial-Fourier domain as in Eqs. (6.6) and (6.12)-(6.14d), respectively. The difference between the phase shifts which describe the one-way propagation of the electric field and the zero-offset two-way wavefield extrapolator is a substitution of $k \rightarrow 2k$, which is equivalent to the substitution of $c \rightarrow c/2$. Note that there is not such a simple relation between the amplitude factors of the one way propagation of the electric field and the two-way wavefield extrapolator.

The phase shift of the two-way forward wavefield extrapolator in the space-frequency domain as given in Eq. (6.6) yields

$$\exp(-2jkR) \quad (6.15)$$

and the phase shift of the two-way forward wavefield extrapolator in the spatial Fourier domain as given in Eq. (6.12) yields

$$\exp(-jk_3|x_3|), \quad (6.16)$$

where Eq. (6.13) indicates the region of the propagating waves and evanescent waves. It will be shown that the basis of conventional inverse wavefield extrapolators is to correct for the phase shift in either the space-frequency or horizontal Fourier domain.

In the following subsections, the commonly used scalar inverse wavefield extrapolators, the Gazdag phase shift and the Synthetic Aperture Radar (SAR) algorithm, are discussed. These methods of migration are discussed from a more physical point of view by Yilmaz [1987]. Using the stationary phase approximation, equivalent expressions in the space-frequency domain and the horizontal Fourier domain can be obtained for the Gazdag and SAR algorithms, which are originally defined in the horizontal Fourier domain and the space-frequency domain, respectively. This enables a comparison of the two inverse wavefield extrapolators. These inverse wavefield extrapolators do not consider the vector character of the measured scattered wavefield. An approximate inverse wavefield extrapolator is derived for the separate components of the 3D wavefield extrapolator, which takes into account the vectorial character of the measured scattered wavefield.

6.4.1 Gazdag Phase shift extrapolator

Stolt [1978] introduced the Fourier transform methods in seismic migration. A simple mapping from temporal frequency ω to vertical wavenumber k_3 involves interpolation for the required data samples. Gazdag [1978] published his work on the phase-shift method, which led to a further understanding of wavefield extrapolation in the transform domain. Since then, several names were introduced for the Gazdag phase shift method. Some of them are: backpropagation imaging, plane wave method or frequency wavenumber migration¹. Schneider [1978] showed that the Kirchhoff integral extrapolator, which is defined in the space-time domain, is similar to the Gazdag phase shift extrapolator, which is defined in the horizontal Fourier domain for a specific combination of source and receiver types in the acoustic case. The Gazdag phase-shift is commonly used in combination with the exploding reflector assumption, which does not account correctly for geometrical spreading. The inverse wavefield extrapolator, which forms the basis of Gazdag phase-shift imaging, [see Eq. (45) of Gazdag, 1978], is defined in the horizontal Fourier domain and is an approximate inverse of the phase shift given in Eq. (6.16). To obtain a bounded inverse wavefield extrapolator, the complex conjugate of the vertical wavenumber is taken. In reality, this means that only the propagating wave region is used. The Gazdag inverse wavefield extrapolator is given by

$$\tilde{H}^{gd}(k_1, k_2, x_3, \omega) = \exp(jk_3^*|x_3|). \quad (6.17)$$

Note, that within the propagating wave region the amplitude of the inverse wavefield extrapolator given in Eq. (6.17) is unity. Using the stationary phase approximation in Appendix A, the expression for this operator in the space domain is obtained as

$$\hat{H}^{gd}(\mathbf{x}, \omega) = \frac{-jk|x_3|}{\pi R^2} \exp(2jkR). \quad (6.18)$$

6.4.2 Synthetic Aperture Radar imaging

Synthetic Aperture Radar (SAR) imaging was originally developed for remote sensing [Curlander and McDonough, 1991]. This process is in many ways similar to the problem of seismic imaging of the earth's interior and is essentially a ray-tracing algorithm. In seismics, this imaging algorithm is

¹also known as k - f migration, in this case we should actually speak of $k_1 k_2 \omega$ -migration

known as diffraction summation migration. The inverse wavefield extrapolator for the SAR imaging algorithm is defined in the space domain and is the inverse of the phase shift given in Eq. (6.15)

$$\hat{H}^{sar}(\mathbf{x}, \omega) = \exp(2jkR). \quad (6.19)$$

The equivalent of Eq. (6.19) in the spatial Fourier domain is obtained by using the stationary phase approximation and is given by

$$\tilde{H}^{sar}(k_1, k_2, x_3, \omega) = \tilde{h}^{sar}(k_1, k_2, x_3, \omega) \exp(jk_3^*|x_3|), \quad (6.20)$$

where

$$\tilde{h}^{sar}(k_1, k_2, x_3, \omega) = \frac{4\pi jk|x_3|}{(k_3^*)^2}. \quad (6.21)$$

Note that the inverse wavefield extrapolator in the spatial Fourier domain (Eq. (6.20)) has an increasing amplitude for increasing horizontal wavenumbers in the propagating wave region. For wide angle measurements containing horizontal wavenumbers near the propagating and evanescent wave boundary, the amplitude of the inverse wavefield extrapolator is not bounded, because the denominator approaches zero. Note that this conclusion does not hold for Eq. (6.19). Bounded amplitudes for the inverse wavefield extrapolators are required. An expression in the space-frequency domain which is bounded can be unbounded in the horizontal Fourier domain. Note that Eqs. (6.19) and (6.20) are related by the stationary phase approximation, which is based on the assumption of an infinite acquisition plane. In practise this is never the case, so the maximum spatial wavenumber will always be less than the propagating and evanescent wave boundary as indicated in Section 5.7.4. It is therefore very important to consider in which domain the inverse wavefield extrapolator is implemented. The implementation of the SAR inverse wavefield extrapolator in the spatial Fourier domain using Eq. (6.20) can result in unbounded amplitudes of the extrapolator, while the implementation in the space-frequency domain, which inherently is carried out for a bounded acquisition plane, results in a band limitation, which prevents amplitudes of the SAR inverse wavefield extrapolator becoming unbounded. Because the inverse wavefield extrapolator in the horizontal Fourier domain cannot be used for a common offset configuration, which is in practise the case, we will focus on the implementation in the space-frequency domain.

6.4.3 Comparison of scalar inverse wavefield extrapolators

The SAR and Gazdag inverse wavefield extrapolators both consist of a phase shift of the original measured signal weighted with some frequency- and angle-dependent factors (Table 6.1). In the space domain, the phase shift is given by $\exp(2jkR)$ and in the spatial Fourier domain, it is given by $\exp(jk_3^*|x_3|)$.

Table 6.1: Overview of the scalar inverse wavefield extrapolators in the space domain and in the spatial Fourier domain

Inverse extrapolator		space domain \hat{H}	spatial Fourier domain \tilde{H}
Gazdag	H^{gd}	$\frac{-jk x_3 }{\pi R^2} \exp(2jkR)$	$\exp(jk_3^* x_3)$
SAR	H^{sar}	$\exp(j2kR)$	$\frac{4\pi jk x_3 }{(k_3^*)^2} \exp(jk_3^* x_3)$

Note that when these inverse wavefield extrapolators are known in both the space domain and the spatial Fourier domain, the wavefield extrapolation can be carried out in either the space-time domain, the space-frequency domain or the horizontal spatial Fourier domain. Each domain has its own limitations and advantages. The implementation in the space-time domain requires interpolation, which can result in some errors. When some topographic adjustments are needed, implementation in the wavenumber-frequency domain is not an option. Frequency-dependent medium parameters can be taken into account in the space-frequency as well as wavenumber-frequency domain. Furthermore, the wavenumber-frequency domain implementation is more efficient compared with the space-frequency domain implementation; in the space-frequency domain, a two-dimensional horizontal convolution must be carried out, while in the wavenumber-frequency domain, a multiplication has to be carried out. The implementation of the inverse wavefield extrapolation in the wavenumber-frequency domain requires a regular sampling of the measured data. Irregular sampled data must first be regularised using for example the method discussed by Schonewille [2000]. An overview of the specific domain-related properties of the different implementations is given in Table 6.2. When the inverse extrapolator is calculated in the space-

frequency domain, while the actual inverse extrapolation is carried out in the wavenumber-frequency domain, we speak of a combined space-frequency wavenumber-frequency implementation. This is indicated in the table by the third column.

Table 6.2: Overview of the advantages and disadvantages of the different domains of implementation of the scalar inverse wavefield extrapolators

	Domain of implementation			
	Space-time	Space-frequency	Wavenumber-frequency	
Irregular sampling	+	+	-	-
Topographic correction	+	+	-	-
Efficiency	+	-	+	+
Frequency-dependent medium parameters	-	+	+	+

With the application of the inverse wavefield extrapolators in different domains, we need to take care of specific domain-related taper adjustments to avoid oscillations due to Gibbs phenomenon. When an operator is calculated in the space domain, oscillations caused by the limited acquisition plane will occur. The oscillations can be reduced by applying a proper tapering. When the operator is calculated in the spatial Fourier domain, the inverse wavefield extrapolation result in the spatial Fourier domain must be tapered due to the limited spatial bandwidth of the measured data, as discussed in Section 5.7.4.

6.4.4 Inverse of scalar 3-D two-way wavefield extrapolator in a homogeneous space

The Gazdag and SAR operators are basically phase shifts in the spatial Fourier domain and in the space domain, respectively. Neither operator takes into account the vectorial character and the radiation characteristics of the source and receiver antennas. In this section, it is shown that the amplitude of a single-component inverse wavefield extrapolator is not bounded when an

approximate inverse is derived for each separate component of the forward wavefield extrapolator.

The single-component two-way wavefield extrapolators $\tilde{D}_{\alpha\beta}(k_1, k_2, x_3, \omega)$ as given in Eqs. (6.12)-(6.14d) are inverted in the spatial Fourier domain. An exact inverse does not exist, due to the inability of inverting the evanescent wave region (see Eq. (6.13)), so a bounded approximate inverse \hat{H}^{inv} is derived in the spatial Fourier domain. Using the stationary phase approximation (Eqs. (A.11a), (A.11b) and (A.16a)), the expressions in the space domain for the scalar inverse wavefield extrapolators are obtained. The obtained expressions in the spatial Fourier domain and space domain are given in Table 6.3. Note that these single-component inverse wavefield extrapo-

Table 6.3: Overview of the different components of the single-component inverse wavefield extrapolators in space and spatial Fourier domain

Single-component Imaging operator	space domain \hat{H}	spatial Fourier domain \tilde{H}
H_{11}^{inv}	$\frac{-R^2 \exp(2jkR)}{R^2 - x_1^2} \frac{1}{\pi^2 C}$	$\frac{j(2k)^3 x_3 \exp(jk_3^* x_3)}{(2k)^2 - k_1^2} \frac{1}{2\pi C}$
H_{12}^{inv}	$\frac{-R^2 \exp(2jkR)}{x_1 x_2} \frac{1}{\pi^2 C}$	$\frac{j(2k)^3 x_3 \exp(jk_3^* x_3)}{k_1 k_2} \frac{1}{2\pi C}$
H_{21}^{inv}	$\frac{-R^2 \exp(2jkR)}{x_1 x_2} \frac{1}{\pi^2 C}$	$\frac{j(2k)^3 x_3 \exp(jk_3^* x_3)}{k_1 k_2} \frac{1}{2\pi C}$
H_{22}^{inv}	$\frac{-R^2 \exp(2jkR)}{R^2 - x_2^2} \frac{1}{\pi^2 C}$	$\frac{j(2k)^3 x_3 \exp(jk_3^* x_3)}{(2k)^2 - k_2^2} \frac{1}{2\pi C}$

lators are almost the exact reciprocal forward components of the forward single-component operators (see Eqs. (6.6)-(6.7d)). The only differences are the amplitudes and the geometrical spreading $1/R^2$, which are not compensated for by the reciprocal forward operator. The amplitude of \hat{H}_{11} is not bounded when a scatterer near the x_1 -axis is imaged and will "blow-up" the noise. This is already indicated by the forward wavefield extrapolator, which has a low sensitivity for scatterers near the x_1 -axis and is caused by the fact that the radiation characteristic of a horizontal dipole oriented in the x_1 -direction has a zero along the x_1 -axis. Similar conclusions can be drawn for

the other single-component inverse wavefield extrapolators.

When a dipole is present on the interface between two homogeneous half-spaces, the far-field expressions have a zero at the interface. This is discussed in Section 4.6. This indicates that a single-component inverse wavefield extrapolator for two homogeneous half-spaces will not be bounded. In conclusion, we can say that single-component inverse wavefield extrapolations based on the two-way wavefield extrapolator for a homogeneous space are not bounded, and that the inverse wavefield extrapolation has to be carried out by combining more components of the measured scattered electric field. This will result in a bounded multi-component inverse wavefield extrapolator, which is derived in the next section.

6.5 Multi-component imaging algorithm

To combine more components of the emitted and measured electric fields, a tensorial forward wavefield extrapolator is introduced, where each element represents the far-field expression of the scattering formalism for a specific source-receiver combination. Similar to the determination of the scalar inverse wavefield extrapolator in Section 6.4.4, the stationary phase method will be used to obtain a matrix inverse for the tensorial 3-D two-way wavefield extrapolator in the spatial Fourier domain. For a homogeneous space and a zero-offset configuration, it is feasible to determine an analytical solution and thus to determine closed-form expressions for the inverse wavefield extrapolator, which shows us that the obtained inverse 3-D wavefield extrapolator is bounded.

6.5.1 Multi-component 3D two-way wavefield extrapolator in a homogeneous space

To simplify the notation, we use the matrix notation for the different tensors. Similar to Eqs. (6.2) and (6.5) we can write for the zero-offset scattering formalism

$$\hat{\mathbf{E}}(\mathbf{x}^M, \omega) = \hat{S}^J(\omega) \int_{\mathbf{x}^c \in \mathbf{D}^s} \bar{\chi}^{\hat{\eta}}(\mathbf{x}^c) \hat{\mathbf{D}}(\mathbf{x}^M - \mathbf{x}^c, \omega) dV, \quad (6.22)$$

where $\hat{\mathbf{E}}(\mathbf{x}^M, \omega)$ is given by

$$\hat{\mathbf{E}}(\mathbf{x}^M, \omega) = \begin{bmatrix} \hat{E}_{11} & \hat{E}_{12} \\ \hat{E}_{21} & \hat{E}_{22} \end{bmatrix} (\mathbf{x}^M, \omega), \quad (6.23)$$

and $\hat{\mathbf{D}}(\mathbf{x}, \omega)$ is the tensorial 3-D two-way wavefield extrapolator for zero-offset, which is given by

$$\hat{\mathbf{D}}(\mathbf{x}, \omega) = \mathbf{A}(\mathbf{x}, \omega) \exp(-2jkR), \quad (6.24)$$

where

$$\mathbf{A}(\mathbf{x}, \omega) = \begin{bmatrix} \hat{A}_{11} & \hat{A}_{12} \\ \hat{A}_{21} & \hat{A}_{22} \end{bmatrix} (\mathbf{x}, \omega), \quad (6.25)$$

and $\hat{A}_{\alpha\beta}$ are given by Eqs. (6.7a)-(6.7d). To obtain the inverse extrapolated wavefield in the subsurface, we must compensate for the propagation from the plane of measurement to another depth level inside the medium of investigation, or in other words, we have to find an approximate inverse of $\hat{\mathbf{D}}$. This inverse will be determined in the horizontal spatial Fourier domain. To obtain closed-form expressions in the horizontal spatial Fourier domain, the stationary phase approximation is used as in Section 6.4.4. Combining Eqs. (6.12) and (6.14a)-(6.14d), the expression for $\tilde{\mathbf{D}}(k_1, k_2, x_3, \omega)$ is obtained as

$$\tilde{\mathbf{D}}(k_1, k_2, x_3, \omega) = \tilde{\mathbf{d}}(k_1, k_2, x_3, \omega) \exp(-jk_3|x_3|), \quad (6.26)$$

where

$$\tilde{\mathbf{d}}(k_1, k_2, x_3, \omega) = \frac{-2\pi jC(\omega)}{(2k)^3|x_3|} \begin{bmatrix} (2k)^2 - k_1^2 & -k_1k_2 \\ -k_1k_2 & (2k)^2 - k_2^2 \end{bmatrix}. \quad (6.27)$$

6.5.2 Inverse of multi-component 3-D two-way wavefield extrapolator in a homogeneous space

To obtain an approximate inverse of the multi-component 3-D two-way wavefield extrapolator, which is defined as $\tilde{\mathbf{H}}^{inv} = \tilde{\mathbf{D}}^{-1}$ for the propagating waves, a matrix inverse of the expression given in Eq. (6.26) must be determined. The determinant of the matrix in Eq. (6.26) is given by

$$\text{Det} \begin{bmatrix} [(2k)^2 - k_1^2]/(2k)^2 & -k_1k_2/(2k)^2 \\ -k_1k_2/(2k)^2 & [(2k)^2 - k_2^2]/(2k)^2 \end{bmatrix} = \frac{(k_3)^2}{4k^2}. \quad (6.28)$$

The expression for $\tilde{\mathbf{H}}^{inv}$ is approximated by,

$$\tilde{\mathbf{H}}^{inv}(k_1, k_2, x_3, \omega) = \tilde{\mathbf{h}}^{inv}(k_1, k_2, x_3, \omega) \exp(jk_3^*|x_3|), \quad (6.29)$$

where

$$\tilde{\mathbf{h}}^{inv}(k_1, k_2, x_3, \omega) = \frac{jk|x_3|}{\pi C(\omega)(k_3)^2} \begin{bmatrix} (2k)^2 - k_2^2 & k_1 k_2 \\ k_1 k_2 & (2k)^2 - k_1^2 \end{bmatrix}. \quad (6.30)$$

Again, only the propagating wave region will be inverted, so that the complex conjugate of the vertical wavenumber, defined in Eq. (5.46), is taken in the exponent of Eq. (6.29). Note that the original vertical wavenumber is present in Eq. (6.30), because this expression is obtained by inverting the forward wavefield extrapolator.

Using the expressions for the stationary phase approximation given in Appendix A, the spatial equivalents of Eqs. (6.29) and (6.30) can be recognized as

$$\hat{\mathbf{H}}^{inv}(\mathbf{x}, \omega) = \frac{4k^2}{4\pi^2 C(\omega)} \begin{bmatrix} (R^2 - x_2^2)/R^2 & x_1 x_2/R^2 \\ x_1 x_2/R^2 & (R^2 - x_1^2)/R^2 \end{bmatrix} \exp(2jkR). \quad (6.31)$$

Note that the components of the inverse wavefield extrapolator are bounded. A simple relation between $\hat{\mathbf{D}}$ and $\hat{\mathbf{H}}^{inv}$ holds and is given by

$$\hat{\mathbf{H}}^{inv}(\mathbf{x}, \omega) = -\frac{R^2 k^2}{\pi^2 C^2} \begin{bmatrix} 0 & 1 \\ -1 & 0 \end{bmatrix} \hat{\mathbf{D}}^H(\mathbf{x}, \omega) \begin{bmatrix} 0 & 1 \\ -1 & 0 \end{bmatrix}. \quad (6.32)$$

Note that also a simple relation holds between the kernel of the convolution describing the forward and inverse wavefield extrapolation, $\hat{\mathbf{H}}^{inv}$ and $\hat{\mathbf{D}}^{-1}$, which is given by

$$\hat{\mathbf{H}}^{inv}(\mathbf{x}, \omega) = \frac{k^2 |x_3|^2}{\pi^2 R^4} \hat{\mathbf{D}}^{-1}(\mathbf{x}, \omega). \quad (6.33)$$

6.5.3 Inverse of multi-component wavefield extrapolator in two homogeneous half-spaces

Due to the fact that the expressions of the forward two-way wavefield extrapolator were quite elementary in a homogeneous space, an analytical discussion was possible. However, for a homogeneous half-space an analytical approach is not feasible. A numerical implementation to determine the approximate inverse is still possible. An important benefit is that numerical methods allow the offset between the source and receiver to be taken into account. Similar

to Eq. (6.24), we introduce the forward wavefield operator

$$\begin{aligned} \hat{\mathbf{D}}(\mathbf{x}^M, \mathbf{x}^H | \mathbf{x}^c, \omega) = & \\ & \begin{bmatrix} \hat{G}_{1r}^{\text{EJ}}(\mathbf{x}^R - \mathbf{x}^c, \omega) \hat{G}_{1r}^{\text{EJ}}(\mathbf{x}^S - \mathbf{x}^c, \omega) & \hat{G}_{2r}^{\text{EJ}}(\mathbf{x}^R - \mathbf{x}^c, \omega) \hat{G}_{1r}^{\text{EJ}}(\mathbf{x}^S - \mathbf{x}^c, \omega) \\ \hat{G}_{1r}^{\text{EJ}}(\mathbf{x}^R - \mathbf{x}^c, \omega) \hat{G}_{2r}^{\text{EJ}}(\mathbf{x}^S - \mathbf{x}^c, \omega) & \hat{G}_{2r}^{\text{EJ}}(\mathbf{x}^R - \mathbf{x}^c, \omega) \hat{G}_{2r}^{\text{EJ}}(\mathbf{x}^S - \mathbf{x}^c, \omega) \end{bmatrix}, \\ & \mathbf{x}^S = \mathbf{x}^M - \mathbf{x}^H, \\ & \mathbf{x}^R = \mathbf{x}^M + \mathbf{x}^H. \end{aligned} \quad (6.34)$$

To determine the forward wavefield operator, we use the far-field expressions in Cartesian coordinates, as discussed in Section 4.6, for the different components of the Green's tensor functions. The inner product of two elements of the Green's tensor function (see Eq. (6.34)) must be determined for each midpoint position \mathbf{x}^M . Then, a two-dimensional spatial Fourier transformation must be carried out. For each k_1, k_2 combination, an inverse matrix can be numerically determined, which results in a representation of the imaging extrapolator in the spatial Fourier domain. Note that for $\hat{\mathbf{H}}^{\text{inv}}(\mathbf{x}^M, \mathbf{x}^H | \mathbf{x}^c)$ to be bounded, Eq. (5.46) must be satisfied. In practise, this means that the inverse wavefield extrapolator is only determined in the propagating wave region and the evanescent wave region is neglected. Note that also the acquisition plane and the radiation characteristics can influence the usable spatial bandwidth (see Section 5.7.4).

Summarizing, it can be stated that a bounded approximate inverse tensorial 3-D wavefield extrapolator based on the vectorial scattering formalism is derived, which takes into account the radiation patterns of elementary source and receiver antennas present on a dielectric half-space and the offset between the source and receiver antenna.

6.6 Imaging principle

In the preceding section, we have discussed an inverse wavefield extrapolation operator, which compensates for the propagation in the subsurface and the radiation characteristics. The imaging procedure will be derived for the multi-component case, where the forward wavefield extrapolator is given by $\hat{\mathbf{D}}$ (see Eq. 6.24) and the inverse wavefield extrapolator is given by $\hat{\mathbf{H}}^{\text{inv}}$ (see Eq. (6.31)). The result for the single-component case can be simply obtained by rewriting the multi-component result.

First, the forward model for a common offset measurement is repeated, which

is given by Eq. (6.22) yielding,

$$\hat{\mathbf{E}}(\mathbf{x}^M, \omega) = \hat{S}^J(\omega) \int_{\mathbf{x}^c \in \mathbf{D}^s} \hat{\mathbf{D}}(\mathbf{x}^M - \mathbf{x}^c, \omega) \bar{\chi}^{\hat{\eta}}(\mathbf{x}^c) dV. \quad (6.35)$$

The convolution is discretised with respect to depth into separate contributions from different depth levels x_3^i , where $i = 1, N$, and $\mathbf{x}^i = (x_1^i, x_2^i, x_3^i)$. Applying the inverse wavefield extrapolator on the measured data, we obtain for a specific depth level $\mathbf{x}^n = (x_1, x_2, x_3^n)$,

$$\begin{aligned} & \int_{(x_1^M, x_2^M) \in \mathbf{D}^M} \hat{\mathbf{H}}^{inv}(\mathbf{x}^n - \mathbf{x}^M, \omega) \hat{\mathbf{E}}(\mathbf{x}^M, \omega) dA \\ &= \hat{S}^J(\omega) \sum_{i=1}^N \int_{(x_1^M, x_2^M) \in \mathbf{D}^M} \hat{\mathbf{H}}^{inv}(\mathbf{x}^n - \mathbf{x}^M, \omega) \\ & \quad \times \int_{(x_1^i, x_2^i) \in \mathbf{D}^s} \hat{\mathbf{D}}(\mathbf{x}^M - \mathbf{x}^i, \omega) \bar{\chi}^{\hat{\eta}}(\mathbf{x}^i, \omega) dA dA, \\ &= \hat{S}^J(\omega) \left[\langle \hat{\chi}^{\hat{\eta}}(\mathbf{x}^n, \omega) \mathbf{I} \rangle + \hat{\mathbf{P}}(\mathbf{x}^n, \omega) \right], \end{aligned} \quad (6.36)$$

\mathbf{I} being the unity matrix and \mathbf{D}^M is the acquisition plane where $(x_1^M, x_2^M, x_3^M) = (x_1^M, x_2^M, 0)$. The quantity $\langle \hat{\chi}^{\hat{\eta}}(\mathbf{x}^n, \omega) \mathbf{I} \rangle$ is the bandlimited version of the true value given by

$$\begin{aligned} \langle \hat{\chi}^{\hat{\eta}}(\mathbf{x}^n, \omega) \mathbf{I} \rangle &= \sum_{i=n}^n \int_{(x_1^M, x_2^M) \in \mathbf{D}^M} \hat{\mathbf{H}}^{inv}(\mathbf{x}^n - \mathbf{x}^M, \omega) dA \\ & \quad \times \int_{(x_1^i, x_2^i) \in \mathbf{D}^s} \hat{\mathbf{D}}(\mathbf{x}^M - \mathbf{x}^i, \omega) \bar{\chi}^{\hat{\eta}}(\mathbf{x}^i, \omega) dA, \end{aligned} \quad (6.37)$$

and $\hat{\mathbf{P}}(\mathbf{x}^n, \omega)$ is the primary response from depth levels $x_3 \neq x_3^n$, which is given by

$$\begin{aligned} \hat{\mathbf{P}}(\mathbf{x}^n, \omega) &= \sum_{\substack{i \neq n \\ i=1}}^N \int_{(x_1^M, x_2^M) \in \mathbf{D}^M} \hat{\mathbf{H}}^{inv}(\mathbf{x}^n - \mathbf{x}^M, \omega) dA \\ & \quad \times \int_{(x_1^i, x_2^i) \in \mathbf{D}^s} \hat{\mathbf{D}}(\mathbf{x}^M - \mathbf{x}^i, \omega) \bar{\chi}^{\hat{\eta}}(\mathbf{x}^i, \omega) dA. \end{aligned} \quad (6.38)$$

The inverse two-way wavefield extrapolator compensates for the propagation effects in the subsurface. Hence, the inverse two-way wavefield extrapolator

$\hat{\mathbf{H}}^{inv}$ compensates for all amplitudes and travel times involved in the specific subsurface layer, including radiation characteristics of the (point) source and (point) receiver. Next, the imaging principle is applied, which states that the data at zero traveltimes of the inverse extrapolated recordings relate to a bandlimited version of the physical property contrasts of the medium of investigation [Claerbout, 1971; Berkhout, 1981]. As a consequence, we can simply sum the result for all (positive and negative) frequencies to obtain the imaged contrast in the space domain. For isolated objects, the contribution of $\hat{\mathbf{P}}(\mathbf{x}^n, \omega)$ at the depth level $x_3 = x_3^n$ is corrected for, such that we can write for the imaged contrast

$$\langle \bar{\chi}^{\hat{\eta}}(\mathbf{x}^n) \mathbf{I} \rangle = \frac{1}{2\pi} \int \frac{\hat{S}^J(\omega) \left[\langle \hat{\chi}^{\hat{\eta}}(\mathbf{x}^n, \omega) \mathbf{I} \rangle + \hat{\mathbf{P}}(\mathbf{x}^n, \omega) \right]}{\hat{S}^J(\omega)} d\omega, \quad (6.39)$$

Note that if $\hat{\chi}^{\hat{\eta}}$ is frequency-dependent, then Eq. (6.39) yields a frequency averaged estimate. Combining the results in Eqs. (6.36) and (6.39) we can write for the multi-component imaging algorithm

$$\langle \bar{\chi}^{\hat{\eta}}(\mathbf{x}^n) \mathbf{I} \rangle = \frac{1}{2\pi} \int \frac{d\omega}{\hat{S}^J(\omega)} \int_{(x_1^M, x_2^M) \in \mathbf{D}^M} \hat{\mathbf{H}}^{inv}(\mathbf{x}^n - \mathbf{x}^M, \omega) \hat{\mathbf{E}}(\mathbf{x}^M, \omega) dA. \quad (6.40)$$

Note that the diagonal components $\langle \bar{\chi}^{\hat{\eta}}(\mathbf{x}^n) \mathbf{I} \rangle_{11}$ and $\langle \bar{\chi}^{\hat{\eta}}(\mathbf{x}^n) \mathbf{I} \rangle_{22}$ both return the estimated value of the obtained contrast. Each diagonal component consists of the summation of two different measurements, which are imaged separately by using an appropriate inverse wavefield extrapolator for that specific measurement. The finally obtained imaged contrast is the mean value of these two diagonal components in Eq. (6.40) and is given by

$$\langle \bar{\chi}^{\hat{\eta}}(\mathbf{x}^n) \rangle = \frac{\langle \bar{\chi}^{\hat{\eta}}(\mathbf{x}^n) \mathbf{I} \rangle_{11} + \langle \bar{\chi}^{\hat{\eta}}(\mathbf{x}^n) \mathbf{I} \rangle_{22}}{2}. \quad (6.41)$$

The off-diagonal components serve as a quality control, because from Eq. (6.40) it is shown that they have to be zero. When the off-diagonal components $\langle \bar{\chi}^{\hat{\eta}}(\mathbf{x}^n) \mathbf{I} \rangle_{12}$ and $\langle \bar{\chi}^{\hat{\eta}}(\mathbf{x}^n) \mathbf{I} \rangle_{21}$ return a large value compared with the diagonal components $\langle \bar{\chi}^{\hat{\eta}}(\mathbf{x}^n) \mathbf{I} \rangle_{11}$ and $\langle \bar{\chi}^{\hat{\eta}}(\mathbf{x}^n) \mathbf{I} \rangle_{22}$, this indicates that the forward model, given in Eq. (6.22) does not adequately describe the behaviour of the measured electric wavefield.

Imaging principle for single-component imaging algorithms

The foregoing analysis can also be applied for the single-component imaging algorithm. Instead of Eq. (6.35), which was the starting point for the imaging principle for the multi-component imaging algorithm, the starting point for the imaging principle for the single-component is given by Eq. (6.2). Using a similar analysis as carried out to derive the imaging principle for the multi-component imaging, we can now write for the single-component imaging algorithm

$$\bar{\chi}_{\alpha\beta}^{image}(\mathbf{x}^n) = \frac{1}{2\pi} \int \frac{d\omega}{\hat{S}^J(\omega)} \int_{(x_1^M, x_2^M) \in \mathbb{D}^M} \hat{H}^{image}(\mathbf{x}^n - \mathbf{x}^M, \omega) \hat{E}_{\alpha\beta}(\mathbf{x}^M, \omega) dA, \quad (6.42)$$

where \hat{H}^{image} is an image operator, because its application is not based on an approximate inverse, but based on heuristic considerations. Each imaging algorithm has its inverse wavefield extrapolator. The inverse wavefield extrapolators for the Gazdag and the SAR algorithms in the space domain are given by Eqs. (6.18) and (6.19), respectively. Note that also the inverse wavefield extrapolator obtained for the multi-component imaging algorithm can be used for the imaging of one single-component. We will now focus on the inverse wavefield extrapolator of the three imaging algorithms, because the imaging procedure remains the same.

The actual wavefield extrapolation procedure can be applied as a two-dimensional convolution procedure in the space domain. However, the wavefield extrapolation is most conveniently carried out in the spatial Fourier domain, because of the low computation time of a multiplication compared with a convolution. The convolution procedure in Eqs. (6.40) and (6.42) requires filter coefficients, which may include values outside the original range of the section. Hence, if the inverse wavefield extrapolation is carried out in the spatial frequency domain, then the extrapolated data would be distorted by an overlapping effect ('aliasing') in the space domain. Therefore, for inverse extrapolation in the wavenumber-frequency domain, the original data must be extended with zero's to allow filter coefficients outside the original range.

6.7 Spatial resolution functions

The performance of the scalar and multi-component 3-D inverse wavefield extrapolators is investigated by analysing the inverse wavefield extrapolation

of the scattered field due to a point scatterer for a single frequency component, which is denoted as the spatial resolution function. In this way, the correction for the propagation effects by the inverse wavefield extrapolator can be analysed. Due to the suppression of the evanescent field and the influence of the inverse wavefield extrapolator, this results in a limited spatial bandwidth, which limits the spatial resolution.

First, the spatial resolution is investigated for a point scatterer present in a homogeneous domain using a zero-offset configuration. The expressions for the forward and inverse wavefield extrapolators in the space domain and in the spatial Fourier domain are given in Sections 6.4 and 6.5 and enable the derivation of closed-form expressions for the spatial resolution function. In this way, an analytical check is possible, whether of the requirements of a good imaging algorithm as given in Section 6.1 are satisfied. The obtained results for the single-component imaging algorithms are compared with the results of the multi-component imaging algorithm. Finally, a numerical comparison of the different resolution functions is carried out for a point scatterer present in two homogeneous half-spaces.

For the special situation of one diffraction point at position \mathbf{x}^d , with unit amplitude, according to

$$\bar{\chi}^{\hat{n}}(\mathbf{x}) = \delta(\mathbf{x} - \mathbf{x}^d), \quad (6.43)$$

the measured electric field may be expressed in terms of the source function $\hat{S}^J(\omega)$, according to (see Eq. (6.22))

$$\hat{\mathbf{E}}(\mathbf{x}^M, \omega) = \hat{S}^J(\omega) \hat{\mathbf{D}}(\mathbf{x}^M - \mathbf{x}^d, \omega). \quad (6.44)$$

In the following, we consider for convenience a source function with unit amplitude. Similar to Eq. (6.40), the expression for the bandlimited version of the contrast at an arbitrary depth level x_3 reads

$$\langle \hat{\chi}(\mathbf{x}, \omega) \mathbf{I} \rangle = \int_{(x_1^M, x_2^M) \in \mathbb{D}^M} \hat{\mathbf{H}}^{inv}(\mathbf{x} - \mathbf{x}^M, \omega) \hat{\mathbf{E}}(x_1^M, x_2^M, 0, \omega) dA. \quad (6.45)$$

Substitution of the forward model, defined in Eq. (6.44), gives

$$\langle \hat{\chi}(\mathbf{x}, \omega) \mathbf{I} \rangle = \int_{(x_1^M, x_2^M) \in \mathbb{D}^M} \hat{\mathbf{H}}^{inv}(\mathbf{x} - \mathbf{x}^M, \omega) \hat{\mathbf{D}}(\mathbf{x}^M - \mathbf{x}^d, \omega) dA. \quad (6.46)$$

Using some basic results of Fourier theory, we may express Eq. (6.46) in

terms of the Fourier transforms of $\hat{\mathbf{H}}^{inv}$ and $\hat{\mathbf{D}}$, according to

$$\begin{aligned} \langle \hat{\chi}(\mathbf{x}, \omega) \mathbf{I} \rangle &= \frac{1}{4\pi^2} \int_{(k_1, k_2) \in \mathbb{R}^2} \tilde{\mathbf{H}}^{inv}(k_1, k_2, x_3, \omega) \tilde{\mathbf{D}}(k_1, k_2, x_3^d, \omega) \\ &\quad \times \exp[-j(k_1\{x_1 - x_1^d\} + k_2\{x_2 - x_2^d\})] dA. \end{aligned} \quad (6.47)$$

The quantity $\tilde{\mathbf{D}}$ consists of a phase factor given in Eq. (6.26) and an amplitude factor given in Eq. (6.27). Similarly, the quantity $\tilde{\mathbf{H}}^{inv}$ consists of a phase factor given by Eq. (6.29) and an amplitude factor given by Eq. (6.30). Substitution of these expressions into Eq. (6.47), which enables a separate analysis of the phase factors and the amplitude factors, yields

$$\begin{aligned} &\langle \hat{\chi}(x_1, x_2, x_3, \omega) \mathbf{I} \rangle \\ &= \frac{1}{4\pi^2} \int_{prop.} \int_{waves} \tilde{\mathbf{h}}^{inv}(k_1, k_2, x_3, \omega) \tilde{\mathbf{d}}(k_1, k_2, x_3^d, \omega) \exp[-jk_3'(|x_3^d| - |x_3|)] \\ &\quad \times \exp[-j(k_1\{x_1 - x_1^d\} + k_2\{x_2 - x_2^d\})] dk_1 dk_2 \\ &+ \frac{1}{4\pi^2} \int_{evan.} \int_{waves} \tilde{\mathbf{h}}^{inv}(k_1, k_2, x_3, \omega) \tilde{\mathbf{d}}(k_1, k_2, x_3^d, \omega) \exp[-jk_3'(|x_3^d| + |x_3|)] \\ &\quad \times \exp[-j(k_1\{x_1 - x_1^d\} + k_2\{x_2 - x_2^d\})] dk_1 dk_2. \end{aligned} \quad (6.48)$$

From Eqs. (6.27) and (6.30) it is obvious that

$$\tilde{\mathbf{h}}^{inv}(k_1, k_2, x_3, \omega) \tilde{\mathbf{d}}(k_1, k_2, x_3^d, \omega) = \frac{|x_3|}{|x_3^d|} \mathbf{I}, \quad (6.49)$$

for the multi-component inverse extrapolator. We continue the analysis in general, such that the obtained results can also be used for the scalar inverse wavefield extrapolators. Next, we evaluate Eq. (6.48), ignoring the erroneous contribution of the evanescent waves. This is done most conveniently if we introduce polar coordinates, according to

$$x_1 - x_1^d = r \cos(\phi), \quad (6.50a)$$

$$x_2 - x_2^d = r \sin(\phi), \quad (6.50b)$$

$$k_1 = \kappa \cos(\phi - \theta), \quad (6.50c)$$

$$k_2 = \kappa \sin(\phi - \theta), \quad (6.50d)$$

and $dk_1 dk_2 = \kappa d\theta d\kappa$. Hence, for the first integral in Eq. (6.48), we now obtain for the diffractor depth $x_3 = x_3^d$

$$\begin{aligned} & \langle \hat{\chi}(r, \phi, x_3^d, \omega) \mathbf{I} \rangle \\ &= \frac{1}{4\pi^2} \int_{\kappa=0}^{k_{max}} \left(\int_{\theta=0}^{2\pi} \tilde{\mathbf{h}}^{inv}(\kappa, \theta, x_3^d, \omega) \tilde{\mathbf{d}}(\kappa, \theta, x_3^d, \omega) \exp[-j\kappa r \cos(\theta)] d\theta \right) \kappa d\kappa, \end{aligned} \quad (6.51)$$

where we have used the goniometric identity given in Eq. (2.25). Due to the suppression of the evanescent waves, the maximum radial spatial frequency component equals $k_{max} = 2k$. This suppression of the evanescent field limits the resolution of the point scatterers image. Note that also the forward and inverse wavefield extrapolator and the dimensions of the acquisition plane influence the spatial resolution, resulting in $k_{max} < 2k$ (see also Section 5.7.4).

Spatial resolution function for single-component imaging algorithms

To obtain the spatial resolution function for single-component imaging algorithms, a similar analysis is carried out which was used to derive the resolution function for the multi-component imaging algorithm. Substitution of Eq. (6.2) for one diffraction point only at position \mathbf{x}^d as in Eq. (6.43) into Eq. (6.42) and using a source function with unit amplitude, the spatial resolution function for single-component imaging algorithms is obtained as

$$\begin{aligned} & \hat{\chi}_{\alpha\beta}^{image}(r, \phi, x_3^d, \omega) \\ &= \frac{1}{4\pi^2} \int_{\kappa=0}^{k_{max}} \int_{\theta=0}^{2\pi} \tilde{h}^{image}(\kappa, \theta, x_3^d, \omega) \tilde{d}_{\alpha\beta}(\kappa, \theta, x_3^d, \omega) \exp[-j\kappa r \cos(\theta)] \kappa d\theta d\kappa. \end{aligned} \quad (6.52)$$

For SAR imaging, the factor \tilde{h}^{image} is defined by $\tilde{h}^{image} = \tilde{h}^{sar}$ as given in Eq. (6.21), whereas for the Gazdag algorithm the factor \tilde{h}^{image} is defined by $\tilde{h}^{image} = \tilde{h}^{gd} = 1$, which can be derived from Eq. (6.17).

In the following sections, the integrals occurring in Eqs. (6.51) and (6.52) are evaluated resulting in closed-form expressions for the spatial resolution functions of the SAR, Gazdag and Multi-component inverse wavefield extrapolators.

6.7.1 Spatial resolution for Gazdag phase shift operator

The amplitude of the Gazdag phase shift method for wave equation migration is given by $\tilde{h}^{gd} = 1$, which can be derived from Eq. (6.17). Substitution of the amplitude factor for the Gazdag phaseshift operator and the amplitude for factor \tilde{d}_{11} (6.14a) into Eq. (6.52), yields

$$\hat{\chi}_{11}^{gd}(r, \phi, x_3^d, \omega) = \frac{-jC(\omega)}{2\pi k |x_3^d| (2k)^2} \int_{\kappa=0}^{k_{max}} \int_{\theta=0}^{2\pi} [4k^2 - \kappa^2 \cos^2(\phi) + (\cos^2(\phi) - \sin^2(\phi)) \kappa^2 \sin^2(\theta)] \kappa \cos[\kappa r \cos(\theta)] d\theta d\kappa.$$

Using the fact that, [Eq. (9.120), Abramowitz and Stegun, 1964]

$$J_\nu(z) = \frac{(\frac{1}{2}z)^\nu}{\sqrt{\pi}\Gamma(\nu + \frac{1}{2})} \int_0^\pi \cos[z \cos(\theta)] \sin^{2\nu}(\theta) d\theta, \quad (6.53)$$

we obtain

$$\hat{\chi}_{11}^{gd}(r, \phi, x_3^d, \omega) = \frac{-jC}{2k |x_3^d| (2k)^2} \times \int_{\kappa=0}^{k_{max}} \left\{ [4k^2 - \kappa^2 \cos^2(\phi)] \kappa J_0(\kappa r) + [\cos^2(\phi) - \sin^2(\phi)] \kappa^2 \frac{J_1(\kappa r)}{r} \right\} d\kappa. \quad (6.54)$$

Using the fact that, [Eqs. (9.127) and (9.130), Abramowitz and Stegun, 1964]

$$J_{\nu+1}(z) = \frac{2\nu}{z} J_\nu(z) - J_{\nu-1}(z), \quad (6.55a)$$

$$\int z^\nu J_{\nu-1}(z) dz = [z^\nu J_\nu(z)], \quad (6.55b)$$

we obtain

$$\hat{\chi}_{11}^{gd}(r, \phi, x_3^d, \omega) = \frac{-jC}{2k |x_3^d| (2k)^2} \left(k_{max} (4k^2 - k_{max}^2 \cos^2(\phi)) \frac{J_1(k_{max} r)}{r} + [3 \cos^2(\phi) - \sin^2(\phi)] k_{max}^2 \frac{J_2(k_{max} r)}{r^2} \right). \quad (6.56)$$

For an infinitely large acquisition plane, $k_{max} = 2k$, and Eq. (6.56) reduces to

$$\hat{\chi}_{11}^{gd}(r, \phi, x_3^d, \omega) = \frac{-jC}{|x_3^d|} \left(\sin^2(\phi) \frac{J_1(2kr)}{r} + [3 \cos^2(\phi) - \sin^2(\phi)] \frac{J_2(2kr)}{2kr^2} \right). \quad (6.57)$$

This result represents the bandlimited resolution function of the point diffractor for one single frequency and supplies us valuable information about the bandwidth and the capabilities of the Gazdag imaging operator. The limited resolution is due to the suppression of the evanescent field. Analysing the result in detail, we observe that the resolution function is not circularly symmetric, whereas the diffractor is circularly symmetric. The Gazdag filter is a symmetric operator, but the scattered wavefield has non-symmetric properties as shown in Section 5.8. Another drawback of this result is that the amplitude of the resolution function is inversely proportional to the depth of the diffractor, whereas one would expect it to be independent of x_3^d (bear in mind that inverse wavefield extrapolation should compensate for the propagation effects). Scaling the result by x_3^d , results in a modified operator, which will be introduced in Section 6.7.4.

6.7.2 Spatial resolution for SAR operator

The SAR imaging operator is denoted by \tilde{H}^{sar} in the spatial Fourier domain and is given by Eq. (6.20). Substitution of the amplitude factor of the SAR imaging operator \tilde{h}^{sar} and \tilde{d}_{11} (cf. Eq. (6.14a)) into Eq. (6.52), yields

$$\begin{aligned} \hat{\chi}_{11}^{sar}(r, \phi, x_3^d, \omega) = & \\ & \frac{2C(\omega)}{(2k)^2} \int_{\kappa=0}^{k_{max}} \int_{\theta=0}^{2\pi} \left[1 + \frac{\kappa^2 (\sin^2(\phi) + \sin^2(\theta) [\cos^2(\phi) - \sin^2(\phi)])}{4k^2 - \kappa^2} \right] \kappa \times \\ & \exp\{-j[\kappa r \cos(\theta)]\} d\theta d\kappa. \end{aligned} \quad (6.58)$$

Using Eqs. (6.53), (6.55a) and (6.55b) we obtain

$$\begin{aligned} \hat{\chi}_{11}^{sar}(r, \phi, x_3^d, \omega) = & \frac{2\pi k_{max} C(\omega)}{(2k)^2} \frac{J_1(k_{max} r)}{r} \\ & + \frac{C(\omega)}{(2k)^2} \int_{\kappa=0}^{k_{max}} \left[\frac{\kappa^2 \sin^2(\phi)}{4k^2 - \kappa^2} \kappa J_0(\kappa r) + \frac{\kappa^2 [\cos^2(\phi) - \sin^2(\phi)]}{4k^2 - \kappa^2} \frac{J_1(\kappa r)}{r} \right] d\kappa. \end{aligned} \quad (6.59)$$

It is not feasible to obtain a closed-form expression for the last integral representation. However, the result shows that an angle dependent resolution function is obtained, which is not dependent on the depth of the diffractor.

6.7.3 Spatial resolution for 3-D downward extrapolation using the multi-component operator

Substitution of the multi-component inverse wavefield extrapolator given in Eq. (6.30) and $\tilde{\mathbf{D}}$ given in Eq. (6.27) into Eq. (6.51) yields

$$\begin{aligned}
 \langle \hat{\chi}(r, \phi, x_3^d) \mathbf{I} \rangle &= \frac{1}{4\pi^2} \int_0^{k_{max}} \left(\int_0^{2\pi} \mathbf{I} \exp[-j\kappa r \cos(\theta)] d\theta \right) \kappa d\kappa, \\
 &= \frac{1}{2\pi} \int_0^{k_{max}} \left(\frac{1}{\pi} \int_0^\pi \mathbf{I} \cos[\kappa r \cos(\theta)] d\theta \right) \kappa d\kappa, \\
 &= \frac{1}{2\pi} \int_0^{k_{max}} \mathbf{I} J_0(\kappa r) \kappa d\kappa = \frac{k_{max}}{2\pi} \frac{J_1(k_{max} r)}{r} \mathbf{I}. \quad (6.60)
 \end{aligned}$$

Note that $\tilde{\mathbf{H}}^{inv}$ is the exact inverse of $\tilde{\mathbf{D}}$ for propagating waves, resulting in the unity matrix \mathbf{I} , whereas it suppresses evanescent waves, resulting in a bounded radial spatial frequency component $k_{max} = 2k$. This suppression of the evanescent field results in the limited resolution for the image of the point scatterer. The result for the multi-component imaging is a circularly symmetric resolution function. We finalize this section by analyzing the result for the situation of an infinite horizontal perfect reflector at depth x_3^d . This reflector may be seen as a continuous distribution of point diffractors at depth level x_3^d , hence, the downward extrapolation result is simply obtained by integrating Eq. (6.60) along x_1^d and x_2^d , according to

$$\begin{aligned}
 \int \int_{(x_1, x_2) \in \mathbf{R}^2} \langle \hat{\chi}(r, \phi, x_3^d) \mathbf{I} \rangle dx_1^d dx_2^d &= \frac{k_{max}}{2\pi} \mathbf{I} \int_{-\infty}^{\infty} \int_{-\infty}^{\infty} \frac{J_1(k_{max} r)}{r} dx_1^d dx_2^d, \\
 &= \frac{k_{max}}{2\pi} \mathbf{I} \int_0^{\infty} \int_0^{2\pi} \frac{J_1(k_{max} r)}{r} r d\phi dr, \\
 &= k_{max} \mathbf{I}. \quad (6.61)
 \end{aligned}$$

Note that for true-amplitude imaging, a correction factor of $(k_{max})^{-1}$ should be applied prior to the integration along the frequency axis.

6.7.4 Modified scalar inverse wavefield extrapolators

An important requirement of an inverse wavefield extrapolator is to compensate for the propagation effects. In Section 6.7.1, it was shown that the Gazdag inverse wavefield extrapolator does not satisfy this requirement.

Therefore, it is suggested to introduce a modified operator which does compensate for the propagation effects. This is simply achieved by a scaling with $|x_3^d|$. Another requirement was that the obtained image represents the scatterer adequately. In the preceding sections, the resolution functions for the Gazdag, SAR and the multi-component inverse wavefield extrapolators were derived. The scatterer had a real-valued contrast with the background, which finds expression in Eq. (6.43). A representative resolution function will return also a real-valued resolution function. When we analyse the obtained resolution functions, we observe that the resolution function using the Gazdag operator returns an imaginary resolution function, whereas the SAR operator returns a real-valued resolution function with a negative peak. The multi-component operator returns a real-valued resolution function with a positive peak giving a representative image of the point scatterer. In Table 6.4, the results of the different inverse wavefield extrapolators are given. For the multi-component inverse extrapolator, an equal spatial resolution for the x_1 and the x_2 -axis is obtained, while for the Gazdag inverse extrapolator better resolution is obtained along the x_2 -axis than along the x_1 -axis. The peaks of the results obtained with both scalar inverse extrapolators do

Table 6.4: Width of the main lobe (measured at the first zero) for the resolution function at the depth level of the diffractor using the closed-form expressions

Inverse extrapolator	Width of the main lobe		Proportional to
	x_1 -plane	x_2 -plane	
Multi-component	0.64λ	0.64λ	$k/2\pi$
Gazdag	0.84λ	0.60λ	$-jC/ x_3^d $
SAR			$C/2k$

not represent the properties of the point scatterer. Therefore, modified extrapolators are introduced, which render a representative reconstruction of the point scatterer. The modified Gazdag operator consists of the original Gazdag extrapolator multiplied with $|x_3^d|$. Also, multiplication with $-j$ is required to obtain a real-valued resolution function with a positive peak. The modified SAR operator consists of the original SAR extrapolator multiplied by -1 to obtain a real-valued resolution function with positive peak. The adjusted extrapolators are given in Table 6.5 (Compare with Table 6.1).

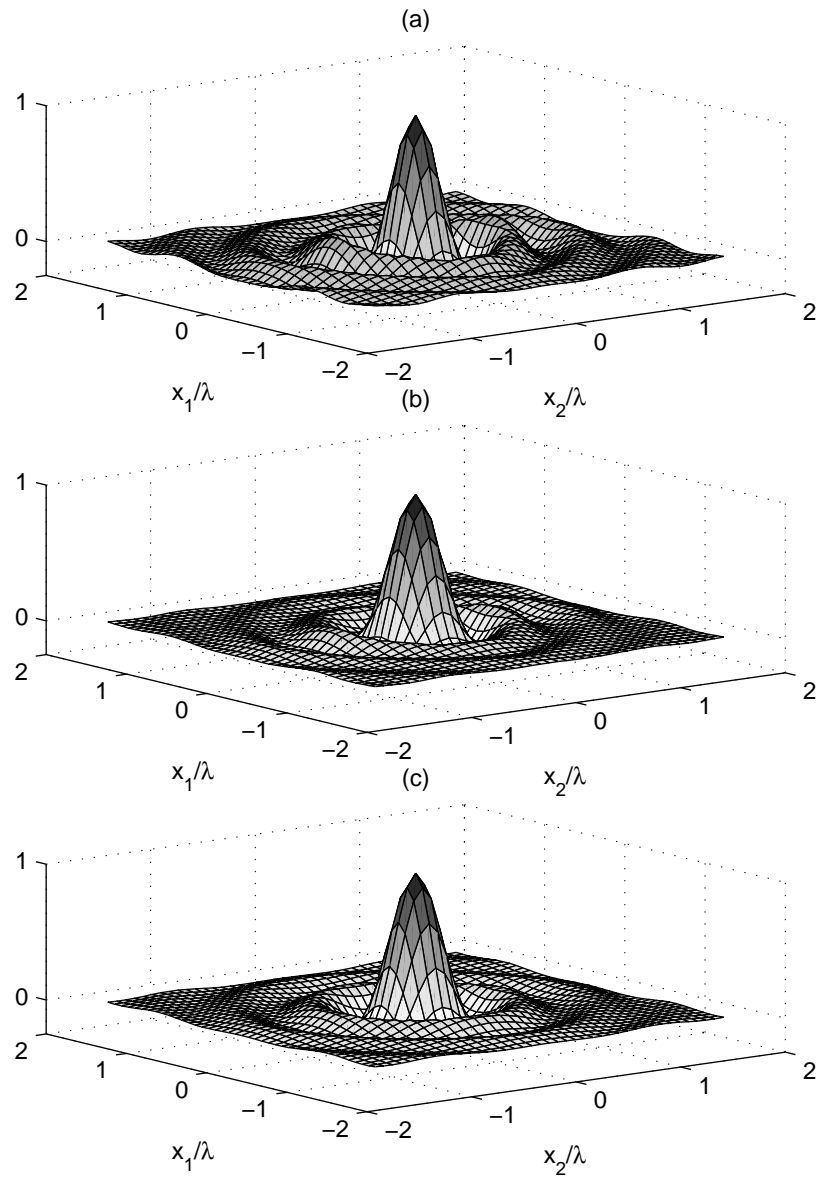


Figure 6.3: Comparison of real part of spatial resolution function using (a) modified SAR (b) modified Gazdag (c) Multi-component inverse extrapolators in a homogeneous space.

Note, that the amplitudes of the resolution functions are proportional to $-C/(2k)$ and $-C$ for the SAR and the Gazdag operators, respectively. Figure

Table 6.5: Overview of the different modified inverse wavefield extrapolators in space and spatial Fourier domain

Inverse extrapolator		space domain \hat{H}^{image}	spatial Fourier domain \tilde{H}^{image}
Gazdag	H^{gd}	$\frac{-k x_3 ^2}{\pi R^2} \exp(j2kR)$	$-j x_3 \exp(jk_3^* x_3)$
SAR	H^{sar}	$-\exp(j2kR)$	$\frac{-4\pi jk x_3 }{(k_3^*)^2} \exp(jk_3^* x_3)$

6.3 shows the real part of the spatial resolution functions using the (a) modified SAR, (b) modified Gazdag and (c) the Multi-component inverse wavefield extrapolators for $f = 500$ MHz for a point scatterer present in a homogeneous space at a depth of 1 meter. The inverse wavefield extrapolation, which is written as a two-dimensional spatial convolution is carried out using a multiplication in the spatial Fourier domain. The multi-component imaging algorithm is implemented by using the far-field expressions. Due to the introduction of the modified scalar inverse wavefield extrapolators, all resolution functions have a positive peak amplitude. Furthermore, it can be observed that the SAR and the Gazdag operators do not result in circularly symmetric resolution functions. In Figure 6.4 the results using the three inverse extrapolators are compared for the x_1 - and the x_2 -axis, respectively. As already indicated in Table 6.4, the width of the main lobe is larger along the x_1 -axis for the Gazdag operator, while the width is smaller in the x_2 -axis. Note that the obtained results can only be compared qualitatively, because in Figure 6.3 a finite acquisition plane was used to calculate the resolution functions, whereas the results given in Table 6.4 were obtained using the closed-form expressions for the resolution functions. The SAR operator has a similar width of the main lobe in the x_1 -axis compared to the multi-component operator. The main lobe in the x_2 -axis is smaller compared to the multi-component operator. However, the amplitude of the oscillations is quite significant. From the expressions for the modified operators given in

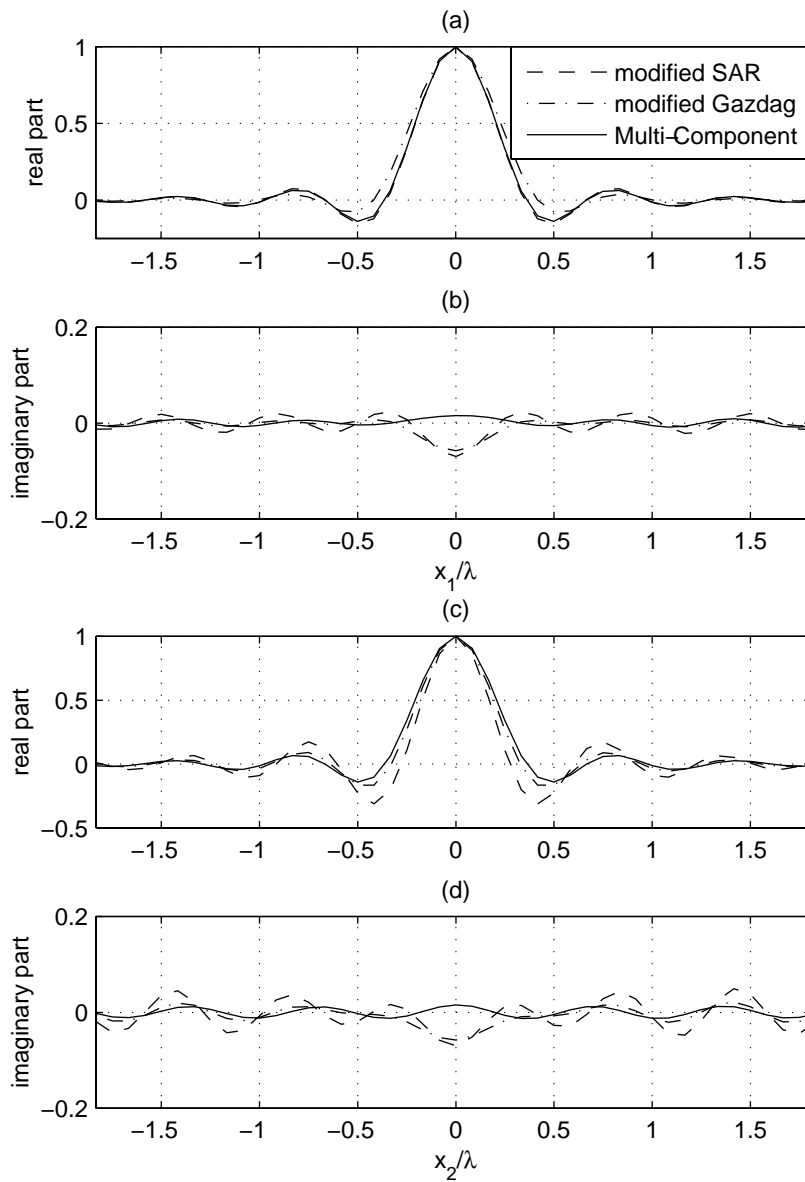


Figure 6.4: Comparison of real and imaginary parts of the spatial resolution functions (a), (b) along x_1 -axis and (c), (d) along x_2 -axis, respectively, in a homogeneous space.

Table 6.5, it can be observed that it is not feasible to take into account the offset $2\mathbf{x}^H$ between the source and receiver antennas when the operators are implemented in the spatial Fourier domain. However, in the space domain the offset between the source and receiver antennas can be easily incorporated as follows,

$$\hat{H}^{gd}(\mathbf{x}^M, \mathbf{x}^H | \mathbf{x}^c, \omega) = j \sqrt{\frac{k}{\pi}} \frac{|x_3^d|}{R^S} \exp(jkR^S) \times j \sqrt{\frac{k}{\pi}} \frac{|x_3^d|}{R^R} \exp(jkR^R), \quad (6.62a)$$

$$\hat{H}^{sar}(\mathbf{x}^M, \mathbf{x}^H | \mathbf{x}^c, \omega) = j \exp(jkR^S) \times j \exp(jkR^R), \quad (6.62b)$$

where

$$R^S = |\mathbf{x}^M - \mathbf{x}^H - \mathbf{x}^d|, \quad (6.63a)$$

$$R^R = |\mathbf{x}^M + \mathbf{x}^H - \mathbf{x}^d|. \quad (6.63b)$$

In this way, the propagation from source to scatter position and the propagation from scatter position towards the receiver is accounted for by two separate phase shifts. Note that for the SAR-operator, each separate phase-shift is supplemented by a factor j , while for the Gazdag-operator each separate phaseshift is supplemented by a factor which consists of a spatial taper $|x_3^d|/R$ and a frequency-dependent factor k and is given by $j\sqrt{k/\pi}|x_3^d|/R$. It is obvious that the two modified operators consist of the appropriate phase-shift, whereas it is recommended to check the validity of the amplitude factor of the Gazdag phase shift by numerical analysis.

6.7.5 Spatial resolution function for a point scatterer in two homogeneous half-spaces

It is not feasible to derive closed-form expressions for the resolution functions of a point scatterer in a homogeneous half-space. Therefore, numerical analyses are carried out for two homogeneous half-spaces. Again a point scatterer is present at a depth of 1 m. The total electric field is calculated using the integral expressions given in Section 4.5. A real-valued contrast with unit amplitude is used to calculate the scattered electric field as in Eq. (6.43). The inverse wavefield extrapolator is derived as discussed in Section 6.5.3 using the far-field expressions for the Greens tensor functions as given in Section 4.4.

In Figure 6.5, the real and imaginary parts of the obtained image for the SAR algorithm are shown. A non-circularly symmetric resolution function

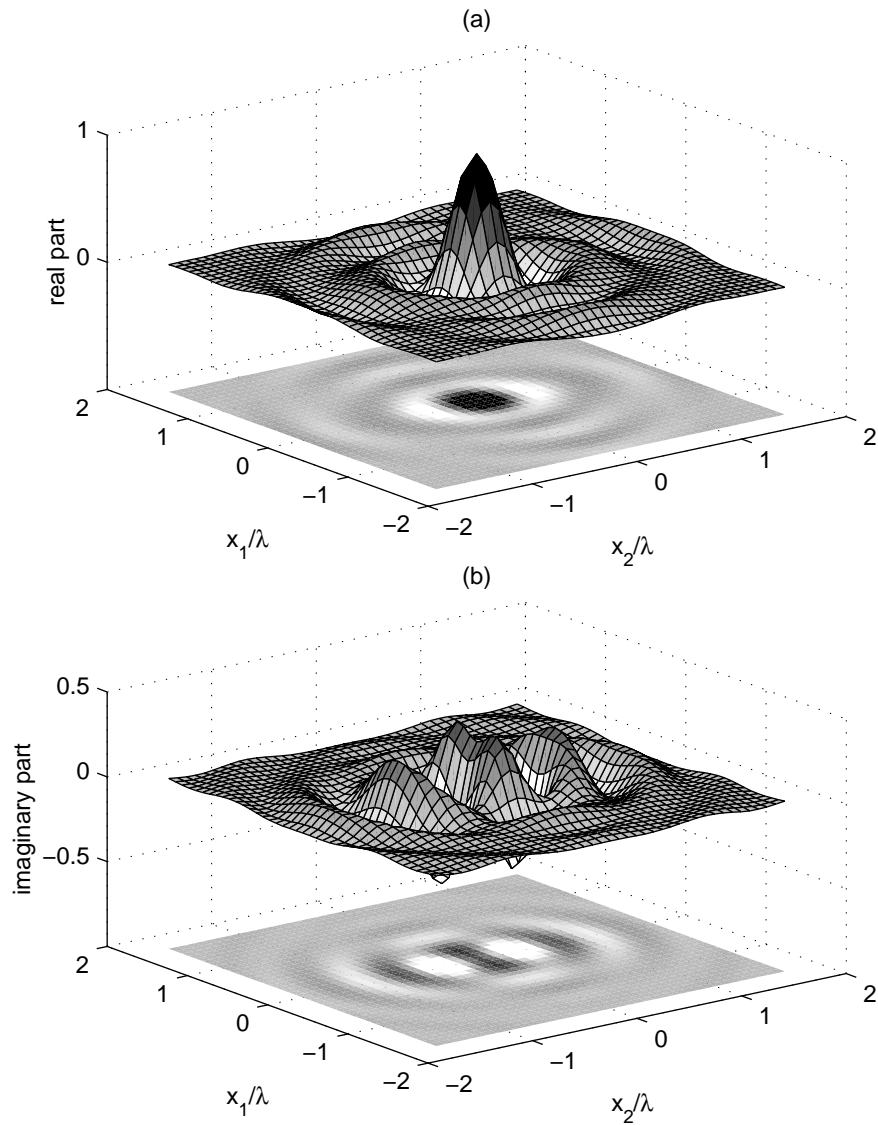


Figure 6.5: (a) Real part and (b) imaginary part of spatial resolution function using the modified SAR imaging algorithm in two homogeneous half-spaces.

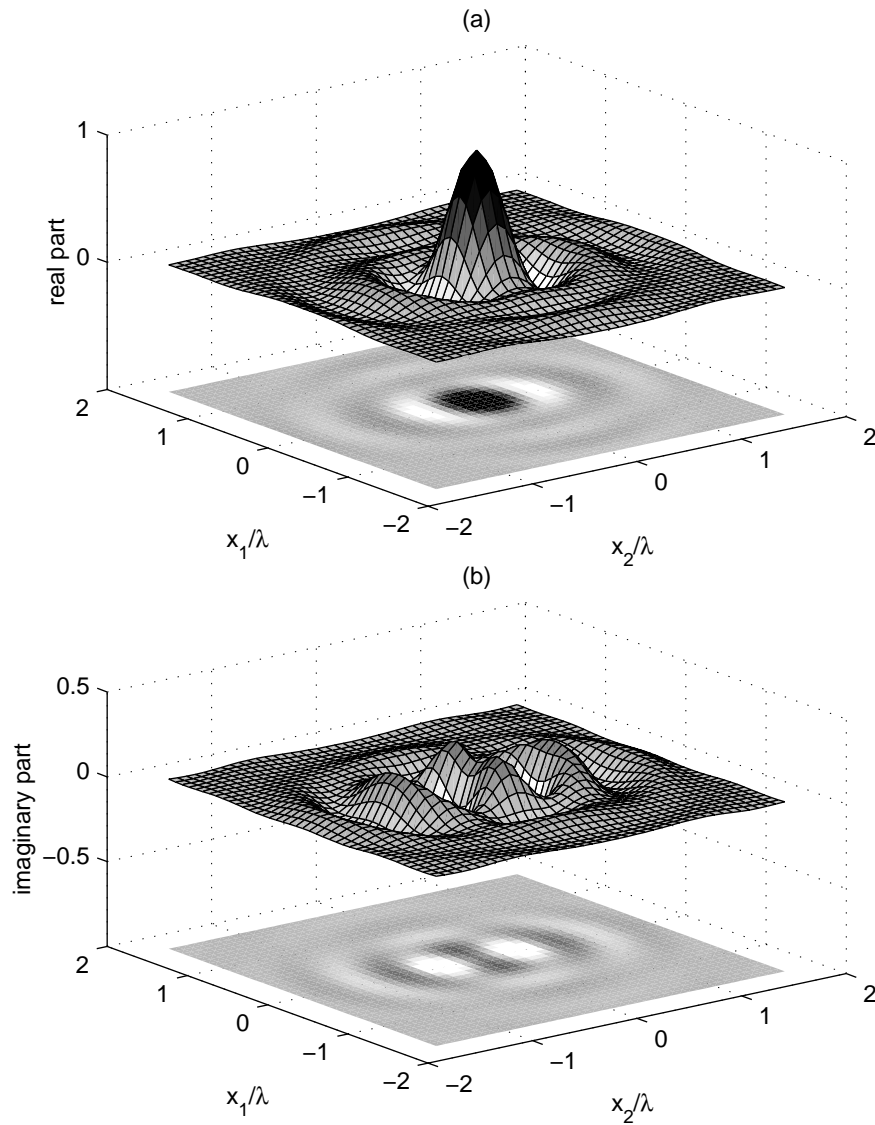


Figure 6.6: (a) Real and (b) Imaginary part of spatial resolution function using the modified Gazdag imaging algorithm in two homogeneous half-spaces.

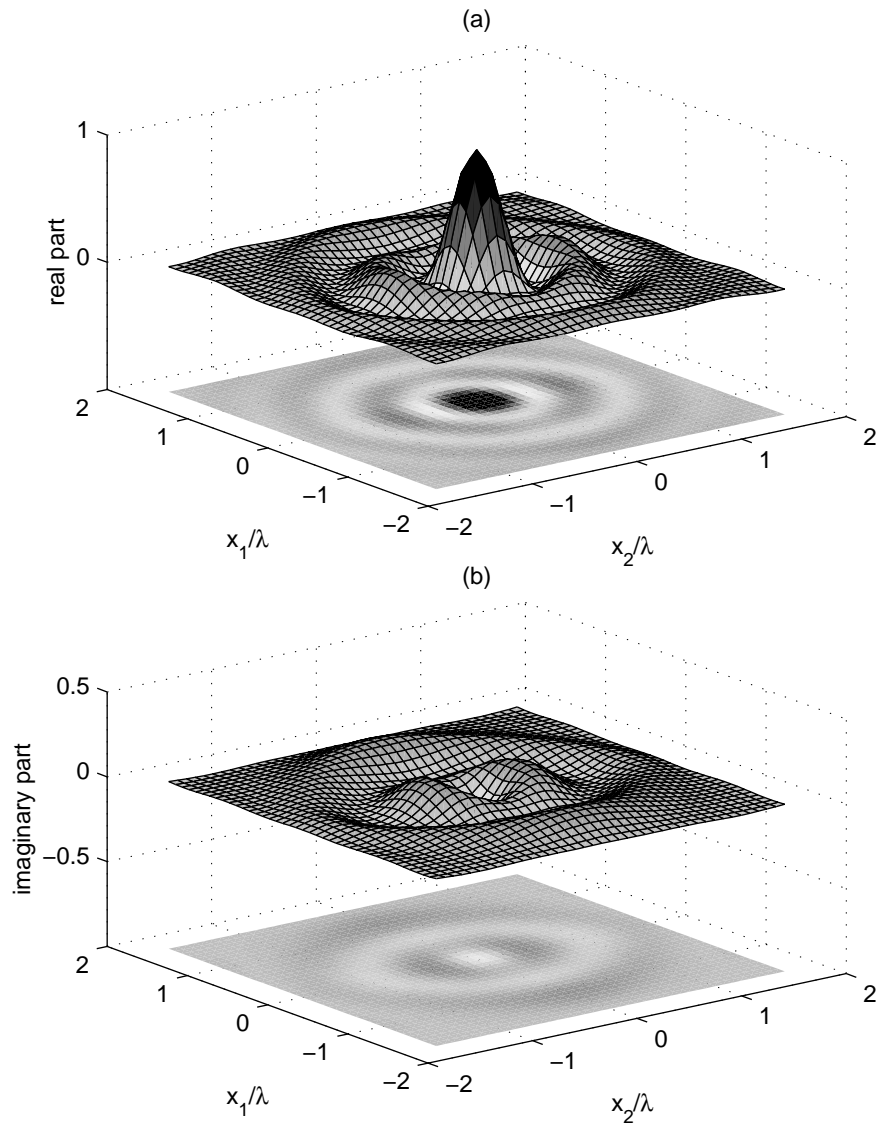


Figure 6.7: (a) Real and (b) Imaginary part of spatial resolution function using Multi-component imaging algorithm in two homogeneous half-spaces.

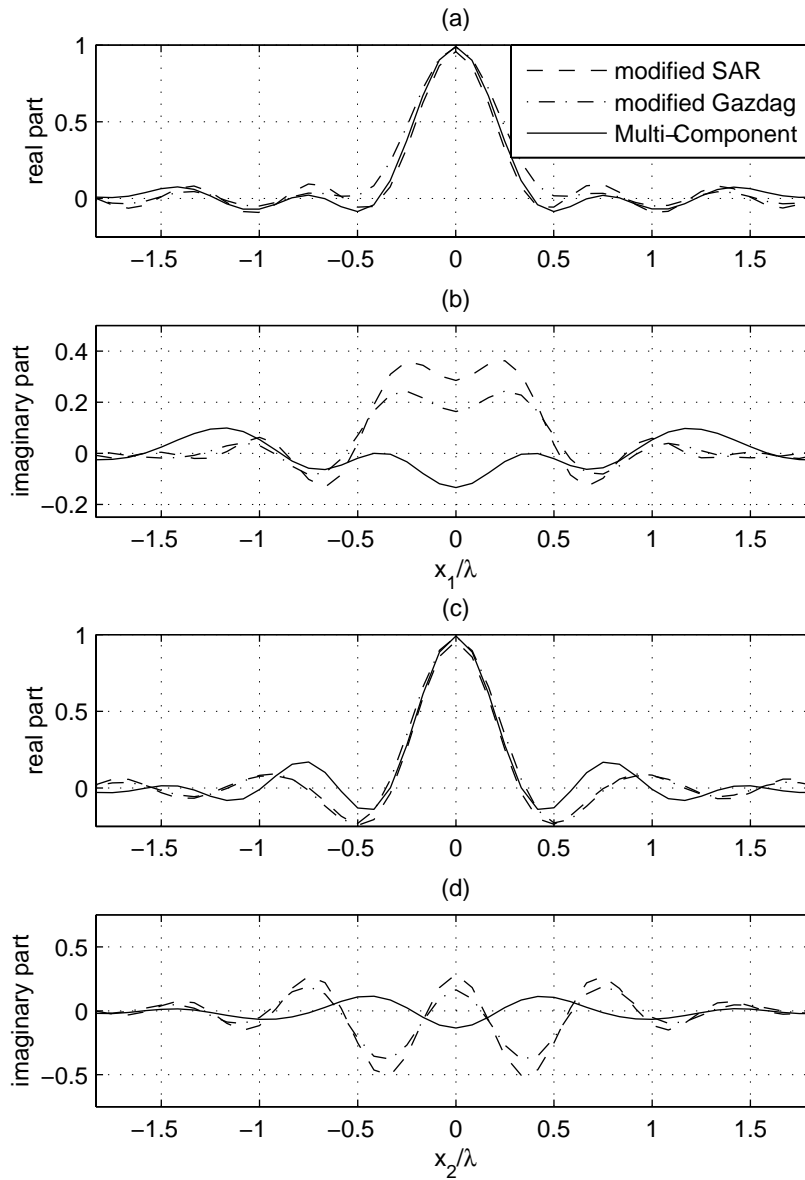


Figure 6.8: Comparison of real and imaginary parts of the spatial resolution functions (a), (b) along x_1 -axis and (c), (d) along x_2 -axis, respectively, in a homogeneous half-space.

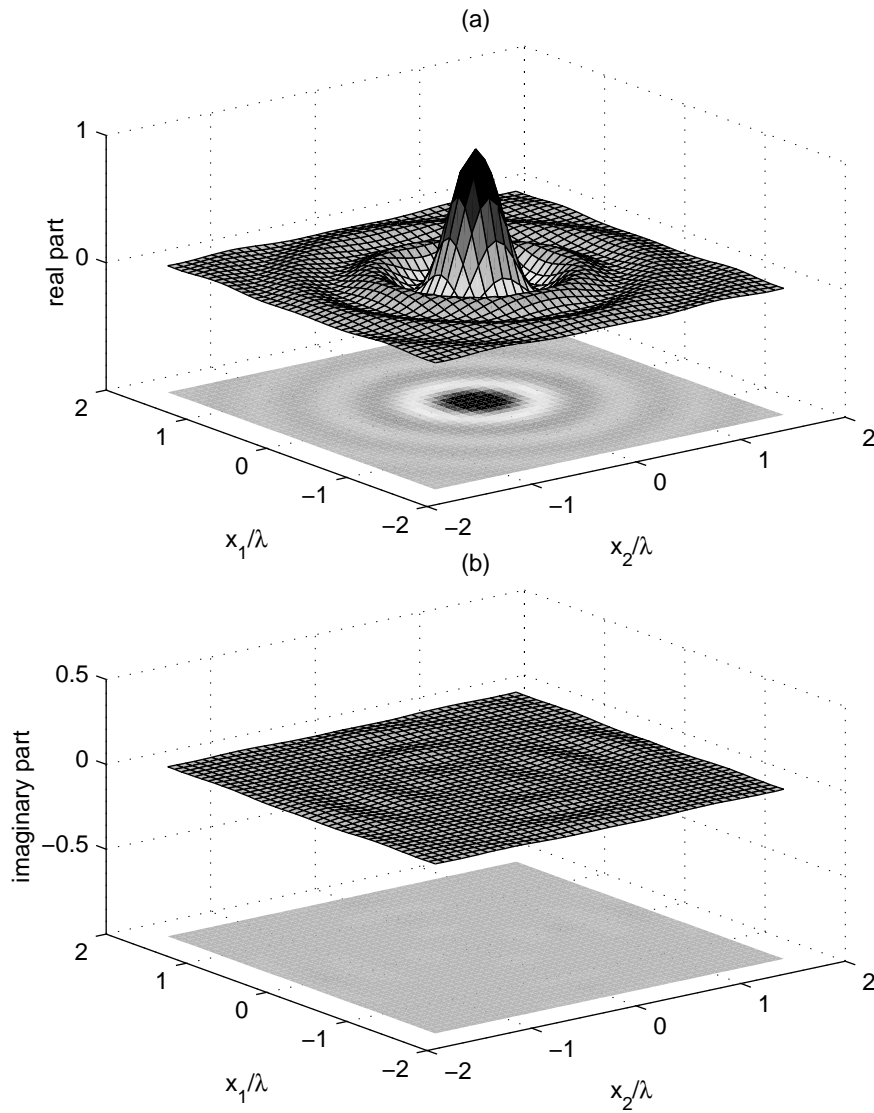


Figure 6.9: (a) Real and (b) Imaginary part of spatial resolution function using multi-component imaging algorithm in two homogeneous half-spaces using the total-field expressions for the inverse wavefield extrapolation.

is obtained. Note that also a non-zero imaginary part is obtained. In Figure 6.6 the real and imaginary parts of the obtained image for the Gazdag algorithm are shown. Again, a non-circularly symmetric resolution function is obtained and a non-zero imaginary part is obtained. Note that the results using the Gazdag operator have fewer oscillations in the tails of the resolution function compared to the SAR imaging results. This is in agreement with Kagalenko and Weedon [1996], who compared the imaging results using the Gazdag phase shift and the SAR imaging algorithms for a two-dimensional configuration and showed that the Gazdag phase shift resulted in a higher image resolution and fewer artifacts than the SAR imaging. Gunawardena and Longstaff [1998] formulated a wave equation-based SAR algorithm which is equal to the Kirchhoff migration algorithm [Schneider, 1978]. They showed that the conventional SAR algorithm is a special case of the wave equation-based SAR algorithms, when the signal is monochromatic, the antenna is narrow beam, and the imaging is done in the Fresnel zone of the synthetic aperture. This explains why conventional SAR algorithms are less appropriate for widebeam applications, such as ground penetrating radar. This result is in agreement with the results obtained for the SAR algorithm in this section, where it is observed that the amplitude of the SAR operator is not bounded for horizontal wavenumbers approaching the boundary between the propagating and evanescent wave region. This explains the relatively large oscillations for the resolution function obtained using the SAR algorithm (see Figures 6.4 and 6.8).

In Figure 6.7 the real and imaginary parts of the obtained image for the multi-component algorithm are shown. The obtained resolution function is more circularly symmetric than the results obtained with the single-component results. The imaginary part obtained with the multi-component imaging algorithm has smaller amplitudes than the single-component imaging results. Note that the use of the far-field expressions, which are used to perform the inverse wavefield extrapolation, do not completely correct for the propagation of the total electric field for a scatterer present at 1 m depth. Due to the fact that an error exists between the total field and the far field, as is discussed in Section 4.6, this results in the real part not being completely circularly symmetric and the imaginary part of the obtained image being unequal to zero. The results are compared for the x_1 - and the x_2 -plane in Figure 6.8. It can be observed that the peaks in the tail for the real part of the multi-component imaging results are located at the same position relative to the maximum, while for the SAR and the Gazdag algorithm the peaks are located

at different positions on the x_1 and the x_2 axes. This again indicates that the results obtained with the multi-component imaging algorithm are more circularly symmetric than the results obtained with the single-component imaging algorithms. Due to the fact that not only a maximum real part is obtained for a real-valued contrast, a phase difference is obtained compared with the expected result, which should be only real valued. The maximum obtained for the SAR algorithm has a phase difference of 17° with the angle of the actual real-valued contrast (0°). The maximum for the Gazdag algorithm has a phase difference of 9° and the multi-component result has a phase difference of -8° . Note that the phase errors are larger over the whole range for the SAR and Gazdag algorithm than for the multi-component algorithm. Using the scalar imaging algorithms for the imaging of the \hat{E}_{21} -component would result in a zero amplitude for a point scatterer, because of the opposite phase characteristics of the tails of the hyperbolas (see also Figure 5.14b). In Figure 6.9 the total-field expressions are used for the inverse wavefield extrapolation of the multi-component imaging algorithm. The result is circularly symmetric and real-valued, while the imaginary part equals zero. This is the best result which could be obtained using the multi-component imaging algorithm. However, it takes an enormous amount of computing time to calculate these total-field expressions as presented in Section 4.5. This indicates that closed-form expressions, which approximate the total-field expressions better than the far-field expressions, will result in improved imaging results.

■

The performance of the scalar imaging algorithms and the multi-component imaging algorithm were investigated by comparing the resolution functions obtained by imaging the response of a point scatterer for a single frequency component. For a homogeneous space, closed-form expressions for the resolution function were obtained. For a real-valued contrast, the scalar inverse wavefield extrapolators do not represent the scatterer adequately. This is the reason why modified scalar inverse wavefield extrapolators are introduced. Still, the scalar imaging results do not show a circularly symmetric resolution function, which is an indication that the radiation characteristics of the source and receiver still influence the obtained image for conventional scalar imaging schemes. The amplitude of a scalar inverse wavefield extrapolator based on the linearised scattering formalism is not bounded. This is the reason why more components are used containing more complete information, in order to arrive at a bounded inverse wavefield extrapolator.

A combination of the four possible source-receiver combinations facilitates the derivation of a bounded multi-component inverse wavefield extrapolator. A multi-component electromagnetic image reconstruction technique has been derived, which is based on the vectorial wave equation. The result for the multi-component imaging of a point scatterer in a homogeneous space for a single frequency component is a more circularly symmetric resolution function than produced by the single-component imaging algorithms. For two homogeneous halfspaces, it is not feasible to carry out a similar analytical approach. However, in a numerical sense, the same procedure can be carried out, which has the important benefit that the offset between the source and receiver can also be taken into account. The resolution function obtained with the inverse wavefield extrapolator, based on the total field, shows a real-valued circularly symmetric resolution function. However, this implementation requires an enormous amount of computing time, so it is not feasible to use the total-field expression in the imaging algorithm. Using the far-field expressions to determine the inverse wavefield extrapolator the resolution function obtained with the multi-component algorithm showed a more circularly symmetric resolution function than the scalar imaging algorithms. In Chapter 7, experimental results are shown of imaging results using the multi-component imaging algorithm, which are compared with the results using scalar imaging algorithms.

Experimental results at the testing site

In this chapter, we will describe the multi-component experiments. The multi-component experiments are carried out in a controlled environment. First, a short description of the construction of the testing site is given. Next, the adaptations to a commercial GPR system are described, which were needed to perform multi-component measurements. The acquisition parameters are discussed and some results of the measurements are given. The multi-component imaging results are compared with the imaging results using the modified scalar Gazdag and SAR algorithms.

7.1 Testing site

For controlled experiments, a testing site is constructed in Scheveningen as a cooperation between the Section of Applied Geophysics, Delft and FEL-TNO, Scheveningen in the framework of a research project funded by the Dutch Technology Foundation (STW). No metallic objects are used for the construction to prevent interference or other unwanted reflections during the measurements. The dimensions of the testing site are 10 meter by 10 meter and 3 meter deep. Since the location is in a protected area, the testing site



Figure 7.1: *The construction of the testing site, where the drainage pipe is visible on the bottom of the testing site.*

is shielded off from its environment. A drainage pipe was present on the bottom of the testing site to enable the control of the water level, which can be observed in Figure 7.1.

In order to obtain a homogeneous distribution of the sand at the testing site, water was pumped into the closed system. Using the drainage pipe the water was pumped out after a certain time to obtain a homogeneous distribution. A tent covers the testing site to protect it from external influences. Along one side of the testing site, an area of 3 meter by 4 meter is used to carry out the measurements. A plastic pipe surrounds this area and is used as a reference frame for accurate localisation of the measurements. The plastic pipe, which is laid down in a square, is visible in Figure 7.2.

7.2 Buried objects

Several steel pipes were buried with a different orientation with respect to the survey lines. One plastic and several metallic spheres were also buried



Figure 7.2: *The area of 3 meter by 4 meter at the testing site in which the multi-component measurements were carried out.*

in the sand. The position of the objects is schematically shown in Figure 7.3 and the properties are given in Table 7.1.

7.3 Description of the measurement set-up

A precise location of each measurement is essential to obtain reliable imaging results. Our imaging algorithm requires as input a regular sampling of the measurements in both spatial directions. To obtain such a regular sampling a trigger must be supplied to the GPR system at each regular sampled grid-point to start a measurement. This trigger is supplied by an external device, also called wheel or string odometer. Usually, the odometer device uses a wheel. The wheel generates a trigger for a certain programmable distance, the spatial sampling distance Δx^M . In this specific experiment, very dry sand was present at the top of the subsurface. This resulted in a slipping of

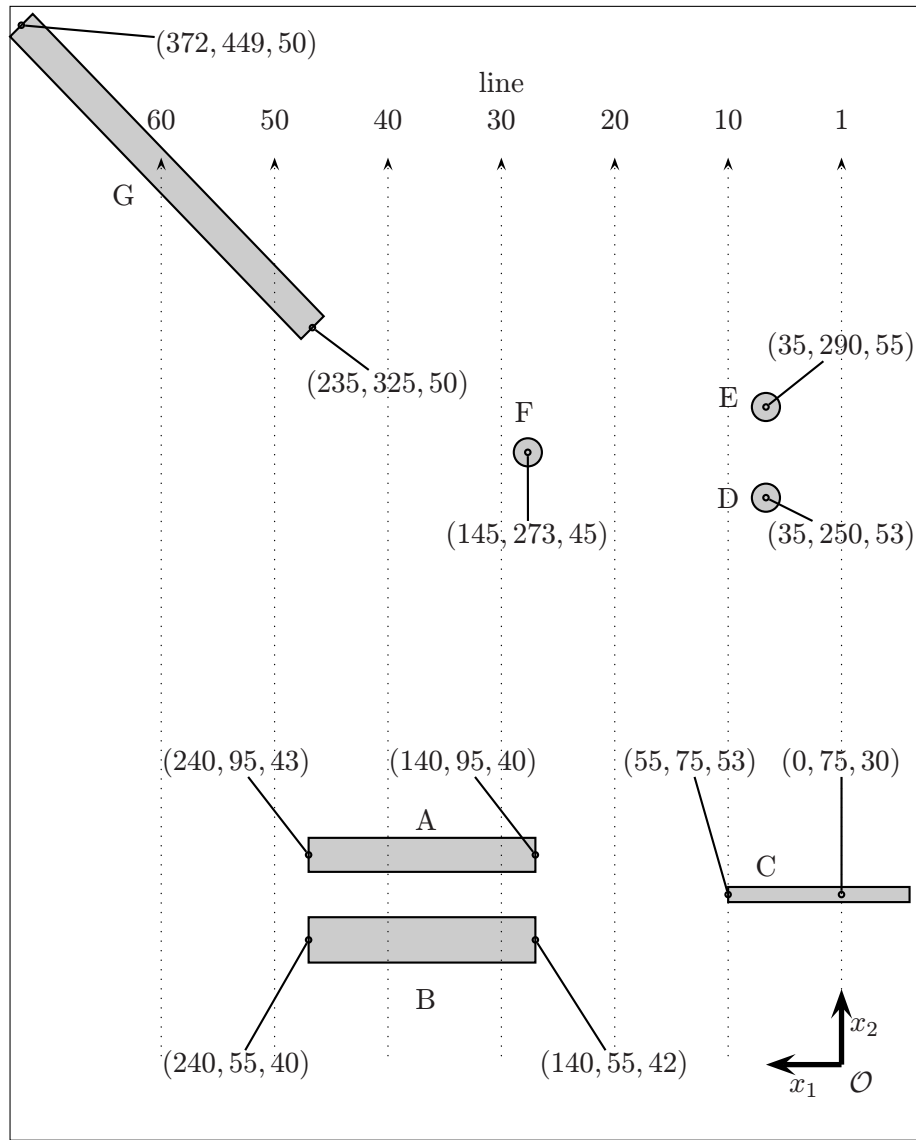


Figure 7.3: Plan view of the buried objects at the testing site (position in (x_1, x_2, x_3) cm).

Table 7.1: Overview of the properties of the buried objects in cm

Object	Material	Length	Diameter	Position (top)
A	Metal pipe	100.0	15.9	(140,95,40) (240,95,43)
B	Metal pipe	100.0	22.3	(140,55,42) (240,55,40)
C	Metal pipe	99.5	6.2	(-35,75,15) (55,75,53)
D	Metal sphere		19.1	(35,250,53)
E	Metal sphere		19.1	(35,290,55)
F	Plastic sphere		21.0	(145,273,45)
G	Metal pipe	185.0	9.0	(235,325,50) (372,449,50)

the odometer wheel, which subsequently resulted in an inaccurate positioning of the measured data. To solve this problem the string setting of the odometer was used. In this way, a string was fixed at the plastic reference frame and a trigger was produced by unwinding the string. Consequently, a more accurate inline positioning of the measurements was obtained. To achieve an accurate crossline positioning, the plastic reference frame was used on which strings were positioned at specified positions on each side of the survey line. The string is visible on Figure 7.4. Along these strings the radar system must be aligned. In this way, a reasonably accurate crossline positioning was achieved. Measurements were made with the pulseEKKO 1000 system using the four inline orientations of the source and receiver antennas shown in Figure 5.2. To enable different orientations necessary for the multi-component measurements, a very rigid frame was constructed to ensure that the offset and the alignment between the two antennas remained fixed. This frame enables the four inline orientations of the source and the receiver antennas as shown in Figure 7.5.

7.4 Acquisition parameters

The multi-component measurements were carried out on a survey grid consisting of 60 lines with an inline and crossline spatial sampling of $\Delta x_1^M = \Delta x_2^M = 5$ cm. The offset between the source and receiver antennas was $2\Delta x_2^H = 35$ cm, which was chosen in such a way that for all orientations no clipping of the measured electric field occurs. The locations of every tenth

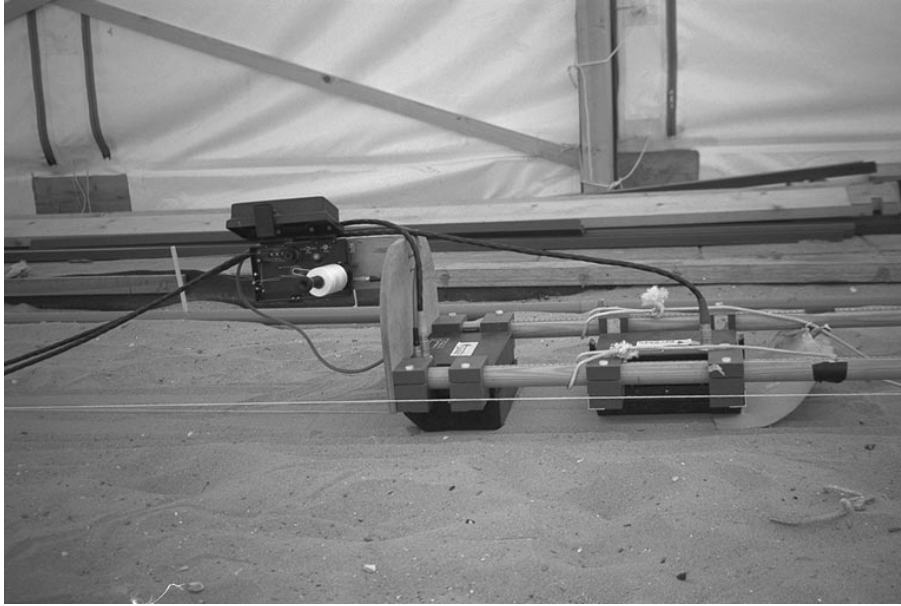


Figure 7.4: *The pulseEKKO 1000 with the odometer using a string for localisation.*

survey line are indicated in Figure 7.3. Note that only part of the reflections coming from pipe G are measured. A stacking fold of 16 was used to increase the signal to noise ratio. The temporal sampling interval was 50 ps, which was used to obtain 1000 samples, which resulted in a time window of 50 ns. The specified center frequency of the antennas is 900 MHz.

7.5 Pre-processing

First of all, the measured data of the different survey lines are aligned. This alignment is carried out by aligning the maximum and minimum values of the direct air wave. Our imaging algorithm assumes that only scattered data are measured. In reality, direct waves are also measured, the air- and ground-wave. To remove these direct waves, which are equal for each measurement in the case of a homogeneous top layer, a simple average subtraction is carried out. Note that in Figure 7.4 it can be observed that the surface of the ground is not flat, so that the direct waves will differ for different locations and the average subtraction will result in an error.

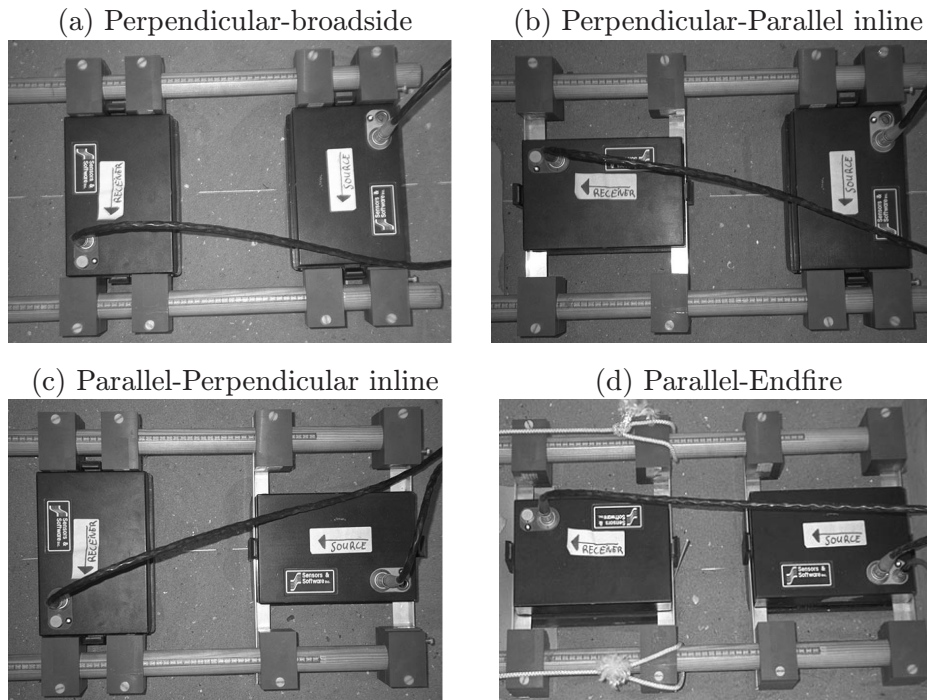


Figure 7.5: Four inline orientations in a rigid frame used for the multi-component experiments with an offset of 35 cm.

7.6 Medium properties

The most important parameter for accurate imaging is the phase velocity. Therefore, it is very important to know the relative permittivity, which determines the phase velocity (see also Eq. (4.1)). To obtain more insight into the permittivity distribution at the testing site, Time Domain Reflectometry (TDR) measurements were carried out with two different lengths of the TDR probes¹. In TDR, the (apparent) dielectric constant is determined from the time it takes for an electromagnetic wave to travel along the TDR probe, which is inserted in the soil [Heimovaara, 1994; Nguyen, 1999; Dam and Schlager, 2000]. The measurements were carried out in a pit in August 1998. By analysing the traveltime along the TDR probe, the relative permit-

¹These measurements were carried out in co-operation with the VU Amsterdam

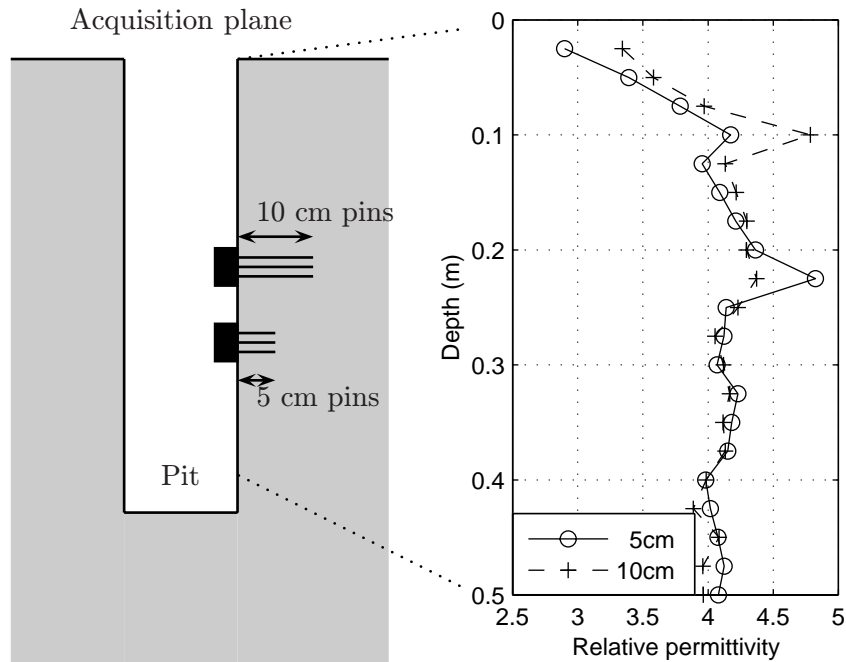


Figure 7.6: Estimates of the relative permittivity using TDR probes with a length of 5 and 10 cm in the side of a pit.

tivity was determined. It is depicted in Figure 7.6 as a function of the depth. A strong gradient is present near the surface. A low relative permittivity is present at the surface and increases with depth. Note that these travel times are obtained by time-domain analysis and valid for the frequency range of the pulse which has traveled along the TDR probes. A frequency-dependent phase velocity cannot be obtained using this time-domain analysis.

These TDR measurements show that the shallow part of the subsurface has different medium properties compared with the soil present deeper in the subsurface due to e.g. a dry period or recent precipitation. This fact has important consequences, as is also indicated in Section 5.9.

Frequency-domain analysis of TDR measurements enable the determination of frequency-dependent medium properties. The Debye equation [Debye, 1929] is often used to describe the frequency-dependency of the relative permittivity with a limited number of unknowns [Nguyen, 1999]. Recently, Friel

and Or [1999] have shown a more complete picture of TDR responses in the frequency-domain, resulting in a frequency-dependent phase velocity and attenuation. However, for high frequencies the results of Friel and Or [1999] often show erratic behaviour. One of the causes is the nonhomogeneous constituent distribution and composition of natural porous media. It is not feasible to obtain local frequency-dependent medium properties in the domain of interest, because a destructive TDR measurement at each position would be required. However, it is recommended to determine effective medium properties which describe the main characteristics of the frequency-dependent and location-dependent medium properties. TDR measurements can give an indication of the permittivity distribution. The vertical permittivity distribution is probably the most important factor to know. It is caused by the influence of the weather on the shallow part of the subsurface.

In Juli 1999, the multi-component measurements were carried out. Due to the protection against external influences such as rain, the topsoil was even more dehydrated than the relative permittivity results obtained in August 1998 with the TDR measurements. This forced us to use an overall effective relative permittivity of 3.1. In the following analysis, we assume a frequency independent relative permittivity of 3.1.

7.7 Three-dimensional imaging results

The data were imaged using an effective relative permittivity for the lower homogeneous halfspace of $\varepsilon_r = 3.1$, while taking into account the radiation patterns in a homogeneous halfspace and the offset between the source and receiver as described in Section 6.5.3. The obtained results are compared with the results obtained using the modified SAR and modified Gazdag operator, as described in Section 6.7.4. The inverse wavefield extrapolation for each depth level is described in Section 6.6 as a convolution of the measured scattered electric field $\hat{\mathbf{E}}$ with the inverse wavefield extrapolator $\hat{\mathbf{H}}^{inv}$. For all three imaging operators, the inverse wavefield extrapolators are calculated in the space domain. The two-dimensional Fourier transformation of the inverse wavefield extrapolator and the measured electric field is determined, which enables the actual inverse wavefield extrapolation to be carried out by a multiplication in the spatial Fourier domain. Next, the image is obtained by an inverse spatial Fourier transformation at each depth level. The imaging principle given in Eq. (6.39) is performed using a summation of 45 frequencies in the range of 100-960 MHz, which has been carried out for positive frequencies

only. This facilitates the analysis of real and imaginary parts of the obtained contrast, separately. In our analysis, the source wavelet is not taken into account. As a consequence, the properties of the scattered objects cannot be extracted. However, the analysis of real and imaginary parts separately, is the most appropriate way to investigate differences between the different imaging algorithms. Due to the fact that the inverse wavefield extrapolation is carried out in the spatial Fourier domain with a regular spatial sampling of $x_1^M = x_2^M = 5$ cm, the spatial sampling in the imaging domain is also 5 cm in both horizontal directions. The spatial sampling in the vertical direction is 5 cm, but can be chosen independently of the horizontal sampling.

The actual multi-component measurements were carried out using the four inline source-receiver combinations as depicted in Figure 7.5. The survey lines are oriented in the x_2 -direction. The scattered electric field measured in the perpendicular-broadside configuration and the perpendicular-parallel inline-configuration are represented by E_{11} and E_{21} , respectively. The multi-component imaging algorithm combines these two measurements, which results in the contrast quantity $\langle \bar{\chi}^{\hat{\eta}}(\mathbf{x}^n) \mathbf{I} \rangle_{11}$ derived from Eq. (6.40). Similarly, the scattered electric field measured in the parallel-perpendicular inline-configuration and the parallel-endfire inline-configuration are represented by E_{12} and E_{22} , respectively. The multi-component imaging algorithm combines these two measurements to give the contrast quantity $\langle \bar{\chi}^{\hat{\eta}}(\mathbf{x}^n) \mathbf{I} \rangle_{22}$ as derived from Eq. (6.40). The imaging results $\langle \bar{\chi}^{\hat{\eta}}(\mathbf{x}^n) \mathbf{I} \rangle_{22}$ were of lower quality than the results of $\langle \bar{\chi}^{\hat{\eta}}(\mathbf{x}^n) \mathbf{I} \rangle_{11}$. A possible explanation is the fact that for the parallel-endfire configuration, the main energy is measured from near the critical angle where the far-field radiation characteristic, which is used by the imaging algorithm, does not describe correctly the actual electric field. In addition, Slob [2001] shows that the radiation characteristics for a finite antenna differ considerably from the radiation characteristics from a point source. Another explanation is ringing which has a higher amplitude for the parallel-endfire configuration. This is probably caused by the fact that the radial component of the electric field in the E -plane is relatively large compared with the electric field in the H -plane (see Figures 4.7 and 4.9). In our case, it is also observed from Figure 7.3 that the buried objects are parallel to the orientation of the perpendicular-broadside configuration. This configuration will return the maximum energy for the specific objects. However, for cases without a priori knowledge, it is recommended that all four components are measured to obtain the image result as given in Eq. (6.41). Based on the obtained results, it is recommended to measure with

the parallel-broadside crossline measurements, or a perpendicular-broadside inline-measurements with a reoriented measurement grid as was shown in Section 5.6.4. In this way, both components in Eq. (6.41) can be used to obtain the image. Because of the low quality of $\langle \bar{\chi}^{\hat{\eta}}(\mathbf{x}^n) \mathbf{I} \rangle_{22}$, we only show the results for $\langle \bar{\chi}^{\hat{\eta}}(\mathbf{x}^n) \mathbf{I} \rangle_{11}$, which consist of a real and an imaginary part at each position in the image domain.

7.7.1 Equi-amplitude surfaces for the multi-component imaging results in a three-dimensional volume

To obtain an overall picture of the obtained results, surfaces of constant absolute value in the image domain were used to depict the different objects in a representative way. The threshold for this surface of constant amplitude must be chosen relative to the maximum amplitude of the object. Because the imaged contrast of the different objects had different maximum amplitudes, different thresholds were used. These are indicated in Figure 7.7 for the multi-component imaging results $\langle \bar{\chi}^{\hat{\eta}}(\mathbf{x}^n) \mathbf{I} \rangle_{11}$. In Figures 7.8 and 7.9, these results are depicted for different observation angles. The metal pipes A and B have the largest amplitude and the plastic sphere F has the smallest amplitude. Some other anomalies are present, which have amplitudes comparable with the amplitude of the imaged plastic sphere (F). The distribution of the obtained imaging results is probably due to positioning errors and the combination of two separate measurements for E_{11} and E_{21} . The off-diagonal components $\langle \bar{\chi}^{\hat{\eta}}(\mathbf{x}^n) \mathbf{I} \rangle_{12}$ and $\langle \bar{\chi}^{\hat{\eta}}(\mathbf{x}^n) \mathbf{I} \rangle_{21}$ in Eq. (6.40), which served as a quality control had smaller amplitudes than the diagonal components. Relatively large amplitudes for the off-diagonal components were observed at the endpoint of pipes A and B, for the dipping pipe C and for the oblique pipe G. Note that the equi-amplitude results are only shown to give an overall view of the different objects present at the testing site.

7.7.2 Comparison between the imaging algorithms in different planes

The original SAR algorithm would return an image which would have an opposite sign to the results obtained with the multi-component imaging algorithm, whereas the Gazdag algorithm would return an imaged contrast with a maximum value which is out of phase with the multi-component imaging result (see also Section 6.7). The use of the modified SAR and Gazdag algorithms, which are given in Section 6.7.4, enable a thorough comparison, because the three algorithms return for a certain scatterer an imaged con-

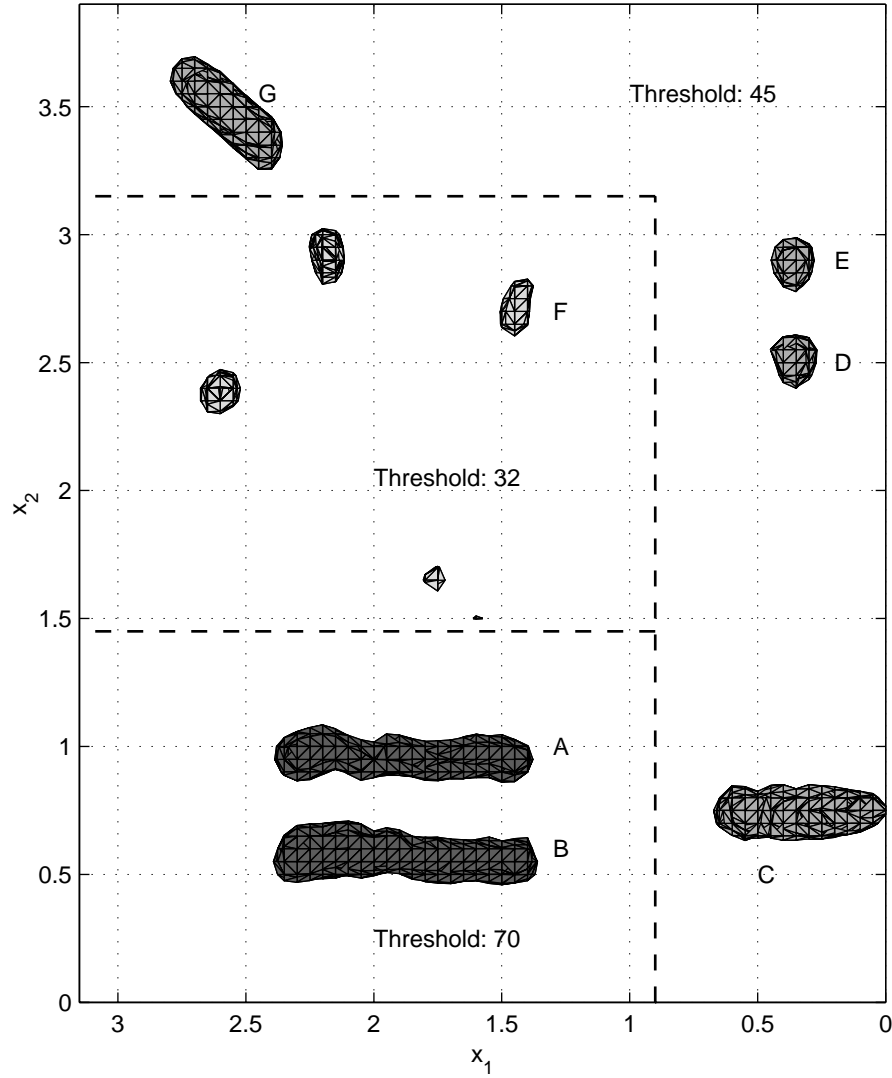


Figure 7.7: Plan view of the multi-component imaging results $\langle \bar{\chi}^{\hat{n}}(\mathbf{x}^n) \mathbf{I} \rangle_{11}$ using pulseEKKO 1000, 900 MHz antennas in the perpendicular-broadside configuration and the perpendicular-parallel inline-configuration.

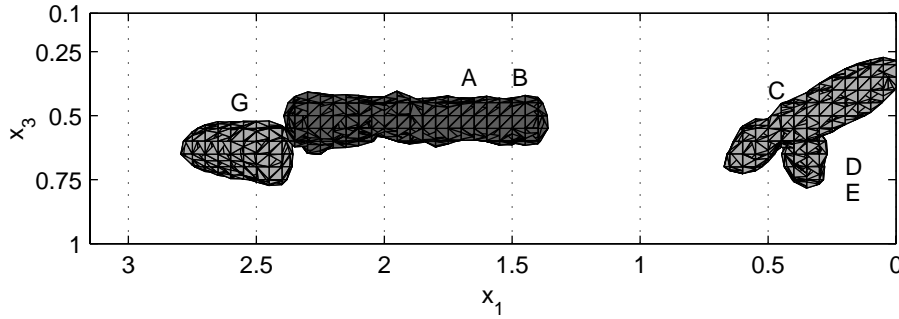


Figure 7.8: Side view of the multi-component imaging results $\langle \bar{\chi}^{\hat{n}}(\mathbf{x}^n) \mathbf{I} \rangle_{11}$ using pulseEKKO 1000, 900 MHz antennas in the perpendicular-broadside configuration and the perpendicular-parallel inline-configuration.

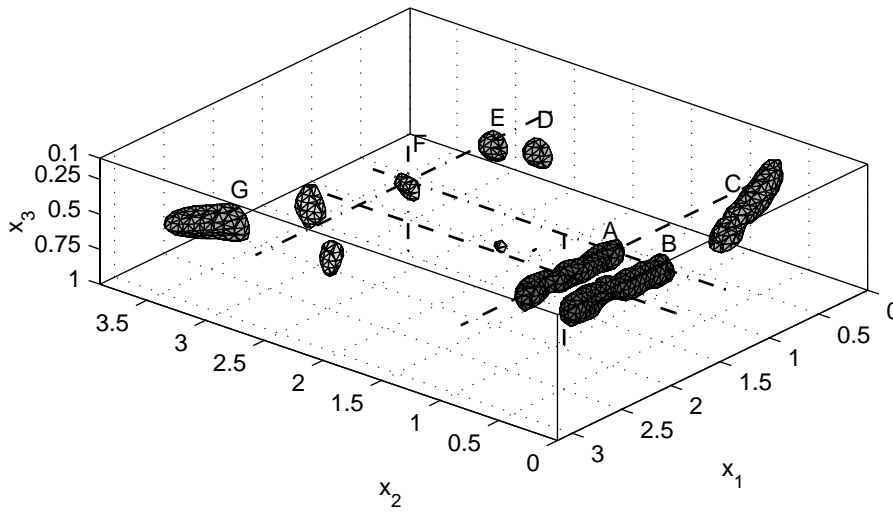


Figure 7.9: Perspective view of the multi-component imaging results $\langle \bar{\chi}^{\hat{n}}(\mathbf{x}^n) \mathbf{I} \rangle_{11}$ using pulseEKKO 900 MHz antennas in the perpendicular-broadside configuration and the perpendicular-parallel inline-configuration.

trast which represents the properties of the scatterer. Due to the different constants used by the different imaging algorithms, the obtained amplitudes differ. This was already indicated by the results of the resolution functions discussed in Section 6.7.4, which are proportional to $k/(2\pi)$, $-C/(2k)$ and $-C$ for the multi-component, the modified SAR and the modified Gazdag operators, respectively. To enable a comparison, the results of the different imaging algorithms are normalised with respect to the maximum absolute value obtained for the multi-component imaging result. The maximum absolute values for the multi-component, modified SAR and modified Gazdag imaging results were 149 , $4.9 \cdot 10^5$ and $2.6 \cdot 10^6$, respectively and were obtained for the image result of steel pipe B.

To compare the multi-component imaging algorithm with the modified scalar Gazdag and SAR algorithm, the imaged contrast in the image domain are analysed in different slices, in which several objects are present. In Figures 7.10-7.12 the real, imaginary and absolute values of the imaged contrast are plotted for $x_2 = 0.95$, the vertical plane which intersects pipe A. It is observed that artefacts are present using the modified SAR algorithm on each side of the steel pipe (indicated with arrows). This is probably due to the fact that the amplitude for large horizontal wavenumbers is relatively large for the SAR algorithm. This was also discussed in Section 6.4.2. The obtained results are in agreement with Johansson and Mast [1994] and Mast and Johansson [1994], who also showed that the frequency-wavenumber method is better than the SAR imaging algorithm. Note that they implemented the SAR algorithm in the space-time domain, which needs an interpolation of the results in time-domain. In our case the limited acquisition plane has its influence on the performance of the SAR algorithm. Despite the fact that the SAR algorithm is implemented in different domains, the performance is still comparable. Gunawardena and Longstaff [1998] explained why the conventional SAR algorithms are less appropriate for widebeam applications, such as ground penetrating radar.

It is also observed that the dipping pipe C, which is present for $x_2 = 0.75$ m, is vaguely visible in the multi-component image results (indicated with an arrow). These artefacts are not so obvious in the imaging results depicted in Figure 7.12 for the multi-component algorithm, where the absolute values of the imaged contrast are plotted.

In Figures 7.13-7.15 the real, imaginary and absolute values of the obtained image are plotted for $x_1 = 0.35$. This plane intersects objects C, D and E. In Figure 7.15 it can be observed that the amplitude for the imaged

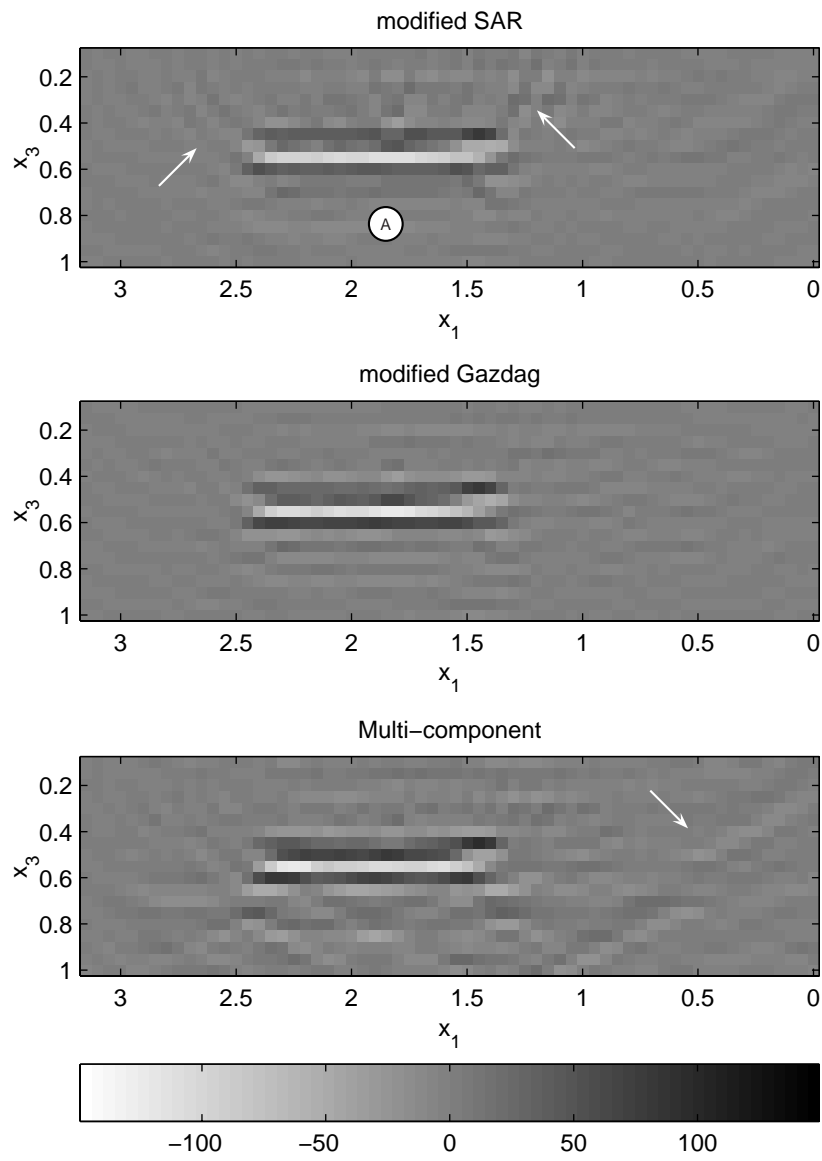


Figure 7.10: Comparison of the real part of the image results for $x_2 = 0.95$ m.

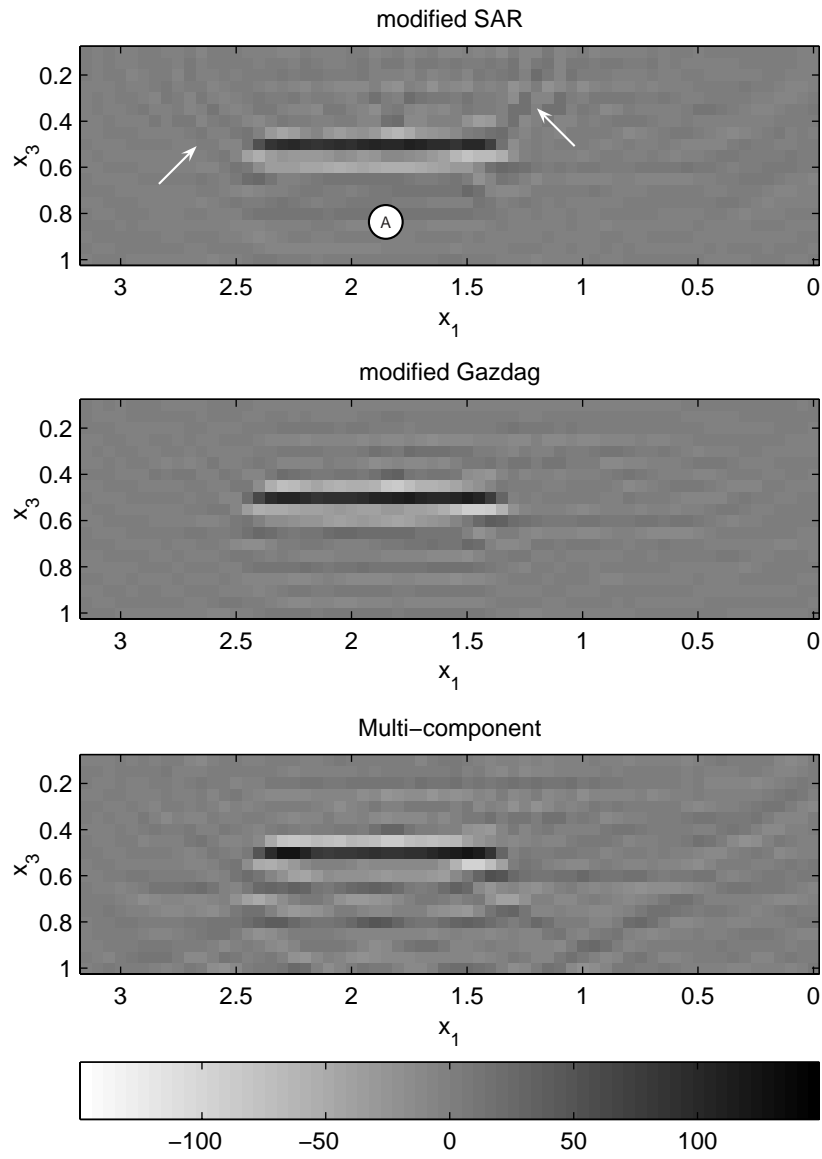


Figure 7.11: Comparison of the imaginary part of the image results for $x_2 = 0.95$ m.

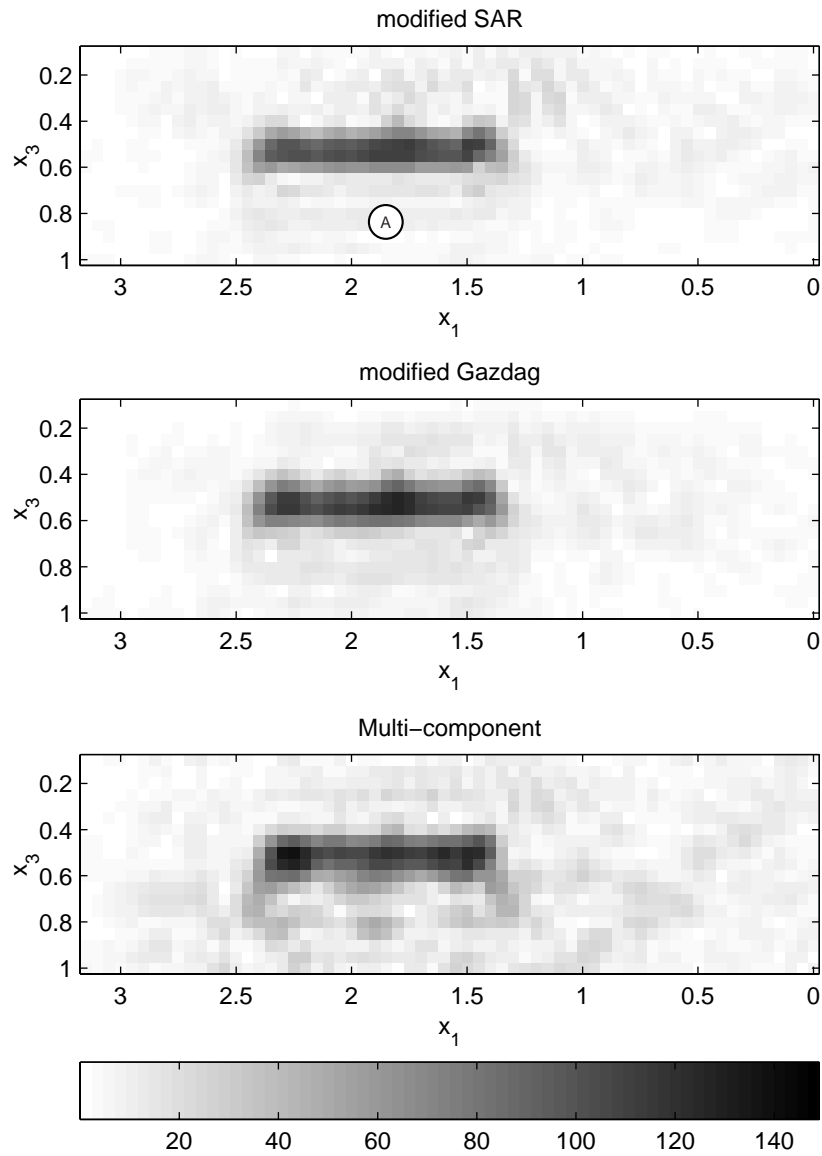


Figure 7.12: Comparison of the absolute values of the image results for $x_2 = 0.95$ m.

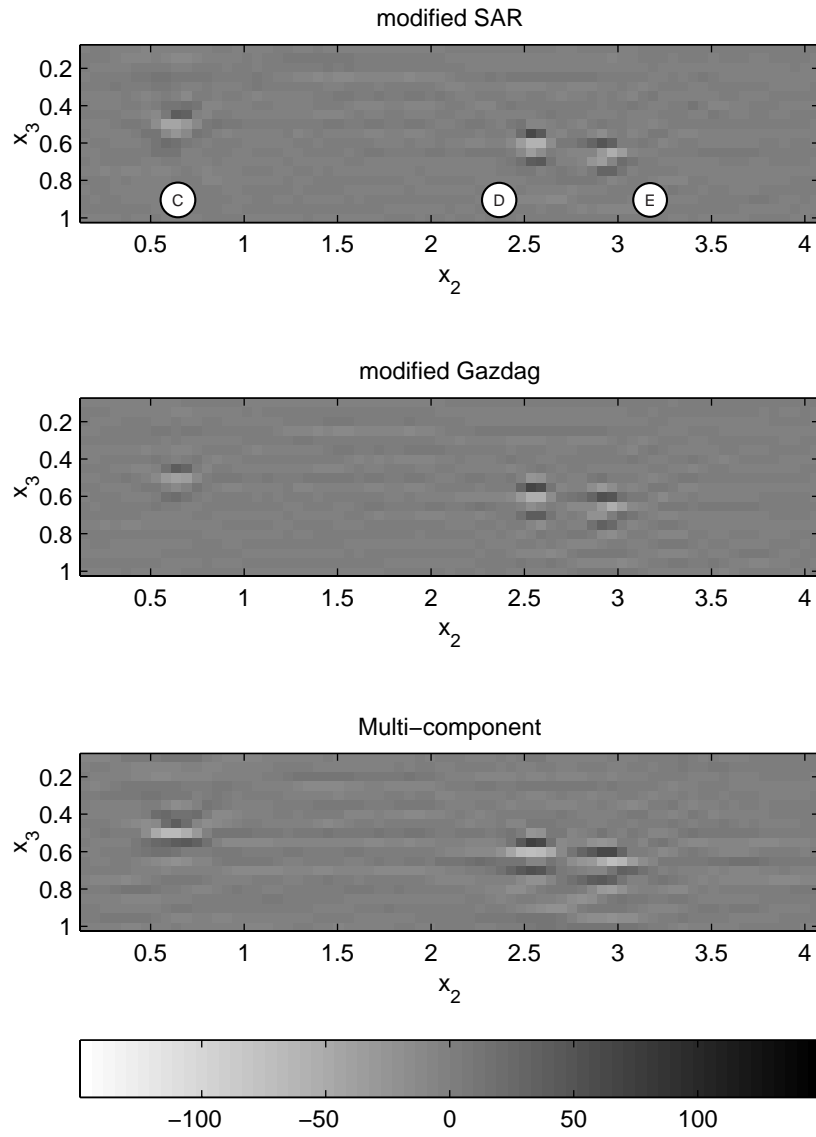


Figure 7.13: Comparison of the real part of the image results for $x_1 = 0.35$ m.

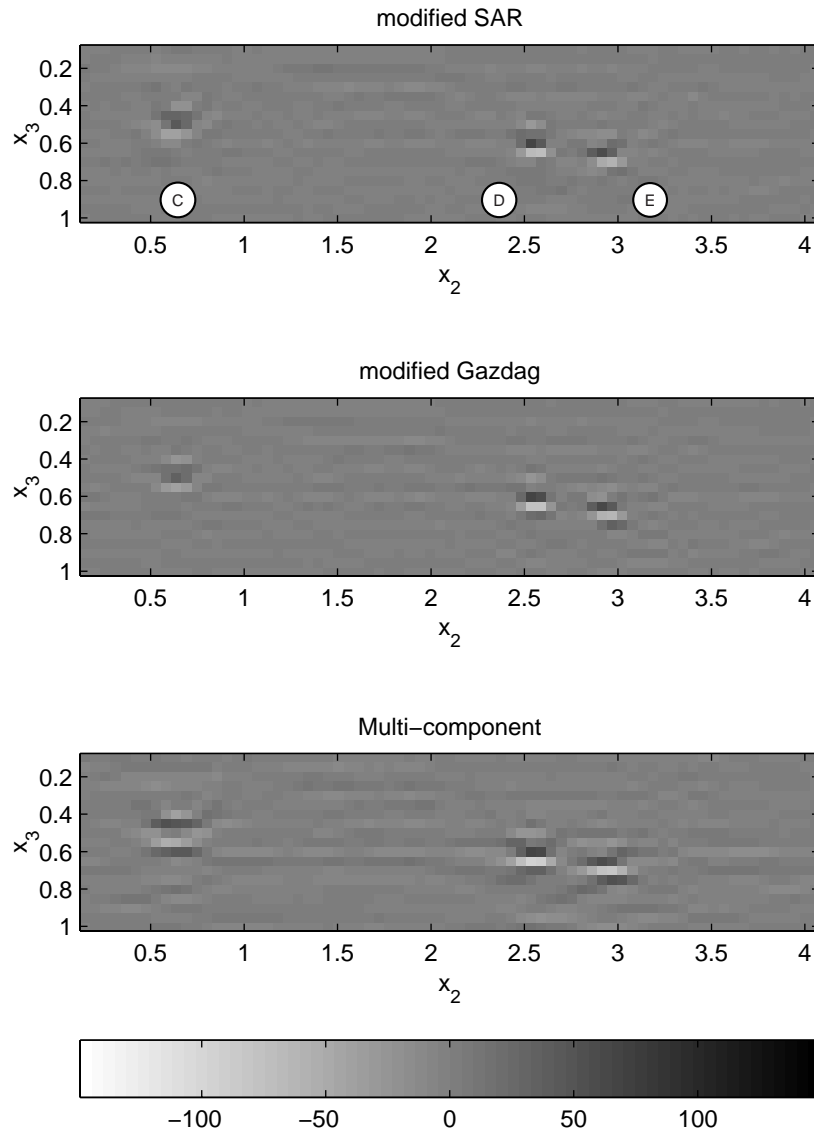


Figure 7.14: Comparison of the imaginary part of the image results for $x_1 = 0.35$ m.

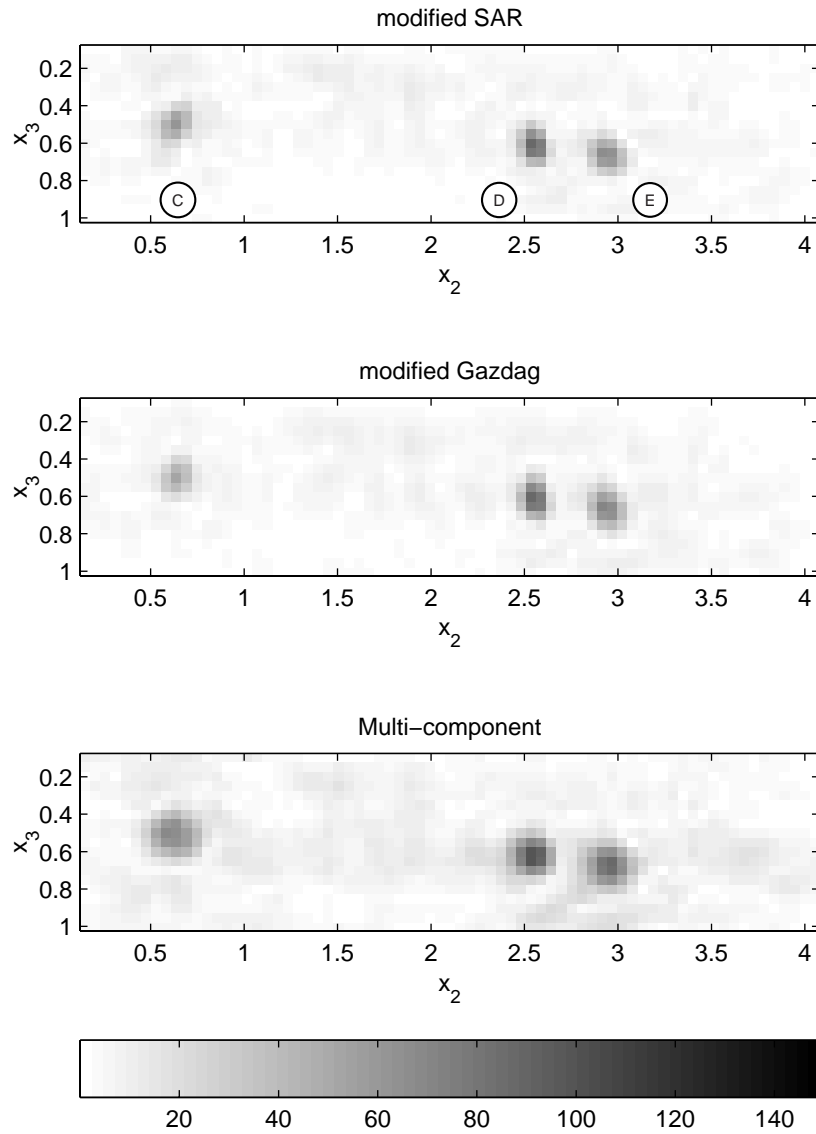


Figure 7.15: Comparison of the absolute values of the image results for $x_1 = 0.35$ m.

results obtained with the multi-component imaging algorithm is large compared with the results of the modified SAR and the results of the modified Gazdag imaging algorithm. However, the spatial resolution of the obtained results using the multi-component algorithm seems to be less than the results obtained by the modified SAR and the modified Gazdag imaging algorithm. However, to analyse the spatial resolution, the results must be normalised with respect to their maximum. In section 7.7.3, the amplitudes along specific lines are analysed. This enables a thorough analysis of the obtained resolution.

In Figures 7.16-7.18, the real, imaginary and absolute values of the obtained image are plotted for $x_3 = 0.6$ m for the region bounded by $2.3 < x_2 < 3.8$ and $0 < x_1 < 3.2$. This plane intersects objects D, E and G. The amplitude of the imaged contrast of object G, which is obtained with the multi-component imaging algorithm is greater than the amplitude obtained with the modified SAR and the modified Gazdag imaging algorithms. This is probably due to the fact that the \hat{E}_{21} -component has its maximum response when both antennas are oriented at a 45 degree angle to the pipe [Daniels et al., 1988]. Due to the fact that we did not measure all possible reflections from pipe G, the amplitudes of the obtained image reduce when approaching the boundary of the image domain.

7.7.3 Comparison between the imaging algorithms along lines

The different slices enable a global comparison between the results obtained by using different imaging algorithms. Another way to compare the different results is to plot the obtained amplitudes along a line which intersects an object. Such an analysis is carried out for the metal pipe A and the plastic sphere F. In Figures 7.19-7.21 the real, imaginary and absolute values of the image result are plotted for the three imaging procedures, along three lines which intersect at the location of object A and are parallel to the x_1 , x_2 and x_3 -axis, respectively. These lines intersect position $\mathbf{x} = (1.95, 0.95, 0.55)$ are also indicated by the dashed line in Figure 7.9. In Figure 7.19, the largest amplitude is obtained for the real part of the imaged contrast for all imaging algorithms. Furthermore it is noted that the imaginary part is small between the endpoints of the pipe for the multi-component imaging result compared with the modified Gazdag and modified SAR result. In Figures 7.20 and 7.21, the obtained resolution for the multi-component imaging result is worse compared with the scalar imaging algorithms. At position $\mathbf{x} = (1.95, 0.95, 0.55)$, the phase of the SAR, Gazdag and multi-component imaging results are

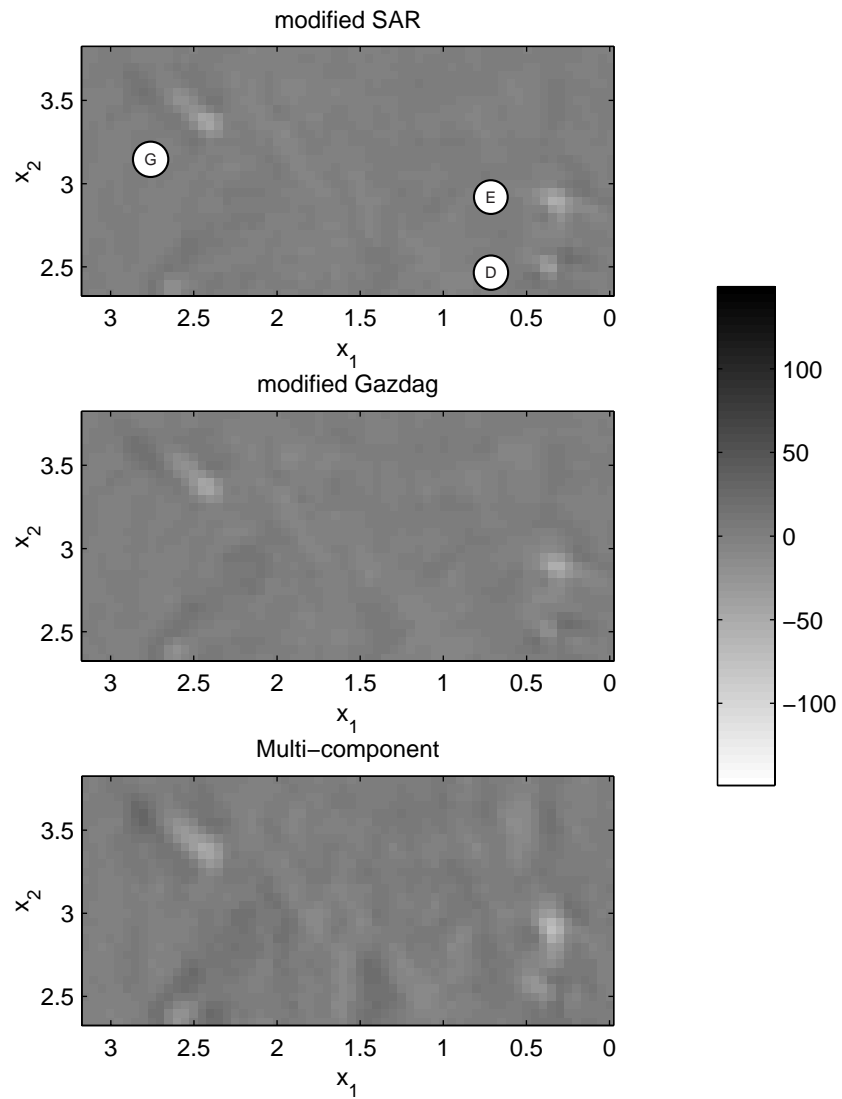


Figure 7.16: Comparison of the real part of the image results for $x_3 = 0.6$ m.

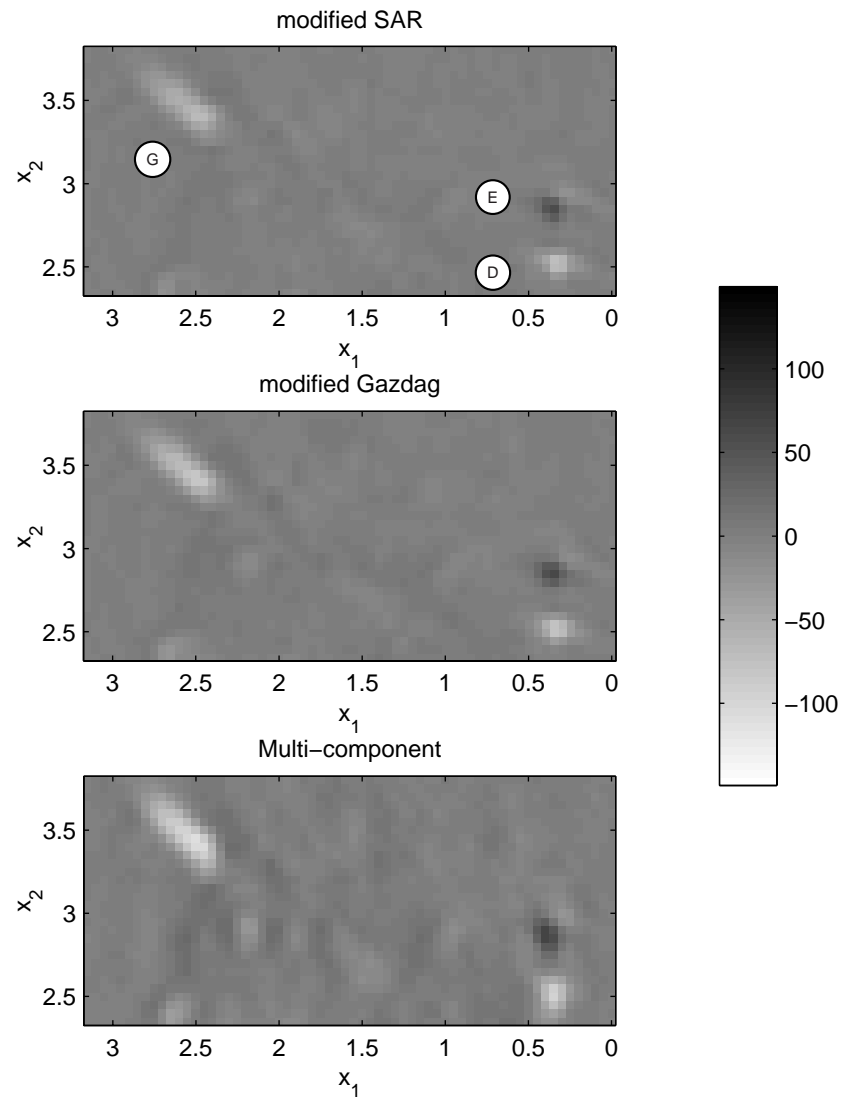


Figure 7.17: Comparison of the imaginary part of the image results for $x_3 = 0.6$ m.

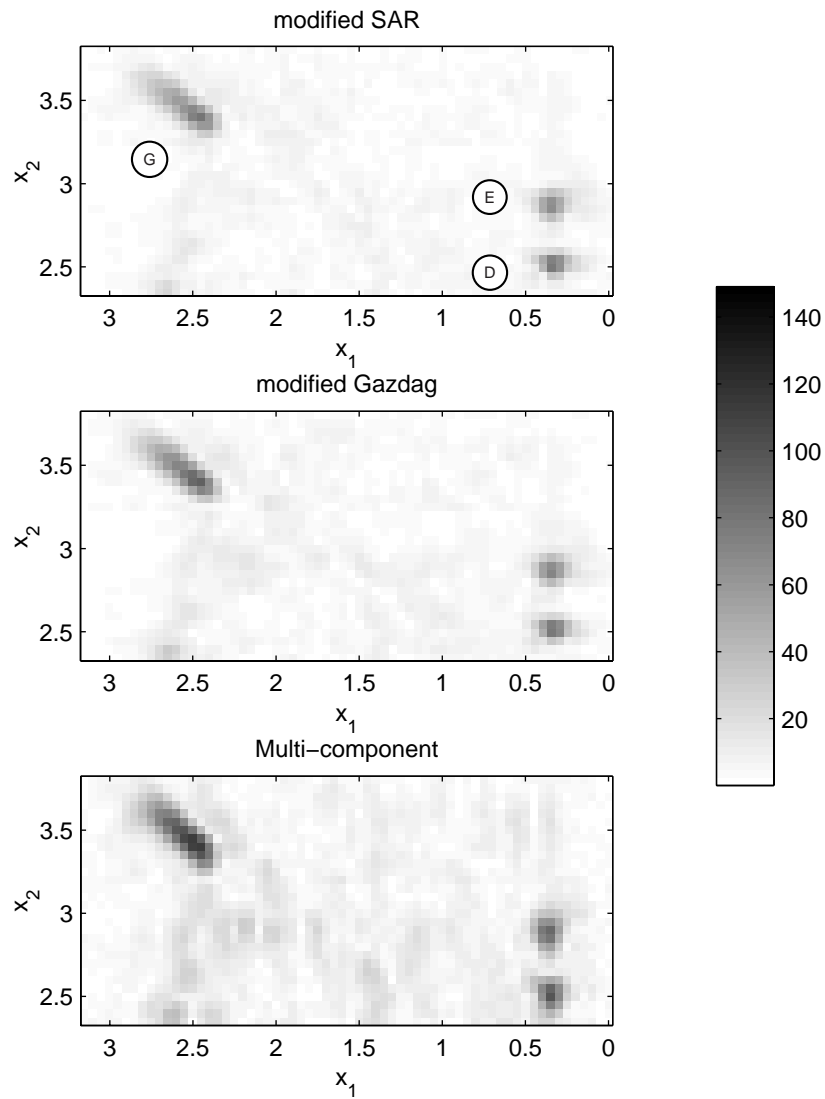


Figure 7.18: Comparison of the absolute values of the image results for $x_3 = 0.6$ m.

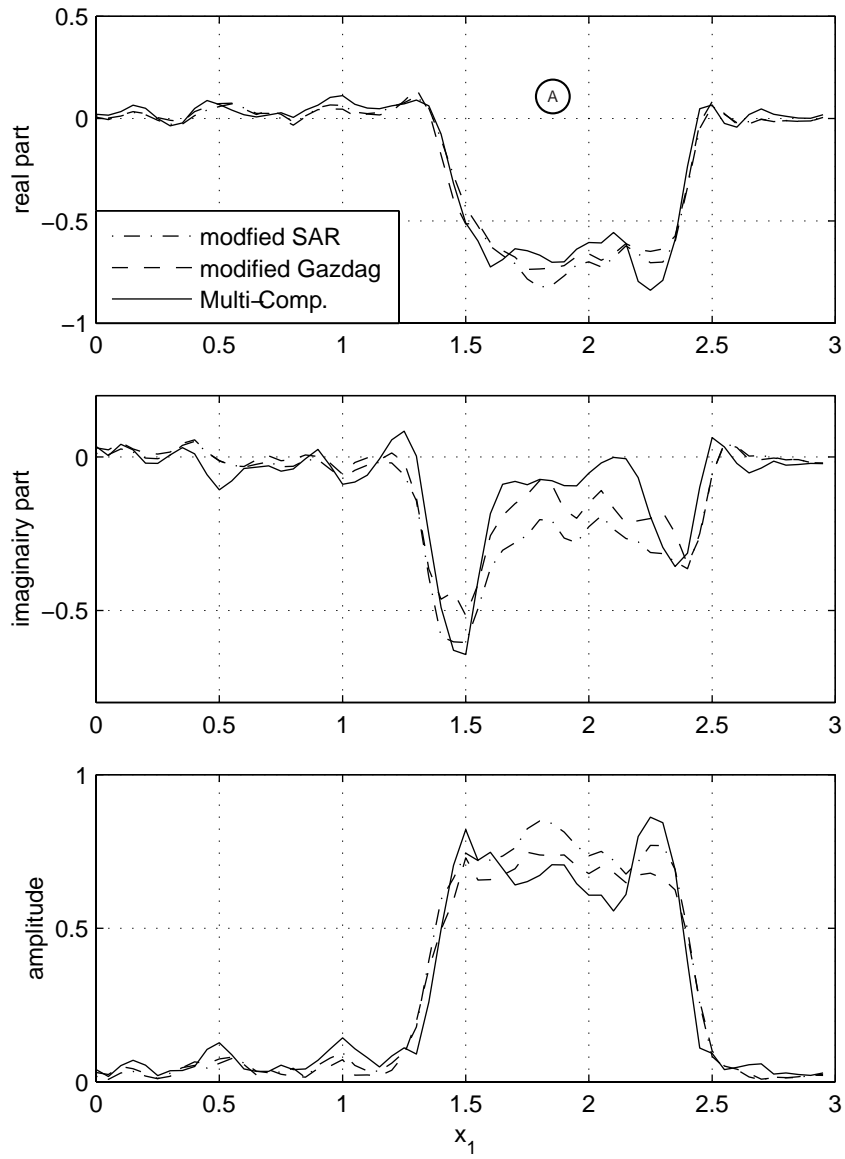


Figure 7.19: Amplitude analysis of the image results for the metal pipe (A) along the line parallel to the x_1 -axis.

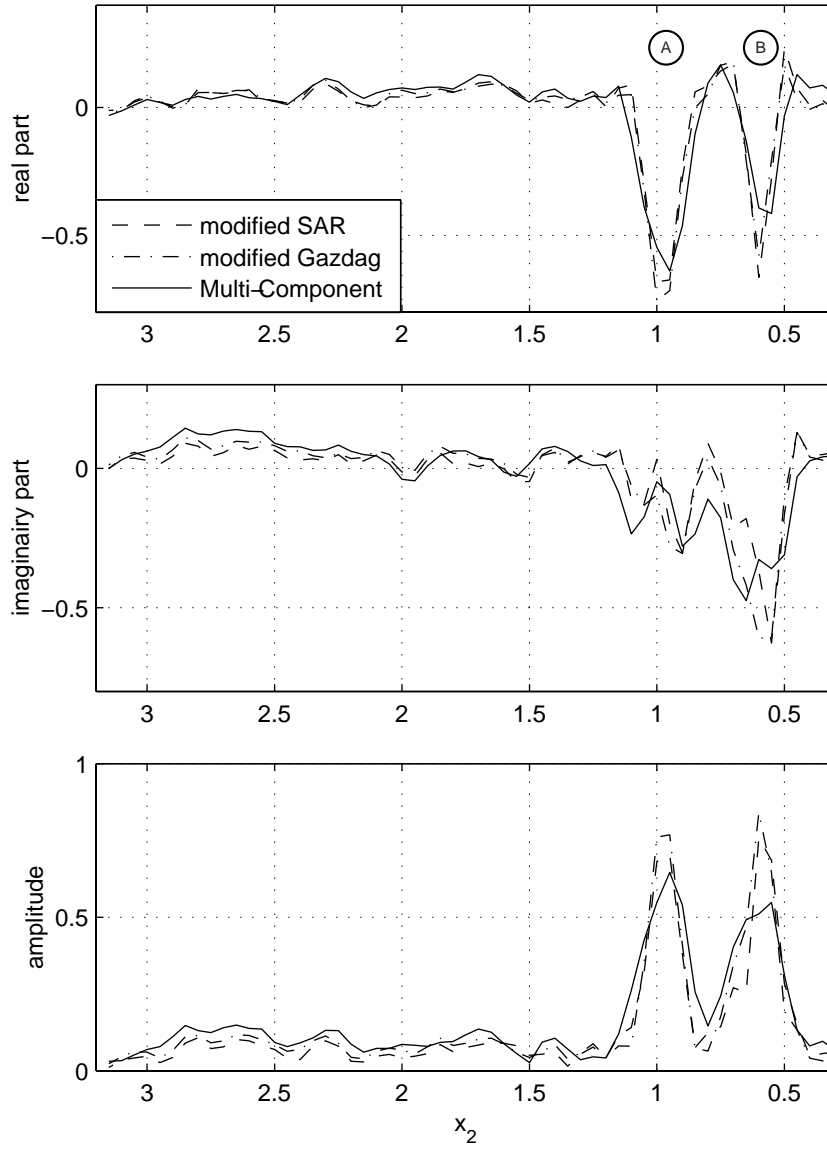


Figure 7.20: Amplitude analysis of the image results for the metal pipe (A) along the line parallel to the x_2 -axis.

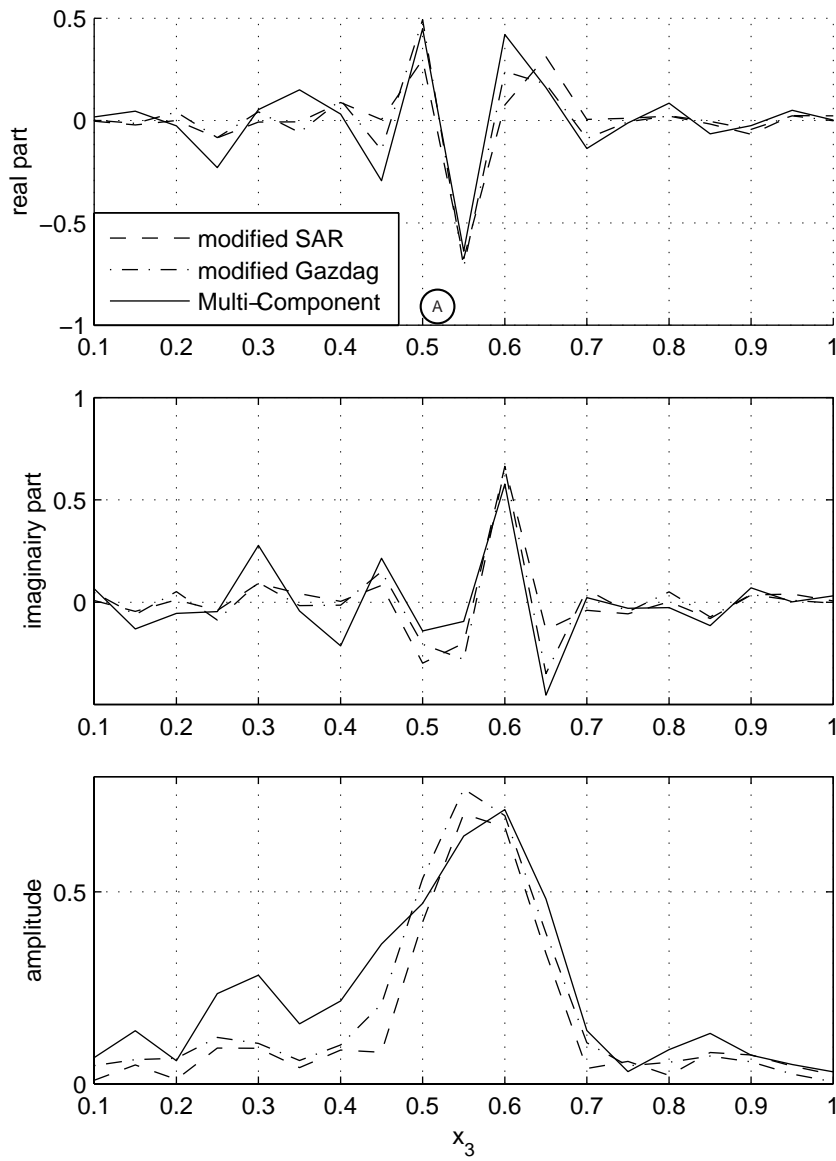


Figure 7.21: Amplitude analysis of the image results for the metal pipe (A) along the line parallel to the x_3 -axis.

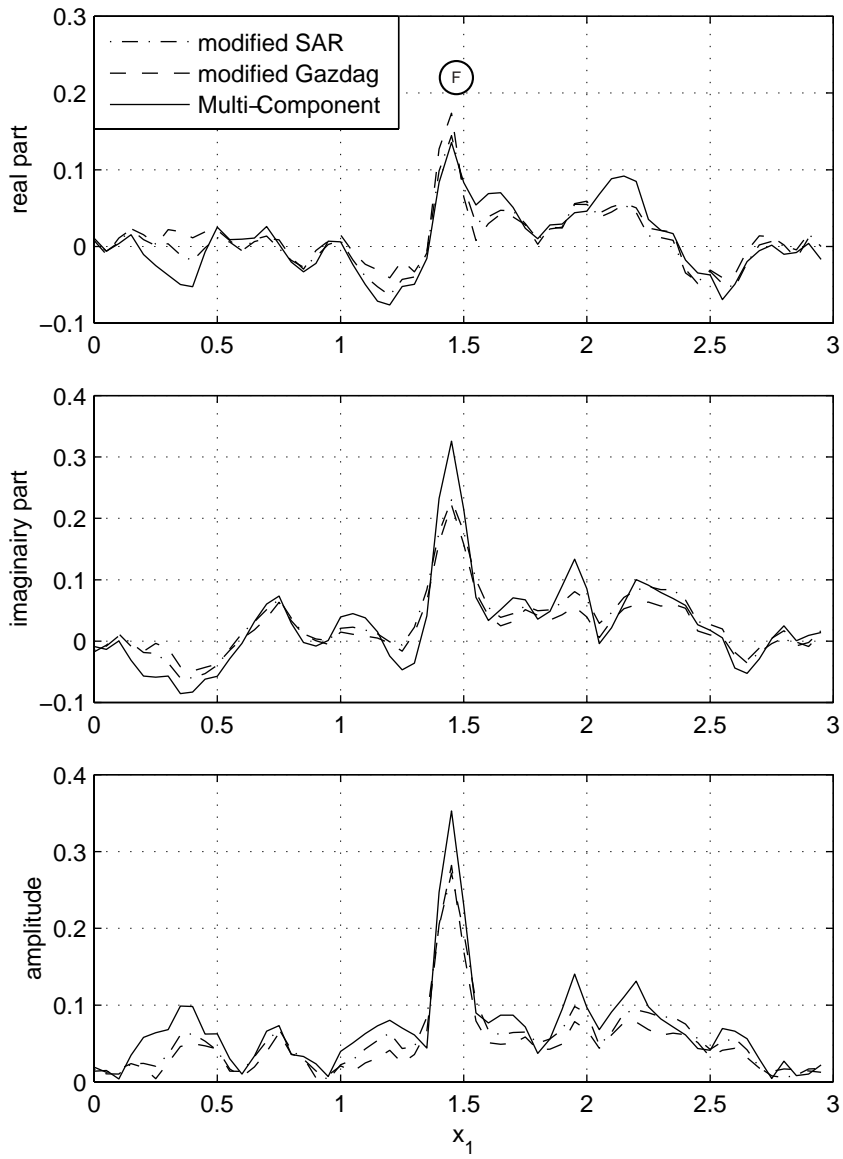


Figure 7.22: Amplitude analysis of the image results for the plastic sphere (F) along the line parallel to the x_1 -axis.

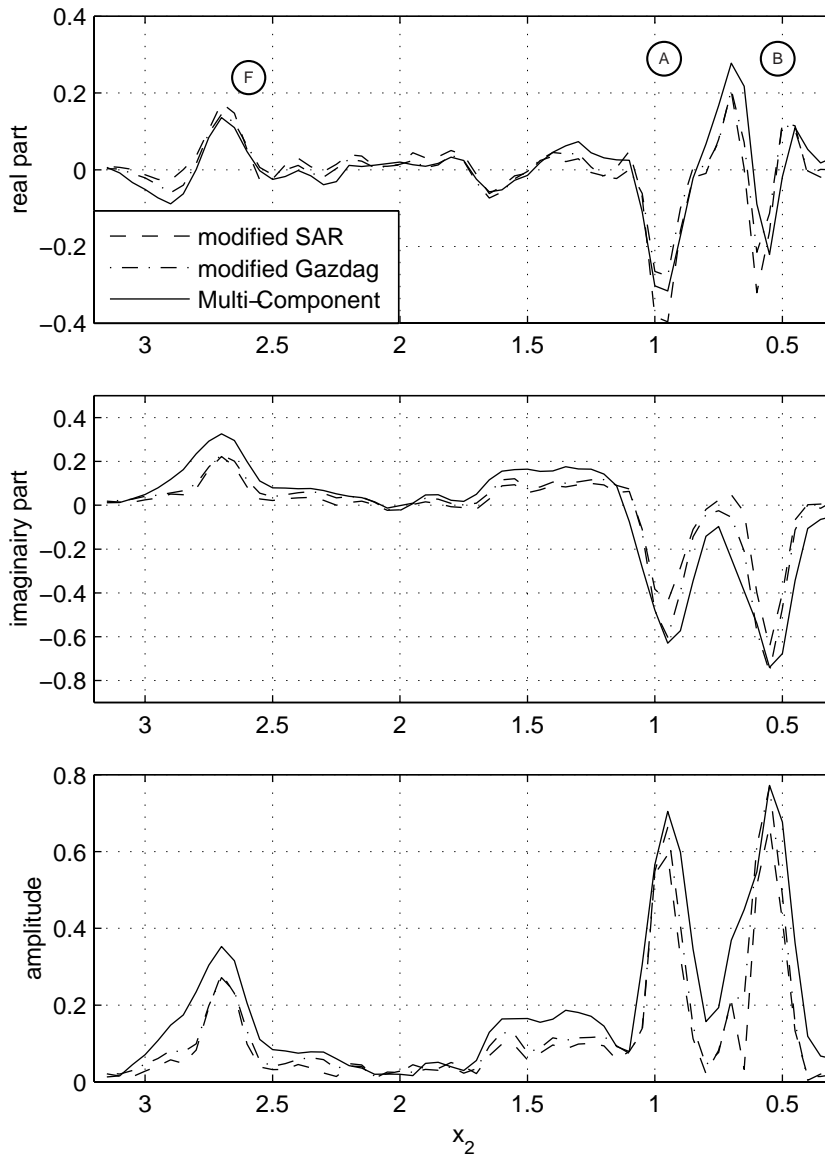


Figure 7.23: Amplitude analysis of the image results for the plastic sphere (F) along the line parallel to the x_2 -axis.

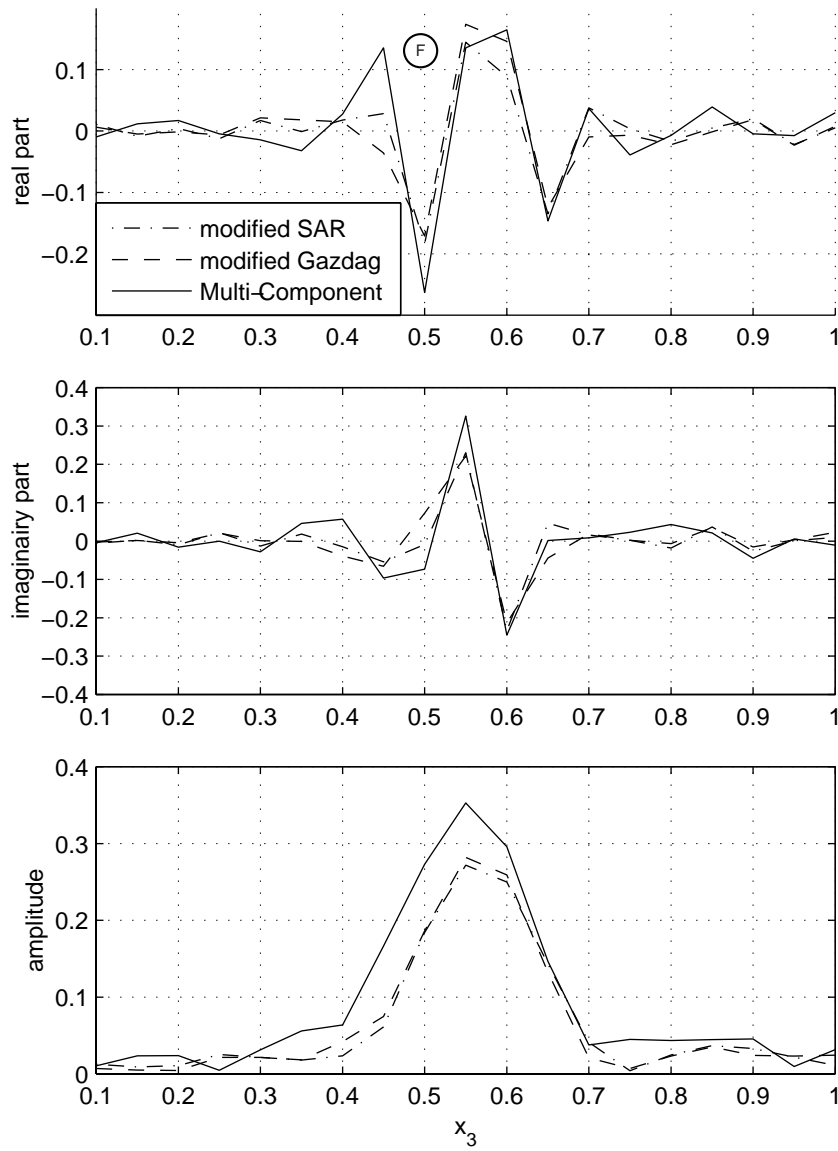


Figure 7.24: Amplitude analysis of the image results for the plastic sphere (F) along the line parallel to the x_3 -axis.

-163° , -159° and -171° , respectively. Thus, the phase of the SAR and the Gazdag results differ with the phase of the multi-component result. Note that the three imaging algorithms use different frequency-dependent filters as discussed in Section 6.7.4. Due to the fact that the wavelet is not known, the analysis to obtain the properties of the object is not feasible. However, the phase differences, which occur in the experimental data are similar to the phase differences obtained with synthetic results as presented in Section 6.7.5. So when the source wavelet is known, the analysis to obtain the medium properties probably can be carried out.

In Figures 7.22, 7.23 and 7.24, the real, imaginary and absolute values of the image result are plotted for the different imaging algorithms along three lines intersecting object F at position $\mathbf{x} = (1.45, 2.7, 0.55)$. These three lines are parallel to the x_1 , x_2 and x_3 -axis and are also indicated by the dash-dotted line in Figure 7.9. A relative large amplitude is obtained for the imaginary part of the imaged contrast compared with the real part for the multi-component algorithm. At position $\mathbf{x} = (1.45, 2.7, 0.55)$ the phase of the SAR, Gazdag and multi-component imaging results are 52° , 58° , and 67° , respectively. Again, the phase differences of the SAR and the Gazdag algorithm differ from the phase of the multi-component result. These phase differences indicate the possible error when the properties are determined with the scalar imaging algorithms compared to the multi-component imaging algorithm.

■

Experimental results of the multi-component 3D vectorial electromagnetic imaging scheme have been presented. The radiation patterns in a homogeneous halfspace and the offset between the source and receiver have been taken into account and several objects were correctly imaged. The use of the modified scalar imaging algorithms, as derived in Chapter 6, enabled a useful comparison between the different imaging operators which have similar phase characteristics. The amplitudes of the image using the multi-component imaging algorithm for the oblique metal pipe G and the plastic sphere F have a larger amplitude than that of the scalar imaging algorithms. This is probably due to the fact that the \hat{E}_{21} -component has its maximum response when both antennas are oriented at a 45 degree angle to the pipe [Daniels et al., 1988]. The improved results for the plastic sphere F is probably a consequence of twice as much information being used to image the data (\hat{E}_{11} and \hat{E}_{21}).

Note that most objects shown in Figure 7.3 are oriented parallel to the orientation of the antennas using the perpendicular-broadside inline-configuration, which will return the maximum response from the buried objects. When objects are present which are oriented perpendicular to the orientation of the antennas using the perpendicular-broadside inline-configuration, it is recommended to carry out also parallel broadside crossline measurements or perpendicular-broadside inline measurements with a reoriented measurement grid as well (see Section 5.6.4).

An important fact that needs improvement is the reduction of the positioning errors, which can be destructive for the imaging results when two subsequent measurements are needed, which is the case for the multi-component imaging algorithm. It is therefore expected that when the two components can be measured simultaneously, the positioning of both measurements is equal and the obtained imaging results will improve. Another option is to use a measurement frame, which enables an accurate positioning [Groenenboom et al., 2001].

The phase of the SAR and Gazdag results differ with the phase of the multi-component result. These phase differences indicate the possible error when the properties are determined with the scalar imaging algorithms compared to the multi-component imaging algorithm. The next step to determine the medium properties of the scatterers is to take into account the source wavelet and the radiation characteristics of a finite length antenna, including the influence of the intermediate field. When the source wavelet is known and used in the multi-component imaging algorithm, it might be possible to distinguish between conductivity and permittivity contrasts for small objects.

Conclusions and Recommendations

In the first part of this thesis, aspects of electromagnetic wave propagation, radiation characteristics of horizontal electric dipoles and the electromagnetic scattering formalism were discussed. All these topics contributed to the final presentation in Chapter 6: the three-dimensional imaging of ground penetrating radar data. The imaging algorithm, called the multi-component imaging algorithm, is based on the vectorial scatter formalism and the radiation characteristics of horizontal electric dipoles. In Chapter 7, experimental results using the multi-component imaging algorithm were discussed. This last chapter summarises the main conclusions of this thesis.

In Chapter 3 and 4 of this thesis we focused on the determination of closed-form expressions for the electric field radiated by a horizontal dipole present on a *dielectric* half-space. These closed-form expressions were needed to keep the computation time for the imaging algorithm within practical limits because they form the basis of our imaging algorithm. The far-field closed-form expressions describe the body waves in the air and in the ground and are proportional to $1/R$. A comparison was made between these far-field expressions and the total-field, which was calculated by numerical evaluation of the integral expressions. This showed that a relatively large difference was present between the far-field and the total-field values near the critical angle and near

the interface, at a distance of a few wavelengths from the source. Thus, the intermediate-field has a relatively large influence in the area, where ground penetrating radar data is used to obtain an image of the subsurface. This is the reason to determine the intermediate-field, which is proportional to $1/R^2$.

The known asymptotic expressions for the intermediate-field in a *high-loss* two-media configuration are used to obtain expressions for the intermediate-field in a *dielectric* two-media configuration. This choice was made because the far-field solutions for the electric field of an interfacial infinitesimal dipole on a *lossless* dielectric half-space and on a *high-loss* two-media configuration are similar, except for the complex propagation constants. The intermediate electric field contributions are the most interesting at the angles where the far-field contributions are zero: near the interface and at the critical angle in the E -plane. Comparison of the results shows that the intermediate-field expressions describe the electric field near the interface quite well. However, the obtained expressions for the intermediate field are not bounded at the critical angle in the lower half-space, and can, therefore, not be used as a forward model used by our imaging algorithm. This is an important topic for future research.

In Chapter 5, the theory of a ground penetrating radar survey was discussed. The linearised vectorial scattering formalism, which describes the wavefield scattered from a given object, is derived using a modified Born approximation, where it is assumed that a finite scatterer can be considered as several independent point scatterers. The acquisition set-up is discussed, with emphasis on appropriate choices for temporal and spatial sampling intervals. The pertaining temporal and spatial bandwidth is determined, which depends on the dimensions of the acquisition plane and the radiation characteristics of the antennas. In this way, the temporal and spatial bandwidths available can be adequately used by the imaging algorithm to obtain an image of the subsurface. Using the linearised vectorial scattering formalism, synthetic data examples are calculated which demonstrate the vectorial behaviour of the scattered electric field coming from a point scatterer for different acquisition set-ups.

The thorough analysis of the radiation characteristics for the total electric field in Chapter 4 together with the vectorial scattering formalism as discussed in Chapter 5 is used as a basis to determine the sensitivity to a possible reflection from a certain object. This, together with the fact that the largest

reflections occur when the polarisation of the electric field is parallel to the object causing the reflection, shows how the sensitivity to subsurface reflections can be increased. On the other hand, these results show how to reduce the sensitivity to unwanted reflections coming from objects on or above the surface. These unwanted reflections from above the surface can be measured by a GPR system, because the system also radiates energy into the air. The radiation characteristics show that a relatively large amplitude is present near the interface for the vertical electric field in the E -plane, whereas a relatively small amplitude is present near the interface for the horizontal electric field in the H -plane. Consequently, vertical objects (e.g. trees) present in the E -plane are, in particular, responsible for unwanted reflections in GPR data. Three-dimensional numerical modelling shows that the unwanted reflections from a vertical object (tree) can be reduced by a factor of 21 by choosing an appropriate orientation of the source and receiver antennas. Further investigation showed that the shallowest part of the earth has a strong influence on the amplitude of the electric field near the interface. A high contrast subsoil with a high permittivity results in a relatively larger amplitude of the unwanted reflection compared with a small contrast subsoil. In conclusion, the influence of unwanted reflections from an object present above the surface can be reduced, by choosing the antenna configuration so that the polarisation of the electric field is perpendicular to the orientation of the object.

Based on the vectorial scattering formalism as formulated in Chapter 5, algorithms are derived for the three-dimensional imaging of GPR data in Chapter 6. The objective is to obtain an imaging algorithm, which takes into account the vectorial character of the electromagnetic waves and the radiation characteristics of the source and receiver antennas. An imaging algorithm basically consists of two steps. The first step eliminates the propagation effects for each separate frequency component (inverse wavefield extrapolation); the second step involves a time zero selection for each position, which is carried out by adding all (positive and negative) frequencies. This is known as the imaging principle. The imaging principle is equal for all imaging algorithms discussed. The discussion of the inverse wavefield extrapolators is based on the vectorial scatter formalism, which describes the forward wavefield extrapolation. The forward wavefield extrapolator is a combination of the propagation of the vector electric field from the source towards the scatterer and from the scatterer back to the receiver. This results in simple closed-form expressions for a zero-offset measurement in a homogeneous space. These closed-form ex-

pressions for the forward wavefield extrapolator are compared with the scalar inverse wavefield extrapolators, used by the Gazdag phase shift and the SAR imaging algorithm. This comparison shows that the SAR algorithm and the Gazdag phaseshift correct for the phaseshift of the forward wavefield extrapolator in the space domain and the spatial Fourier domain, respectively. The scalar imaging algorithms do not correct for the radiation characteristics of the source and receiver antennas, and do not take into account the vectorial character.

The electromagnetic scattering formalism has been used as point of departure in order to derive an inverse wavefield extrapolator systematically. It has been shown that the single-component inverse wavefield extrapolator is not bounded. This is the reason why more components were used to arrive at a bounded inverse wavefield extrapolator. Therefore, four possible measurement set-ups are combined to enable a matrix inversion of the tensorial forward wavefield extrapolator. This leads to a multi-component imaging algorithm, which takes into account the phase velocity, polarisation and amplitudes of the scattered electric field.

A comparison of the performance of the multi-component imaging algorithm with the scalar Gazdag and SAR imaging algorithms is carried out by imaging synthetic data from a point scatterer with a real-valued contrast present in a *homogeneous space* using a zero-offset configuration. This results in a resolution function for a single frequency component. The ideal reconstruction of a point scatterer would be a circularly symmetric real-valued resolution function. Due to the closed-form expressions for the forward and inverse wavefield extrapolators, closed-form expressions are obtained for the resolution functions. Both scalar inverse wavefield extrapolators do not reconstruct the point scatterer adequately, because the maximum amplitude of the resolution function was not real-valued with a positive peak. This is the reason why modified scalar inverse wavefield extrapolators are introduced to reconstruct a real-valued resolution function with a positive peak. Still, the modified SAR and Gazdag extrapolators do not reconstruct a circularly symmetric resolution function. On the contrary, the multi-component imaging algorithm results in a circularly symmetric resolution function, which represents the point scatterer adequately.

It is shown that the same approach can be applied to derive an inverse wavefield extrapolator for the common-offset GPR configuration where the source and receiver are present on a *dielectric half-space*. Due to the complexity of these far-field radiation characteristics it is not feasible to obtain closed-form

expressions for the inverse wavefield extrapolators. However, a numerical implementation to derive the inverse wavefield extrapolator is still possible. This numerical implementation has the advantage that the offset between source and receiver can also be taken into account. Far-field expressions are used to describe the radiation characteristics of the source and receiver antennas, because the intermediate-field expressions, derived in Chapter 4 were not bounded and the calculation of the total-field expressions is too time consuming to be used in an imaging algorithm.

The resolution functions for the revised scalar inverse wavefield extrapolators show a non-circularly symmetric resolution function and also a non-zero imaginary imaged contrast. The multi-component algorithm represents the point scatterer most appropriately, because it shows a more circularly symmetrical resolution function compared to the single component imaging algorithms. The amplitude of the imaginary part of the resolution function for the multi-component imaging algorithm is small compared to the scalar imaging algorithms, which results in a smaller phase error for the multi-component imaging algorithm compared to the scalar imaging algorithms. For a real-valued contrast the phase of the obtained maximum of the imaged contrast should be 0° . Because far-field radiation characteristics are used to obtain the inverse wavefield extrapolator, a relatively small phase error of 8° occurs using the multi-component imaging algorithm. A circularly symmetric and real-valued resolution function with the correct phase is obtained using the total-field expressions, to determine the inverse wavefield extrapolator. This indicates that closed-form expressions, which approximate the total-field radiation characteristics better than the far-field radiation characteristics, will result in better imaging results. Still, the multi-component algorithm represents the point scatterer most appropriately using the far-field radiation characteristics within reasonable computation time. From these synthetic results it is indicated that using the multi-component imaging algorithm it may be possible to distinguish between different types of contrasts.

Experimental results of the multi-component 3D vectorial electromagnetic imaging scheme were presented in Chapter 7. The far-field radiation characteristics and the offset between the source and receiver present on a dielectric half-space were taken into account by the multi-component imaging algorithm. The modified scalar imaging algorithms which are described in Chapter 6 enable a useful comparison with the multi-component imaging algorithm. Several buried objects with different medium properties and in

different orientations were imaged. Despite the fact that a velocity gradient was present, an effective homogeneous velocity distribution is sufficient to obtain a representative image of the buried objects.

In the synthetic data it has been observed that phase differences occur between the scalar and multi-component imaging algorithms. In the experimental results similar phase shifts occur which indicate that a more representative image of the subsurface is obtained using the multi-component imaging algorithm. The amplitudes of the images resulting from the multi-component imaging algorithm for the oblique metal pipe G and the plastic sphere F were larger than the results from the scalar imaging algorithms. This is probably caused by incorporation of the cross-polarised data which has its maximum response when both antennas are oriented at a 45° angle to the pipe. These experimental results showed that the multi-component imaging algorithm gives a better image for oblique objects and spheres.

Some recommendations can be formulated, which indicate directions for further research. It has been shown that a few wavelengths from the source and receiver a relatively large difference between the far-field results and the total-field results exists, especially near the critical angle. A combination of far-field, and intermediate-field expressions probably approximate the total-field results in a better way. However, the amplitudes for the closed-form expressions for the intermediate field are not bounded near the critical angle. The characterisation of the radiation of an electric dipole present on a dielectric medium can be improved substantially when bounded expressions are obtained for these intermediate expressions. The next step could be to derive the radiation characteristics of a finite length antenna [Arcone, 1995]. A better characterisation of the source and the receiver antennas will probably improve the imaging results.

When the propagation effects are corrected for by the multi-component imaging algorithm, a distinction between a conductivity or a permittivity contrast of a relatively small spherical scatterer can be made. In reality, we have to take into account the source wavelet, which has to be deconvolved from the measured scattered electric field to determine the medium properties.

From the experiments it has been observed that a significant vertical permittivity distribution can be present in the first 10 cm of the subsurface. It is important to investigate the influence of this velocity gradient on the scattered electric field. In principle, when the scattering formalism describes the propagation through a layered half-space the multi-component imaging

algorithm can in principle be used to obtain an image of the subsurface. One thing that needs improvement is the reduction of the positioning errors. For a conventional scalar 3D imaging algorithm, these positioning errors result in a distribution of the obtained imaging results. When two different measurements are combined to obtain an image of the subsurface, as for the multi-component imaging algorithm, the implications of positioning errors can be more severe. An error in the positioning of these two different measurements can mean that the image is not improved by combining two different measurements, as indicated by the theory, but can result in a deterioration of the imaging result. Therefore, it is important to reduce the positioning errors. When the two components can be measured simultaneously, the positioning of both measurements should be equal and the obtained imaging results should improve. Another option is to use a measurement frame, which enables an accurate positioning.

A

Use of Stationary phase approximation for horizontal Fourier transformation

In this appendix the stationary phase approximation is used to derive an analytical expression for the forward and inverse 3D two-way wave field extrapolator in the spatial Fourier domain by approximating the horizontal Fourier integral using a stationary phase approximation. In this way closed-form expressions can be obtained for the forward and inverse wavefield extrapolators in the space-frequency domain and the horizontal Fourier domain.

From Chapter 6 it can be observed that the forward wavefield extrapolator and the inverse wavefield extrapolator can be written in generalised form as

$$\hat{f}^{\pm}(\mathbf{x}, \omega) = \hat{g}(\mathbf{x}, \omega) \exp[\pm 2kR(\mathbf{x})], \quad (\text{A.1})$$

where the positive and the negative sign in the exponent is valid for the inverse wavefield extrapolator and the forward wavefield extrapolator, respectively. The two-dimensional spatial Fourier transform of $\hat{f}(\mathbf{x}, \omega)$, which

is defined in Eq. (2.19), can be written as

$$\begin{aligned}\tilde{f}^{\pm}(k_1, k_2, x_3, \omega) &= \int_{(x_1, x_2) \in \mathbb{R}^2} \hat{f}^{\pm}(\mathbf{x}, \omega) \exp(jk_1 x_1 + k_2 x_2) dA, \\ &= \int_{(x_1, x_2) \in \mathbb{R}^2} \hat{g}(\mathbf{x}, \omega) \exp\left[j\frac{\omega}{c}\phi^{\pm}(\mathbf{x})\right] dA,\end{aligned}\quad (\text{A.2})$$

where $\phi^{\pm}(\mathbf{x})$ is given by

$$\begin{aligned}\phi^{\pm}(\mathbf{x}) &= \pm 2R + \frac{k_1}{k}x_1 + \frac{k_2}{k}x_2, \\ &= \pm 2R + p_1 x_1 + p_2 x_2,\end{aligned}\quad (\text{A.3})$$

where

$$p_1 = \frac{k_1}{k}, \quad (\text{A.4a})$$

$$p_2 = \frac{k_2}{k}, \quad (\text{A.4b})$$

and $k = \omega/c$. Using the method of stationary phase, Eq. (A.2) may be approximated for large ω by (See Felsen and Marcuvitz [1973] and Bleistein [1984]).

$$\begin{aligned}\tilde{f}^{\pm}(k_1, k_2, x_3, \omega) \\ \simeq \frac{2\pi \hat{A}^{\pm}(\bar{x}_1^{\pm}, \bar{x}_2^{\pm}, x_3) \exp\left[j\left(\frac{\omega}{c}\phi^{\pm}(\bar{x}_1^{\pm}, \bar{x}_2^{\pm}, x_3) + \mu_{x_1}^{\pm}\pi/4 + \mu_{x_2}^{\pm}\pi/4\right)\right]}{\sqrt{h^{\pm}(\bar{x}_1^{\pm}, \bar{x}_2^{\pm}, x_3)}},\end{aligned}\quad (\text{A.5})$$

with

$$\mu_{\{x_1, x_2\}}^{\pm} = \text{sign}\left(\partial_{\{1,2\}}^2 \phi^{\pm} \Big|_{\bar{x}_1^{\pm}, \bar{x}_2^{\pm}}\right), \quad (\text{A.6})$$

$$h^{\pm}(\bar{x}_1^{\pm}, \bar{x}_2^{\pm}, x_3) = \text{Det}\left(\begin{bmatrix} \partial_1^2 \phi^{\pm} & \partial_1 \partial_2 \phi^{\pm} \\ \partial_1 \partial_2 \phi^{\pm} & \partial_2^2 \phi^{\pm} \end{bmatrix} \Big|_{\bar{x}_1^{\pm}, \bar{x}_2^{\pm}}\right), \quad (\text{A.7})$$

and $(\bar{x}_1^{\pm}, \bar{x}_2^{\pm})$ being the point where $\phi^{\pm}(\mathbf{x})$ is stationary, i.e.

$$\partial_1 \phi^{\pm} \Big|_{\bar{x}_1^{\pm}, \bar{x}_2^{\pm}} = \partial_2 \phi^{\pm} \Big|_{\bar{x}_1^{\pm}, \bar{x}_2^{\pm}} = 0. \quad (\text{A.8})$$

First the point of stationary phase is determined. From Eq. (A.3) we obtain

$$\partial_1 \phi^\pm \Big|_{\bar{x}_1^\pm, \bar{x}_2^\pm} = \frac{\pm 2x_1}{R} + p_1 = 0, \quad (\text{A.9a})$$

$$\partial_2 \phi^\pm \Big|_{\bar{x}_1^\pm, \bar{x}_2^\pm} = \frac{\pm 2x_2}{R} + p_2 = 0. \quad (\text{A.9b})$$

Solving \bar{x}_1^\pm and \bar{x}_2^\pm using Eq. (A.8) results in

$$\bar{x}_1^\pm = \mp \frac{p_1 \sqrt{(\bar{x}_2^\pm)^2 + x_3^2}}{\sqrt{4 - p_1^2}}, \quad (\text{A.10a})$$

$$\bar{x}_2^\pm = \mp \frac{p_2 \sqrt{(\bar{x}_1^\pm)^2 + x_3^2}}{\sqrt{4 - p_2^2}}. \quad (\text{A.10b})$$

Substitution of Eq. (A.10b) in Eq. (A.10a) and vice versa, results in the following stationary point,

$$\bar{x}_1^\pm = \mp \frac{p_1 x_3}{p_3^\pm}, \quad (\text{A.11a})$$

$$\bar{x}_2^\pm = \mp \frac{p_2 x_3}{p_3^\pm}, \quad (\text{A.11b})$$

where p_3^\pm is given by

$$p_3^\pm = \sqrt{4 - p_1^2 - p_2^2}. \quad (\text{A.12})$$

Substitution of both \bar{x}_1^\pm and \bar{x}_2^\pm into Eq. (A.3) results in

$$\phi^\pm(\bar{x}_1^\pm, \bar{x}_2^\pm, x_3) = \pm p_3^\pm x_3. \quad (\text{A.13})$$

Note that for the final expression in Eq. (A.5) to be stable the following condition for p_3^\pm must be satisfied,

$$p_3^\pm = \begin{cases} \sqrt{4 - p_1^2 - p_2^2}, & \text{for } p_1^2 + p_2^2 \leq 4, \\ \pm j \sqrt{p_1^2 + p_2^2 - 4}, & \text{for } p_1^2 + p_2^2 > 4, \end{cases} \quad (\text{A.14})$$

which is similar with neglecting the evanescent waves as om Eq. (5.46). To obtain an expression for $g^\pm(\bar{x}_1^\pm, \bar{x}_2^\pm, x_3)$ we first calculate

$$\partial_1^2 \phi^\pm = \pm \frac{2}{R} \mp \frac{2x_1^2}{R^3}, \quad (\text{A.15a})$$

$$\partial_1 \partial_2 \phi^\pm = \partial_2 \partial_1 \phi^\pm = \mp \frac{2x_1 x_2}{R^3} \quad (\text{A.15b})$$

$$\partial_2^2 \phi^\pm = \pm \frac{2}{R} \mp \frac{2x_2^2}{R^3}, \quad (\text{A.15c})$$

With

$$\bar{R}^\pm = \frac{2x_3}{p_3^\pm}, \quad (\text{A.16a})$$

$$\frac{\bar{x}_1^\pm}{\bar{R}^0} = \mp \frac{p_1}{2}, \quad (\text{A.16b})$$

$$\frac{\bar{x}_2^\pm}{\bar{R}^\pm} = \mp \frac{p_2}{2}, \quad (\text{A.16c})$$

$$\frac{\bar{x}_3^\pm}{\bar{R}^\pm} = \mp \frac{p_3^\pm}{2}, \quad (\text{A.16d})$$

and substitution of the stationary points, Eqs. (A.11a) and (A.11b), into Eqs. (A.15a)-(A.15c) gives

$$\partial_1^2 \phi^\pm \Big|_{x_1^0, x_2^0} = \pm \frac{p_3^\pm (p_2^2 + p_3^2)}{4x_3}, \quad (\text{A.17a})$$

$$\partial_1 \partial_2 \phi^\pm \Big|_{\bar{x}_1^\pm, \bar{x}_2^\pm} = \partial_2 \partial_1 \phi^\pm \Big|_{\bar{x}_1^\pm, \bar{x}_2^\pm} = \mp \frac{p_3^\pm p_1 p_2}{4x_3}, \quad (\text{A.17b})$$

$$\partial_2^2 \phi^\pm \Big|_{\bar{x}_1^\pm, \bar{x}_2^\pm} = \pm \frac{p_3^\pm (p_1^2 + p_3^2)}{4x_3}. \quad (\text{A.17c})$$

Substitution of the former results yields for $h^\pm(\bar{x}_1^\pm, \bar{x}_2^\pm)$

$$h^\pm(\bar{x}_1^\pm, \bar{x}_2^\pm, x_3) = \frac{p_3^4}{4x_3^2}, \quad (\text{A.18})$$

and Eq. (A.5) yields

$$\begin{aligned} \tilde{f}^\pm(k_1, k_2, x_3, \omega) &\simeq 2\pi \hat{g}(\bar{x}_1^\pm, \bar{x}_2^\pm, x_3) \exp \left[\pm j \left(\frac{\omega}{c} p_3^\pm x_3 + \pi/2 \right) \right] \frac{2x_3}{p_3^2}, \\ &\simeq 2\pi \hat{g}(\bar{x}_1^\pm, \bar{x}_2^\pm, x_3) \exp[\pm j(k_3^\pm x_3 + \pi/2)] \frac{2kx_3}{k_3^2}. \end{aligned} \quad (\text{A.19})$$

In this way closed-form expressions can be obtained for the forward and inverse wavefield extrapolators in the space-frequency domain and the horizontal Fourier domain.

Bibliography

- M. Abramowitz and I.A. Stegun. *Handbook of Mathematical Functions With Formulas, Graphs, and Mathematical Tables*. National Bureau of Standards Applied Mathematics Series 55. U.S. Department of Commerce, 1964.
- L. Amundsen and A. Reitan. Decomposition of multicomponent sea-floor data into upgoing and downgoing P- and S-waves. *Geophysics*, 60(2):563–572, 1995.
- A.P. Annan. Radio interferometry depth sounding: part I- theoretical discussion. *Geophysics*, 38:575–580, 1973.
- A.P. Annan. Transmission dispersion and GPR. *Journal of Environmental and Engineering Geophysics*, 0(2):125–136, 1996.
- A.P. Annan, W.M. Waller, D.W. Strangway, J.R. Rossiter, J.D. Redman, and R.D. Watts. The electromagnetic response of a low-loss, 2-layer, dielectric earth for horizontal electric dipole excitation. *Geophysics*, 40:285–298, 1975.
- S.A. Arcone. Numerical studies of the kings of resistively loaded dipoles. *Journal of Applied Geophysics*, 33:39–52, 1995.
- A. Baños. *Dipole radiation in the Presence of a conducting Half-space*. Pergamon press, New York, 1966.

- M. Bano, F. Pivot, and J. Marthelot. Modelling and filtering of surface scattering in ground-penetrating radar waves. *First Break*, 17(6):215–222, 1999.
- A.J. Berkhout. Wave field extrapolation techniques in seismic migration, a tutorial. *Geophysics*, 46(12):1638–1656, 1981.
- A.J. Berkhout. *Handbook of geophysical exploration, Section 1. Seismic exploration Vol. 12 Seismic resolution, a quantitative analysis of resolving power of acoustical echo techniques*. Geophysical press, London, 1984.
- A.J. Berkhout and C.P.A. Wapenaar. One-way versions of the Kirchhoff integral. *Geophysics*, 54(4):460–467, 1989.
- J. Binningsbø, E.S. Eide, and J.F. Hjeltnad. 3D migration of GPR array-antenna data. In *Proceedings of the Eighth International Conference on Ground-Penetrating Radar, Gold Coast, Australia*, pages 459–463, 2000.
- N. Bleistein. *Mathematical methods for wave phenomena*. Academic press, London, 1984.
- M. Born and E. Wolf. *Principles of Optics*. Pergamon press, London, 1965.
- J.F. Claerbout. Toward a unified theory of reflector mapping. *Geophysics*, 36(3):467–481, 1971.
- J.C. Curlander and R.N. McDonough. *Synthetic Aperture Radar, systems and signal processing*. Wiley series in remote sensing. Wiley, New York, 1991.
- R.L. Dam and W. Schlager. Identifying causes of ground-penetrating radar reflections using time-domain reflectometry and sedimentological analyses. *Sedimentology*, 47:435–449, 2000.
- D.J. Daniels, D.J. Gunton, and H.F. Scott. Introduction to subsurface radar. *IEE-Proceedings Part F: Communications, Radar and Signal Processing*, 135(4):278–321, 1988.
- J.W.M. Dankbaar. Separation of P- and S-waves. *Geophysical Prospecting*, 33:970–986, 1985.
- A.T. de Hoop. *Handbook of Radiation and Scattering of Waves*. Academic Press, Amsterdam, 1995.

-
- A.T. de Hoop. A general correspondence principle for time-domain electromagnetic wave and diffusion fields. *Geophysical Journal International*, 127: 757–761, 1996.
- P.J.W. Debye. *Polar molecules*. Dover Publication, New York, 1929.
- J. Dunbar, L. Nordt, and J. Abraham. Ground-penetrating radar transect across the barrier flat of galveston island, texas. In *67th Ann. Internat. Mtg., Soc. Expl. Geophys., Expanded Abstracts, Dallas, Texas*, pages 768–771, 1997.
- N. Engheta, C.H. Papas, and C. Elachi. Radiation patterns of interfacial dipole antennas. *Radio Science*, 17(6):1557–1566, 1982.
- L.B. Felsen and N. Marcuvitz. *Radiation and scattering of waves*. Prentice-Hall, Englewood Cliffs, N.J., 1973.
- E. Fisher, G.A. McMechan, and A.P. Annan. Acquisition and processing of wide-aperture ground-penetrating radar data. *Geophysics*, 57(3):495–504, 1992a.
- E. Fisher, G.A. McMechan, A.P. Annan, and S.W. Cosway. Examples of reverse-time migration of single-channel, ground-penetrating radar profiles. *Geophysics*, 57(4):1342–1351, 1992b.
- J.T. Fokkema and P.M. van den Berg. *Seismic Applications of Acoustic Reciprocity*. Elsevier, Amsterdam, 1993.
- R. Friel and D. Or. Frequency analysis of time-domain reflectometry (TDR) with application to dielectric spectroscopy of soil constituents. *Geophysics*, 64(3):707–718, 1999.
- J. Gazdag. Wave equation migration with the phase-shift method. *Geophysics*, 43:1342–1351, 1978.
- M. Grasmueck. 3-D ground-penetrating radar applied to fracture imaging in gneiss. *Geophysics*, 61(4):1050–1064, 1996.
- J. Groenenboom. *Acoustic Monitoring of hydraulic fracture growth*. PhD thesis, Delft University of Technology, 1998.
- J. Groenenboom, J. van der Kruk, and J.H. Zeeman. 3D GPR data acquisition and the influence of positioning errors on image quality. In *Extended*

- abstracts of the 63rd conference and Technical Exhibition of the EAGE, Amsterdam, 2001.*
- A. Gunawardena and D. Longstaff. Wave equation formulations of synthetic aperture radar (SAR) algorithms in the time-space domain. *IEEE transactions on Geoscience and Remote Sensing*, 36(6):1995–1999, 1998.
- J.G. Haagedoorn. A process of seismic reflection interpretation. *Geophysical Prospecting*, 2:85–127, 1954.
- T.J. Heimovaara. Frequency domain analysis of time domain reflectometry waveforms, 1. measurement of the complex dielectric permittivity of soils. *Water resources research*, 30(2):189–199, 1994.
- G.T. Herman, H.K. Tuy, K.J. Langenberg, and P.C. Sabatier. *Basic methods of Tomography and Inverse Problems*. Malvern physics series 4. Bristol: Adam Hilger, 1987.
- K. Holliger and T. Bergmann. Accurate and efficient modeling of ground-penetrating radar antenna radiation. *Geophysical Research Letters*, 25: 3883–3886, 1998.
- J. Irving and R. Knight. Estimation and correction of wavelet dispersion in GPR data. In *Proceedings of the Eighth International Conference on Ground-Penetrating Radar, Gold Coast, Australia*, pages 561–566, 2000.
- Y. Jiao, G.A. McMechan, and E. Pettinelli. In situ 2-D and 3-D measurements of radiation patterns of half-wave dipole gpr antennas. *Journal of Applied Geophysics*, 43:69–89, 2000.
- E.M. Johansson and J.E. Mast. Three-dimensional ground penetrating radar imaging using synthetic aperture time-domain focusing. In *Proceedings of SPIE The International Society for Optical Engineering*, volume 2275, pages 205–214, 1994.
- M.B. Kagalenko and W.H. Weedon. Comparison of backpropagation and synthetic aperture imaging algorithms for processing GPR data. In *Proceedings of the 1996 AP-S International Symposium and URSI Radio Science Meeting. Part 3 (of 3)*. Baltimore, MD, USA, pages 2179–2182, 1996.
- R.W.P. King and G.S. Smith. *Antennas in Matter; Fundamentals, Theory and Applications*. MIT Press, London, 1981.

-
- B.J. Kooij. *Analysis of transient electromagnetic fields in an electrical utility substation environment*. PhD thesis, Delft University of Technology, 1994.
- S.W. Lee, J. Boersma, C.L. Law, and G.A. Deschamps. Singularity in Green's function and its numerical evaluation. *IEEE Transactions on Antennas and Propagation*, 28:311–317, 1980.
- F. Lehmann. *Automation in 3D georadar investigations: new acquisition and processing techniques*. PhD thesis, Swiss federal institute of technology (ETH) Zurich, 1999.
- F. Lehmann, D. Boerner, K. Holliger, and A.G. Green. Vectorial nature of georadar data. In *Proceedings of the Eighth International Conference on Ground-Penetrating Radar, Gold Coast, Australia*, pages 824–829, 2000.
- C. Leuschen and R. Plumb. A matched-filter approach to wave migration. *Journal of Applied Geophysics*, 43:271–280, 2000.
- J.M. Lopez-Sanchez and J. Fortuny-Guasch. 3-D radar imaging using range migration techniques. *IEEE Transactions on Antennas and Propagation*, 48(5):728–737, 2000.
- J.E. Mast and E.M. Johansson. Three-dimensional ground penetrating radar imaging using multi-frequency diffraction tomography. In *Proceedings of SPIE The International Society for Optical Engineering*, volume 2275, pages 196–203, 1994.
- M.L. Moran, R.J. Greenfield, S.A. Arcone, and A.J. Delaney. Multidimensional GPR array processing using Kirchhoff migration. *Journal of Applied Geophysics*, 43:281–295, 2000.
- M.N. Nabighian. *Electromagnetic methods in applied geophysics, applications. Part A*. Society of Exploration Geophysicists, Tulsa, 1991.
- B. Nguyen. *Dielectric measurements, Saturation Determination*. PhD thesis, Delft University of Technology, 1999.
- S.J. Radzevicius and J.J. Daniels. GPR H-plane antenna patterns for a horizontal dipole on a halfspace interface. In *Proceedings of the Eighth International Conference on Ground-Penetrating Radar, Gold Coast, Australia*, pages 712–717, 2000a.

- S.J. Radzevicius and J.J. Daniels. Ground penetrating radar polarization and scattering from cylinders. *Journal of Applied Geophysics*, 45:111–125, 2000b.
- R.F. Remis. *Reduced-Order modeling of transient electromagnetic fields*. PhD thesis, Delft University of Technology, 1998.
- K.M. Schalkwijk, C.P.A. Wapenaar, and E. Verschuur. Decomposition of multicomponent ocean-bottom data in two steps. In *68th Ann. Internat. Mtg., Soc. Expl. Geophys., Expanded Abstracts*, pages 1425–1428, 1998.
- W.A. Schneider. Integral formulation for migration in two and three dimensions. *Geophysics*, 43(1):49–76, 1978.
- M.A. Schonewille. *Fourier reconstruction of irregularly sampled seismic data*. PhD thesis, Delft University of Technology, 2000.
- R.E. Sheriff. *Encyclopedic Dictionary of Exploration Geophysics*. Society of Exploration Geophysics, P.O. Box 702740, Tulsa, Oklahoma, 74170-2740, 1984.
- E.L. Shuck, T.L. Davis, and R.D. Benson. Multicomponent 3-D characterisation of a coalbed methane reservoir. *Geophysics*, 61(2):315–330, 1996.
- M.I. Skolnik. *Introduction to radar systems*. McGraw-Hill, Singapore, 1980.
- E.C. Slob. *Scattering of transient diffusive electromagnetic fields*. PhD thesis, Delft University of Technology, 1994.
- E.C. Slob. Modelling finite electric dipoles on the air/earth interface. *submitted to Journal of Applied Geophysics*, 2001.
- G.S. Smith. Directive properties of antennas for transmission into a material half-space. *IEEE Transactions on Antennas and Propagation*, 32(3):232–246, 1984.
- A. Sommerfeld. *Partial differential equations*. Academic Press, New York, 1949.
- R.H. Stolt. Migration by Fourier transform. *Geophysics*, 43(1):23–48, 1978.
- J. Sun and R.A. Young. Recognizing surface scattering in ground-penetrating radar data. *Geophysics*, 60(5):1378–1385, 1995.

-
- G. Turner. Subsurface radar propagation deconvolution. *Geophysics*, 59(2): 215–223, 1994.
- G. Turner and A.F. Siggins. Constant Q attenuation of subsurface radar pulses. *Geophysics*, 59(8):1192–1200, 1994.
- R.G. van Borselen. *Removal of Surface-Related Multiples from Marine Seismic Data*. PhD thesis, Delft University of Technology, 1995.
- J.H.M.T. van der Hijden. *Propagation of Transient Elastic Waves in Stratified Anisotropic Media*. PhD thesis, TUD, 1987.
- J. van der Kruk. Removal of surface related wave phenomena in electromagnetic prospecting. Technical report, Delft University of Technology, 1993. Report number Et/EM 1993-39.
- J. van der Kruk and E.C. Slob. Determination of the effective source wavelet. In *Proceedings of the Seventh International Conference on Ground-Penetrating Radar, Lawrence, Kansas, USA*, volume 2, pages 625–630, 1998.
- J. van der Kruk and E.C. Slob. Background of ground-penetrating radar measurements. *Geology en Mijnbouw*, 77:177–188, 1999.
- J. van Gestel and P.L. Stoffa. Migration using multi-configuration GPR data. In *Proceedings of the Eighth International Conference on Ground-Penetrating Radar, Gold Coast, Australia*, pages 448–452, 2000.
- T. Wang and M.L. Oristaglio. GPR imaging using the generalised radon transform. *Geophysics*, 65(5):1553–1559, 2000.
- C.P.A. Wapenaar and A.J. Berkhout. *Elastic wave field extrapolation: redatuming of single-and multi-component seismic data*. Advances in Exploration Geophysics 2. Elsevier Science, Amsterdam, 1989.
- C.P.A. Wapenaar, P. Herrmann, D.J. Verschuur, and A.J. Berkhout. Decomposition of multicomponent seismic data into primary P- and S-wave responses. *Geophysical Prospecting*, 38:633–661, 1990.
- O. Yilmaz. *Seismic data processing*. Investigations in Geophysics, Volume 2. Society of exploration geophysicists, Tulsa, 1987.

- X. Zeng, G.A. McMechan, and T. Xu. Synthesis of amplitude-versus-offset variations in ground-penetrating radar data. *Geophysics*, 65(1):113–125, 2000.
- J. Zhe and S.A. Greenhalgh. Prestack multicomponent migration. *Geophysics*, 62(2):598–613, 1997.
- A.P.M. Zwamborn and P.M. van den Berg. The three-dimensional weak form of the conjugate gradient FFT method for solving scattering problems. *IEEE Transactions on Microwave Theory and Techniques*, 40(9):1757–1766, 1992.

Summary

The shallow subsurface is of growing importance for engineering activities, environmental issues and archaeological investigations. Because of this increased activity, it is important to obtain an image of the subsurface to disclose the presence and position of buried objects and the composition of the subsurface. Ground Penetrating Radar (GPR) is an electromagnetic high resolution tool, that has been employed successfully to perform numerous environmental, engineering and archaeological investigations.

Because of similarities between acoustic and electromagnetic prospecting methods, seismic imaging techniques were initially used for the imaging of GPR data. However, there are also important differences between acoustic and electromagnetic prospecting methods. The most important difference is the vectorial character of electromagnetic waves compared to the scalar acoustic waves. The vectorial radiation characteristics of an elementary antenna shows angle-dependent amplitude and polarisation variations. Another difference is the acquisition set-up. A GPR survey is usually carried out with one source and one receiver at a fixed distance, also called common-offset measurement, whereas a seismic survey uses for each source a number of receivers, also called multi-offset measurement. These differences show the need for special adaptations to make the seismic processing methods suitable for GPR data.

The main objective of this thesis is to derive a three-dimensional imaging algorithm for ground penetrating radar data, which maps the measured reflections at the location where they originally came from and returns an image which represents the properties of the scatterer. On the whole, we can

say that the obtained image is the final result of a field survey, which comprises the acquisition of the data in the field, and the imaging procedure in which the appropriate forward model is used. The electromagnetic scattering formalism is derived using the Born approximation and several independent point scatterers are considered to represent a finite object. The electromagnetic scattering formalism, which is used as a forward model, plays a central role.

First of all, the scattering formalism is used to determine the required acquisition parameters, the spatial and temporal sampling ratio. Secondly, a quantitative analysis of the sensitivity to reflections coming from certain objects for a specific acquisition set-up is performed. This analysis shows that the influence of unwanted reflections from an object present above the surface can be reduced by choosing the antenna configuration so that the polarisation of the electric field is perpendicular to the orientation of the object. Thirdly, the electromagnetic scattering formalism is used as a point of departure to derive systematically a three-dimensional imaging algorithm for ground penetrating radar data.

The three important parameters, which must be incorporated in the three-dimensional imaging algorithm are, in order of importance, the wave speed, the polarisation and the amplitude characteristics. The electromagnetic scattering formalism, which incorporates these three parameters, is used to determine an inverse wavefield extrapolator which corrects for the propagation effects. The far-field vectorial radiation characteristics, which are part of the scattering formalism, show that at a specific angle no energy is emitted or received. Because of these zeros in the far-field radiation characteristics, the single-component inverse wavefield extrapolator is not bounded. This is the reason why more components are used containing more complete information, in order to arrive at a bounded inverse wavefield extrapolator. Therefore, four possible measurement set-ups are combined to enable a matrix inversion of the tensorial forward wavefield extrapolator. This leads to a multi-component imaging algorithm, which takes into account the phase velocity, the polarisation and the amplitudes of the scattered electric field. The performance of the multi-component algorithm is investigated by comparing it to scalar imaging algorithms, the SAR and the Gazdag algorithms. The imaging of a point scatterer is analysed for one single frequency at a certain depth, which results in a resolution function. The multi-component imaging algorithm returns a circularly symmetric resolution function, which shows that the radiation characteristics of the source and receiver anten-

nas do not influence the obtained image, because their influence is corrected for by the multi-component imaging algorithm. This is in contrast to the scalar imaging algorithms, which return a non-circularly symmetric resolution function, indicating that the radiation characteristics of the source and receiver antennas still influence the obtained image. Another benefit of the multi-component imaging algorithm is that it represents the properties of the point scatterer more accurately than the scalar imaging algorithms. This is indicated by the phase difference compared with the expected phase of the imaging result, which is the smallest for a multi-component imaging algorithm.

Experimental results of the imaging of several buried objects with different medium properties and different orientations are presented. The multi-component imaging algorithm enables the use of cross-polarised measurements in such a way that a relatively larger amplitude is obtained for oblique objects and spherical scatterers, compared with the scalar imaging algorithms. Due to the fact that the wavelet is not known, it is not feasible to obtain the properties of the object. However, the phase differences, which occur in the experimental data, are similar to the phase differences obtained with synthetic results. This indicates that using the multi-component imaging algorithm a more representative image is obtained than with the scalar imaging algorithms.

To conclude, the multi-component imaging algorithm, which is based on the electromagnetic scattering formalism, shows a lot of potential. The improved results are obtained because the multi-component imaging algorithm incorporates all three important parameters for imaging: the wave speed, the polarisation and the amplitude characteristics of the scattered electric field.

J. van der Kruk

Samenvatting

De ondiepe ondergrond wordt steeds belangrijker voor technologische activiteiten, milieu onderzoek en archeologische opsporingen. Hiervoor is het belangrijk om een goed beeld te krijgen van de aanwezigheid en positie van begraven objecten en de samenstelling van de ondiepe ondergrond. Grondradar is een elektromagnetisch systeem met een hoge resolutie, dat succesvol gebruikt wordt om deze onderzoeken uit te voeren.

Omdat er veel overeenkomsten bestaan tussen de akoestische en elektromagnetische exploratie, werden in eerste instantie seismische beeldvormingstechnieken gebruikt om van grondradar-data een beeld van de ondergrond te vormen. Er zijn echter ook belangrijke verschillen tussen de akoestische en de elektromagnetische exploratie methodes. Het belangrijkste verschil ten opzichte van de scalaire akoestische methode is het vectoriële karakter van de elektromagnetische golven. De vectoriële stralingskarakteristieken van een elementaire antenne laat een hoekafhankelijke amplitude en polarisatie van het elektrische veld zien. Een ander verschil is de opzet van de acquisitie. Waar voor een seismische meting voor een enkele meting één bron en meerdere ontvangers worden gebruikt, wordt een grondradar meting meestal uitgevoerd met één bron en één ontvanger op een vaste afstand. Deze verschillen laten zien dat er speciale aanpassingen vereist zijn om de akoestische algoritmes geschikt te maken voor het toepassen op grondradar-data.

Het voornaamste doel van dit proefschrift is om een drie-dimensionaal beeldvormingsalgoritme af te leiden voor grondradar-data, dat een representatief beeld weergeeft van de ondergrond. Het verkregen beeld is het uiteindelijke resultaat van het gebruik van de metingen in het veld als invoer voor het

beeldvormingsalgoritme, welke gebruik maakt van een geschikt voorwaarts model. In dit proefschrift wordt het elektromagnetisch verstrooiingsformalisme gebruikt voor het voorwaartse model dat is afgeleid met behulp van de Born-benadering. Een eindig object wordt beschouwd te zijn opgebouwd uit meerdere onafhankelijke puntverstrooiers.

Het elektromagnetische verstrooiingsformalisme heeft een centrale rol. Als eerste is het verstrooiingsformalisme gebruikt om de benodigde acquisitie parameters, de ruimtelijke en temporele bemonstering, te bepalen. Ten tweede is een kwalitatieve analyse uitgevoerd om de gevoeligheid te bepalen voor verschillende antenneconfiguraties voor reflecties welke van bepaalde objecten komen. Deze analyse toont aan dat de invloed van ongewilde reflecties van een object, dat aanwezig is in de lucht, verkleind kan worden door de antenneconfiguratie zo te kiezen dat de polarisatie van het elektrische veld loodrecht staat op de oriëntatie van het object. Ten derde is het verstrooiingsformalisme als uitgangspunt gebruikt om systematisch een drie-dimensionaal beeldvormingsalgoritme voor grondradar-data af te leiden.

De drie belangrijke parameters die het drie-dimensionale beeldvormingsalgoritme moet bevatten zijn de golfsnelheid, de polarisatie en de amplitude karakteristieken. Het elektromagnetische verstrooiingsformalisme dat deze drie parameters correct beschrijft, wordt gebruikt om een inverse golfveld extrapolator af te leiden welke corrigeert voor de propagatie effecten. De verreveld vectoriële stralingskarakteristieken, welke onderdeel zijn van het verstrooiingsformalisme, laten zien dat voor een specifieke hoek er geen energie wordt uitgezonden of ontvangen. Door deze nulpunten in de stralingskarakteristiek is de inverse golfveld extrapolator niet begrensd wanneer één component gebruikt wordt. Dit motiveert het gebruik van meerdere componenten, welke meer en completere informatie bevatten, om zo een begrensde inverse golfveld extrapolator af te leiden. Om dit te bereiken worden er vier antenneconfiguraties gebruikt die een matrix inverse mogelijk maken van de tensoriële voorwaartse golfveld extrapolator. Dit leidt tot het multicomponenten beeldvormingsalgoritme, dat de fase snelheid, de polarisatie en de amplitudes van het verstrooide elektrische veld in rekening neemt.

De prestatie van het multicomponenten beeldvormingsalgoritme is onderzocht door de resultaten te vergelijken met scalaire beeldvormingsalgoritmes. De beeldvorming van een puntverstrooier is onderzocht voor één frequentie op een bepaalde diepte wat resulteert in een resolutie functie. Het gebruik van het multicomponenten beeldvormingsalgoritme resulteert in een circulair symmetrische resolutie functie, wat aantoont dat de stralingskarakter-

ristieken van de bron- en ontvangstantennes het verkregen beeld niet beïnvloeden, omdat voor hun invloed gecorrigeerd is door het multicomponenten beeldvormingsalgoritme. Dit is in tegenstelling met het gebruik van de scalaire beeldvormingsalgoritmes, wat resulteert in een niet-circulair symmetrische resolutie functie. Dit resultaat toont aan dat de stralingskarakteristieken van de bron- en ontvangstantennes het verkregen beeld beïnvloeden. Een ander voordeel van het multicomponenten beeldvormingsalgoritme is dat het de eigenschappen van de puntverstrooier beter weergeeft dan de scalaire beeldvormingsalgoritmes. Dit wordt duidelijk doordat de faseverschillen vergeleken met de verwachte fase van het beeldvormingsresultaat het kleinste zijn voor het multicomponenten beeldvormingsalgoritme.

Experimentele resultaten van de beeldvorming van verschillende begraven objecten met verschillende mediuimeigenschappen en verschillende oriëntaties zijn geanalyseerd. Het multicomponenten beeldvormingsalgoritme maakt gebruik van kruisgepolariseerde metingen. Een relatief grotere amplitude wordt verkregen voor schuine objecten en sferische objecten, vergeleken met scalaire beeldvormingsalgoritmes. Door het feit dat de bronsignatuur niet bekend is, is het echter niet mogelijk om de eigenschappen van de objecten te bepalen. Echter, de faseverschillen welke zich voordoen in de experimentele data zijn vergelijkbaar met de faseverschillen welke verkregen zijn met de gemodelleerde data. Deze resultaten geven aan dat het gebruik van het multicomponenten beeldvormingsalgoritme resulteert in een representatiever beeld vergeleken met de scalaire beeldvormingsalgoritmes.

Samenvattend kunnen we zeggen dat het multicomponenten beeldvormingsalgoritme veelbelovend is. De verbeterde resultaten zijn verkregen omdat het multicomponenten beeldvormingsalgoritme alle drie de belangrijke parameters voor beeldvorming in rekening neemt; de golfsnelheid, de polarisatie en de amplitude karakteristieken.

J. van der Kruk

Curriculum Vitae

Jan van der Kruk was born at Monster (near The Hague), the Netherlands, on the 29th of June 1972. He attended secondary school at the Zandeveld College in 's-Gravenzande, where he obtained the Atheneum diploma in 1990. In that year he started his study Electrical Engineering at Delft University of Technology.

He received his bachelors degree ('propedeuse') in 1991 and continued for his M.Sc. degree ('Ingenieur'). In 1995 he finished his M.Sc. in the Laboratory of Electromagnetic Research, under the supervision of Professor dr. P.M. van den Berg. His M.Sc. thesis dealt with the determination of an apparent resistivity of the Earth from electromagnetic sounding with magnetic dipoles. This apparent resistivity method was used in several field surveys during a three montly period at the National Institute of Applied Geoscience TNO under supervision of Dr. J.A.C Meekes.

In 1996, he started his Ph.D. research at the section of Applied Geophysics, department of Applied Earth Sciences at the Delft University of Technology supervised by his promotors Professor dr. ir. J.T. Fokkema and Professor dr. ir. P.M. van den Berg. During this Ph.D. research he presented his results twice a year at the progress meeting of the user committee of the STW project, "Improved Ground Penetrating Radar Technology", consisting of several companies. In addition, he presented his work at several international conferences. His research resulted in several international publications.

Dankwoord /Acknowledgements

Als afsluiting wil ik in dit dankwoord alle mensen noemen die in belangrijke mate hebben bijgedragen tot de totstandkoming van dit proefschrift en die mij tot steun zijn geweest om dit promotie onderzoek uit te voeren.

Jacob Fokkema en Peter van den Berg voor het optreden als promotoren van dit proefschrift. Jacob Fokkema, die voor de vele randvoorwaarden voor een goed onderzoek zorgde en ondanks zijn drukke agenda toch altijd tijd voor mij vrij maakte. Ook de persoonlijke betrokkenheid heb ik zeer op prijs gesteld. Peter van den Berg, ook mijn afstudeerprofessor, die in de laatste fase van het onderzoek de tijd en rust had om mij de juiste knopen door te laten hakken.

Kees Wapenaar, die met zijn onuitputtelijke kennis over seismische beeldvorming een grote bron van inspiratie was voor het multi-componenten beeldvormings algoritme.

Evert Slob, bedankt voor de vele discussies over numerieke en analytische onderwerpen. Jouw open deur liet altijd ruimte om binnen te lopen en allerlei onderwerpen te bespreken.

Jeroen Groenenboom, bedankt voor de vele kritische vragen en diepgaande discussies. Jouw nuchtere kijk op de zaken werkte veelal relativerend. Ook de L^AT_EX-layout en de matlab scripts hebben zeker bijgedragen tot de vormgeving van dit proefschrift.

In de begin van mijn promotie waren er de TNO-ers Ronnie van Overmeeren en Wim van Dalftsen die hun ervaring op grondradar gebied graag met mij deelden. Zij organiseerden bij TNO het AIO overleg. Tijdens dit overleg bespraken verschillende AIO's/promovendi en TNO-ers de verschillende as-

pecten van grondradar metingen. Door deze discussies met Ronnie, Wim, Sjef, Remke, Sander, Bart, Rogier en Vincent werden vele ervaringen uitgewisseld. Tijdens deze discussies kwam ook het probleem van oppervlakte reflecties ter sprake. Dit was de aanleiding voor het onderzoek beschreven in Sectie 5.9.

The time spent by the commission members and their suggestions to improve the thesis are all very much appreciated. I thank Peter Annan for the many inspiring discussions on many conferences. He always came to the essence of the research and gave valuable suggestions to extend the research, such as the influence of the top layer on the unwanted reflections from above surface objects as discussed in Section 5.9.

Voor dit onderzoek zijn er ook meerdere experimenten uitgevoerd. Deze experimenten zijn voornamelijk soepel verlopen door de hulp van Leo de Groot en Albèr Hemstede, die ook het multi-componenten frame geconstrueerd hebben (Figuur 7.5).

Remke van Dam wil ik bedanken voor de hulp bij de time domain reflectometry (TDR) metingen, waarvan een resultaat beschreven is in Sectie 7.6.

Rob Remis wil ik bedanken voor het gebruik van zijn 3D voorwaartse modeleringsprogramma, waarvan de resultaten beschreven zijn in Sectie 5.9.

De STW gebruikerscommissie wil ik bedanken voor al de discussies die hebben bijgedragen tot een beter begrip van de verschillende aspecten die van belang zijn bij grondradar metingen.

Alle studenten en studentes wil ik bedanken voor het meehelpen met de metingen tijdens de vele veldwerken.

Mijn Collega's: Gerd Swinnen, Rob Hegge, Michel Schonewille, Menno Dillen, Philippe Steeghs, Rutger van Spaendonck, Jan Willem Schoolmeesters, Lourens van Zanen, Jeroen Goudswaard, Guy Drijkoningen, Ranajit Ghose, DOGS, Miranda, Jolanda en Monica, bedankt voor alles!

Fredrik, Isabelle, Maarten en Pierre, bedankt voor de vele etentjes.

Ilona en Henk, Stephan en Wilma, Rinze en Annelies, Beatrijs, Gerard, Andre, bedankt voor alles!

Ûlepanne, bedankt voor de vele uitwaaidagen op de Friese meren.

Mijn familieleden, in het bijzonder mijn ouders Wim en Nel en mijn zussen Marian en Greet, hebben mij door al die jaren heen gesteund in al mijn bezigheden.

Nogmaals, iedereen bedankt die mij de energie, steun en het vermogen heeft gegeven om deze promotie af te ronden.